Aseismic Deformation in Subduction Megathrusts: Central Andes and North-East Japan

Thesis by

Francisco Hernán Ortega Culaciati

In Partial Fulfillment of the Requirements

for the Degree of

Doctor of Philosophy

California Institute of Technology

Pasadena, California

2013

(Defended May 28, 2013)

A mis padres Hernán y Rosita
y a mi nono Fortunato

"For the chief malady of man is restless curiosity about things which he cannot understand; and it is not so bad for him to be in error as to be curious to no purpose"

Blaise Pascal

Acknowledgments

It has been a bit more than seven years since I first set foot in Caltech. I do not want to say here how much effort and how hard was to get to finally write these words, as I believe that everyone that is about to earn a doctorate, especially at Caltech, has walked through similar and extremely bumpy roads as I have done up to this moment. I will offer here excuses for my “chilenglish” and just say, it has been seven years. Seven years which at first sight seem a long time, but there were short, as time flies when one is doing what one likes the most and when one is surrounded by the best people, both from here and back at home. Is in this pages, the last I write here in my thesis, in which I wish to convey my extreme gratitude to everyone that made these words possible, the last words that seal this thesis and this period of my life.

I would like to start with my parents, Hernán and Rosita, and my Nonno Fortunato, whom always, with an infinite love, made an extreme effort to give me the best education, always pushing me to improve myself in every aspect of my life, regardless of the situation and how much effort it could take. They supported me in every decision I made, even the ones that took me away from them, I would not be here if not for them. I would like to thank as well the rest of my family, Rosita – Giancarlo, Valentina – Jaime, Esteban, Jaime, Haydee, Daniela, Julio, Lola, Pablo, Fani for being with me, everyone in its own way, no matter what, even from far away. Thanks a lot!!!

I would like to give thanks to all my professors, to Herminia, because I could not have made it too far without your teaching and encouragement. To Diana Comte, who showed me what geo-

sciences looks like and for being the professor and friend I have to thank for literally throwing me into that lab room where all the Caltech professors were at that time in Chile. That single and simple action ended up in what I am becoming today. I'd like to thank as well to all the professors in DGF–UCHILE whose support and encouragement I received during all this time.

At Caltech I always received the best support, not only from all the professors, but from everyone that works or worked here. I cannot avoid to start with Vlad and Marina, my first great friends here, which made life so much easier when starting my studies, thanks a lot for your care, and for those long conversations and for sharing with me those moments that only true friends can share. I would like to give a big thanks to all the professors here at Caltech, in particular to my TAC and Thesis committee Rob, Pablo, Jean-Philippe and especially to my mentor and friend, Mark, which not only educated me in geosciences and in sciences in general, and to be as practical as possible when it comes to get stuff done, but also supported me under any circumstances, and encouraged me to be a better scientist and to "de-Chilenize" my biological clock and adjust it to the American one. Thanks Mark for everything, it was a real pleasure learning from you and to work with you, and it will be as well to continue working with you in the future. I cannot forget to give thanks to Donna, Sarah, Rosemary, Julia, Viola, Lisa and Heather for being always there fully loaded with energy to help us all the time.

I would like to give a special thanks to my friends, both from Chile – Phillipo, Monica, Pancha, Pato, Jenny, Polo, Marcelo, Cristobal, Ana, Ninja, Cindy, Felipe, Carola, Beto, and especially to Fabian, Carolina and Sofía, with which I spend great moments here in L.A. and were the best support I ever had here – and from USA – Laura Alisic, Walter, Laura Perez, Daniel, Margarita, Carlos, Ruby, Pablo, Enrique, Inés, Jeff, John, Jean, Javier, Roberto, and especially to Rodrigo, Javiera, Andrés and Rayito who let me stay at their place these last few days and allowed me to share a lot with them and to have a great company during these, my last days in the USA. Thanks

to all of you, for being that, my friends!!!.

If for some reason I involuntarily left someone in the ink pot, my excuses, I am sure you deserve the best of thanks here.

Finally, I want to end these words with a phrase that always made sense to me,

“ The four cardinal points are three, the south and the north ”

(Altazor – Vicente Huidobro)

Abstract

We aim to characterize fault slip behavior during all stages of the seismic cycle in subduction megathrust environments with the eventual goal of understanding temporal and spatial variations of fault zone rheology, and to infer possible causal relationships between inter-, co- and post-seismic slip, as well as implications for earthquake and tsunami hazard. In particular we focus on analyzing aseismic deformation occurring during inter-seismic and post-seismic periods of the seismic cycle. We approach the problem using both Bayesian and optimization techniques. The Bayesian approach allows us to completely characterize the model parameter space by searching *a posteriori* estimates of the range of allowable models, to easily implement any kind of physically plausible *a priori* information and to perform the inversion without regularization other than that imposed by the parameterization of the model. However, the Bayesian approach computational expensive and not currently viable for quick response scenarios. Therefore, we also pursue improvements in the optimization inference scheme. We present a novel, robust and yet simple regularization technique that allows us to infer robust and somewhat more detailed models of slip on faults. We apply such methodologies, using simple quasi-static elastic models, to perform studies of inter-seismic deformation in the Central Andes subduction zone, and post-seismic deformation induced by the occurrence of the 2011 Mw 9.0 Tohoku-Oki earthquake in Japan. For the Central Andes, we present estimates of apparent coupling probability of the subduction interface and analyze its relationship to past earthquakes in the region. For Japan, we infer high spatial variability in material

properties of the megathrust offshore Tohoku. We discuss the potential for a large earthquake just south of the Tohoku-Oki earthquake where our inferences suggest dominantly aseismic behavior.

Contents

List of Figures

List of Tables

Chapter 1

Introduction

Space geodesy allows us to monitor crustal deformation at the surface of the Earth – deformation that is caused by a diversity of geophysical processes. Examples of such processes include motion of the tectonic plates, regional distributed deformation at plate boundaries, deformation of the crust associated with the elastic earthquake cycle and aseismic slip on faults, seasonal deformation associated with hydrologic forcing and volcanic deformation. In particular, geodetic networks of receivers of the Global Positioning System (GPS) that record continuously can be used to monitor the spatial and temporal evolution of crustal deformation. These observations, together with seismological observations, allow one to infer the character of fault slip and eventually to constrain mechanical models. In the context of subduction megathrusts, such estimates allow us to improve our understanding of spatial and temporal variations of fault behavior throughout the seismic cycle and its implications for earthquake and tsunami hazard. Inverse methodologies play a key role in this "quest for information" (*Tarantola and Valette*, 1982), allowing us to estimate parameters defining subsurface processes using surface measurements. Regardless of the details of the methodology, the use of a priori knowledge will bias our estimates. Thus, one must take care with the use of a priori information, especially given our limited access to the actual physical system.

The temporal scale of the seismic cycle in subduction zones spans from seconds to thousands of years. The global seismological network was established by the end of the 1960's, while continuous

and widespread geodetic monitoring of crustal deformation did not begun until the end of the 20^{th} century. Thus, we have been able to continuously and densely observe only a small fraction of the evolution of the megathrust seismic cycle. This limited period of observations is manifest in our limited knowledge of the physics controlling earthquake occurrence in subduction zones. As an example, the 11 March 2011 ($M_w 9.0$) Tohoku-Oki earthquake and its associated tsunami in Japan, took the scientific community by surprise as it had an extent and location that was not predicted by coupling models using recent geodetic measurements nor by seismic hazard studies analyzing megathrust events from the last 500 years[†]. Events such as the Tohoku-Oki earthquake motivate much of the effort in this thesis. For example, in chapter 3 we discuss the effects of commonly adopted *a priori* information in linear least square estimates of subsurface fault slip and propose theoretical improvements to ameliorate shortcomings of such analyses.

Observations of crustal deformation during the inter-seismic and post-seismic periods can be used to differentiate the seismogenic regions of the subduction megathrust from those that tend to behave aseismically. To fully exploit such observations, we need to solve an inverse problem that is intrinsically ill-posed. Thus, one must devise schemes that provide robust estimates and minimize bias introduced by our *a priori* knowledge on the subduction system as well as limit the use of *a priori* information to be as physical as possible. In this thesis, we analyze two approaches to infer the kinematics of the subduction interface based on surface observations. A fully Bayesian approach, which allows us to completely characterize the solutions and uncertainties of the inverse problem and allows us to use only physically justifiable *a priori* information without the need of additional regularization; and the optimization approach which gives biased solutions due to the need of regularization of the solutions because of the ill-posed nature of the inverse problem. In the optimization approach, we propose a novel regularization scheme that allows us to infer more stable

[†]Although there were some insights from the 869 July 17 Jogan earthquake, which may have closely resembled the 2011 event (*Minoura et al.*, 2001).

and robust estimates of slip on faults in a case such as the Japan megathrust where there is a large spatial variation of the sensitivity of fault slip to available onland observations.

In Chapter 2 of this thesis we analyze positional time series of crustal deformation in the Central Andes and Japan Trench subduction zones, where we isolate earthquake, seasonal, secular and anthropogenic signals that are later used as constraints for inter-seismic coupling models in the Central Andes subduction zone and for inferences of after-slip triggered by the occurrence of the Tohoku-Oki earthquake in Japan.

In Chapter 3, we first review the optimization approach for regularized linear static fault slip inversion problems and discuss the pros and cons of commonly used regularization schemes. We then derive a simple yet robust regularization scheme that accounts for the spatial variability of the constraints on-land geodetic measurements typically provide on estimates of slip on different regions of a given fault. Since fully Bayesian inference schemes are coming of age due to the increase in computational power, we develop a Bayesian framework within which we can use a priori information that is related to quantities typically used in the common optimization approach. Most importantly, these developments provide a theoretical understanding and a unified formulation to aid interpretation of many regularization techniques under a Bayesian framework.

In Chapter 4, we analyze post-seismic deformation associated to the Tohoku-Oki earthquake. Since this earthquake was unexpected by the scientific community, we are particularly interested in inferences of the behavior in the shallow portion of the Japan Trench megathrust just south of the rupture area of the Tohoku-Oki event with the aim of studying the potential for a future earthquake in the region. Although not definitive, our modeling suggests that this portion of the megathrust is undergoing aseismic fault slip. Based on variations in the characteristic time scale of postseismic fault slip, we also infer strong heterogeneity in the spatial distribution of the mechanical properties of the Japan Trench megathrust.

In Chapter 5 we develop a novel and simple model of inter-seismic coupling in subduction zones. We use a fully Bayesian approach as an inference scheme, where we propose a representation of the ensemble of models obtained during the Bayesian inversion as estimates of apparent coupling probability and we analyze and compare our inferences of coupling with co- and post-seismic slip behavior associated to past earthquakes in the region.

In the final chapter, we summarize and analyze the main results of this thesis and we give some insights on the continuation of this work in the future.

Chapter 2

Post-processing of GPS Time Series

2.0 My contribution in this chapter

- Development of computational codes to post-process positional time series and isolate signals modeled in equation (2.1).
- Catalog of displacements associated to various earthquakes recorded by GEONET and CAnTO GPS networks (Figures 2.7 - 2.22, 2.25, 2.26).
- Estimation of secular rates using GEONET and CAnTO GPS networks in Japan and Central Andes, respectively.
- Estimation of post-seismic displacements associated to the March 11, 2011 Tohoku-Oki ($Mw9.0$) earthquake. Post-seismic displacements are estimated between mainshock time and September 22, 2012.

2.1 Introduction

The Global Positioning System (GPS) is a space-based navigation system consisting of a constellation of satellites that enables positioning, within a given reference frame, of a specialized GPS receiver antenna that has direct line of sight with at least 4 satellites of the constellation. Geodetic

networks of GPS receivers can be used to monitor and study the surface deformation of the Earth, produced by a wide variety of geophysical processes, at spatial scales that are only limited by the extent and density of the GPS networks. Among examples of geophysical processes studied based on measurements of surface deformation sampled with the aid continuous GPS networks are: the estimation of global plate motions (e.g., *Sella et al.*, 2002; *Argus et al.*, 2010), regional deformation of the crust at plate boundaries (e.g., *Sagiya et al.*, 2000; *Aoki and Scholz*, 2003; *Meade and Hager*, 2005; *McCaffrey et al.*, 2013), co- and post- seismic deformation (e.g., *Heki et al.*, 1997; *Hsu et al.*, 2006; *Simons et al.*, 2011; *Vigny et al.*, 2011; *Ozawa et al.*, 2011, 2012), deformation associated to aseismic events (e.g., *Dragert et al.*, 2001; *Miller et al.*, 2002; *Sagiya*, 2004; *Hirose and Obara*, 2005; *Radiguet et al.*, 2011), seasonal deformation (e.g., *Heki*, 2006), and volcanic deformation (e.g., *Owen et al.*, 2000; *Puskas et al.*, 2007; *Larson et al.*, 2010), etc. We focus in the analysis of positional GPS time series sampling crustal deformation associated with all the stages of the seismic cycle. In particular we try to isolate tectonic signals within positional time series obtained from continuously recording GPS networks in the regions of the Central Andes and Japan Trench subduction zone megathrusts.

2.2 Methodology

Positional time series are obtained by a process of trilateration based on estimates of GPS receiver-satellite pseudo-distances obtained during the processing of the raw data received from the visible portion of the satellite constellation (For a general description of the procedure see *Blewitt*, 1997, 2007). Typically, global and regional processes such as solid Earth tides, ocean tidal loads and atmospheric delay of the GPS signal, are estimated or modeled independently and used to produce positional time series not influenced by such processes. The resulting GPS positional time series contain signals coming from different sources at different spatial and temporal scales. The sources

include geophysical processes, artifacts in the actual positioning system itself and anthropogenic non-tectonic sources. Geophysical signals may include secular motion due to inter-seismic tectonic loading, earthquake associated deformation (co-seismic deformation and post-seismic relaxation), quasi-periodic terms associated with hydrological forcing, and transient signals that may be caused by aseismic dislocation on faults, processes related to volcanism, etc. The GPS position estimation process also produces visible signals on the positional data. For example, a periodic sidereal signal is observed for sub-daily positioning estimates ranging from a few centimeters to meters. As the GPS satellites orbit the Earth the satellite constellation is constantly changing, repeating the same configuration approximately every 23 hours and 56 minutes (*Larson et al.*, 2007). The motion of the satellite constellation changes scattering patterns of the GPS signal electromagnetic waves in the immediate vicinity of the GPS antenna, thus changing the estimations of its position. There are also apparent motions that are coherent across the whole GPS network, commonly referred to as Common Mode Error (CME). CME may be interpreted as errors in the determination of the reference frame for each epoch produced by uncertainties in the position of the GPS satellites as well as in satellite clocks. CME ranges from a few millimeters to centimeters, thus its identification and removal is essential if our eventual goal is to identify subtle tectonic signals.

We aim to analyze long-term deformation signal associated with all the stages of the seismic cycle in subduction zone megathrusts, particularly we are interested in analyzing deformation patterns induced by tectonic loading due to inter-seismic coupling and post-seismic deformation after large earthquakes, both processes have associated time-scales that goes from months to several years, therefore we choose to use daily estimations of the GPS receiver positions to explore for such processes. Daily positional time series average over the sidereal period and are thus ignored here. If we ignore the signals potentially produced by transient aseismic events such as the ones observed in southern Japan (e.g., *Ozawa et al.*, 1999, 2003, 2004), we can approximate daily positional time

series with a functional form such as,

$$u(t) = u_0 + vt + \sum_i \left[c_i(t) + p_i(t)\right] + \sum_k h_k(t) + s(t) + \text{CME}(t) \tag{2.1}$$

$$c_i(t) = u_c^i \text{H}(t - t_0^i) \tag{2.1a}$$

$$p_i(t) = \alpha_R^i \log\left(1 + \frac{(t - t_0^i)}{\tau}\text{H}(t - t_0^i)\right) \tag{2.1b}$$

$$h_k(t) = \beta^k \text{H}(t - t^k) \tag{2.1c}$$

$$s(t) = \gamma_1 \sin\left(\frac{t}{T_1} + \phi_1\right) + \gamma_2 \sin\left(\frac{t}{T_2} + \phi_2\right) \tag{2.1d}$$

where $\text{H}(\cdot)$ is a Heaviside function, $T_1 = 1$yr, $T_2 = 0.5$ yrs, τ is the decay time of the post-seismic relaxation signal. The positional time series in equation (2.1) are separated into a constant offset (u_0), secular motion due to inter-seismic tectonic loading (v), earthquake associated deformation (co- and post- seismic, $c_i(t)$, $p_i(t)$), seasonal terms $s(t)$ associated with hydrologic forcing, as well as anthropogenic signals $h_k(t)$ related to changes in hardware or location of the site. Here, t_0^i and t^k indicate the time of occurrence for the i-th earthquake and k-th anthropogenic step, respectively. In the context of this model, if we find transient signals, we proceed to model them as a single jump at the middle of the signal time span and to increase the uncertainties (by a factor of 1000) of the positional data during such transients, effectively treating the transient temporal evolution as noise. In future analysis we will include a parameterized model for the aseismic process using, for example, spline functions.

We identify and separate the components of the time series in (2.1) through an iterative process similar to *Dong et al.* (2006), in which the CME is also estimated and removed. The process is illustrated in Figure 2.1(b). We first examine positional time series to identify the time of occurrence of any earthquakes and anthropogenic signals, we then fit for the different components of the time series in the model (2.1) using a traditional weighted least squares method, where the weights

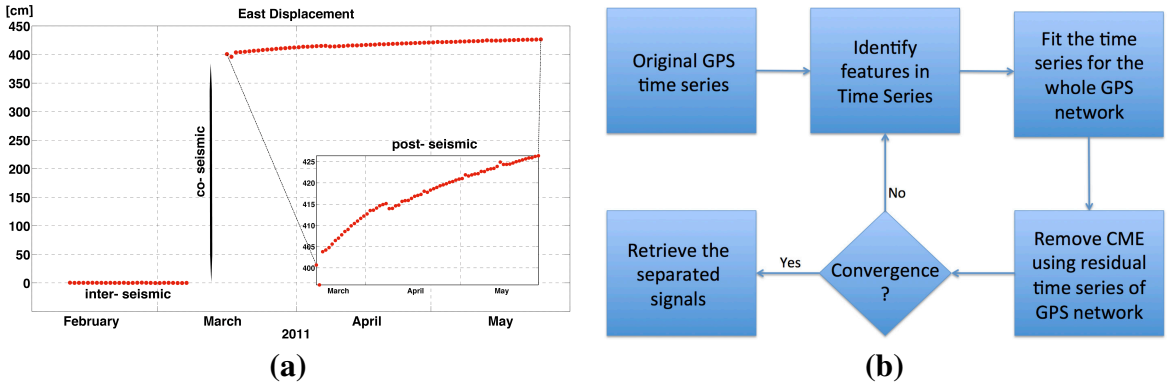

Figure 2.1. (a) Example of a daily positional time series from continuous GPS observations in Japan. The 3 stages of the seismic cycle are labeled, where the co-seismic jump corresponds to the one of the 11 March 2011, Tohoku-Oki earthquake. The inset shows the induced post-seismic motion as well as signals from several aftershocks. (b) Iterative workflow used to identify and separate the different components present in the positional time series.

are chosen as the reciprocal of the positional variances. Then, based on high-pass-filtered post-fit residuals, we calculate and remove the CME from the original data. We repeat the process until no new features are identified in the positional time series. The residual time series are filtered by removing a long period signal calculated from a running median filter computed using a running window of 1 month centered at each sample. During the production of the original positional time series, orbital parameters are re-estimated for each epoch, causing CME to be dominantly a high frequency signal. High-pass-filtering residuals avoids contaminating estimates of CME with misfits from crudely modeled long period transient signals. Nevertheless, transient signals with a duration of less than a month may affect the estimation of the CME.

During the least squares fitting process, observational uncertainties are rescaled to achieve a reduced chi-squared of 1. We first fit the positional time series using the formal errors of the positional time series as uncertainties for the misfit function. Then we do a second fit in which we use a scaled version of the formal errors with a scale factor defined as the standard deviation of the first residual fit over the average value of the formal errors of the positional time series. We isolate the signals in the positional time series using the fit with the rescaled uncertainties.

As part of the signal identification process in the positional time series, we identify annual and semi-annual seasonal signals. Figures 2.6 and 2.24 show estimates of phase and maximum amplitude of the seasonal components for the positional time series in northeast Japan and Central Andes subduction zones. Those figures show phase as the orientation of a couple of blue and red arrows, which points in opposite directions indicating the time of the year in which the seasonal component reaches it maximum and minimum value of movement respectively. The size of the arrows indicate the maximum amplitude of the seasonal component on each GPS site. Figure 2.2 shows the legend needed to interpret the phase in of each seasonal component as the time of the year in which their maximum amplitudes occur. For example, if the blue-red arrows in Figure 2.2 represent the annual and semi-annual signal for the vertical (up is positive) component of the positional time series, the orientation of the arrows indicates that for the annual seasonal signal, maximum uplift and subsidence occurs in June and December, respectively. For the semi-annual seasonal signal, the diagram indicates that maximum uplift occurs in March and September, and maximum subsidence in June and December.

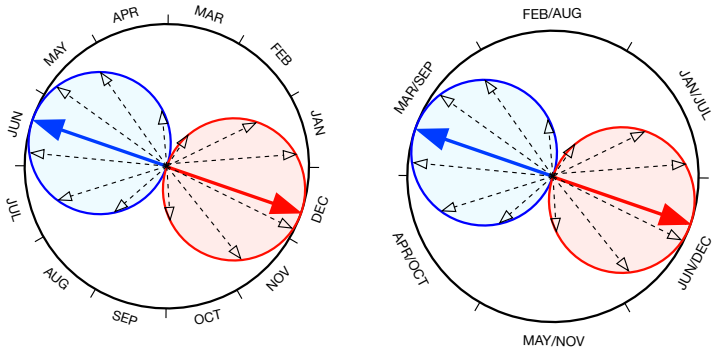

(a) Annual (b) Semi-Annual

Figure 2.2. Legend for annual and semi-annual seasonal component phase and amplitude. Blue and red arrows indicate the time of the year in which each seasonal signal reaches its maximum amplitude in the positive and negative direction of the considered component of positional time series, respectively. Blue and red circles show the amplitudes at different times of the period considered for the seasonal component. Black dashed arrows show the amplitude of the seasonal component at randomly selected times.

2.3 Japan GPS time series post-processing

We estimate post-seismic crustal deformation following the Great Tohoku-Oki ($M_w 9.0$) mainshock using positional time series at GPS sites in northeast Japan. We use +16 years of data provided by the Geospatial Information Authority (GSI) of Japan to produce daily positional time series using the software GIPSY/OASIS (JPL) referenced to ITRF 2008. Processing of the raw GPS data was performed by Susan Owen and Angelyn Moore at the Jet Propulsion Laboratory (JPL) as part of the ARIA (Advanced Rapid Imaging and Analysis) project, a collaboration between Caltech and JPL.

The positional time series measured near the region affected by the Tohoku-Oki ($M_w 9.0$) earthquake are dominated by large co- and post- seismic displacements with amplitudes much larger than any other signal in the positional data. To avoid any bias induced by mismodeling of these large amplitude processes, we perform a two stage analysis based on the procedure described in the methodology section. We first model the positional time series using only the observations prior to the Tohoku-Oki main shock. Then, we remove the modeled signal from the positional data including the observed period after the $M_w 9.0$ earthquake. The resulting dataset consist of uncorrelated noise before the Tohoku-Oki mainshock and positional data after such event which only contains co-seismic and post-seismic signals. We proceed with the analysis of the resulting dataset to isolate the post-seismic positional time series by removing any step-like signals as well as any signal originated by processes not occurring in the subduction megathrust such as the signals produced by the April 11, 2011 ($M_w 6.6$) shallow Fukushima aftershock. A foreshock event occurred 3 days before the Tohoku-Oki earthquake, daily positions makes impossible to isolate both events. Thus, the signal of the foreshock, although negligible, will be included in the estimation of the mainshock co-seismic displacements. The foreshock and mainshock signals can be isolated with the use of higher rate GPS positional data, which is left for future work.

Once the co- and post-seismic signals associated to the Tohoku-Oki main shock have been identified and isolated, we proceed to compute post-seismic displacements as the difference of the position of each site at two given times, computed using a linear trend over an ad-hoc 7 day window. Note that the estimation of the post-seismic displacements is independent of any assumption on the post-seismic relaxation process, as it is calculated as a mere difference between the last known position and the position just after the occurrence of the Tohoku-Oki earthquake of the cleaned time series. Figure 2.4 shows the post-seismic displacements over a time period from main shock to September 22, 2012, compared against the inferred co-seismic displacements associated with the Tohoku-Oki ($M_w 9.0$) earthquake. As a byproduct, we also obtain models for secular (inter-seismic) strain rates, seasonal and other earthquake signals present in the time series (Figures 2.5, 2.6, 2.7–2.22).

The GPS positional time series may have data gaps. Some of the causes for such gaps include station malfunction/maintenance, electricity outages, etc. In the particular case of the Tohoku-Oki earthquake, several of the coastal GPS sites may have been destroyed by the tsunami that followed the earthquake. Some of the sites were not included in this analysis due to processing issues. For example, Figure 2.3 shows several of the GPS sites have observations that stop on December 2011 due to an upgrade of their antenna, which requires us to reprocess these data. We will include the full data set in a future work. Since we are interested in studying co- and post-seismic displacements associated with the 2011 earthquake, we discard any site that do not have at least 90 daily positions after the earthquake. We also require at least 5 years worth of samples before the $M_w 9.0$ mainshock in order to properly isolate secular and seasonal signals on the positional data.

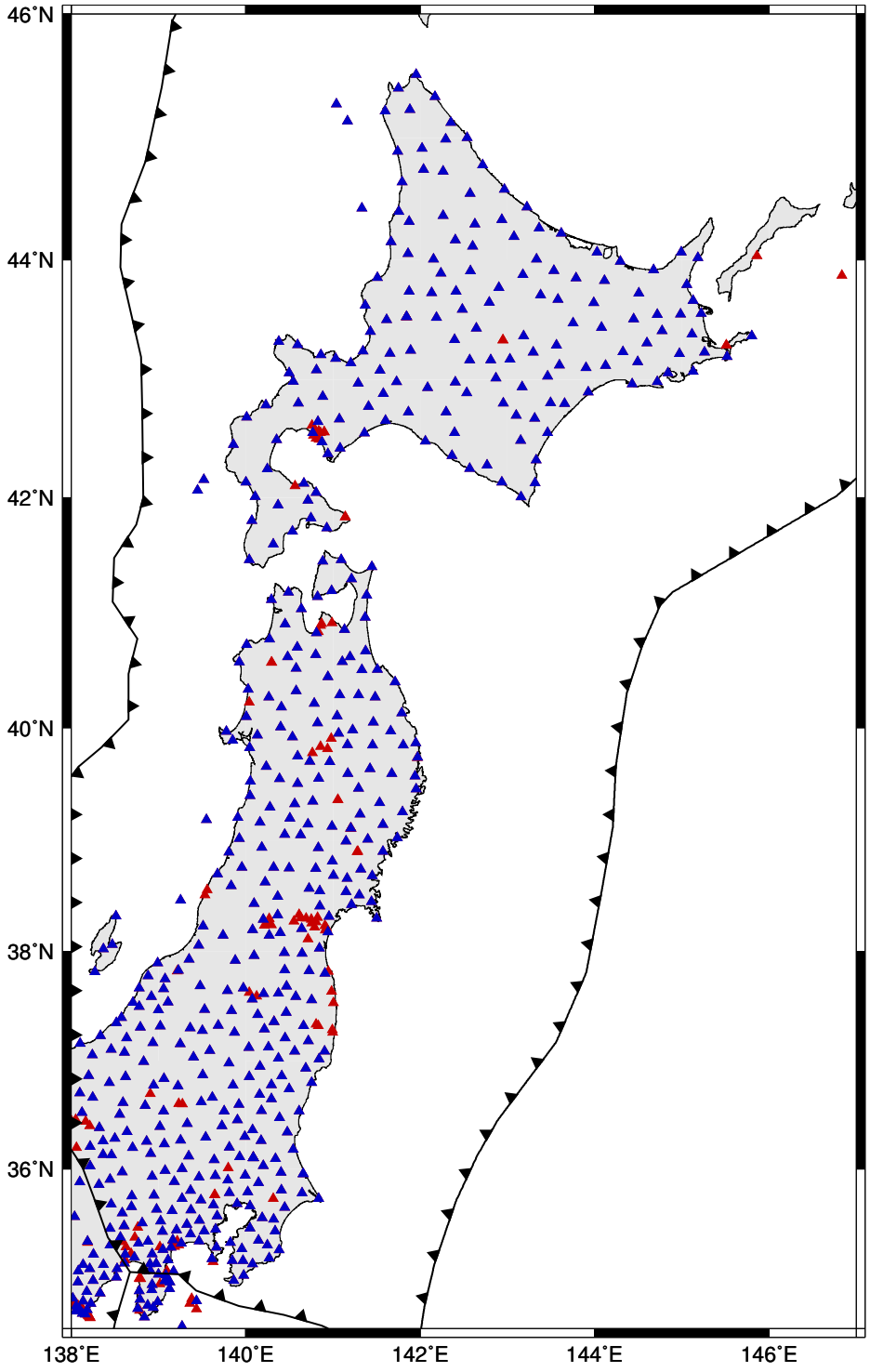

Figure 2.3. Blue and red triangles show the location of the GEONET GPS sites in northeast Japan. Red color indicates sites with missing data due to processing issues.

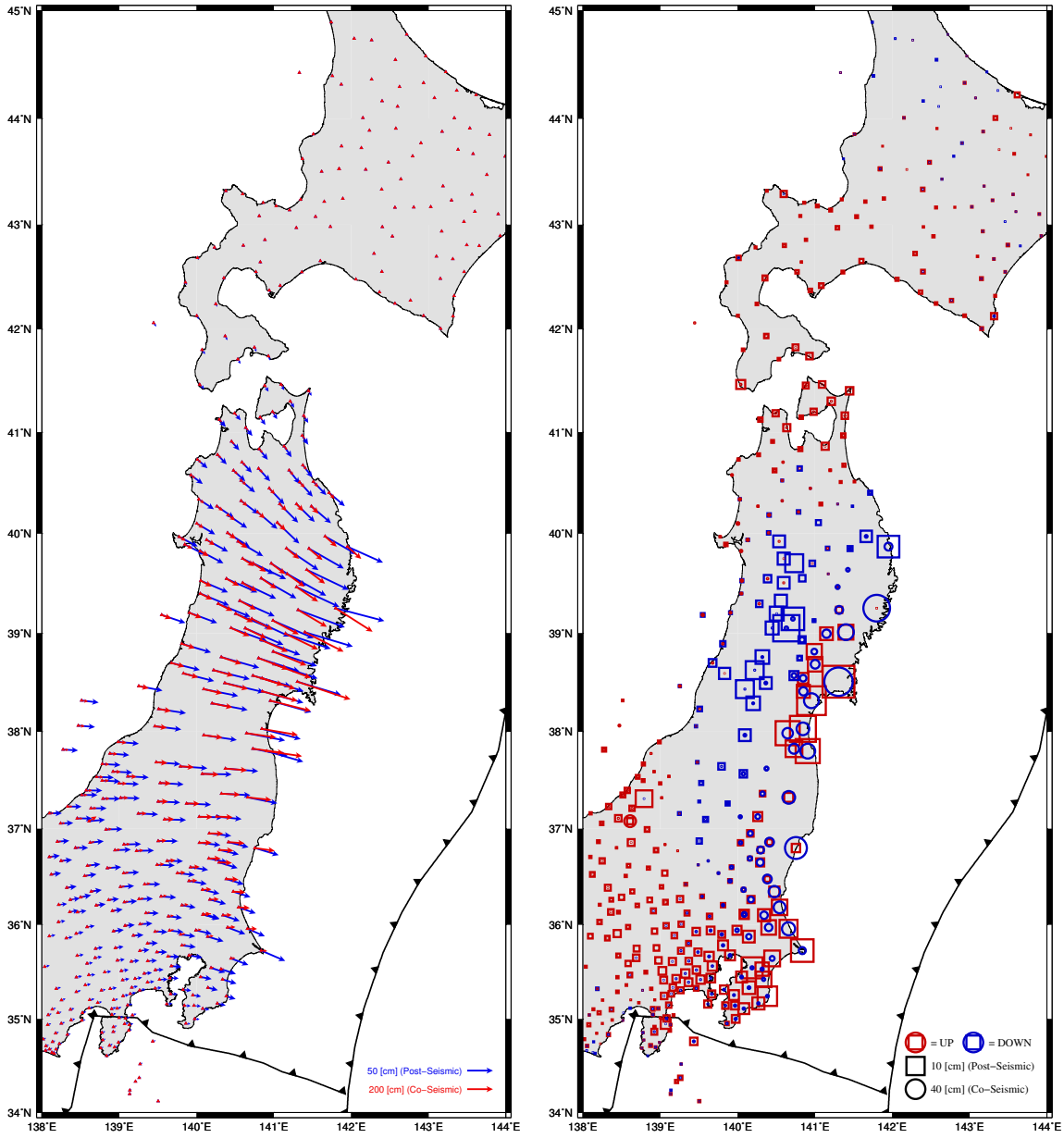

(a) Horizontal **(b) Vertical**

Figure 2.4. Horizontal (a) and vertical (b) co- and post- seismic displacements associated with the 11 March 2011 (M_w9.0) Tohoku-Oki earthquake. Post-seismic displacements are estimated up to September 22, 2012. Note the change in direction of the horizontal post-seismic displacements with respect to co-seismic in northern Honshu, as well as the change in the vertical hinge line from off-shore for the main shock to inland for the post- seismic displacements. A similar picture of the spatial complexity in the displacement field is described in (*Ozawa et al.*, 2011, 2012)

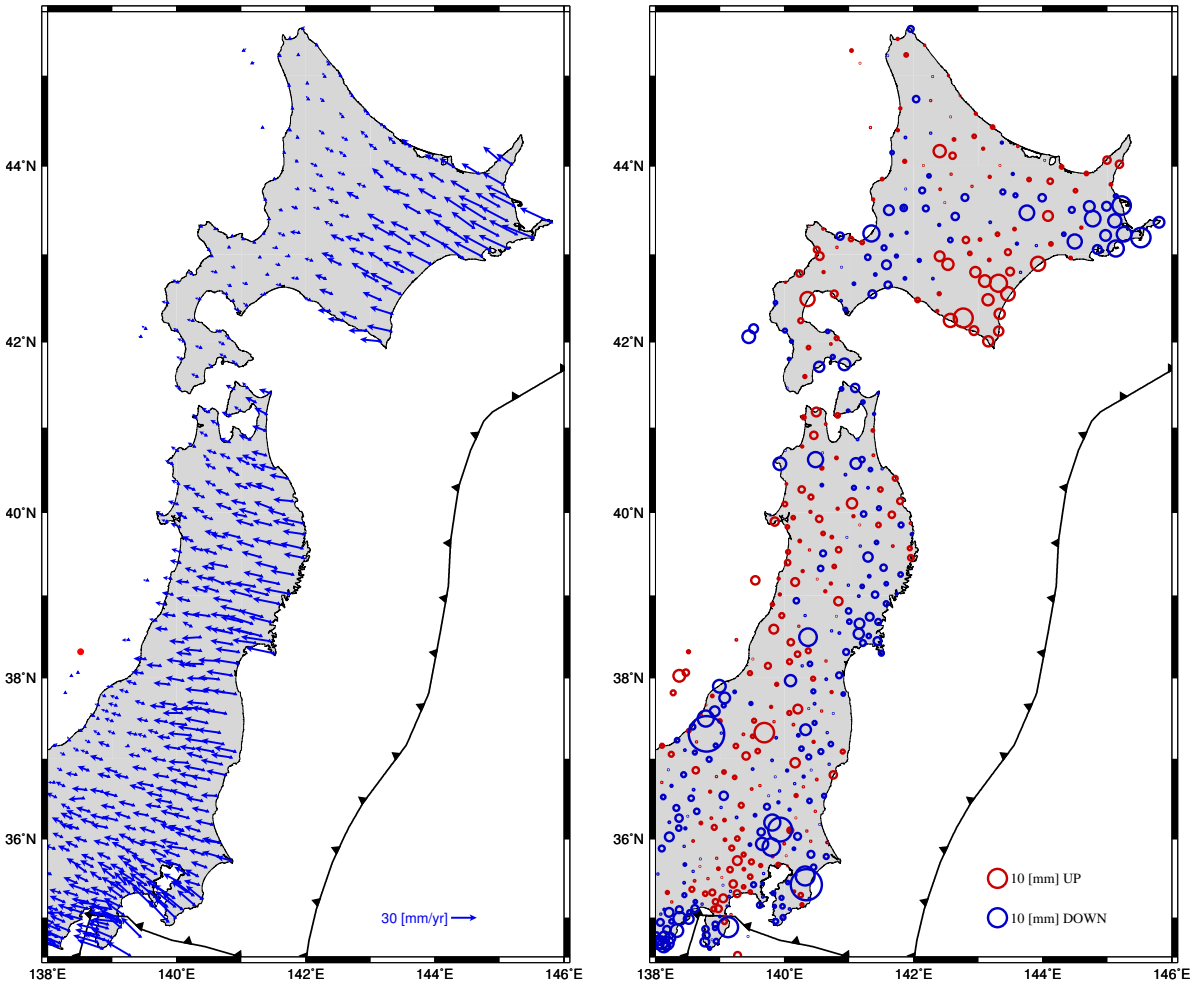

(a) Horizontal **(b) Vertical**

Figure 2.5. GPS inferred horizontal and vertical inter-seismic secular rates. Horizontal rates are calculated relative to GPS site 0232 (red dot close to 138.5E, 38.5N).

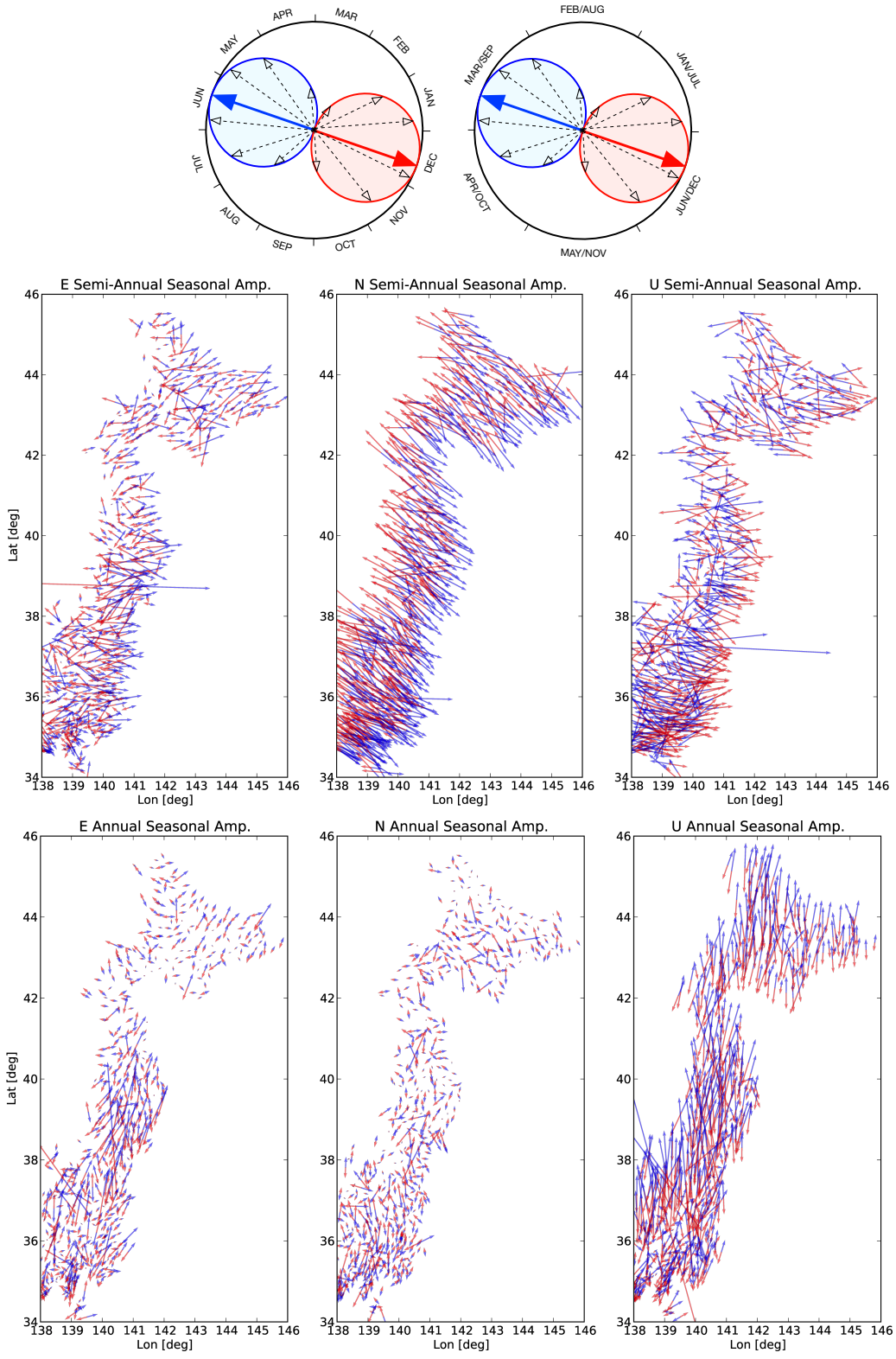

Figure 2.6. Semi-annual and annual seasonal signal. Note the spatial coherency of the semi-annual component, especially for E component, we can not find any obvious explanation for such coherency. For the annual term, the horizontal components are scattered but the vertical component is coherent. For the latter it may be associated with hydrological forcing. Orientation and length of the blue-red arrows indicate phase and amplitude of the respective seasonal term (see Figure 2.2).

2.3.1 North-East Japan GEONET earthquake catalog

Information obtained from PDE catalog from USGS earthquake archive.

Date - Time [UTC]		Lat	Lon	Dep	Mag	Location	Name	Figure
yyyy-mm-dd	hh:mm	[deg]	[deg]	[km]				
2003-07-25	22:13:29	38.415N	140.996E	6	6.1	Miyagi		2.7
2003-09-25	19:50	41.775N	143.904E	27	8.3	Offshore Hokkaido	Tokachi-Oki EQ.	2.8
2003-10-08	09:06	42.648N	144.570E	32	6.7	Offshore Hokkaido	-	2.9
2004-10-23	08:56	37.231N	138.753E	16	6.6	West Honshu	Niigata Chuetsu EQ.	2.10
2004-11-28	18:32	43.006N	145.119E	39	7.0	Offshore Hokkaido	-	2.11
2004-12-06	14:15	42.900N	145.228E	35	6.8	Offshore Hokkaido	-	2.12
2005-08-16	02:46	38.276N	142.039E	36	7.2	Offshore Miyagi	Miyagi-Oki EQ.	2.13
2007-07-15	01:13	37.535N	138.446E	12	6.6	West coast of Honshu	-	2.14
2008-06-13	23:43	39.030N	140.881E	7.8	6.9	Honshu	Iwate-Miyagi Nairiku EQ.	2.15
2008-07-19	02:39	37.552N	142.214E	22	7.0	Offshore Miyagi		2.16
2009-12-17	14:45	34.934N	139.179E	13.6	4.9	Shizuoka near Izu-Tobu volcano		2.17
2011-03-11	05:46	38.297N	142.373E	29	9.0	Offshore Tohoku	Tohoku-Oki EQ.	2.18
† 2011-03-11	06:08	39.927N	143.002E	30.9	7.4	Offshore Iwate	-	2.19
† 2011-03-11	06:15	36.106N	141.777E	8.7	7.7	Offshore Ibaraki	-	2.20
2011-04-11	08:16	37.001N	140.401E	11	6.6	Fukushima	-	2.21
2011-10-29	-	-	-	-	-	Chiba Prefecture	-	2.22

Table 2.1. Earthquakes detected using GEONET GPS time series in North-Japan

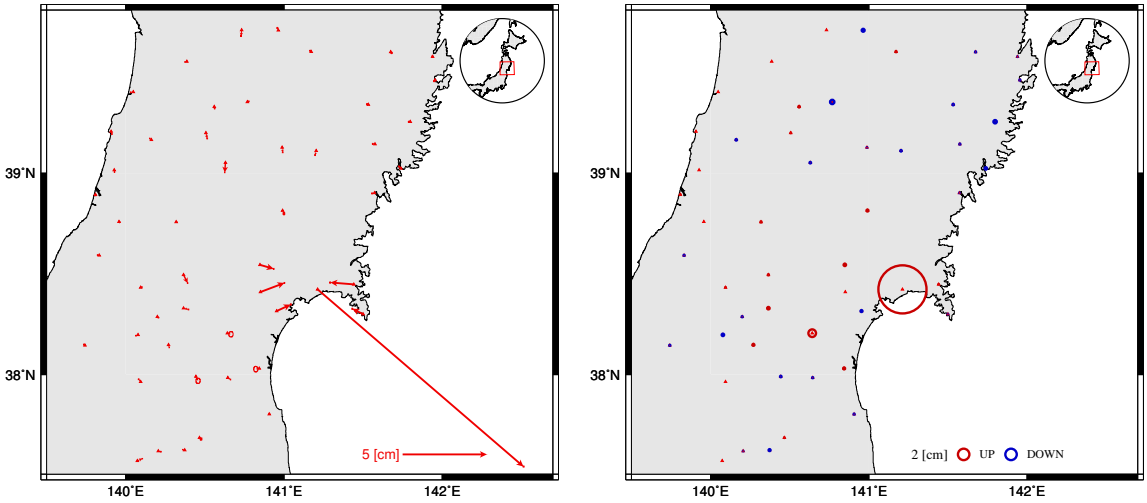

Figure 2.7. Displacements associated with the July 25, 2003 (M_w6.1) earthquake in Miyagi. Offsets derived from daily epochs.

†Location and magnitude from *Nishimura et al.* (2011). GPS co-seismic displacements for these events are obtained from high-rate continuous GPS positional time series.

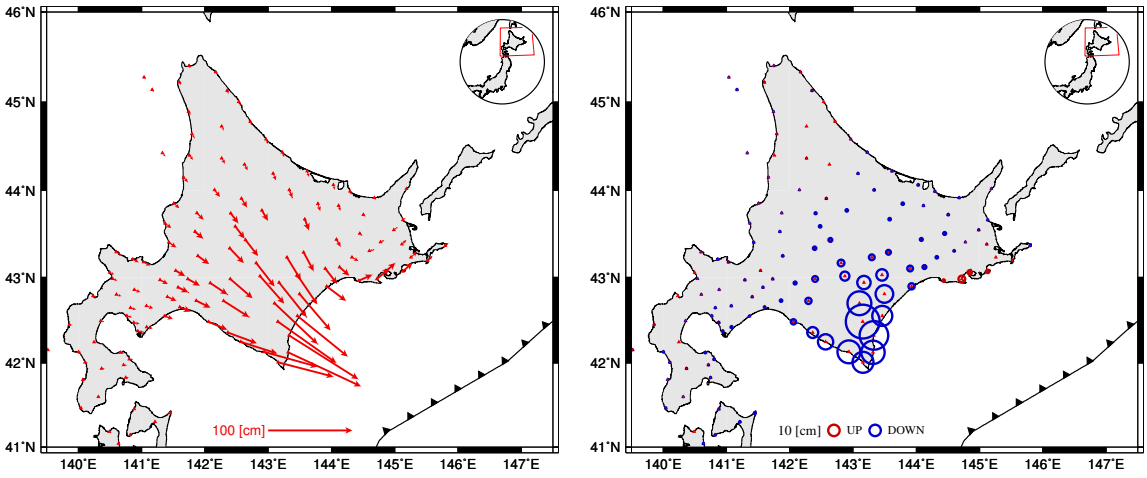

Figure 2.8. Displacements associated with the September 26, 2003 Tokachi-Oki (M_w 8.3) earthquake. Offsets derived from daily epochs.

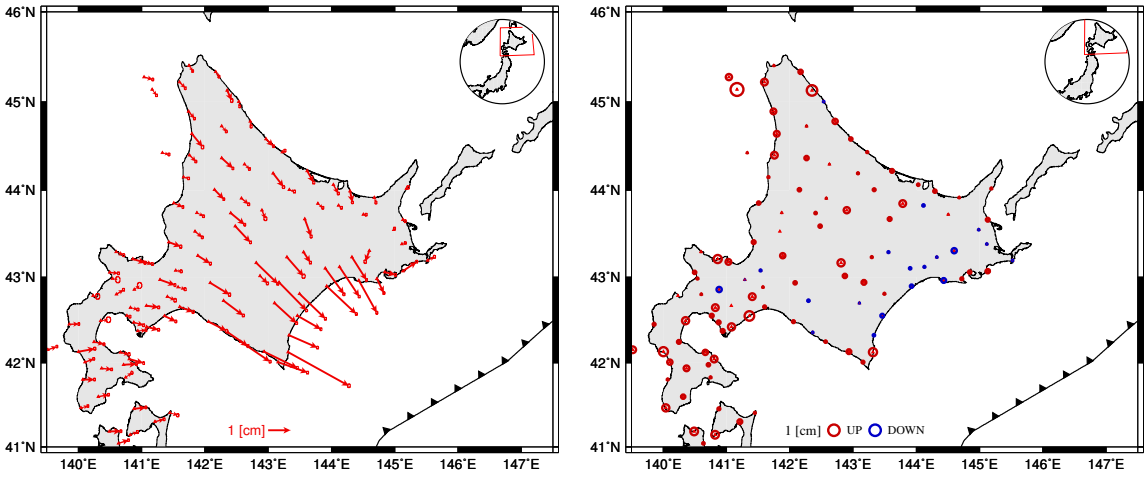

Figure 2.9. Displacements associated with the October 08, 2003 offshore Hokkaido (M_w 6.7) earthquake. Offsets derived from daily epochs.

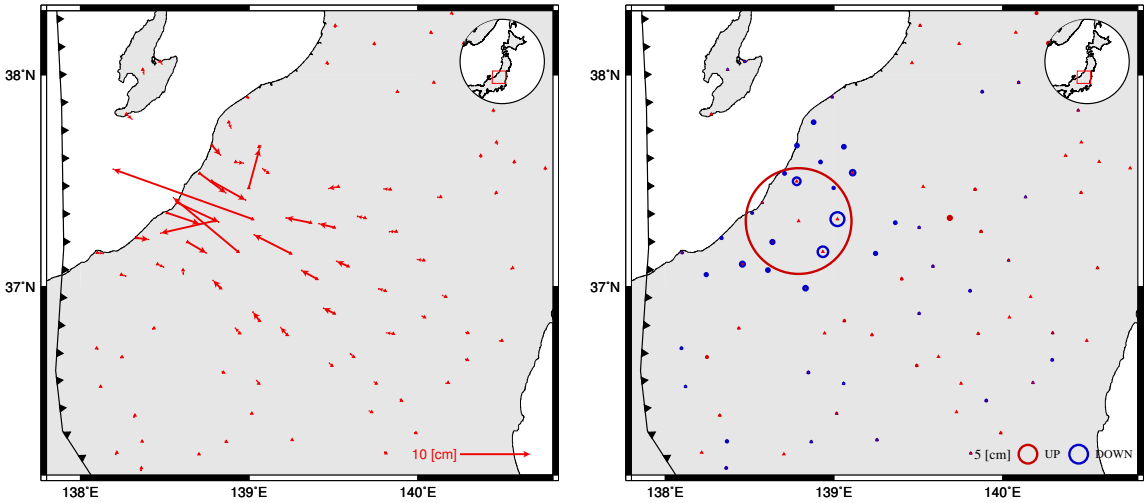

Figure 2.10. Displacements associated with the October 23, 2004 Niigata Chuetsu (M_w 6.6) earthquake. Offsets derived from daily epochs.

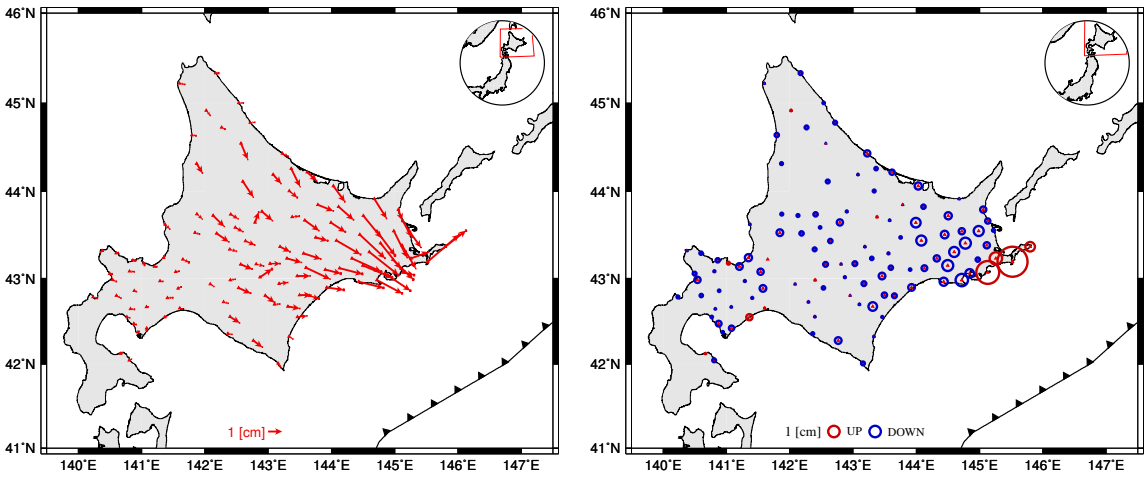

Figure 2.11. Displacements associated with the November 28, 2004 offshore Hokkaido (M_w 7.0) earthquake. Offsets derived from daily epochs.

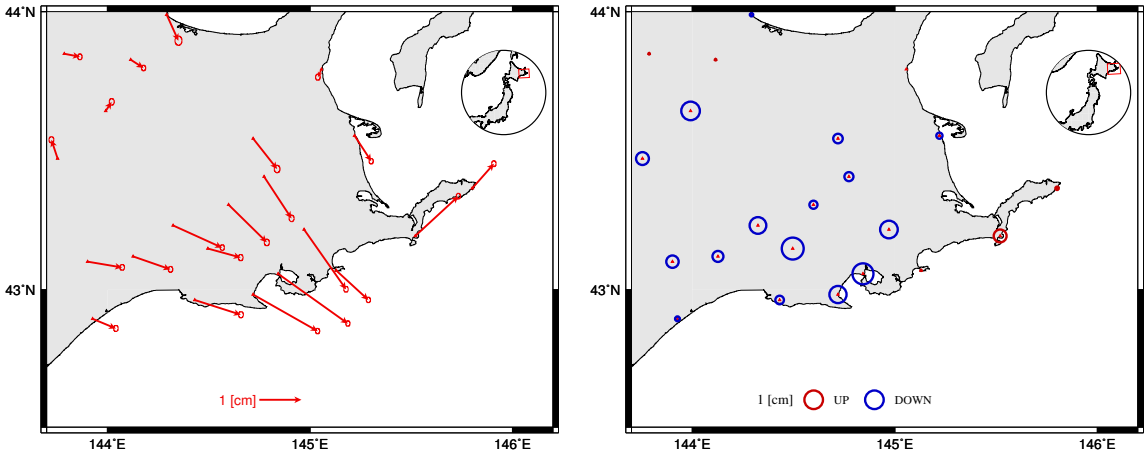

Figure 2.12. Displacements associated with the December 6, 2004 offshore Hokkaido (M_w 6.8) earthquake. Offsets derived from daily epochs.

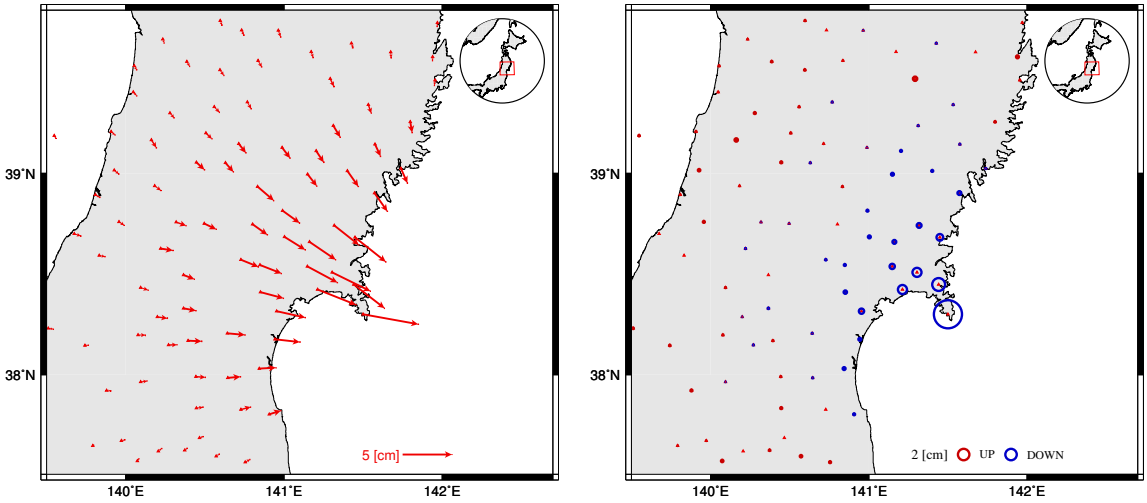

Figure 2.13. Displacements associated with the August 16, 2005 Miyagi-Oki (M_w7.2) earthquake. Offsets derived from daily epochs.

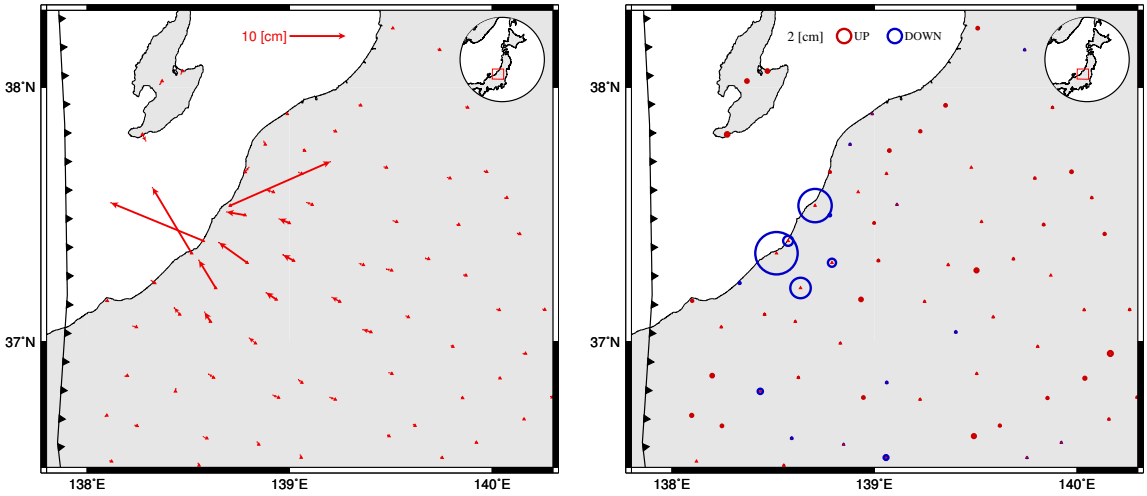

Figure 2.14. Displacements associated with the July 15, 2007 west coast of Honshu (M_w6.6) earthquake. Offsets derived from daily epochs.

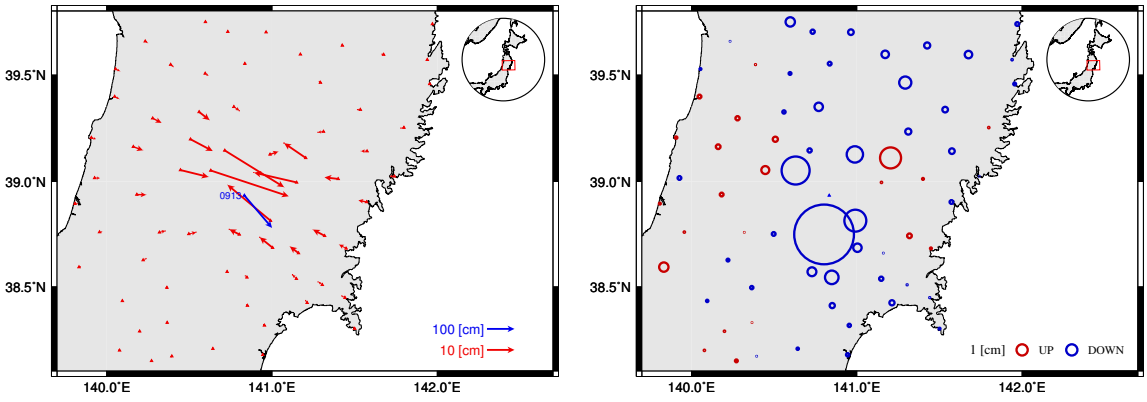

Figure 2.15. Displacements associated with the June 13, 2008 Iwate-Miyagi Nairiku (M_w6.9) earthquake. Offsets derived from daily epochs.

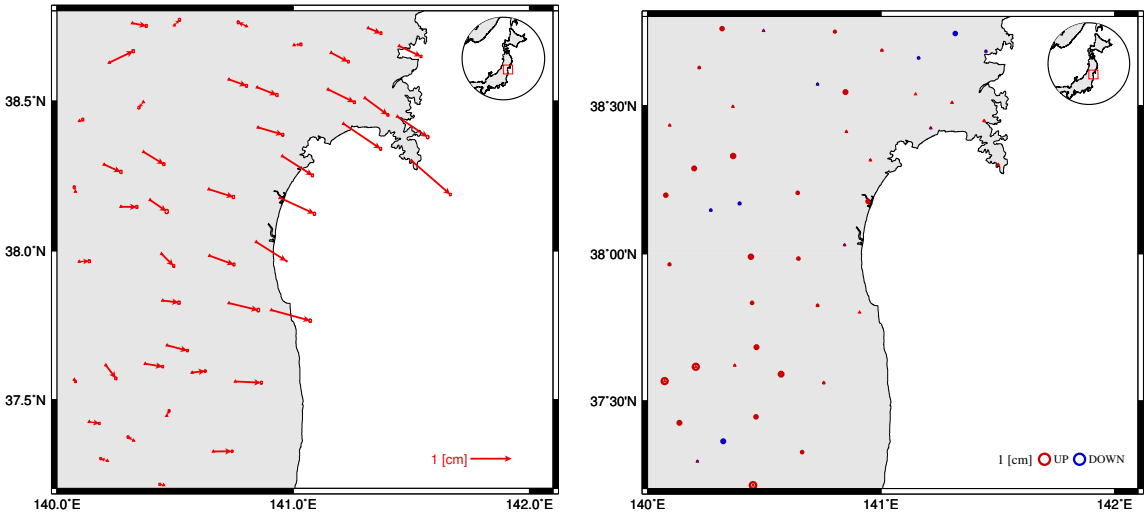

Figure 2.16. Displacements associated with the July 19, 2008 offshore Miyagi (M_w7.0) earthquake. Offsets derived from daily epochs.

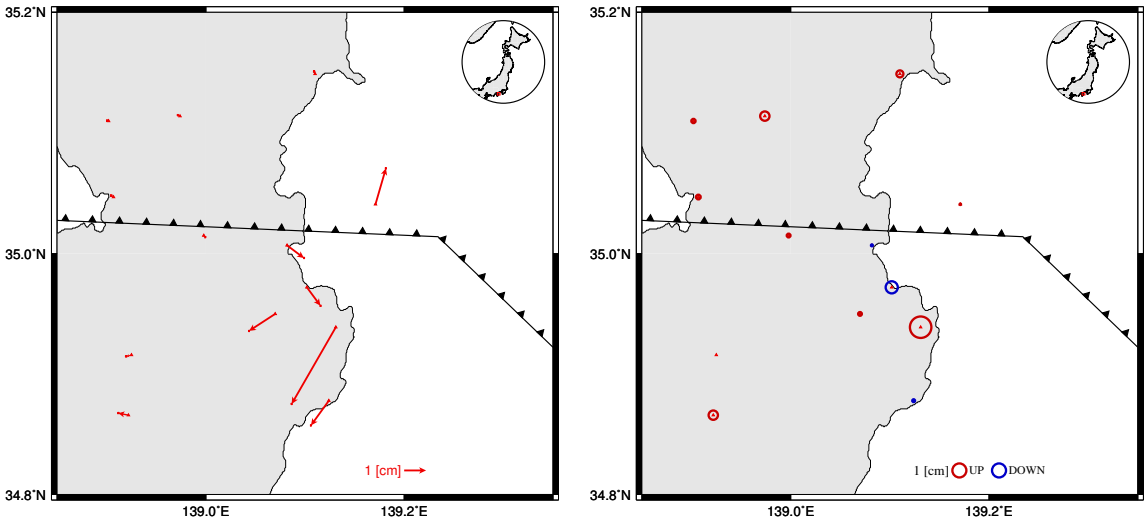

Figure 2.17. Displacements associated with the December 17, 2009 (M_w4.9) earthquake. Offsets derived from daily epochs.

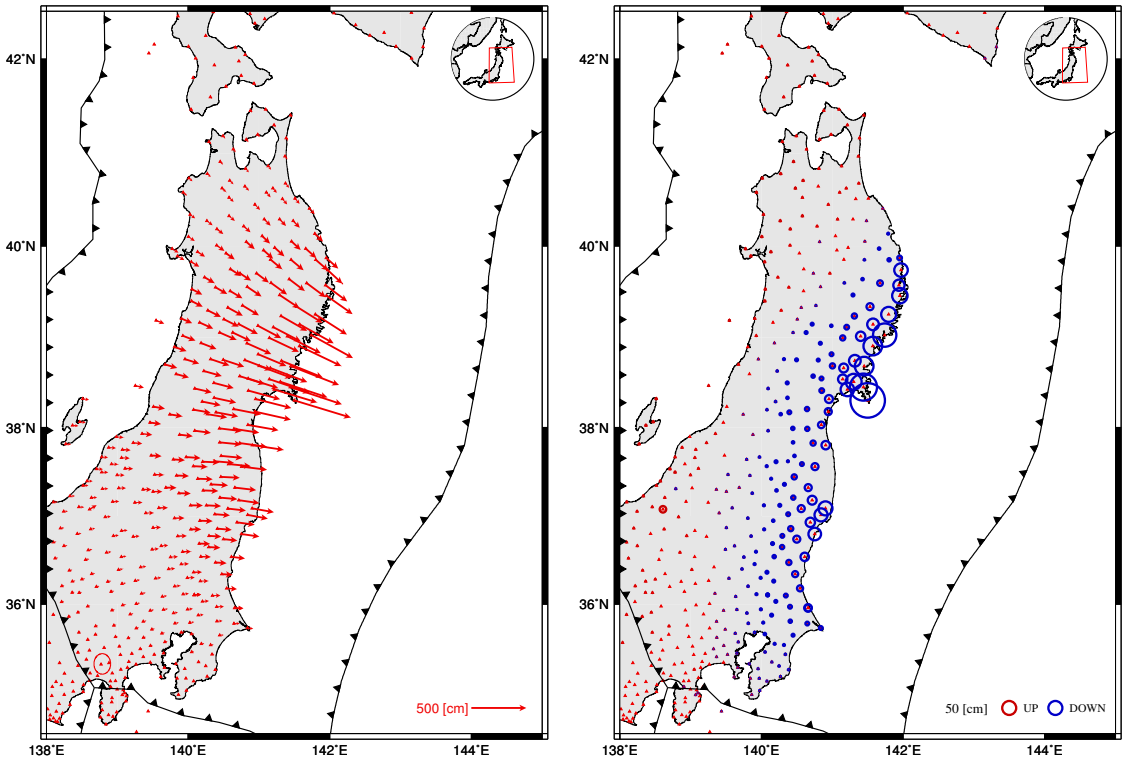

Figure 2.18. Displacements associated with the March 11, 2011 Tohoku-Oki (M_w9.0) earthquake. Offsets derived from daily epochs.

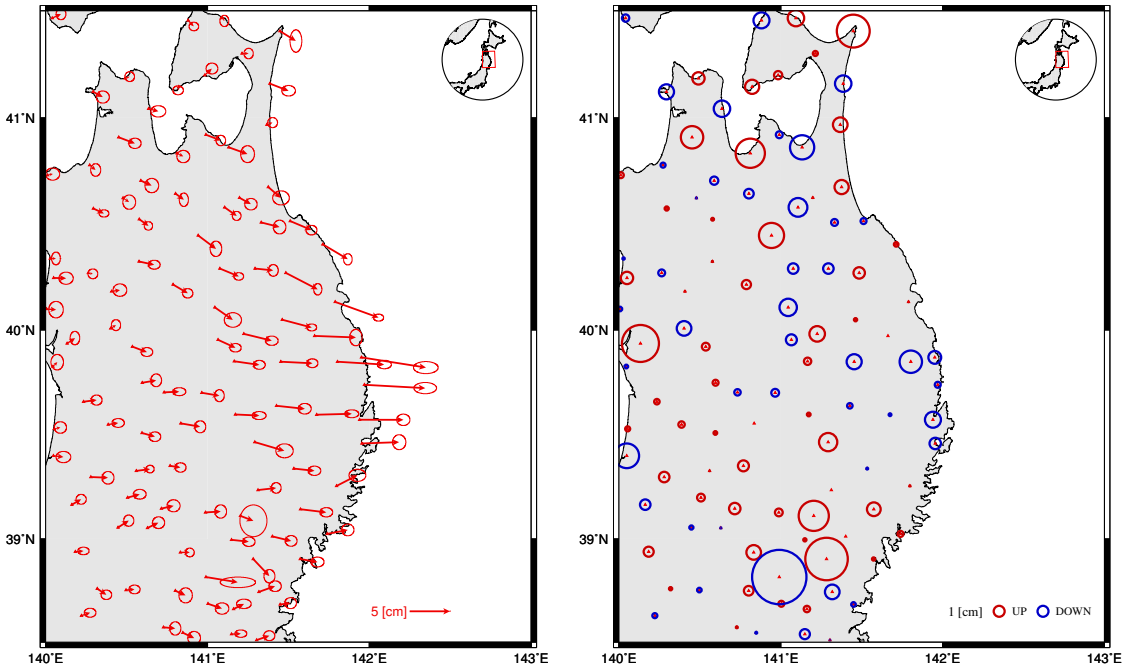

Figure 2.19. Displacements associated with the March 11, 2011 (M_w7.4) offshore Iwate aftershock of the Tohoku-Oki earthquake. Co-seismic displacements obtained by fitting a bilinear function and a co-seismic jump. Offsets derived from 30 second epochs.

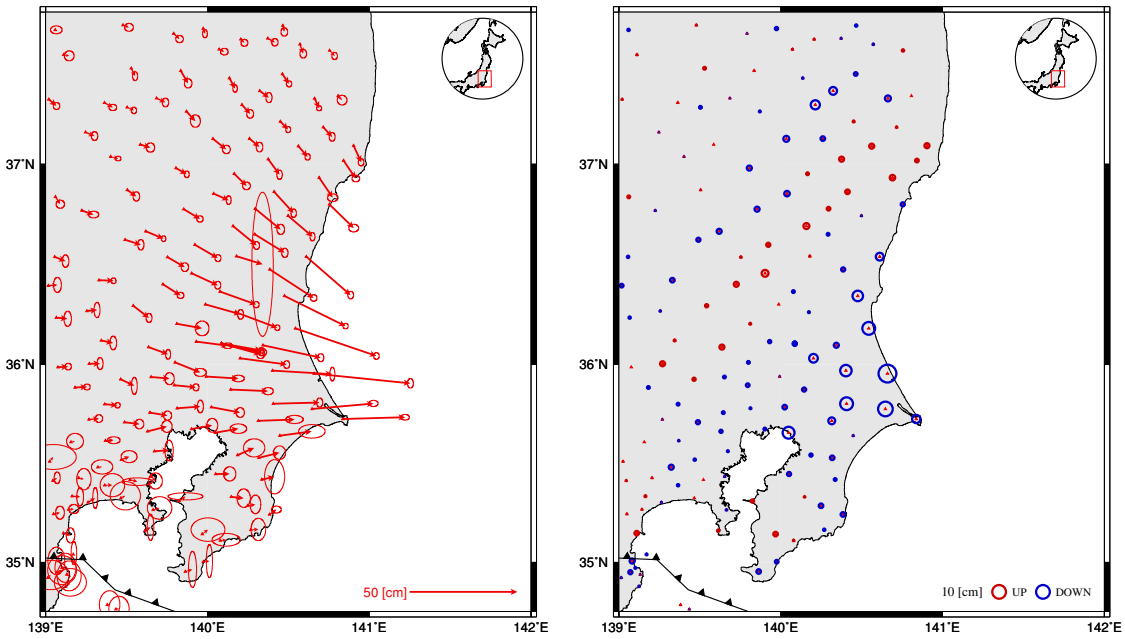

Figure 2.20. Displacements associated with the March 11, 2011 (M_w7.9) offshore Ibaraki aftershock of the Tohoku-Oki earthquake. Co-seismic displacements obtained by fitting a bilinear function and a co-seismic jump. Offsets derived from 5 minute epochs.

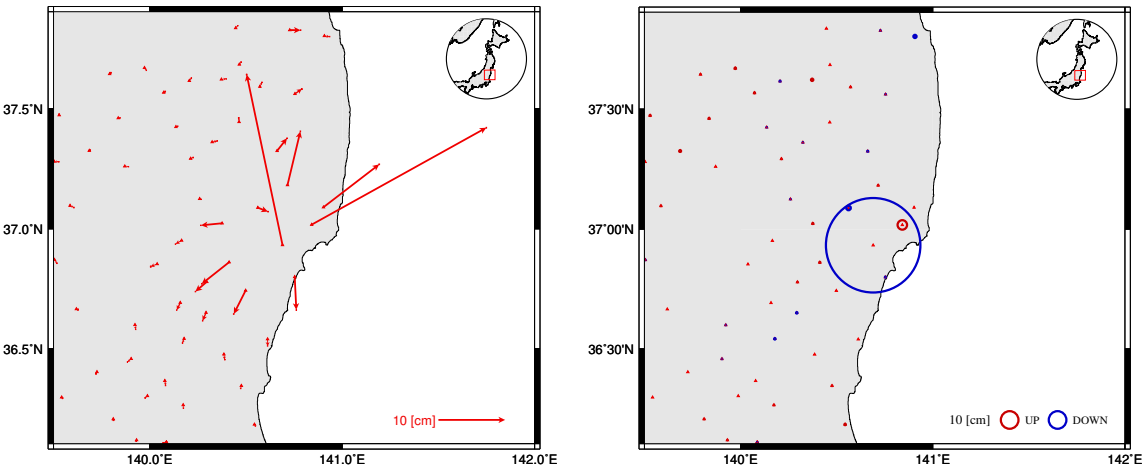

Figure 2.21. Displacements associated with the April 11, 2011 Fukushima (M_w6.6) earthquake. Offsets derived from daily epochs.

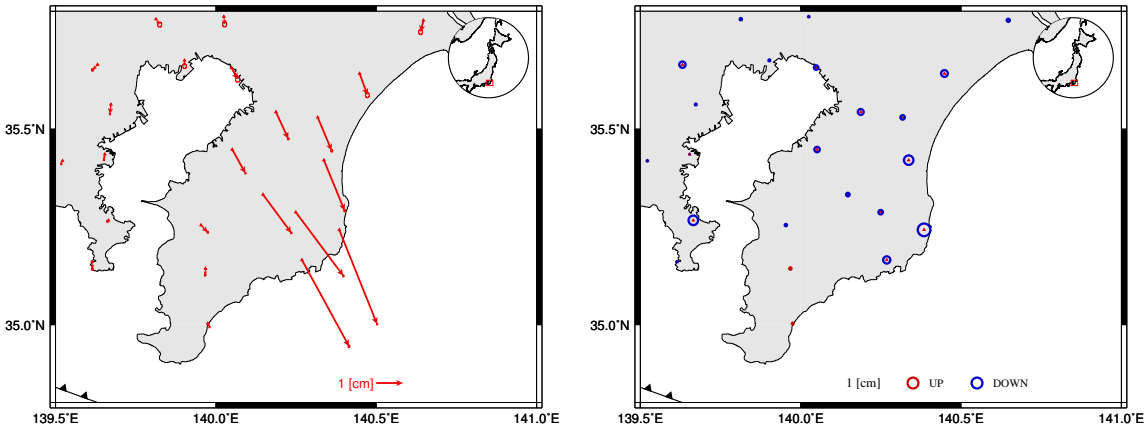

Figure 2.22. Displacements associated with the October 29, 2011 event. Offsets derived from daily epochs. Time series suggests this may be a transient event.

2.4 Central Andes GPS time series post-processing

Our primary goal is to obtain estimates of crustal secular rates that sample the strain accumulation induced by the plate coupling at the subduction megathrust between Nazca and South-American plates. We use 3 component positional time series from a recently established continuous GPS network in the region in a collaborative effort of scientists from Chile, France, Peru and United States as a part of the Central Andes Tectonic Observatory (CAnTO). The positional time series referenced from ITRF2005 are estimated by Jeff Genrich (Caltech) using daily generated RINEX files and the software GAMIT/GLOBK.

Using the procedure described in the methodology section, we obtain 3 component inter-seismic crustal velocities (Figure 2.23) from the positional time series, as well as, annual and semiannual seasonal (phase and amplitude, Figure 2.24) and earthquake signals (Figures 2.25–2.26). In particular we identify co-seismic displacements corresponding to 2 large earthquakes in the region, the June 13, 2005 Tarapacá ($M_w 7.8$) deep earthquake and the November 14, 2007 Tocopilla ($M_w 7.7$) earthquake (Figures 2.25 and 2.26, respectively).

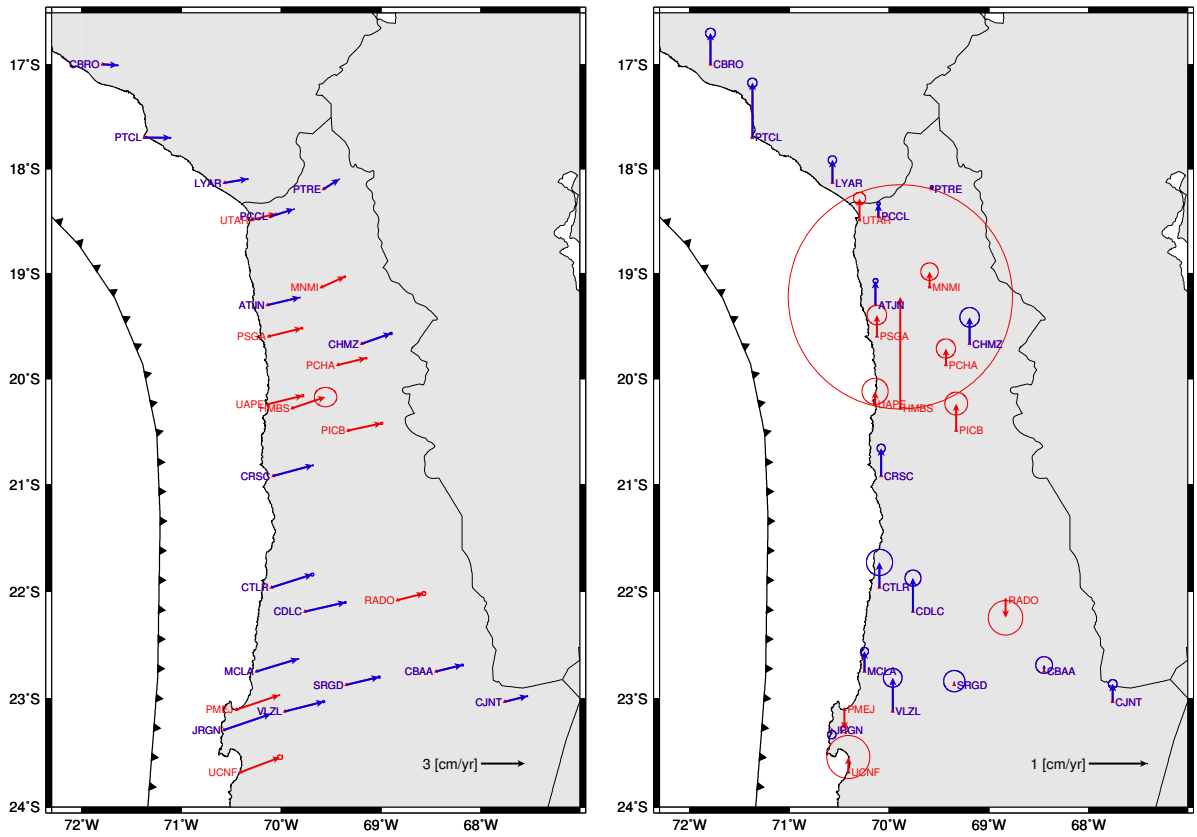

Figure 2.23. Horizontal and vertical components of GPS secular rates with respect to stable South America. Blue arrows correspond to CAnTO GPS sites installed by Caltech. The time span of the positional time series used in its derivation goes from September 2005 to September 2009.

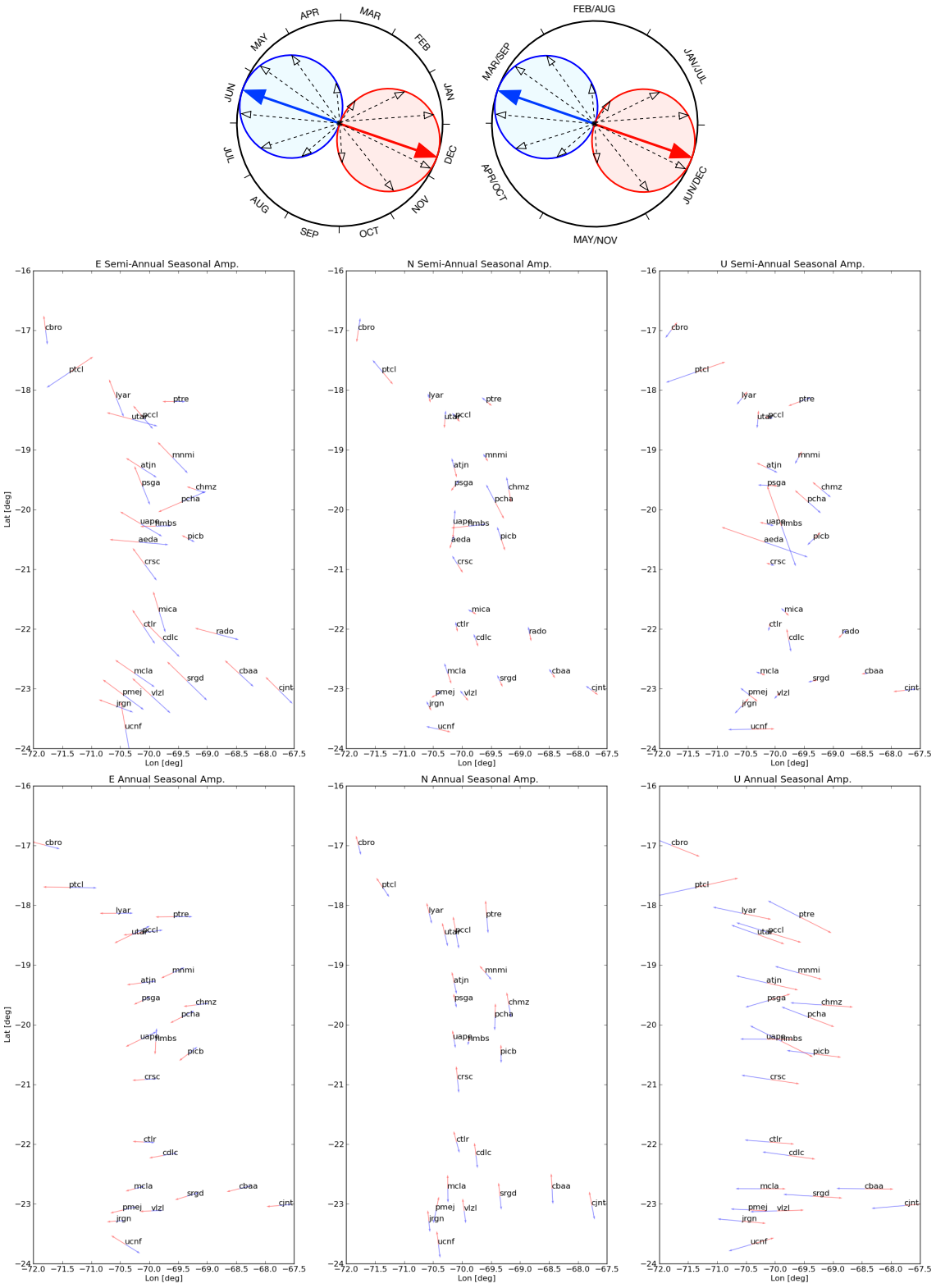

Figure 2.24. Semi-annual and annual seasonal signal.

2.4.1 Central Andes Tectonic Observatory GPS observed earthquake catalog

Date - Time [UTC]		Lat	Lon	Dep	Mag	Location	Name	Figure
yyyy-mm-dd	hh:mm	[deg]	[deg]	[km]				
2005-06-13	22:44	19.987S	69.197W	115.6	7.8	Tarapacá	Tarapacá EQ.	2.25
2007-11-14	15:40	22.247S	69.890W	40	7.7	Offshore Tocopilla	Tocopilla EQ.	2.26

Table 2.2. Earthquakes detected using GPS time series in Central Andes

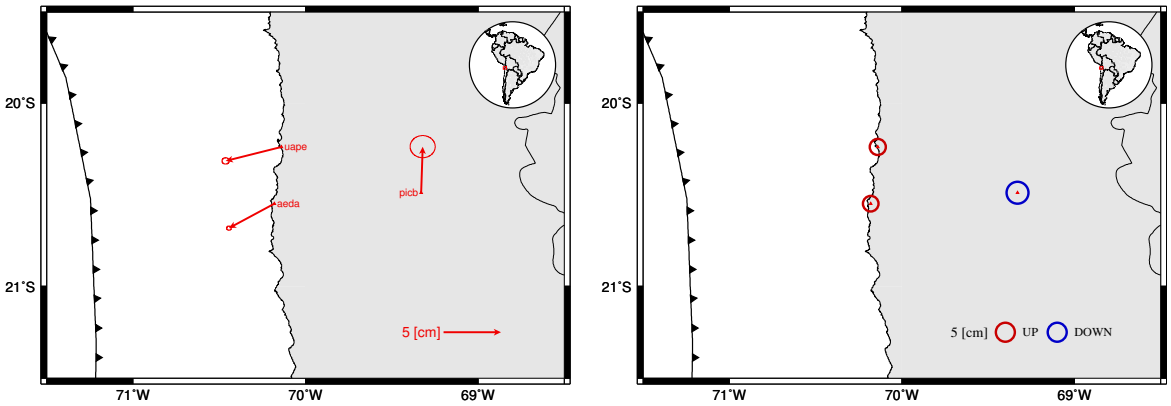

Figure 2.25. Estimation of the horizontal and vertical components of GPS co-seismic displacements for the June 13, 2005 Tarapacá (M_w7.8) deep earthquake. Offsets derived from daily epochs.

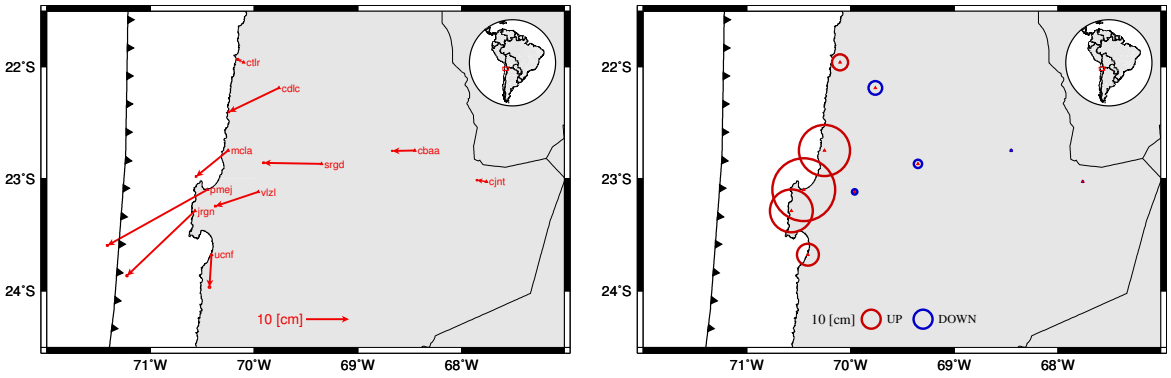

Figure 2.26. Estimation of the horizontal and vertical components of GPS co-seismic displacements for the November 14, 2007 Tocopilla (M_w7.7) earthquake. Offsets derived from daily epochs.

Chapter 3

Inverting for Fault Slip Distributions

3.0 My contribution in this chapter

- Recognizing the spatial variability of the constraint provided by unevenly distributed surface observations on fault-slip, I develop a novel spatially variable smoothing regularization methodology for the least squares quasi-static slip inversion problem based on the sensitivity of the fault to the observables. Such methodology allows us to obtain slip estimates that are more stable under noisy observations and somewhat more detailed than those obtained by utilization of previous regularization schemes for the least squares problem.

- I deduce a variant of the Bayesian inversion framework found in *Tarantola* (2005) in which I introduce an additional quantity that can be used to introduce *a priori* information on the model parameters. I express and interpret the novel regularization scheme proposed in this work, in the context of the modified Bayesian formulation.

- Development of the computational codes to solve for the regularized least squares problem proposed in this work.

3.1 Introduction

During all the stages of the seismic cycle, earthquakes, aseismic slip, or even the onset of locking on the fault, may produce geodetically measurable deformation at the surface of the Earth. For example, we can use space geodetic observations to measure crustal deformation associated to such phenomena (e.g., §2; *Pritchard et al.*, 2007). We are interested with the inversion problem dealing with estimation of the source for such observations given a "physical" forward model that links the observations (generally made at the earth surface) with the distribution of slip behavior that caused them. For the static slip inversion problem, the relationship between slip on a fault and surface displacements can be described in a general form by the Fredholm integral equation of the first kind:

$$\int_{\Omega} \mathcal{K}(\Phi, \Omega)\mathbf{m}(\Omega)d\Omega = \mathbf{d}(\Phi) \tag{3.1}$$

where Ω, Φ are the coordinates describing the fault surface and the observations respectively, $\mathcal{K}(\Phi, \Omega)$ the elastic response of the earth for a dislocation on a point of the fault surface and $\mathbf{d}(\Phi)$ the observations. In an approach to numerically solve the slip inversion problem, one could perform a finite discretization of the fault surface into non-overlapping regions such that $\Omega = \bigcup_{j=1}^{N_p} \Omega_j$ in which it is assumed that slip is constant on each discretized element ($\mathbf{m}(\Omega_j) = m_j$). Now, if the

observations are made at N_{obs} discrete points Φ_i ($\mathbf{d}(\Phi_i) = d_i$), we can write (3.1) as

$$\sum_{j=1}^{N_p} \int_{\Omega_j} \mathcal{K}(\Phi_i, \Omega_j)\mathbf{m}(\Omega_j)d\Omega_j = \mathbf{d}(\Phi_i) \tag{3.2a}$$

$$\sum_{j=1}^{N_p} m_j \int_{\Omega_j} \mathcal{K}(\Phi_i, \Omega_j)d\Omega_j = \mathbf{d}(\Phi_i) \tag{3.2b}$$

$$\sum_{j=1}^{N_p} m_j G_{ij} = d_i \tag{3.2c}$$

$$\mathbf{Gm} = \mathbf{d} \tag{3.2d}$$

where $G_{ij} = \int_{\Omega_j} \mathcal{K}(\Phi_i, \Omega_j)d\Omega_j$ is the response of the Earth at the observation points Φ_j to a unit slip on the fault surface discretization Ω_j.

Due to the integral nature of the Fredholm equation and that of the response of the media ($\mathcal{K}$), unless the observations are made very close to the fault surface (which may be unpractical or unfeasible in most of the cases), any model prediction $\mathbf{d}$ is insensitive to the high frequency component of the slip distribution on the fault surface, leading to a discrete ill-posed linear inverse problem (e.g., *Hansen*, 1998). Thus, in estimating the slip distribution, $\mathbf{m}$, constrained by the observations, $\mathbf{d}$, any errors on either the measurements or the physical model, can be spuriously mapped into a high frequency slip distribution, leading to unstable and "unrealistic" distributions of slip behavior. Producing precise and realistic estimates of the distributions of slip behavior in faults is a critical step to understand the physics controlling the behavior of faults throughout the seismic cycle. Thus, we need to use methods that minimize spurious signals that the inherent instability may add to the solution of the inverse problem.

There are two general end member approaches to estimate the distribution of slip on a fault that deals with the inherent instability of the inverse problem: An unregularized, computationally expensive, fully Bayesian approach (e.g., *Minson et al.*, 2013) and a much more expedient but

less complete optimization approach using some form of regularized least squares (e.g., *Segall and Harris*, 1987). In the Bayesian formulation, the solution of the inverse problem is the a posteriori probability density function of the model parameters, which describes the plausibility of such set of models constrained by a priori information and observables. Posing the inverse problem in this way ensures the uniqueness of its solution (*Tarantola*, 2005). An important property of the Bayesian approach over the classic optimization techniques is our ability to limit ourselves to physically justifiable a priori information (e.g., we do not expect to find normal slip on a subduction megathrust) without imposing other a priori behavior (e.g., smoothness) beyond that imposed by the model parameterization itself. In contrast, optimization approaches use some form of regularization to avoid numerical instabilities and over-fitting of errors. In practice, this error includes both observational errors and limitations in our physical modeling (e.g., assumed elastic structure and fault geometry), a.k.a. prediction or epistemic error. In many cases, such as for large earthquakes, the prediction error is probably larger than the observation error (*Minson et al.*, 2013). The optimization approach inherently requires one to determine the amount of regularization applied - sometimes posed as a penalty parameter or as a correlation length (e.g., *Segall and Harris*, 1987; *Tarantola*, 2005; *Radiguet et al.*, 2011; *Menke*, 2012). Some inversion methods use a Bayesian approach to inferring the penalty parameter (e.g., *Fukuda and Johnson*, 2008) in what is otherwise an optimization approach.

A major limitation to application of the unregularized Bayesian approach is that the estimates of the a posteriori distributions for the model parameters are only as good as the a priori misfit covariance model including both observation and prediction error. Reasonable estimates of the prediction error, including the covariance between neighboring observations, remains an unsolved problem (e.g., *Tarantola*, 2005; *Minson et al.*, 2013). More practically, but equally problematic, the unregularized Bayesian approach is computationally expensive (*Minson*, 2010). Thus, while

we generally prefer to move in the direction of a Bayesian methodology, we continue to pursue improvements in the least squares optimization approach.

3.2 Slip inversion with spatially variable regularization

Recapitulating, we want to find the discretized values of slip $\mathbf{m}$ constrained by the observations $\mathbf{d}$ and a model of the elastic media representing the Earth $\mathbf{G}$ by solving the system of N_{obs} equations

$$\mathbf{Gm} = \mathbf{d} \tag{3.3}$$

An equivalent version of (3.3) can be obtained when considering the observational and/or model prediction errors by defining a matrix $\mathbf{W}_\chi$ that weights the different equations of the system:

$$\mathbf{W}_\chi^{1/2}\mathbf{Gm} = \mathbf{W}_\chi^{1/2}\mathbf{d} \tag{3.4}$$

Here, $\mathbf{W}_\chi$ can be considered as the inverse of the covariance matrix $\mathbf{C}_\chi$ representing the uncertainties in both our observations and our forward model. Typically, modeling errors are assumed to be negligible and observations are assumed to be uncorrelated, leading to a weight matrix that is diagonal with values given by the reciprocal of the measurement standard deviations (e.g., *Harris and Segall*, 1987; *Segall and Harris*, 1987).

Depending on the refinement of the model parameterization, the static slip inversion problem quickly becomes an ill-posed problem. Thus, slip inversions need to be regularized when the solution is obtained through optimization methodologies. There are two flavors of the optimization approach, one where regularization is achieved through penalizing a norm of some function of the model parameters (e.g., *Segall and Harris*, 1987; *Radiguet et al.*, 2011; *Evans and Meade*, 2012) or alternatively by adjusting the actual parameterization of the model to control the solution (e.g.,

Pritchard et al., 2002; *Barnhart and Lohman*, 2010). Both, *Pritchard et al.* (2002) and *Barnhart and Lohman* (2010), optimize the parameterization of the fault surface by adjusting the discretization of the fault to achieve a quasi-uniform resolving power.

Here, we seek a simple hybrid approach, one that uses an arbitrarily fine discretized fault surface (only limited by computer resources) and adopts a regularization that allows for a smoothly varying correlation length. As in *Barnhart and Lohman* (2010) our approach regularizes the slip inversion by augmenting the spatial correlation length of the inferred values of slip at less constrained regions of the fault. The main difference between the two approaches, and the key advantage for our methodology, lies in how the regularization is performed, ours by varying the strength of a slip smoothing operator over an evenly sized and finely discretized fault and *Barnhart and Lohman* (2010) by adjusting the size of the dislocation region. The latter approach has the benefit of effectively imposing a spatially variable correlation length (i.e., constant slip over a variably sized fault patch) that obviates the need for additional smoothing of the model. Note that the final discretization used will depend on the amount of other information one chooses to use (e.g., a priori knowledge on the direction of slip) and on the method used to refine the fault discretization. However, the approach leads to model discretizations that tend to include regions with large uniform behavior with sharp discontinuities which may lead to unrealistic distributions of stress, potentially limiting the usability of the inferred slip distribution. As an aside, one could reduce this problem by modifying the approach to include smoothly varying basis function as opposed to piecewise constant dislocations. Our approach is also more amenable to an eventual extension to include seismic observations to perform a kinematic slip inversion. *Barnhart and Lohman* (2010) method makes difficult the extension to a kinematic inversion as it produces highly variable patch sizes and the method is computationally expensive.

3.2.1 The damped least squares method

Given the linear inverse problem $\mathbf{Gm} = \mathbf{d}$, we would like to find a model $\mathbf{m}_{est}$ that minimizes some measure of the amount of error between the prediction of the model $\mathbf{d}_{pred} = \mathbf{Gm}_{est}$ and the observations $\mathbf{d_{obs}}$.

Following *Menke* (2012), the least squares method defines a prediction error, or misfit $\mathbf{e} = \mathbf{d}_{obs} - \mathbf{d}_{pred}$ and it searches for $\mathbf{m}_{est}$ such that it minimizes the total measure of length of the error, calculated as the L_2-norm of the misfit $E = \|\mathbf{e}\|_2^2 = \mathbf{e}^T\mathbf{e}$. Here the total measure of length of the error E correspond to the squared Euclidean norm of the misfit vector $\mathbf{e}$ [†]. In a more general case, the total error E, or sometimes called misfit function, can be calculated using the $\mathbf{W}$ matrix-induced L_2-norm of the misfit as a measure of length of the total error,

$$E(\mathbf{m}) = \left\|\mathbf{W}_\chi^{1/2}\mathbf{e}\right\|_2^2 = \left\|\mathbf{W}_\chi^{1/2}(\mathbf{d}_{obs} - \mathbf{Gm})\right\|_2^2 = (\mathbf{Gm} - \mathbf{d}_{obs})^T\mathbf{W}_\chi(\mathbf{Gm} - \mathbf{d}_{obs}) \tag{3.5}$$

In order to find the model that minimizes the total error, we impose the optimality condition $\nabla E(\mathbf{m}) = \mathbf{0}$, which leads to the normal equations:

$$\left(\mathbf{G}^T\mathbf{W}_\chi\mathbf{G}\right)\mathbf{m} \;=\; \mathbf{G}^T\mathbf{W}_\chi\mathbf{d}_{obs} \tag{3.6}$$

then, if the inverse of the matrix $\mathbf{G}^T\mathbf{W}_\chi\mathbf{G}$ exists, the least squares solution to the inverse problem is given by

$$\mathbf{m}_{est} \;=\; \left(\mathbf{G}^T\mathbf{W}_\chi\mathbf{G}\right)^{-1}\mathbf{G}^T\mathbf{W}_\chi\mathbf{d}_{obs} \tag{3.7}$$

In the case where $\left(\mathbf{G}^T\mathbf{W}_\chi\mathbf{G}\right)^{-1}$ can not be calculated, either because $\mathbf{G}$ is the discretization of

[†]Norms other than the Euclidean norm could be used (e.g., *Evans and Meade*, 2012, use an L_1-norm on model parameters to promote sparse estimates of slip), in general any L_p-norm. The chosen norm has an impact on how sensitive the inversion results are to noise and especially outliers in the observations (see *Menke*, 2012, §3.2). Generally the L_2-norm is utilized because it allows the derivation of closed forms for the inverse problem solution and the results have a direct relationship with a Gaussian probability density.

an ill-posed problem or the system of equations is underdetermined, the model parameters can be estimated by minimizing the sum of a measure of length of the model prediction $E(\mathbf{m})$ and some measure of "simplicity" of the solution $L(\mathbf{m})$, thus solving the minimization problem

$$\min_{\mathbf{m}} \left\{ E(\mathbf{m}) + \varepsilon^2 L(\mathbf{m}) \right\} \tag{3.8}$$

where the parameter ε is chosen either by trial and error to produce a solution that has a reasonable prediction error $E(\mathbf{m})$ (*Menke*, 2012, and references therein) or, for example, by a cross validation technique (e.g., *Efron and Gong*, 1983; *Aster et al.*, 2012). The measure of "simplicity" of the solution can be expressed as the general measure of length,

$$L(\mathbf{m}) = \left\| \mathbf{W}_m^{1/2} (\mathbf{m} - \mathbf{m}^*) \right\|_2^2 = (\mathbf{m} - \mathbf{m}^*)^T \mathbf{W}_m (\mathbf{m} - \mathbf{m}^*) \tag{3.9}$$

where $\mathbf{m}^*$ is a known model given by previously obtained knowledge or beliefs on the model parameters (what we believe $\mathbf{m}_{est}$ should be) and $L(\mathbf{m})$ measures how distant is the model $\mathbf{m}$ from the a priori model $\mathbf{m}^*$ with a metric defined by the weighting matrix $\mathbf{W}_m$. The resulting inverse problem is called the weighted damped least squares problem,

$$\min_{\mathbf{m}} \left\{ (\mathbf{G}\mathbf{m} - \mathbf{d}_{obs})^T \mathbf{W}_\chi (\mathbf{G}\mathbf{m} - \mathbf{d}_{obs}) + \varepsilon^2 (\mathbf{m} - \mathbf{m}^*)^T \mathbf{W}_m (\mathbf{m} - \mathbf{m}^*) \right\} \tag{3.10}$$

with normal equations,

$$\left(\mathbf{G}^T \mathbf{W}_\chi \mathbf{G} + \varepsilon^2 \mathbf{W}_m \right) \mathbf{m}_{est} = \mathbf{G}^T \mathbf{W}_\chi \mathbf{d}_{obs} + \varepsilon^2 \mathbf{W}_m \mathbf{m}^* \tag{3.11}$$

and a unique solution, for each value of ε, can be obtained when the matrix $\left(\mathbf{G}^T \mathbf{W}_\chi \mathbf{G} + \varepsilon^2 \mathbf{W}_m \right)$ has full rank,

$$\mathbf{m}_{est}(\varepsilon) = \left(\mathbf{G}^T \mathbf{W}_\chi \mathbf{G} + \varepsilon^2 \mathbf{W}_m \right)^{-1} \left(\mathbf{G}^T \mathbf{W}_\chi \mathbf{d}_{obs} + \varepsilon^2 \mathbf{W}_m \mathbf{m}^* \right) \tag{3.12}$$

Note that both $\mathbf{W}_\chi$ and $\mathbf{W}_m$ are required to be semi-definite positive matrices in order to ensure the convexity of the objective function and the existence of a solution of the minimization problem (3.10).

3.2.2 Commonly used regularization schemes

The slip regularization is given by the measure of simplicity of the model (3.9). Here the regularization operator (the weight matrix $\mathbf{W}_m^{1/2}$), is assumed to be linear and can be chosen according to a priori beliefs on the distribution of fault slip. For example, one can use 0^{th} order Tikhonov† regularization $\mathbf{W}_m^{1/2} = \mathbf{I}$, $L(\mathbf{m}) = \|\mathbf{m} - \mathbf{m}^*\|_2^2$ in which the solutions of the inverse problem minimize the total amount of fault slip if $\mathbf{m}^* = \mathbf{0}$. If $\mathbf{m}^* \neq \mathbf{0}$, it will minimize the total difference between $\mathbf{m}_{est}$ and $\mathbf{m}^*$, i.e., it will try to find models similar to the *a priori* one. A problem arises when trying to find a proper $\mathbf{m}^*$, especially for the slip inversion problem, it is very unlikely if not impossible to define absolute *a priori* values for slip on faults without inducing large artifacts in the estimated *a posteriori* values.

A different *a priori* can be to assume a smoothly varying distribution of fault slip, which can be achieved by the 2^{nd} order Tikhonov† regularization $\mathbf{W}_m^{1/2} = \nabla^2$, $L(\mathbf{m}) = \left\|\nabla^2(\mathbf{m} - \mathbf{m}^*)\right\|_2^2$ where ∇^2 is the Laplacian operator defined on fault slip surface coordinates. Here, the regularization will try to produce models that have smooth deviations from the *a priori* model $\mathbf{m}^*$, but does not ensure that $\mathbf{m}_{est}$ will be smooth as $\mathbf{m}^*$ can be any model of our choice, in particular it could be a rough one. The use of the Laplacian operator in our measure simplicity of slip translate into minimizing the roughness of slip distributions (or maximizing the smoothness). Thus, to be consistent with our *a priori* assumptions, we should select $\mathbf{m}^*$ to be the smoothest model possible, a constant one. Then the measure of simplicity can be written as $L(\mathbf{m}) = \left\|\nabla^2\mathbf{m}\right\|_2^2$. For the smoothing regularization

†Strictly speaking, Tikhonov regularization also imposes that the *a priori* model belongs to the null space of the regularization operator $\mathbf{W}_m^{1/2}$ (see §4 of *Aster et al.* (2012))

operator over a discretized fault, the continuous Laplacian operator can be replaced by a finite difference counterpart (e.g., *Desbrun et al.*, 1999).

In general, any matrix $\mathbf{W}_m$ could be used to construct a measure of length of the model parameters as long as $\mathbf{W}_m$ is semi-definite positive. To ensure that, one could define a filter (regularization) operator $\mathbf{F}$ and then construct $\mathbf{W}_m = \mathbf{F}^T\mathbf{F}$ which is semi-definite positive[†].

In a naive word of warning, if one chooses to design a regularization operator, one must check how the operator bias the solution of the inverse problem and how effective it is at stabilizing the solution of the ill-posed inverse problem. Table 3.1 shows the regularization schemes typically used to regularize the slip inversion problem. In the following we analyze some of the regularization schemes in Table 3.1 with the aim to explore their implications for the estimates of slip on faults. We use the Japan Trench megathrust and the location of the GPS sites of the GEONET network in Japan as the fault where slip is estimated and the location of the (synthetic) observations (see §2.3, §4). The location of the GPS sites and fault geometry are the same as used in the study of post-seismic deformation presented in Chapter 4 of this thesis. The synthetic dataset consists of null GPS displacements (or equivalently, $\mathbf{m}_{true} = \mathbf{0}$) at the GEONET GPS network with same uncertainties as the ones of the post-seismic displacements used in Chapter 4 of this thesis. We do not add noise to the synthetic observations with the aim to observe only the influence of the regularization on the solution[‡].

In a first case, we present damped least squares estimates of fault slip (3.12) using two regularization schemes that minimize the amplitude of $\mathbf{m} - \mathbf{m}^*$, 0^{th} order Tikhonov ($\mathbf{W}_m^{1/2} = \mathbf{I}$) and a measure of simplicity that additionally imposes a correlation between the model parameters $\mathbf{m}$

[†]This is the reason why we previously name $\mathbf{W}_m^{1/2}$, the square root of the regularization operator $\mathbf{W}_m$. Here we use the definition of square root of a matrix as $\mathbf{B} = \mathbf{A}^{1/2}$ if $\mathbf{A} = \mathbf{B}^T\mathbf{B}$.

[‡]We consider that the effect of any numerical rounding error is negligible as the regularized system of equations are numerically well posed for a well defined range of damping factors if the null spaces of $\mathbf{G}$ and $\mathbf{W}_m^{1/2}$ only intersect at the trivial point $\mathbf{m} = \mathbf{0}$.

Typical regularization operators			
Examples	Operator	Effects	
Tikhonov regularization if $\mathbf{W}_m^{1/2}\mathbf{m}^* = \mathbf{0}$ *Segall and Harris* (1987) $\rightarrow$	$\mathbf{W}_m^{1/2} = \mathbf{I}$	minimizes amplitude of $\mathbf{m} - \mathbf{m}^*$	
	$\mathbf{W}_m^{1/2} = \nabla$	minimizes gradient of $\mathbf{m} - \mathbf{m}^*$	impose correlation length on $\mathbf{m}$
	$\mathbf{W}_m^{1/2} = \nabla^2$	minimizes roughness of $\mathbf{m} - \mathbf{m}^*$	
Tarantola (2005) *Radiguet et al.* (2011)	$\mathbf{W}_m^{1/2} = \mathbf{C}_m^{-1/2}$	minimizes amplitude of $\mathbf{m} - \mathbf{m}^*$	

Table 3.1. Typical regularization operators used in slip inversion problems.

through an *a priori* model covariance matrix ($\mathbf{W_m} = \mathbf{C}_m^{-1}$). The latter corresponds to the regularization scheme similar to the used by *Radiguet et al.* (2011) in a study characterizing a slow slip subduction event in Mexico[†]. As mentioned before, absolute values of the *a priori* model $\mathbf{m}^*$ will be associated with large uncertainties. Thus, we choose an a priori model that is essentially wrong ($\mathbf{m}^* = \mathbf{300}$ cm) with the aim to test the consequences of such wrong model for our slip inversion. We use the Generalized Cross Validation technique (*Aster et al.*, 2012) to select the damping parameter ε. Our estimates of slip are shown in Figure 3.1.

Not surprisingly, the inversion results in Figure 3.1 clearly shows that both regularization schemes bias the slip estimates towards the *a priori* slip model. Note that the near trench regions of the fault tend to present the larger biases. The slip solution obtained with 0^{th} order Tikhonov regularization presents high frequency slip variations throughout the whole fault surface, thus showing the inability of this type of regularization to completely reduce the checkerboarding. On the other hand, the use of the regularization based on an *a priori* model covariance matrix results in smooth solutions with a much lower degree of bias. Nevertheless, given the bias induced in fault slip estimates by the tested regularization methods, we do not recommend the use of any form of regularization that relies in absolute values of an *a priori* slip model[‡].

[†]Note that the damping parameter ε here controls the correlation length between the model parameters imposed by the covariance matrix $C_m(\varepsilon)$. The damped least squares solution for this case has the same form as (3.12), but the damping parameter is "absorbed" by the *a priori* covariance matrix, i.e., $\mathbf{m}_{est}(\varepsilon) = \left(\mathbf{G}^T\mathbf{W}_\chi\mathbf{G} + \mathbf{C}_m^{-1}(\varepsilon)\right)^{-1}\left(\mathbf{G}^T\mathbf{W}_\chi\mathbf{d}_{obs} + \mathbf{C}_m^{-1}(\varepsilon)\mathbf{m}^*\right)$.

[‡]Normally the true model has a finite value and the *a priori* model is set to zero. Given the symmetry between observations and the predictions of the *a priori* model our conclusions do not change (see equation 3.37 in *Tarantola*,

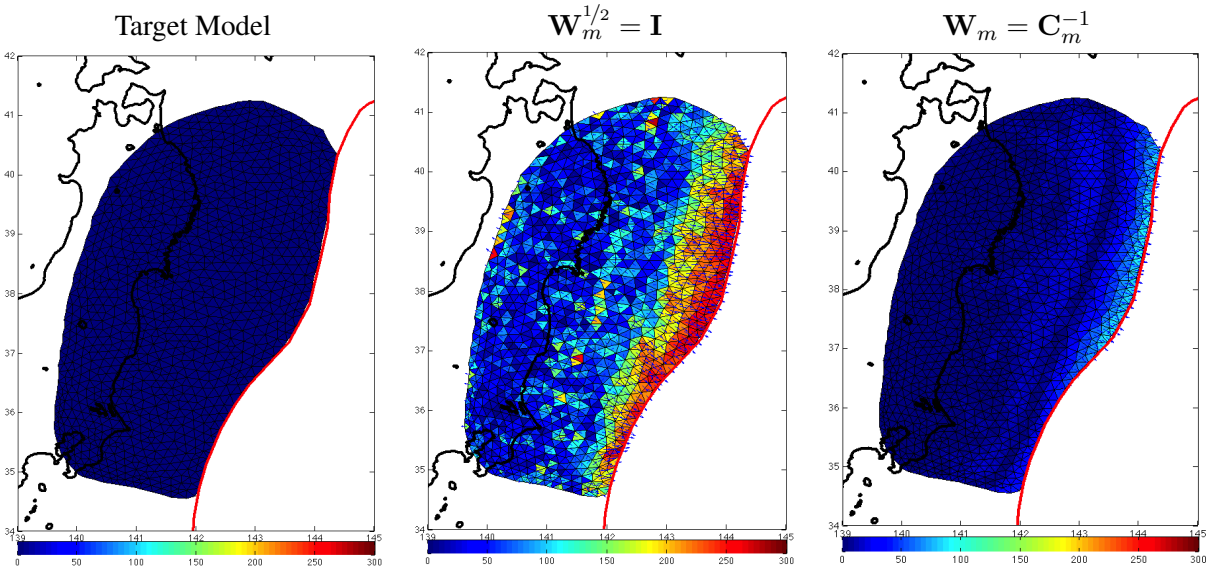

(a) $\mathbf{m}_{true}$ (b) $\mathbf{m}_{est}$ (c) $\mathbf{m}_{est}$

Figure 3.1. Estimates of fault slip (colorbar in cm) constrained by noise free synthetic observations generated with the null slip model (a) using 0^{th} order Tikhonov regularization (b) and a measure of simplicity induced by an *a priori* covariance matrix of the model parameters (c). Note the bias in the estimated slip caused by intentional use of a wrong *a priori* model $\mathbf{m}^*$.

We performed a second suite of test, under the same assumptions, but this time using a 2^{nd} order Tikhonov regularization with an approximation of the Laplacian operator (*Desbrun et al.*, 1999). Here the *a priori* model $\mathbf{m}^* = \mathbf{300}$ cm is constant, and we successfully recover the target model (Figure 3.1a). Since the *a priori* model belongs to the null space of the Laplacian operator, there are no sources for perturbations in the solution of the inverse problem. At this point, our results suggests that the Laplacian operator is a preferred choice for the regularization of the slip inversion problem (e.g., *Segall and Harris*, 1987), but before reaching any conclusions, let's perform a more challenging test on this operator, a checkerboard test with noisy synthetic observations.

We generate two sets of synthetic observations using a checkerboard pattern of slip (Figure 3.2a) that differ only in the realization of the added random noise (Noise_1 and Noise_2), which the same variances as the observations that are used for the inversion of post-seismic deformation in §4. Figure 3.2b,c shows slip estimates constrained with the synthetic observations with added noise

2005). The examples are shown using a null true model because it is easier to observe the bias in the solutions.

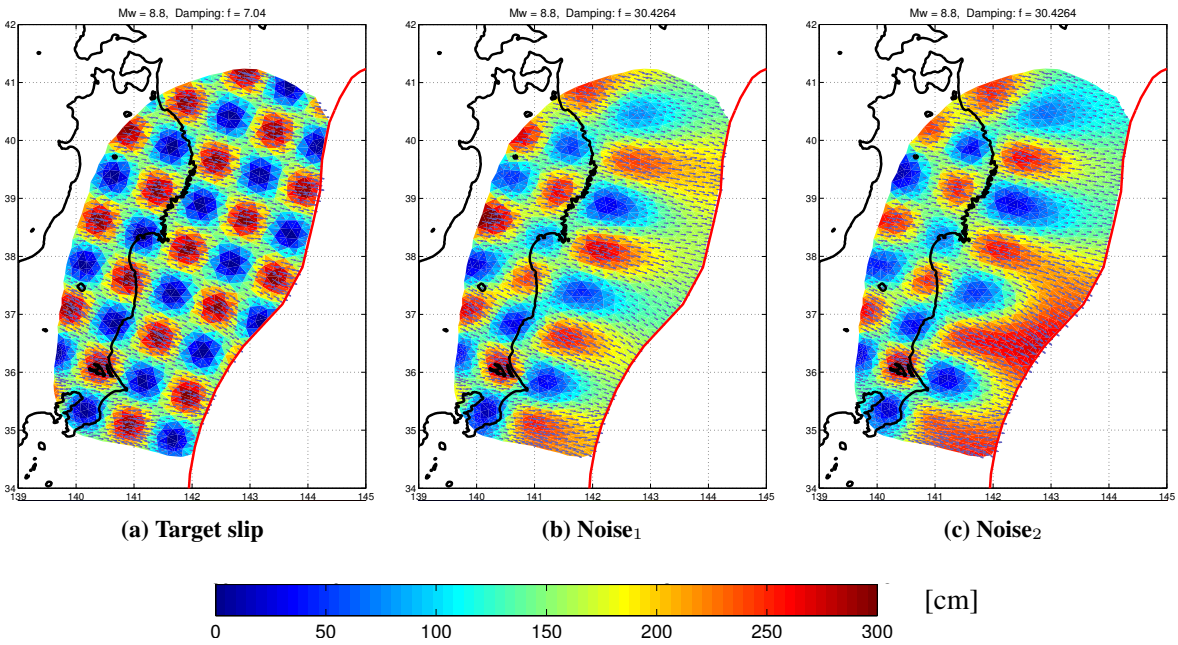

(a) Target slip **(b) Noise$_1$** **(c) Noise$_2$**

Figure 3.2. (a) Input checkerboard-like slip model used to generate synthetic displacements at positions corresponding to GPS sites located in Japan. Two sets of synthetic observations are generated by independent realizations of the same Gaussian noise, Noise$_1$ and Noise$_2$, based on observational variances described in §4. (b) and (c) show estimates of slip constrained by the synthetic observations with added Noise$_1$ and Noise$_2$, respectively.

realizations Noise$_1$ and Noise$_2$ respectively. For this synthetic inversion, we define the optimum damping parameter ε as the one that produces the best recovery of the target slip model. Note how the recovered solution varies greatly when changing the realization of the synthetic noise. Although slip estimates are well resolved at the fault patches beneath Japan, near trench slip is much more unstable and show slip values that tend to be smeared values of the ones at the nearest well resolved region (Figures 3.2b and 3.2e). If one attempts to avoid this problem by increasing the damping constant, one overdamps the solution in well resolved areas. This behavior suggests the need for spatially variable damping.

3.2.3 Spatially variable smoothing

In the previous section, we performed inversion tests with synthetic datasets with the goal of exploring the bias that different types of regularization operators impose in our fault slip estimates as well

as to evaluate the stability of the solution of the inverse problem. We find that the regularization operator that minimizes the 2^{nd} order differential of the spatial distribution of slip ($\mathbf{W}_m^{1/2} = \nabla^2$ and $\mathbf{W}_m^{1/2}\mathbf{m}^* = \mathbf{0}$) may be the best suited for slip inversion. Nevertheless, such regularization scheme is spatially uniform, i.e., the strength of the smoothing imposed by the Laplacian operator is the same for every slip patch on the fault. Thus, leading to solutions that trade-off overdamping in some regions with underdamping in others. Moreover, regardless of the type of regularization tested in the previous section, we observe a strong dependence between fault – observation distance and the location of larger bias or instability in the slip estimates. Therefore, we would like to explore such a relationship. For that purpose, we will give a step back to first analyze the original problem (3.4) in which no regularization is applied and then propose a measure of simplicity (regularization) that stabilizes the slip estimates evenly across the fault.

We aim to find estimates of slip by solving the least squares problem,

$$\mathbf{W}_\chi^{1/2}\mathbf{G}\mathbf{m} \quad = \quad \mathbf{W}_\chi^{1/2}\mathbf{d} \tag{3.13}$$

where $\mathbf{W}_\chi$ is typically the inverse of the covariance matrix associated to the misfit ($\mathbf{C}_\chi$), $\mathbf{G}$ represents the physical model, $\mathbf{m}$ the values of slip on each fault patch, and $\mathbf{d}$ the observations from the onland GPS sites in Japan. The solution of the least squares problem can be found by minimization of the misfit function

$$E(\mathbf{m}) = (\mathbf{G}\mathbf{m} - \mathbf{d})^T\mathbf{W}_\chi(\mathbf{G}\mathbf{m} - \mathbf{d}) \tag{3.14}$$

where $\mathbf{W}_\chi$ is the inverse of the covariance matrix associated to the misfit.

Let $\widetilde{\mathbf{m}}$ be the model that minimizes the quadratic form $E(\mathbf{m})$. We will analyze now the stability of the misfit function values upon perturbations from the optimum model. The misfit function in

terms of the deviations from the least squares solution $\Delta\mathbf{m} = \mathbf{m} - \tilde{\mathbf{m}}$

$$E(\Delta\mathbf{m}) = \Delta\mathbf{m}^T\mathbf{G}^T\mathbf{W}_\chi\mathbf{G}\Delta\mathbf{m} + \mathbf{R}^T\mathbf{W}_\chi\mathbf{R} \tag{3.15}$$

where $\mathbf{R} = \mathbf{G}\tilde{\mathbf{m}} - \mathbf{d}$ is the fit residual. Now, we can calculate the variation (increase) of the misfit function due to a perturbation ϵ from the optimum slip for the fault patch i, $\Delta\mathbf{m}_i = \epsilon\hat{\mathbf{e}}_i$ as

$$\begin{aligned}\Delta E(\Delta\mathbf{m}_i) &= \epsilon^2 \left(\mathbf{G}^T\mathbf{W}_\chi\mathbf{G}\right)_{ii} \\ &= \epsilon^2 S_i\end{aligned} \tag{3.16}$$

where we define the sensitivity of the fault slip patches $\mathbf{S} = \text{diag}(\mathbf{G}^T\mathbf{W}_\chi\mathbf{G})$, which can be interpreted as a relative measure of how sensitive is the model prediction to slip on different fault patches. Indirectly, $\mathbf{S}$ can be taken as a measure of the strength of the constraints provided by the observations (e.g., onland GPS) to the slip on each fault patch. Figure 3.3 shows the strike-slip and

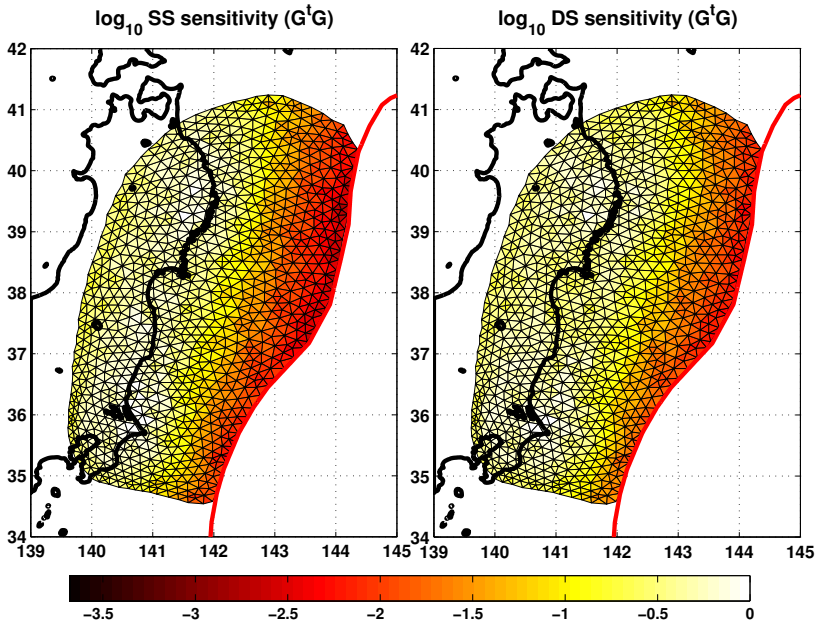

Figure 3.3. Sensitivity calculated for the Japan Trench megathrust assuming that observations are uncorrelated and have the same variance (i.e., $\mathbf{S} = \text{diag}(\mathbf{G}^T\mathbf{G})$). SS and DS indicate strike-slip and dip-slip, respectively.

dip-slip sensitivities normalized by its maximum value for the case in which all the observations are uncorrelated and have unit variance (i.e., $\mathbf{W}_\chi = \mathbf{I}$). Note that for this particular case of observational covariances the sensitivity is the norm squared of the Green's functions. Based on the norm of the Green's functions, *Loveless and Meade* (2011) shows an image similar to Figure 3.3, referring to it as the power of GEONET GPS network to constrain the plate interface behavior, showing its strong spatial variability.

Going back to equation (3.16), the change of the misfit function upon a perturbation from the optimum slip on a single fault patch is proportional to the sensitivity of such fault patch. In order to solve the least squares problem, we search for a solution by a process of minimization of the misfit function. If there is a large spatial variability in the sensitivity of the fault patches, errors on the observations or the physical model will be preferably mapped as slip into the fault patches with smaller sensitivity as it minimizes the variation (increase) of the misfit function. Thus, we would like to regularize the inverse problem using a method that searches to artificially equalize the sensitivity of all fault patches, so that potential perturbations get mapped into slip distributed along all fault patches.

In a first intuition driven approach, we want to derive a regularization scheme that only accounts for the variations in the degree to what a unit slip on each fault patch contribute to the predicted displacements. Thus, we use $\mathbf{S} = \text{diag}(\mathbf{G}^T\mathbf{G})$, where we assume uncorrelated observations with unit variance. As defined, the sensitivity is the norm squared of the Green's functions associated to each fault patch, i.e.,

$$\mathbf{S} = \text{diag}(\mathbf{G}^T\mathbf{G}) \tag{3.17}$$

$$S_i = \|\mathbf{g}_i\|^2 \tag{3.18}$$

where $\mathbf{g}_i$ is the i-th column of the design matrix $\mathbf{G}$. Note that for the problem of elastic dislocation,

if the fault discretization if fine enough, $\mathbf{g}_i$ is proportional to the source surface area. The Laplacian regularization has the ultimate effect of imposing a spatial correlation length on slip among neighboring patches (§A), providing us with a tool to artificially increase the source surface area of the slip patches. Therefore, by changing the relative strength of the Laplacian applied to each fault patch we are effectively changing the correlation length associated to such fault patch relative to the others in the parameterized fault surface. We propose a measure of simplicity $L(\mathbf{m})$ that accounts for the spatial variability of sensitivity, the sensitivity modulated regularization,

$$L(\mathbf{m}) = \left\| \mathbf{S}^{-1/2} \nabla^2 \mathbf{m} \right\|_2^2 = (\nabla^2 \mathbf{m})^T \mathbf{S}^{-1} (\nabla^2 \mathbf{m}) \tag{3.19}$$

where $\mathbf{S}$ is the sensitivity of each fault patch.

The definition of the sensitivity as $\mathbf{S} = \text{diag}(\mathbf{G}^T\mathbf{G})$ has the inconvenience that it does not consider the regularization itself in its calculation. It is an intuitive attempt to consider the fact that different regions of the fault surface have a different capacity to be constrained by the data based on the sensitivity of each fault slip patch. Here we present an information content criterion to calculate the regularization weights in (3.19).

Recall that we are solving the damped least squares problem[†],

$$\min_{\mathbf{m}} \left\{ (\mathbf{G}\mathbf{m} - \mathbf{d}_{obs})^T \mathbf{W}_\chi (\mathbf{G}\mathbf{m} - \mathbf{d}_{obs}) + \varepsilon^2 (\mathbf{m} - \mathbf{m}^*)^T \mathbf{W}_m (\mathbf{m} - \mathbf{m}^*) \right\} \tag{3.20}$$

with family of solutions and associated *a posteriori* covariance matrix,

$$\mathbf{m}_{est}(\varepsilon) = \left(\mathbf{G}^T \mathbf{W}_\chi \mathbf{G} + \varepsilon^2 \mathbf{W}_m \right)^{-1} \left(\mathbf{G}^T \mathbf{W}_\chi \mathbf{d}_{obs} + \varepsilon^2 \mathbf{W}_m \mathbf{m}^* \right) \tag{3.21}$$

$$\widetilde{\mathbf{C}}_m(\varepsilon) = \left(\mathbf{G}^T \mathbf{W}_\chi \mathbf{G} + \varepsilon^2 \mathbf{W}_m \right)^{-1} \tag{3.22}$$

[†]For the purposes of this section, we are ignoring the possible implementation of positivity constraints. Although their implementation should not change significantly our weights calculation, these are considered an approximation when positivity constraints are present due to the inability to directly compute an *a posteriori* covariance matrix of the model parameters.

where $\mathbf{W}_\chi$ is the data weights matrix [†] defined as the Cholesky decomposition of the inverse of the misfit covariance matrix, and $\mathbf{W}_m^{1/2} = \mathbf{W}_S\mathbf{T}$ is the weighted Laplacian regularization operator ($\mathbf{T}$ is a finite difference approximation of the Laplacian operator ∇^2).

The Laplacian operator imposes a correlation between neighboring fault patches (§A). By changing the regularization weights one can control the induced correlation length in different parts of the fault surface. From an information theory perspective, a high correlation between neighboring patches is equivalent to saying that they share the information obtained from the observations. Also, as discussed later, the information contained within an inferred parameter is related to its variance if the parameter follows a Normal PDF.

We propose to calculate the regularization weights ($\mathbf{W}_S$) by imposing the a priori constraint that the information content obtained from the data must be the same for all fault slip patches.

A measure of the information content on a continuous random variable is given by the differential entropy. If $f(x)$ is the PDF of the continuous random variable X, its differential entropy is defined as,

$$h(x) = -\int_X f(x)\log(f(x))dx \tag{3.23}$$

Also, Kullback-Leibler divergence gives us a measure of the "distance" from the PDF of the random variable x ($f(x)$) to another PDF associated to the same random variable ($\mu(x)$),

$$D_{KL}(f\|\mu) = -\int_X f(x)\log\left(\frac{f(x)}{\mu(x)}\right)dx \tag{3.24}$$

If the variable x is a Cartesian parameter and $\mu(x)$ is a uniform PDF representing its state of homogeneous information (see *Tarantola*, 2005), $\mu(x)$ is constant, and the Kullback-Leibler divergence

[†] In this particular study we assume $\mathbf{W}_\chi$ to be diagonal, i.e., we ignore possible correlations between the different observations.

of $f(x)$ with respect to $\mu(x)$ is proportional to the differential entropy. From here on, we assume that the *a priori* PDFs for slip can be approximated by uniform distributions (uninformative) as we derive a measure of simplicity based on the second spatial differential of slip and not in the actual values of slip.

Each component of $\mathbf{m}$ inferred through eq (3.21) follows a Normal PDF and its differential entropy depends only on the marginal variance of the parameter,

$$h(x) = \frac{1}{2}\ln\left(2\pi e\sigma^2\right) \tag{3.25}$$

then imposing a constraint of equal a posteriori information content on $\mathbf{m}$ is equivalent to imposing that a posteriori marginal variances are the same for all components of $\mathbf{m}$. The equal information constraint is used to modify the regularization weights to in turn modify the covariances of the model parameters in order to achieve equal a posteriori variances. From an information theory perspective, we seek to equalize the information content on each fault patch by manipulating the amount of information shared with its neighbors.

For the damped least squares problem in eq (3.20), the estimated parameters $\mathbf{m}$ follow a Normal PDF with a posteriori covariance matrix

$$\tilde{\mathbf{C}}_m = \left[\mathbf{G}^T\mathbf{W}_\chi\mathbf{G} + \varepsilon^2\mathbf{T}^T\mathbf{W}_S^2\mathbf{T}\right]^{-1} \tag{3.26}$$

We decompose $\tilde{\mathbf{C}}_m$ into a constant diagonal matrix and a symmetric Hollow matrix: $\tilde{\mathbf{C}}_m = \alpha^2\mathbf{I} + \tilde{\mathbf{C}}_H$, so we are imposing that all the a posteriori variances are equal to α^2, leaving the covariances to be determined by the structure of $\mathbf{T}$, $\mathbf{G}$ and $\mathbf{W}_\chi$. By imposing this condition, we obtain the equal information constraint

$$diag\left(\left[\mathbf{G}^T\mathbf{W}_\chi\mathbf{G} + \mathbf{T}^T\mathbf{W}_S^2\mathbf{T}\right]^{-1}\right) = \alpha^2\mathbf{I} \tag{3.27}$$

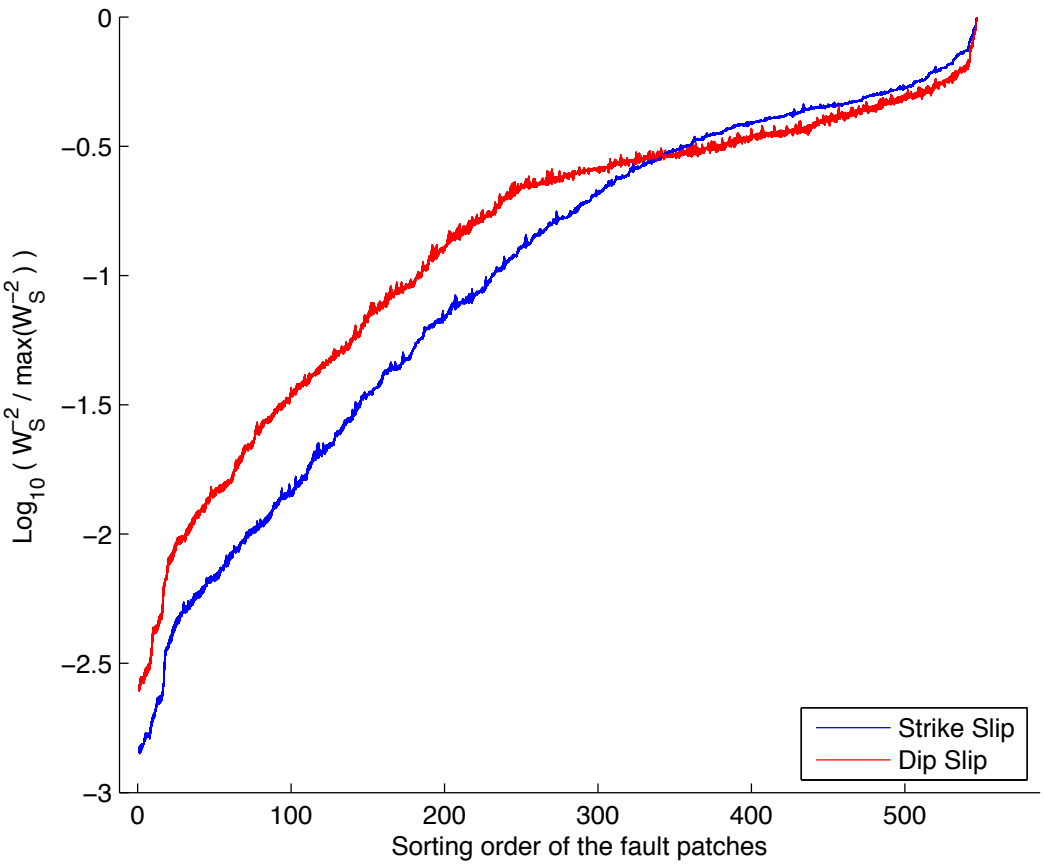

Figure 3.4. Sensitivity representation of the regularization weights inferred using the equal information constraint for 200 random initial values for the iterative optimization algorithm. All models are sorted by the same indexing process. The plot shows the stability and convergence of the optimization process. Strike slip and dip slip sensitivity plots can not be compared because they are sorted independently.

We can then solve this system of nonlinear equations to obtain estimates of $\mathbf{W}_S^2$ and α^2. Note that ε was absorbed by the regularization weights since they are both unknown and that we are assuming that $\mathbf{W}_S$ is a diagonal positive definite matrix. We use MATLAB's lsqnonlin function, using the Levenberg-Marquardt algorithm for the optimization process. In Figure 3.4 we show 200 stacked solutions of $\mathbf{W}_S^2$ (we plot the normalized inverse for comparison purposes with $\mathbf{S}$) obtained using random initial values in the iterative algorithm and obtaining very similar solutions for all cases. Thus showing the stability of the method.

For comparison purposes, we plot in Figure 3.5 the normalized sensitivity inferred from the

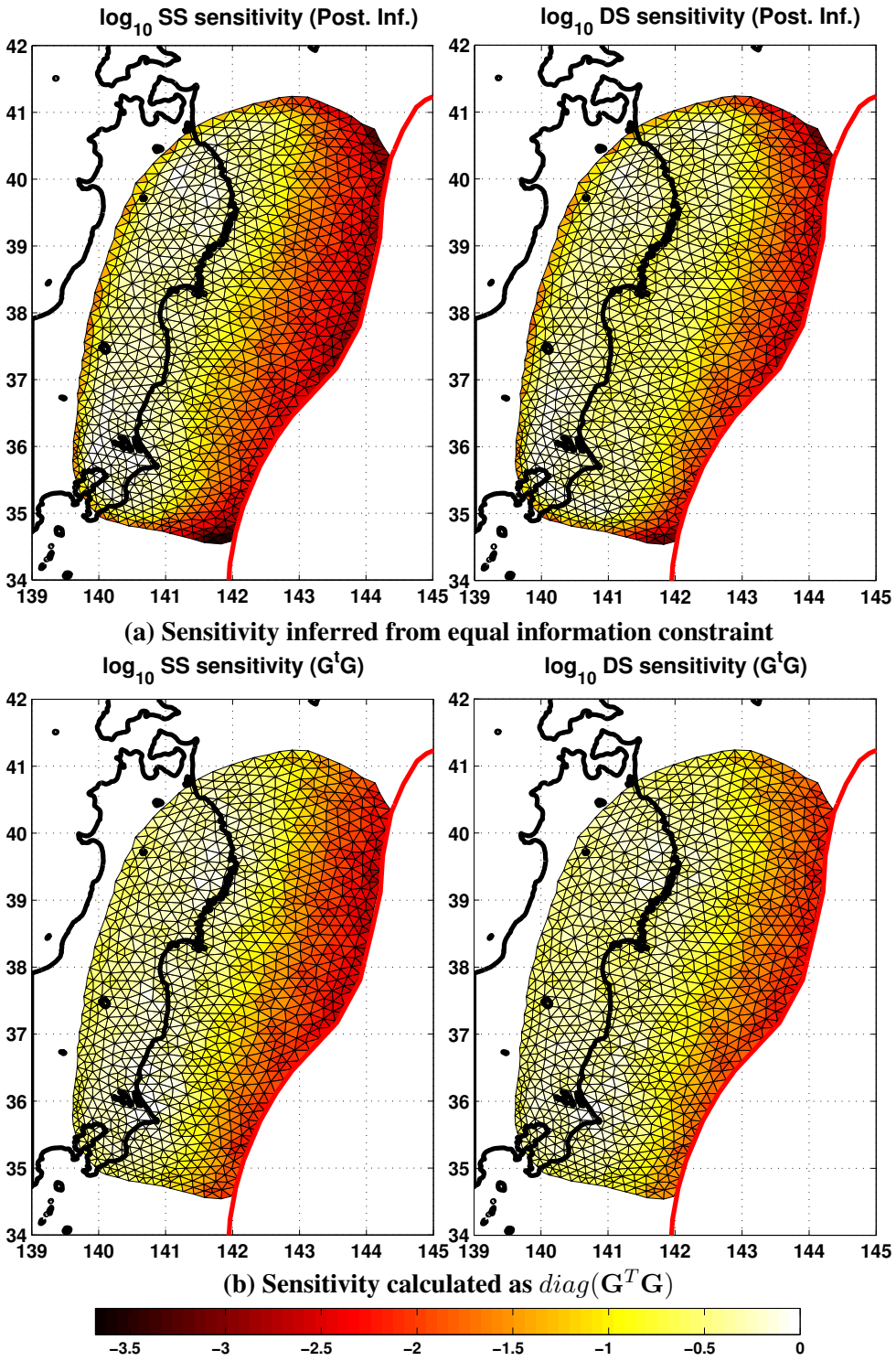

(a) Sensitivity inferred from equal information constraint

(b) Sensitivity calculated as $diag(\mathbf{G}^T\mathbf{G})$

Figure 3.5. Comparison of sensitivity obtained through the equal information constraint (EIC) versus diag($\mathbf{G}^T\mathbf{G}$). SS and DS indicate strike-slip and dip-slip respectively. The major difference occurs at the edges of the parameterized fault surface, where EIC shows a decreased sensitivity due to incorporation of regularization in calculation of its weights.

equal information constraint (EIC) against the one calculated as $\mathbf{S} = \text{diag}(\mathbf{G}^T\mathbf{G})$. EIC regularization weights are consistently larger (lower sensitivity) at the edges of the model, reflecting the difference between the regularization used at the edges and interior of the parameterized surface. Note that we do not include the full set of equations in the calculation of the regularization weights $\mathbf{W}_S$, as these calculations are based on the *a posteriori* covariance matrix on the model parameters which do not depend on the actual observations. Thus, the value of the damping parameter ε may then be different. Here, we find a first approximation of the regularization weights and we are interested in their relative values, therefore we normalize the obtained weights by the maximum value when solving (3.20). A more sophisticated approach would solve a non linear least squares problem in which we impose the equal information constraint on each linearized system during the iterative inversion scheme. The study of such algorithm is left for future work.

We performed inversion tests with synthetic data comparing the results obtained using the two discussed methods to calculate the regularization weights and found no significant differences in the recovered slip distributions (see Figure 3.7). Thus, we use the intuitive approach ($\mathbf{S} = \text{diag}(\mathbf{G}^T\mathbf{G})$) to compute the regularization weights for our slip inversions.

To illustrate the impact of sensitivity modulated regularization we perform 2 checkerboard tests, comparing uniform regularization (previous section) and the sensitivity modulated regularization (Figure 3.6). We use the same synthetic datasets as in previous section, recall that these differ only in the realization of the added random noise, and have the same variances as the data used in our inversion of post-seismic after-slip in Chapter 4. The main advantage of the sensitivity modulated regularization approach is that we avoid introduction of artifacts in low resolution areas and we are able to make reasonable interpretations in these regions. When using the classic uniform regularization the recovered solution varies greatly when changing the realization of the synthetic noise, and the obtained values near the trench tend to be smeared values of the nearest well resolved region

(Figures 3.6b and 3.6e). Such problems can not be avoided by increasing the damping constant, as one overdamps the solution in well resolved areas. Compared to the uniform regularization, sensitivity modulated regularization enables us to recover a much more stable slip distribution, an overall rougher solution while imposing a stronger smoothing in regions with lower sensitivity (See Figure 3.6d) .

For synthetic inversion we can define the optimum damping parameter ε at the minimum of the target slip misfit/roughness curve. Thus, rougher models are considered to be underdamped, and smoother ones overdamped. Comparing both regularization schemes for different noise realizations on the synthetic data, sensitivity modulated regularization provides a much greater stability of the inferred models (see red symbols in Figure 3.6d). Moreover, a comparison of the results with different noise realizations, reveals that the slip roughness/target model misfit values coincide at higher values of ε (lower roughness), and also are much more closer (stable) for underdamped models (higher roughness) when using the sensitivity modulated regularization relative to the ones obtained using the uniform smoothing regularization.

Note in Figure 3.6 that using the proposed regularization approach at the regions of low sensitivity the recovered after-slip is approximately the average of the target model as opposed to the results obtained using the constant Laplacian in which the after-slip distribution is poorly resolved and unstable, obtaining values smeared from the regions of high sensitivity. Also, the sensitivity regularization allows us to improve the stability of the slip distribution and to recover solutions with a smaller misfit and an overall rougher slip distribution while imposing a stronger smoothing at the least sensitive regions of the fault surface.

We use the measure of simplicity (3.19) when solving static linear slip inversion problems. The evaluation and deduction of a generalization of this procedure for a general linear least square inversion problem is left for future work.

As an aside, for completeness purposes, we calculate the sensitivity $\mathbf{S} = \text{diag}(\mathbf{G}^T\mathbf{G})$ for the fault and set of observations used in the study of inter-seismic deformation in the Central Andes subduction zone, which is described in Chapter 5 (Figure 3.8). For a detailed description of the fault and observations see Chapter 5.

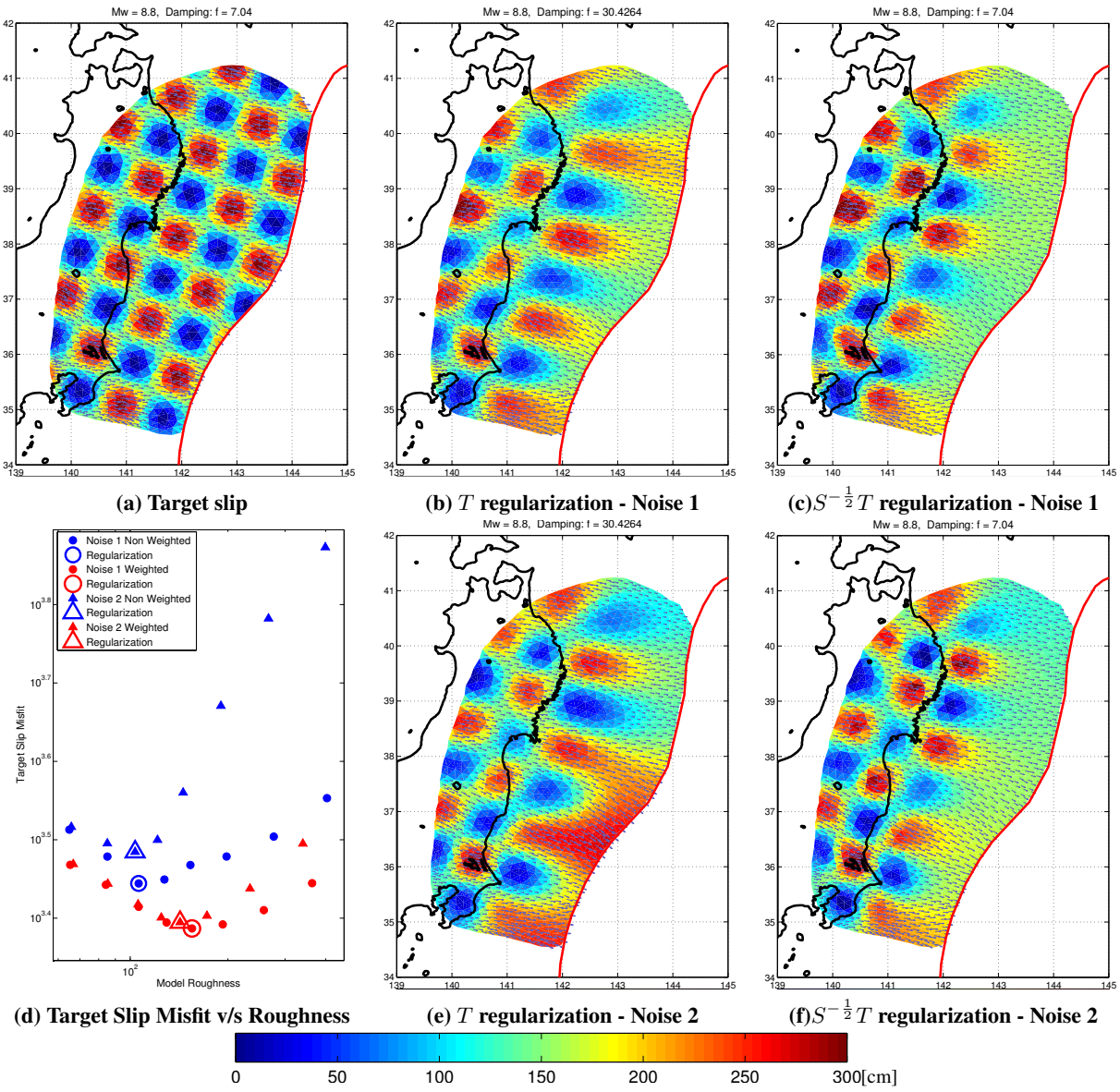

(a) Target slip **(b) T regularization - Noise 1** **(c)$S^{-\frac{1}{2}}T$ regularization - Noise 1**

(d) Target Slip Misfit v/s Roughness **(e) T regularization - Noise 2** **(f)$S^{-\frac{1}{2}}T$ regularization - Noise 2**

Figure 3.6. (a) Input checkerboard-like slip model used to generate synthetic displacements at the GPS sites. Two sets of synthetic observations are generated by independent realizations of the same Gaussian noise, Noise$_1$ and Noise$_2$, based observational variances. We perform slip inversion tests constrained by the synthetic observations using the classic Laplacian regularization of the slip distribution (b and e) and using the sensitivity-based regularization proposed in this study (c and f). (b) and (c) uses the synthetic data with added Noise$_1$, (e) and (f) use Noise$_2$. (d) Target slip RMS residual vs slip roughness for the inversions using both regularization schemes. Open symbols indicate the optimum solutions. For comparison purposes, the roughness is computed as $\|T \cdot m\|_2$ for both regularization cases, where $\mathbf{T}$ is the finite differences representation of the Laplacian operator.

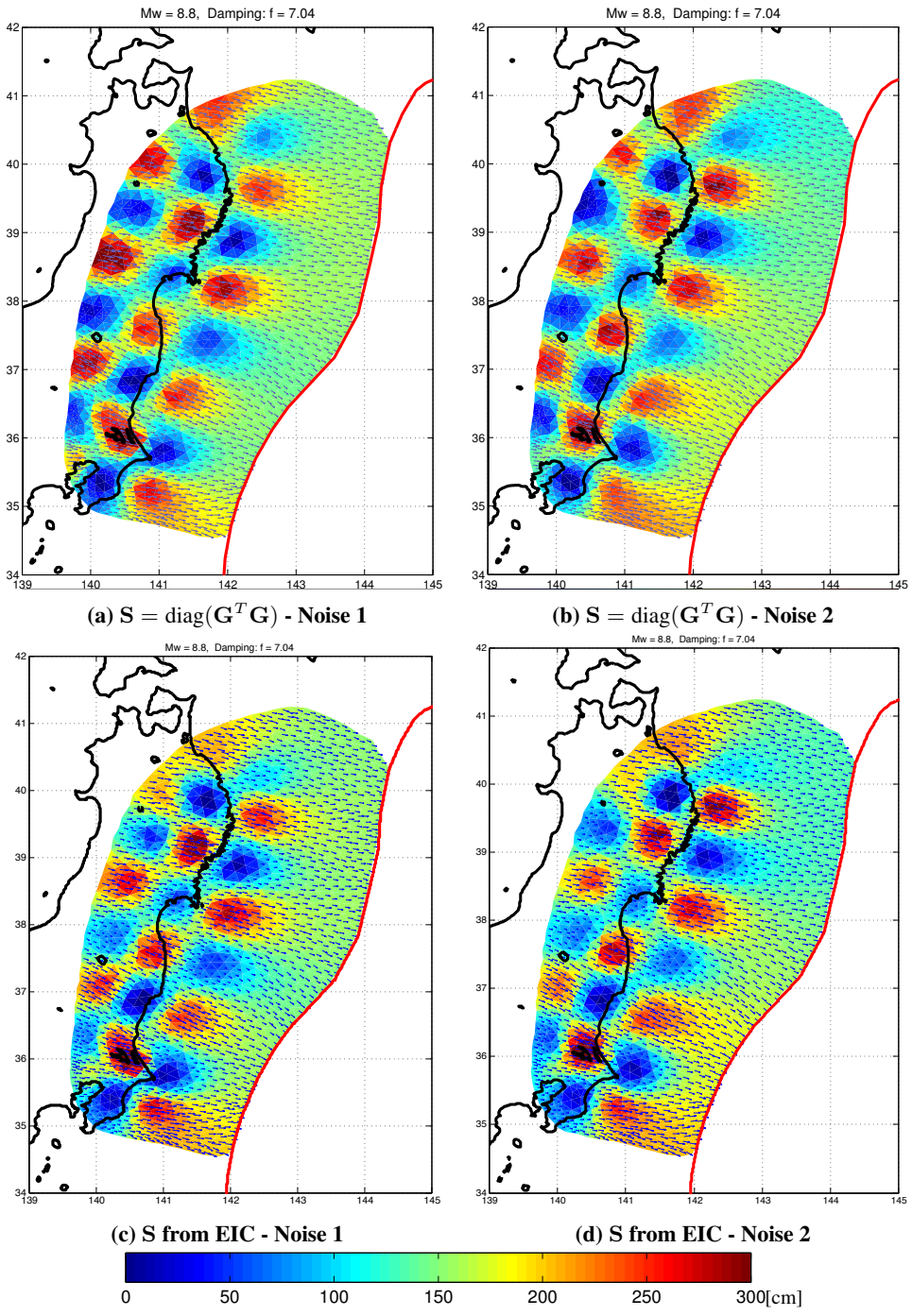

(a) $\mathbf{S} = \mathrm{diag}(\mathbf{G}^T\mathbf{G})$ **- Noise 1**

(b) $\mathbf{S} = \mathrm{diag}(\mathbf{G}^T\mathbf{G})$ **- Noise 2**

(c) S from EIC - Noise 1

(d) S from EIC - Noise 2

Figure 3.7. Estimates of slip constrained by synthetic observations that were generated as explained in Figure 3.6. Here we compare estimates in which the regularization weights are calculated using $\mathbf{S} = \mathrm{diag}(\mathbf{G}^T\mathbf{G})$, panels (a) and (b); and calculated using $\mathbf{S}$ estimated with the equal information constraint (3.27), panels (c) and (d). (see values of sensitivity, $\mathbf{S}$, in Figures 3.5b and 3.5a, respectively).

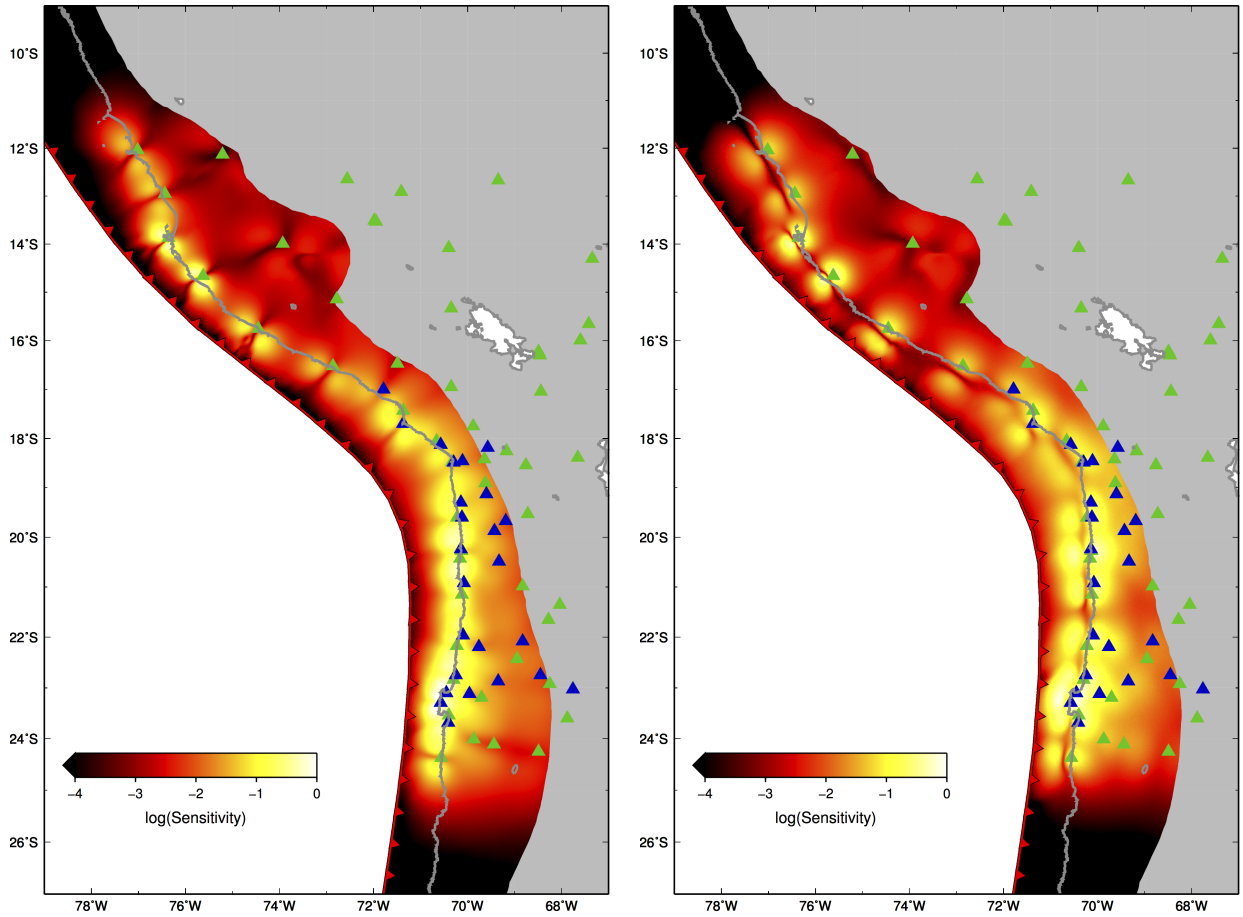

(a) $\mathbf{log}(\mathbf{S}_{\text{strike-slip}})$ **(b)** $\mathbf{log}(\mathbf{S}_{\text{dip-slip}})$

Figure 3.8. Strike-slip (a) and dip-slip (b) sensitivity $\mathbf{S} = \text{diag}(\mathbf{G}^T\mathbf{G})$ for fault surface and observations of inter-seismic secular rates used in Chapter 5. Green and blue triangles indicate GPS sites in which only horizontal and 3 component secular rates were measured, respectively. The size of the discretized elements of the fault is about $2 - 3$ km^2. See Chapter 5 for further detail.

3.3 A Bayesian framework for the regularization of slip inversion

Given the rapid increase in available computational power, the Bayesian approach for inverse problem is being promoted as the standard procedure for inverse modeling, in particular for inferring finite fault earthquake source models (e.g., §5; *Minson et al.*, 2013). Recognizing such advances, here we derive an alternate formulation of the Bayesian inversion problem proposed by *Tarantola* (2005), in which we incorporate the *a priori* information of a derived quantity, that can be, for example, the roughness of slip, and the probability distribution representing the theoretical relationship between the model parameters and the derived quantity.

Following *Tarantola* (2005), we derive a Bayesian formulation of the inverse problem where we take into account a set of observations $\mathbf{d}$, model parameters $\mathbf{m}$, and a some quantity $\mathbf{h}$ that can be estimated from a linear transformation of the model parameters.

Let $\mathfrak{M}$ the model space manifold, with some coordinates (model parameters) $\mathbf{m} = \{m^1, m^2, \ldots, m^{N_p}\}$ and homogeneous probability density $\mu_M(\mathbf{m})$; $\mathfrak{D}$ the data space manifold, with some coordinates (observable parameters) $\mathbf{d} = \{d^1, d^2, \ldots, d^{N_{obs}}\}$ with homogeneous probability density $\mu_D(\mathbf{d})$; and $\mathfrak{H}$ the manifold of the quantity $\mathbf{h}$ with coordinates $\mathbf{h} = \{h^1, h^2, \ldots, h^{N_h}\}$ with homogeneous probability density $\mu_H(\mathbf{h})$. Let $\mathfrak{X}$ be the joint manifold built as the Cartesian product of the three manifolds $\mathfrak{D} \times \mathfrak{H} \times \mathfrak{M}$, with coordinates $\mathbf{x} = \{\mathbf{d}, \mathbf{h}, \mathbf{m}\} = \{d^1, d^2, \ldots, h^1, h^2, \ldots, m^1, m^2, \ldots\}$ and with homogeneous probability density $\mu(x) = \mu(\mathbf{d}, \mathbf{h}, \mathbf{m}) = \mu_D(\mathbf{d})\mu_H(\mathbf{h})\mu_M(\mathbf{m})$.

3.3.1 Representation of theoretical relationships

We represent the correlations between the parameters imposed by the theoretical relationships (together with their uncertainties when applicable) in our modeling by the joint probability density function $\Theta(\mathbf{d}, \mathbf{h}, \mathbf{m})$. Here, by theoretical relationships we mean the equations given by our physical model relating the slip distribution $\mathbf{m}$ with the observations $\mathbf{d}$ as well as the equations describing

the relationship between the slip distribution $\mathbf{m}$ and the derived quantity $\mathbf{h}$. In general, the joint probability density function can be written in terms of the conditional and marginal probabilities. By marginalizing in terms of the model parameters we obtain,

$$\Theta(\mathbf{d}, \mathbf{h}, \mathbf{m}) \quad = \quad \theta(\mathbf{d}|\mathbf{h}, \mathbf{m})\theta(\mathbf{h}|\mathbf{m})\mu_M(\mathbf{m}) \tag{3.28}$$

where $\theta(\mathbf{d}|\mathbf{h}, \mathbf{m})$ represents the theoretical relationship describing our physical model (e.g., the elastic response of the Earth) and $\theta(\mathbf{h}|\mathbf{m})$ the theoretical relationship between the model parameters (slip distribution) and the quantity $\mathbf{h}$.

For the case of the static slip inversion, the physical model gives us predicted observations in the data space through the linear relationship $\mathbf{d} = \mathbf{Gm}$. Recognizing that the physical model is an approximation of the true physics governing the processes that cause our experimental observations, we will assume that our model predictions have uncertainty (i.e., $\mathbf{d} \approx \mathbf{Gm}$) described by the Gaussian probability distribution with expected value $\mathbf{Gm}$ and covariance matrix $\mathbf{C}_p$[†]. Then the state of information given by the physical theory can be written as the probability density,

$$\theta(\mathbf{d}|\mathbf{h}, \mathbf{m}) = \theta(\mathbf{d}|\mathbf{m}) = \text{const.} \quad e^{-\frac{1}{2}(\mathbf{d}-\mathbf{Gm})^T \mathbf{C}_p^{-1}(\mathbf{d}-\mathbf{Gm})} \tag{3.29}$$

Here $\mathbf{C}_p$ will depend exclusively in the ability of the chosen physical model to represent the true physics of the problem in question. Although estimating $\mathbf{C}_p$ remains an open problem (*Tarantola*, 2005; *Minson et al.*, 2013), it is believed that the major source of modeling errors for the co-seismic slip forward model comes from the assumed elastic structure of the medium (*Minson et al.*, 2013), and from the actual elasticity assumption for the case in which slip on the fault is occurring aseismically over a prolonged period of time.

For the relationship between the model parameters $\mathbf{m}$ and the quantity $\mathbf{h}$ we will assume that

[†]The model prediction covariance matrix $\mathbf{C}_p$ is denoted as $\mathbf{C}_T$ in *Tarantola* (2005).

their relationship is linear, $\mathbf{h}(\mathbf{m}) = \mathbf{H}\mathbf{m}$ and that it is exact[†]. Then, the probability density describing the state of information given by such a relationship can be described as

$$\theta(\mathbf{h}|\mathbf{m}) = \text{const.} \quad \delta(\mathbf{h} - \mathbf{H}\mathbf{m}) \tag{3.30}$$

where $\delta(\cdot)$ is the Dirac probability density.

3.3.2 Measurements

We will start here from the fact that no matter how good or advanced our techniques can become, every physical measurement we can make has some inherent noise or uncertainties that will limit the amount of information we can obtain from such observations. Such state of information of the observations can be represented by a probability density $\rho_D(\mathbf{d})$ defined over the data space $\mathfrak{D}$. Typically, we could measure N_{obs} observations and assemble them into a data vector $\mathbf{d}$ and we may obtain obtain the observed values $\mathbf{d}_{obs}$, with uncertainties described by a Gaussian distribution with a covariance matrix $\mathbf{C}_D$. In this case, $\rho_D(\mathbf{d})$ is a Gaussian probability density function centered at $\mathbf{d}_{obs}$,

$$\rho_D(\mathbf{d}) = \text{const.} \quad e^{-\frac{1}{2}(\mathbf{d}-\mathbf{d}_{obs})^T \mathbf{C}_D^{-1}(\mathbf{d}-\mathbf{d}_{obs})} \tag{3.31}$$

where $\mathbf{C}_D$ will depend exclusively on the quality of the instruments and methodologies used to obtain the observations. For example, in the case of GPS positioning, $\mathbf{C}_D$ could contain uncertainties coming from errors in atmospheric models for electromagnetic waves propagation, position of the satellite constellation, scattering of electromagnetic waves in the vicinity of the GPS antenna, etc.

[†] Known without uncertainty since it is an arbitrarily defined mathematical relationship. However, one could argue that there is some uncertainty in the relationship if it corresponds to a discretization of a continuous relationship (e.g., when $\mathbf{H}$ is the umbrella operator approximating the Laplacian operator ∇^2).

3.3.3 *A priori* information

Here we define the a priori information on both model parameters $\mathbf{m}$ and the quantity $\mathbf{h}$. By a priori information we mean that such information is obtained independently of the experimental observations. We also impose the condition that the a priori information obtained for the model parameters $\mathbf{m}$ must be independent on the a priori information on $\mathbf{h}$. We explore the consequences of the latter assumption after we derive the solution of the inverse problem.

The probability density functions $\rho_M(\mathbf{m})$ and $\rho_H(\mathbf{h})$ will denote the state of a priori information for the model parameters $\mathbf{m}$ and the quantity $\mathbf{h}$, respectively. The most obvious case is when we do not have any a priori information on either $\mathbf{m}$ or $\mathbf{h}$, where the state of a priori information is represented by the homogeneous probability density functions $\mu_M(\mathbf{m})$, $\mu_H(\mathbf{h})$.

A general assumption that can be done either for $\mathbf{m}$ and $\mathbf{h}$ is that these are random realizations from a particular Gaussian distribution with a given mean $\mathbf{m}_{prior}$, $\mathbf{h}_{prior}$ and covariance $\mathbf{C}_M$, $\mathbf{C}_H$. Then the a priori information on $\mathbf{m}$ and $\mathbf{h}$ is represented by the following a probability density functions,

$$\rho_M(\mathbf{m}) = \text{const.} \quad e^{-\frac{1}{2}(\mathbf{m}-\mathbf{m}_{prior})^T \mathbf{C}_M^{-1}(\mathbf{m}-\mathbf{m}_{prior})} \tag{3.32}$$

$$\rho_H(\mathbf{h}) = \text{const.} \quad e^{-\frac{1}{2}(\mathbf{h}-\mathbf{h}_{prior})^T \mathbf{C}_H^{-1}(\mathbf{h}-\mathbf{h}_{prior})} \tag{3.33}$$

The main advantage of the Gaussian assumption, as we will see later, is that we can directly obtain a closed form of the inverse problem solution in the least squares sense. More general assumptions can be used as a priori information such as bound constraints, non-linear constraints, but those will require to solve the inverse problem either by the use of an iterative optimization technique or by direct sampling of the model parameters using under the Bayesian framework

3.3.4 Joint *a priori* and *a posteriori* information

As previously defined, the a priori information on model parameters $\mathbf{m}$, the derived quantity $\mathbf{h}$ and the observations $\mathbf{d}$ must be mutually independent. Therefore, the information we have in $\mathbf{m}$, $\mathbf{h}$ and $\mathbf{d}$ can be described by the joint probability density

$$\rho(\mathbf{d},\mathbf{h},\mathbf{m}) \quad = \quad \rho_D(\mathbf{d})\rho_H(\mathbf{h})\rho_M(\mathbf{m}) \tag{3.34}$$

The a priori probability density $\rho(\mathbf{d},\mathbf{h},\mathbf{m})$ represent the information obtained on the observable parameters $\mathbf{d}$ and the a priori information on both model parameters $\mathbf{m}$, and the quantity $\mathbf{h}$. Also, we have defined the theoretical probability density $\Theta(\mathbf{d},\mathbf{h},\mathbf{m})$ which represents the theoretical correlations between $\mathbf{d}$, $\mathbf{h}$ and $\mathbf{m}$ as obtained, for example, from the theory modeling the elastic response of the Earth and the mathematical relationship between the model parameters $\mathbf{m}$ and their derived quantity $\mathbf{h}$.

The theroretical and a priori states of information can be combined to produce the a posteriori state of information. The a posteriori state of information can be obtained by the conjunction of the a priori and theoretical states of information (see *Tarantola and Valette*, 1982; *Mosegaard and Tarantola*, 2002; *Tarantola*, 2005, for the conjunction of states of information). Then, the probability density $\sigma(\mathbf{d},\mathbf{h},\mathbf{m})$ representing the a posteriori information on the space $\mathfrak{D}\times\mathfrak{H}\times\mathfrak{M}$ is:

$$\sigma(\mathbf{d},\mathbf{h},\mathbf{m}) \quad = \quad k\frac{\rho(\mathbf{d},\mathbf{h},\mathbf{m})\Theta(\mathbf{d},\mathbf{h},\mathbf{m})}{\mu(\mathbf{d},\mathbf{h},\mathbf{m})} \tag{3.35}$$

where $\mu(\mathbf{d},\mathbf{h},\mathbf{m})$ represents the homogeneous state of information and k is a normalization constant.

3.3.5 The solution of the inverse problem

Given the a posteriori information in the $\mathfrak{D} \times \mathfrak{H} \times \mathfrak{M}$ space defined in (3.35), the a posteriori in the model space $\mathfrak{M}$ is given by the marginal probability density

$$\sigma_M(\mathbf{m}) = \int_{\mathfrak{H}} \int_{\mathfrak{D}} \sigma(\mathbf{d}, \mathbf{h}, \mathbf{m}) d\mathbf{d} d\mathbf{h} \tag{3.36}$$

In the general case, (3.36) defines the solution of the inverse problem as the a posteriori probability density function of the model parameters $\sigma_M(\mathbf{m})$ (*Tarantola*, 2005).

We now treat the case in which the a priori information is assumed to follow a Gaussian probability density (equations 3.31, 3.33 and 3.32) and using the theoretical information described by the probability densities (3.29) and (3.30). By replacing the chosen densities in (3.36) we obtain:

$$\sigma_M(\mathbf{m}) = k\rho_M(\mathbf{m})\mathcal{H}(\mathbf{m})\mathcal{L}(\mathbf{m}) \tag{3.37}$$

where,

$$\rho_M(\mathbf{m}) = \text{const.} \quad e^{-\frac{1}{2}(\mathbf{m}-\mathbf{m}_{prior})^T \mathbf{C}_M^{-1}(\mathbf{m}-\mathbf{m}_{prior})} \tag{3.38}$$

$$\begin{aligned} \mathcal{H}(\mathbf{m}) &= \text{const.} \int_{\mathfrak{H}} \frac{\theta(\mathbf{h}|\mathbf{m})\rho_H(\mathbf{h})}{\mu_H(\mathbf{h})} d\mathbf{h} \\ &= \text{const.} \int_{\mathfrak{H}} \frac{\delta(\mathbf{h}-\mathbf{H}\mathbf{m}) e^{-\frac{1}{2}(\mathbf{h}-\mathbf{h}_{prior})^T \mathbf{C}_H^{-1}(\mathbf{h}-\mathbf{h}_{prior})}}{\mu_H(\mathbf{h})} d\mathbf{h} \\ &= \text{const.} \quad e^{-\frac{1}{2}(\mathbf{H}\mathbf{m}-\mathbf{h}_{prior})^T \mathbf{C}_H^{-1}(\mathbf{H}\mathbf{m}-\mathbf{h}_{prior})} \end{aligned} \tag{3.39}$$

$$\begin{aligned} \mathcal{L}(\mathbf{m}) &= \text{const.} \int_{\mathfrak{D}} \frac{\theta(\mathbf{d}|\mathbf{m})\rho_D(\mathbf{d})}{\mu_D(\mathbf{d})} d\mathbf{d} \\ &= \text{const.} \int_{\mathfrak{D}} \frac{e^{-\frac{1}{2}(\mathbf{d}-\mathbf{G}\mathbf{m})^T \mathbf{C}_p^{-1}(\mathbf{d}-\mathbf{G}\mathbf{m})} e^{-\frac{1}{2}(\mathbf{d}-\mathbf{d}_{obs})^T \mathbf{C}_D^{-1}(\mathbf{d}-\mathbf{d}_{obs})}}{\mu_D(\mathbf{d})} d\mathbf{d} \\ &= \text{const.} \quad e^{-\frac{1}{2}(\mathbf{G}\mathbf{m}-\mathbf{d}_{obs})^T \mathbf{C}_\chi^{-1}(\mathbf{G}\mathbf{m}-\mathbf{d}_{obs})} \end{aligned} \tag{3.40}$$

$$\mathbf{C}_\chi = \mathbf{C}_D + \mathbf{C}_p \tag{3.41}$$

$\mathcal{L}$ is normally called the Likelihood function $\mathcal{L}(\mathbf{m}) = \rho_D(\mathbf{Gm})$. We can then rewrite (3.37) as

$$\sigma_M(\mathbf{m}) \quad = \quad ke^{-S(\mathbf{m})} \tag{3.42}$$

where k is a normalization constant and the misfit function $S(\mathbf{m})$ is the quadratic form

$$\begin{aligned} S(\mathbf{m}) \quad = \quad & \frac{1}{2}\left[(\mathbf{Gm}-\mathbf{d}_{obs})^T\mathbf{C}_\chi^{-1}(\mathbf{Gm}-\mathbf{d}_{obs}) + (\mathbf{Hm}-\mathbf{h}_{prior})^T\mathbf{C}_H^{-1}(\mathbf{Hm}-\mathbf{h}_{prior})\right. \\ & \left. +(\mathbf{m}-\mathbf{m}_{prior})^T\mathbf{C}_M^{-1}(\mathbf{m}-\mathbf{m}_{prior})\right] \end{aligned} \tag{3.43}$$

Since the misfit function $S(\mathbf{m})$ is a quadratic function of $\mathbf{m}$, we know that the a posteriori density for the model parameters follows a Gaussian distribution with mean value $\widetilde{\mathbf{m}}$ and covariance matrix $\widetilde{\mathbf{C}}_M$ whose density can be written as:

$$\sigma_M(\mathbf{m}) \quad = \quad \text{const.} \quad e^{-\frac{1}{2}(\mathbf{m}-\widetilde{\mathbf{m}})^T\widetilde{\mathbf{C}}_M^{-1}(\mathbf{m}-\widetilde{\mathbf{m}})} \tag{3.44}$$

where,

$$\widetilde{\mathbf{C}}_M \quad = \quad \left(\mathbf{G}^T\mathbf{C}_\chi^{-1}\mathbf{G} + \mathbf{H}^T\mathbf{C}_H^{-1}\mathbf{H} + \mathbf{C}_M^{-1}\right)^{-1} \tag{3.45}$$

$$\widetilde{\mathbf{m}} \quad = \quad \widetilde{\mathbf{C}}_M \cdot \left(\mathbf{G}^T\mathbf{C}_\chi^{-1}\mathbf{d}_{obs} + \mathbf{H}^T\mathbf{C}_H^{-1}\mathbf{h}_{prior} + \mathbf{C}_M^{-1}\mathbf{m}_{prior}\right) \tag{3.46}$$

This result can be easily shown by replacing (3.45) and (3.46) into the exponent of (3.44) and show that $\frac{1}{2}(\mathbf{m}-\widetilde{\mathbf{m}})^T\widetilde{\mathbf{C}}_M^{-1}(\mathbf{m}-\widetilde{\mathbf{m}}) = S(\mathbf{m}) + \nu$, where ν is a constant (independent of $\mathbf{m}$).

For completeness purposes, we will show now the solution of the inverse problem for two particular cases in which the a posteriori density on $\mathbf{m}$ is a Gaussian distribution as shown in (3.44). One particular case is given in *Tarantola* (2005), where the quantity $\mathbf{h}$ is not considered in the derivation

of the problem. Here the a posteriori density of $\mathbf{m}$ is a Gaussian distribution given by (3.44), where

$$\widetilde{\mathbf{C}}_M = \left(\mathbf{G}^T\mathbf{C}_\chi^{-1}\mathbf{G} + \mathbf{C}_M^{-1}\right)^{-1} \tag{3.47}$$

$$\widetilde{\mathbf{m}} = \widetilde{\mathbf{C}}_M \cdot \left(\mathbf{G}^T\mathbf{C}_\chi^{-1}\mathbf{d}_{obs} + \mathbf{C}_M^{-1}\mathbf{m}_{prior}\right) \tag{3.48}$$

The other particular case is defined when there is no a priori knowledge on the model parameters. In this case the a priori information is described by the homogeneous density $\rho_M(\mathbf{m}) = \mu_M(\mathbf{m})$, which is constant if $\mathbf{m}$ is defined in a linear space. Here the a posteriori density of the model parameters is Gaussian as in equation (3.44), where

$$\widetilde{\mathbf{C}}_M = \left(\mathbf{G}^T\mathbf{C}_\chi^{-1}\mathbf{G} + \mathbf{H}^T\mathbf{C}_H^{-1}\mathbf{H}\right)^{-1} \tag{3.49}$$

$$\widetilde{\mathbf{m}} = \widetilde{\mathbf{C}}_M \cdot \left(\mathbf{G}^T\mathbf{C}_\chi^{-1}\mathbf{d}_{obs} + \mathbf{H}^T\mathbf{C}_H^{-1}\mathbf{h}_{prior}\right) \tag{3.50}$$

3.3.6 Bayesian equivalent formulation

Since the measures of length in both the model error $E(\mathbf{m})$ and the simplicity of the model $L(\mathbf{m})$ are quadratic forms of $\mathbf{m}$, the weighted damped least square problem (3.10) can be expressed in the more general Bayesian formulation (3.42) under Gaussian assumptions on both model parameters and observations if the weight matrices $\mathbf{W}_\chi$ and $\mathbf{W}_m$ are symmetric. In general, the observations uncertainties can be approximated to follow Gaussian statistics[†], then here we will treat the case in which $\mathbf{W}_\chi$ is positive definite (full rank) and corresponds to the inverse of the covariance matrix representing the observational uncertainties $\mathbf{C}_D$. For this case, the observations are represented by the density $\rho_D(\mathbf{d})$ (3.31), and the measure of length of the misfit error $E(\mathbf{m})$ is related with the

[†]Mainly because we assume that the observations are obtained as a sequence of several "random" processes, thus the Gaussian approximation for the observables probability density comes directly from the Central Limit Theorem of probabilities.

Likelihood function $\mathcal{L}(\mathbf{m}) = \rho_D(\mathbf{Gm})$ by

$$\mathcal{L}(\mathbf{m}) \quad = \quad \text{const.} \quad e^{-\frac{1}{2}E(\mathbf{m})} \tag{3.51}$$

Note here that finding $\mathbf{m}_{est}$ that minimizes $E(\mathbf{m})$ gives the maximum likelihood solution to the undamped problem $\mathbf{Gm} = \mathbf{d}_{obs}$.

Regarding the measure of simplicity of the model parameters, we distinguish two cases, whether the weight matrix $\mathbf{W}_m$ is semi-definite or definite positive in order to find a Bayesian equivalent of $L(\mathbf{m})$. The straightforward case is presented when $\mathbf{W}_m$ is positive definite as the measure of simplicity can be expressed as the a priori probability density on the model parameters (3.32),

$$\rho_M(\mathbf{m}) \quad = \quad \text{const.} \quad e^{-\frac{1}{2}(\mathbf{m}-\mathbf{m}_{prior})^T\mathbf{C}_M^{-1}(\mathbf{m}-\mathbf{m}_{prior})} \tag{3.52}$$

in which we choose, $\mathbf{m}_{prior} = \mathbf{m}^*$, and $\mathbf{C}_M = \dfrac{\mathbf{W}_m^{-1}}{\varepsilon^2}$.

For the case when $\mathbf{W}_m$ is semi-definite positive, for example, when the regularization operator corresponds to a higher order spatial differential of the slip distribution (e.g., gradient, Laplacian), an *a priori* covariance matrix for the model parameters would have infinite variance in the directions that define the null space of $\mathbf{W}_m$. In this case, we use the *a priori* information on the derived quantity $\mathbf{h}$ which PDF is expressed in equation (3.33). Here the derived quantity can represent steepness if the gradient of slip is used as the regularization operator, or roughness of the slip distribution is we use the Laplacian operator. Let's recall equation (3.33),

$$\rho_H(\mathbf{h}) = \text{const.} \quad e^{-\frac{1}{2}(\mathbf{h}-\mathbf{h}_{prior})^T\mathbf{C}_H^{-1}(\mathbf{h}-\mathbf{h}_{prior})} \tag{3.53}$$

In §3.2 we analyzed the commonly used uniform Laplacian regularization and we derived a sensitivity modulated Laplacian regularization that takes account for the spatial variations on the

strength of the constraint provided by the observations. In both cases we search to minimize the roughness of the solution $\nabla^2\mathbf{m}$. We can say then that $\mathbf{h}$ is the variable representing the roughness of the slip distribution and consequently that equation (3.53) represents the *a priori* distribution on roughness, defined on roughness space, regardless of any value of slip on the models. It is *a priori* information on roughness, as equation (3.31) represent the *a priori* information on the observation space regardless of any relationship between the observation and model spaces. The only requisite is that the *a priori* information on model parameters, derived quantity and observations are obtained independently.

Recapitulating, in §3.2 the discussed measures of simplicity assumed an *a priori* roughness $\mathbf{h}_{prior} = \mathbf{0}$ as we looked for smooth models, and they only differ in the weighting $\mathbf{W}_S$ of the Laplacian operator, recall $L(\mathbf{m}) = (\nabla^2\mathbf{m})^T\mathbf{W}_S^2(\nabla^2\mathbf{m})$. Now, since L is a quadratic form on the roughness of the model, and $\mathbf{W}_S$ is required to be positive definite, we can represent such measure of simplicity through an *a priori* Gaussian PDF for roughness with zero mean ($\mathbf{h}_{prior} = \mathbf{0}$) and covariance matrix $\mathbf{C}_H = \mathbf{W}_S^{-2}$. Here, the uniform regularization imposes an identity matrix for the covariance matrix of roughness $\left(\mathbf{C}_H = \dfrac{\mathbf{I}}{\varepsilon^2}\right)$, and for the sensitivity regularization the corresponding covariance matrix for the roughness is proportional to the sensitivity of the faults patches $\left(\mathbf{C}_H = \dfrac{\mathbf{S}}{\varepsilon^2}\right)$. Recall that ε is the damping parameter of the damped least squares method.

Chapter 4

Post-seismic Deformation of the Great 11 March 2011 Tohoku-Oki $\mathrm{M_w}9.0$ Earthquake and Mechanical Heterogeneity of the Megathrust

4.0 My contribution in this chapter

- In this chapter I analyze the post-seismic deformation associated to the Tohoku-Oki earthquake monitored with the GEONET Japan GPS network. In this analysis, based on my inferences of after-slip and also based on previous studies that analyze co- and inter-seismic stages of the seismic cycle, I suggest that the shallow-most region of the Japan Trench megathrust located south of the rupture region of the Tohoku-Oki earethquake may behave aseismically, as well as that the Japan Trench megathrust may present an heterogeneous distribution of material properties.

4.1 Abstract

The occurrence of the great 2011 Tohoku-Oki earthquake offshore northern Honshu, Japan immediately raised concerns about a potential future earthquake just to the south and closer to Tokyo. The

extent to which this region of the subduction megathrust fault is locked and accumulating elastic stress to be released in a future earthquake is not well constrained. Concerns have been heightened with the proximal 2011 earthquake potentially bringing this region closer to rupture. Alternatively, this portion of the fault may have an intrinsic tendency to creep aseismically thereby at least partially mitigating concerns for a large earthquake in this region. Geophysical observations, particularly those from geodetic networks, permit one to explore the spatial relationship between co-seismic fault slip, post-seismic fault slip and seismicity and to thereby constrain the style of slip on the megathrust fault. Using a novel inference scheme, we find that the distribution of post-seismic fault slip occurs mainly down-dip and south of the source region of the Tohoku-Oki mainshock with negligible slip in regions that slipped during the main rupture. At a spatial resolution near the trench of 100 km along strike and 60 km along dip, the shallowest portion of the megathrust offshore Ibaraki Prefecture experienced over 1 m of aseismic slip in the 18 months following the earthquake – actual slip amplitudes maybe larger if they occur over a smaller scale. The spatio-temporal complexity of inferred fault slip, suggests strong spatial heterogeneity of the mechanical properties on the megathrust. We suggest that the shallow-most region of the Japan Trench megathrust located just south of the rupture area of the 2011 (M_w9.0) Tohoku-Oki earthquake may behave aseismically, thus diminishing the potential (but not excluding the possibility) for a large future earthquake in the region.

4.2 Introduction

The 11 March 2011 (Mw 9.0) Tohoku-Oki, Japan earthquake occurred on the megathrust offshore northern Honshu at the Japan Trench where the Pacific Plate subducts at a rate of about 8.5 cm/yr (*Taira*, 2001; *DeMets et al.*, 2010). This portion of the subduction zone regularly experiences M 7-8 earthquakes, typically at depths of 40-60 km (*Igarashi et al.*, 2001). Large earthquakes have

also occurred at shallower depth, including the 1931, 1968 and 1994 Sanriku-Oki earthquakes (e.g., *Nakayama and Takeo*, 1997), and the 869 July 17 Jogan earthquake (which may have closely resembled the 2011 event (*Minoura et al.*, 2001)). Observations from seismic and geodetic networks before and after the Mw 9.0 event, allow one to study the overall mechanical behavior of the subduction megathrust and the dependencies between distributions of slip behavior throughout the seismic cycle. These data also allow us to examine the potential for a large earthquake just south of the region that slipped co-seismically during the 2011 event.

The primary region of fault slip in the 2011 Tohoku-Oki earthquake occurred over a surprisingly small area but with unexpectedly large amplitude. In places fault slip exceeded 60 m with an overall complex distribution of fault slip (*Simons et al.*, 2011). The southern extent of co-seismic slip offshore Ibaraki and Fukushima Prefectures partially overlapped regions previously inferred to be locked (*Hashimoto et al.*, 2009; *Loveless and Meade*, 2010, 2011; *Simons et al.*, 2011; *Kato and Igarashi*, 2012); while the northern limit of co-seismic rupture coincides with the transition to a region previously inferred to be relatively uncoupled and assumed to be creeping aseismically (*Hashimoto et al.*, 2009; *Loveless and Meade*, 2010, 2011). Analyses of other large megathrust earthquakes around the globe suggest that portions of the megathrust that experience aseismic slip (before or after a large event) are located proximal to regions experiencing significant co-seismic slip during large earthquakes (e.g., *Chlieh et al.*, 2008; *Konca et al.*, 2008; *Kaneko et al.*, 2010; *Perfettini et al.*, 2010). The majority of aftershocks near the megathrust with mechanisms similar to the mainshock also circumscribe regions inferred to have experienced large co-seismic fault slip during the 2011 mainshock (e.g., *Kato and Igarashi*, 2012). Aftershocks occurring off the fault are primarily normal and strike slip events (*Asano et al.*, 2011; *Kato and Igarashi*, 2012; *Ye et al.*, 2012; *Shinohara et al.*, 2012). The largest of the aftershocks (Mw 7.4 and Mw 7.9) occurred on or proximal to the megathrust offshore Iwate and Fukushima (*Asano et al.*, 2011; *Nakajima et al.*,

2011; *Nishimura et al.*, 2011; *Simons et al.*, 2011).

Before the 2011 Tohoku-Oki earthquake, many inter-seismic fault coupling models for the Japan Trench suggested that the portions of the fault inferred to be coupled were broadly limited to regions that had experienced earthquakes over the last few centuries - with either negligible or limited coupling in much of the region that slipped co-seismically in 2011 (*El-Fiky and Kato*, 1999; *Ito et al.*, 2000; *Nishimura et al.*, 2000, 2004; *Suwa et al.*, 2006; *Hashimoto et al.*, 2009; *Loveless and Meade*, 2010, 2011). The shortcomings of these coupling models motivates our need to improve our kinematic description of fault slip during different stages of the seismic cycle in order to both improve our understanding of the rheological nature of the megathrust as well as for seismic and tsunami hazard assessment. From a mechanical perspective, we need to explore the extent to which seismic and aseismic slip may overlap spatially and how to interpret such overlap (or lack thereof) in the context of mechanical fault models (e.g., *Lay and Kanamori*, 1980, 1981; *Scholz*, 2002). In the context of northeast Honshu, Japan, we are particularly concerned with the region offshore of Ibaraki prefecture, just south of the rupture area of the Tohoku-Oki earthquake, where the potential for a large earthquake is still unclear (*Simons et al.*, 2011). Like the region of the Tohoku-Oki rupture (at a similar distance from the trench), this region was believed to be relatively uncoupled with little potential for a large earthquake (e.g., *Loveless and Meade*, 2010, 2011). A great earthquake having now occurred just to the north, it is essential to assess how this portion of the megathrust is responding to the increase in stress induced by the 2011 event. Is this segment of the megathrust locked with the potential to generate another great earthquake or is it experiencing accelerated aseismic creep that may reduce (but not obviate) the concern of a future great earthquake even closer to regions of high population density?

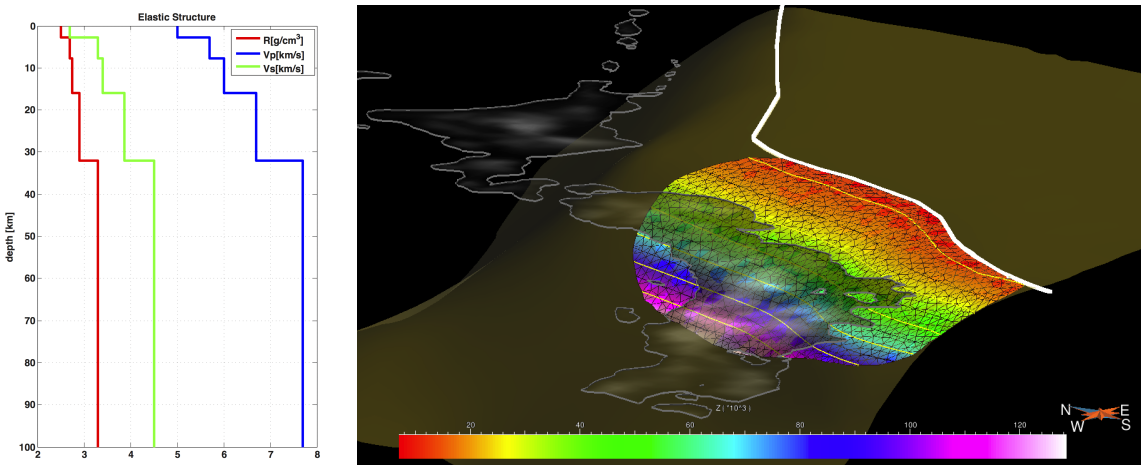

Figure 4.1. Assumed 1D elastic model and 3D view of the 3D fault surface. The elastic properties are computed by averaging the 3D tomography from NIED (Japan National Research Institute of Earth Science and Disaster Prevention) at the epicentral region of the Tohoku-Oki earthquake for the first 16 km depth. The elastic structure is taken from *Takahashi et al.* (2004) below 16 km depth.

4.3 Modeling

We developed a three-dimensional model of the Japan Trench portion of the megathrust constrained by regional seismicity and interpreted seismic profiles available in the published literature (*Simons et al.*, 2011; *Ye et al.*, 2012, and references therein). The media is represented by a 1D layered elastic structure with properties computed by sampling 3D tomography at the main shock epicentral area (Figure 4.1).

The Green's Functions relating an unit dislocation on a given fault patch with the prediction of displacements at the GPS sites (Figure 2.4) are computed by approximating a finite triangular elastic dislocation in the layered elastic half space. Each triangular dislocation is represented by summation of a set of point sources evenly distributed over the triangle's surface. We divide the triangle into sub-triangles and each point source is located at a sub-triangle centroid with a potency proportional to the area of the sub-triangle. We find that a sufficient number of point sources corresponds to when the longest side of the associated sub-triangle has a length that is less than the fourth of the distance between the triangle and its closest GPS site.

Inferring the distribution of offshore subsurface fault slip using geodetic observations onshore is recognized to be a highly ill-posed estimation problem usually requiring some form of regularization or prior information (§3). As such, particular care is needed to avoid inducing artifacts or biasing our interpretations from our choice of regularization. We employ a novel, simple, and robust approach to estimating distributions of subsurface fault slip for cases such as in Japan, where our observational sensitivity to the behavior of different portions of the fault is highly variable (§3). Essentially, our approach adopts a form of regularization that minimizes the roughness of the inferred model with a relative strength that varies spatially depending on the sensitivity of the observations to any given portion of the fault model. As is common in this type of inversion, we assume there is no normal (as opposed to thrust) component of slip. Also, as plate convergence direction is relatively perpendicular to the Japan trench, we expect that the stronger spatial variability will occur on the dip component of slip, reason for that we impose a relatively stronger damping constant on the along strike component of slip.

We can rewrite the optimization problem (3.10) as:

$$\begin{aligned} \min_{\mathbf{m}_\phi \in \Re,\, \mathbf{m}_\delta \geq 0} \quad & \left\| \mathbf{W}_\chi^{1/2} \left([\mathbf{G}_\delta | \mathbf{G}_\phi] \begin{bmatrix} \mathbf{m}_\delta \\ \mathbf{m}_\phi \end{bmatrix} - \mathbf{d} \right) \right\|_2^2 \\ & + \lambda^2 \left\| \mathbf{S}_\delta^{-\frac{1}{2}} \mathbf{T} \mathbf{m}_\delta \right\|_2^2 \\ & + \gamma^2 \left\| \mathbf{S}_\phi^{-\frac{1}{2}} \mathbf{T} \mathbf{m}_\phi \right\|_2^2 \end{aligned} \tag{4.1}$$

where $\mathbf{m}$ describes the distribution of slip, $\mathbf{G}$ the elastic Green's functions, $\mathbf{d}$ the observations, $\mathbf{W}_\chi^{1/2}$ is the Cholesky decomposition of the inverse of the covariance matrix $\mathbf{C}_\chi$ associated to the misfit and λ^2, γ^2 are the associated Lagrange multipliers (damping factors). For simplicity we write $\gamma^2 = \nu^2 \cdot \lambda^2$, in which ν^2 represents a relative weight between the strike- and dip- slip smoothing

constraints. By a process of trial and error, we determine the best value of $\nu^2 = 200$ for our fault slip inversion. We solve the optimization problem using constrained least squares algorithm "lsqlin" in MATLAB.

The use of a least squares method to solve the inverse problem assumes Gaussian statistics for both the errors on the observables $\mathbf{d}$ and a priori model prediction errors. The covariance matrix of the misfit can be written as $\mathbf{C}_\chi = \mathbf{C}_d + \mathbf{C}_p$, where $\mathbf{C}_d$ is a diagonal matrix with the data variances and $\mathbf{C}_p$ is a diagonal matrix representing the fact that our physical model is an approximation of the physical process that drive the observations (e.g., assumed elastic model for the earth). We assume uncorrelated errors for both $\mathbf{C}_d$ and $\mathbf{C}_p$. We set the uncorrelated $\mathbf{C}_p$ errors to $2[mm]$ and $5[mm]$ for horizontal and vertical components of the GPS post-seismic displacements, respectively. The obtained slip distribution is not sensitive to the chosen values of $\mathbf{C}_p$ within a 20% variation. We chose a spatially uniform distribution of $\mathbf{C}_p$ because we lack the knowledge of its error structure. For example, *Minson et al.* (2013) proposes that for the co-seismic slip inversion $\mathbf{C}_p$ variances scale with the square of the observations, assuming that $\mathbf{C}_p$ is mainly due to errors in the assumed elastic structure of the media. For the co-seismic problem an elastic media seems to be a good approximation given the time scale ($\sim$ 1 [min]) of the co-seismic process. Nevertheless, for the post-seismic slip inversion, with a time scale from several months to years, the rheology becomes an important factor. If we compare a viscoelastic model with an elastic one, the displacements predicted at the GPS sites by a given slip distribution will vary in both amplitude an location. Thus, the structure of $\mathbf{C}_p$ will be much more complex than the one assumed by *Minson et al.* (2013) and since we are unable at the moment to compute such a complex structure, we use the simplest possible one, an uncorrelated, spatially uniform one.

4.4 Observations of post-seismic deformation

To constrain the fault slip models we use observations from more than 480 continuously recording Global Positioning System (GPS) sites installed and operated by the Geodetic Survey of Japan (*Miyazaki et al.*, 1997). The GPS positions are estimated once a day to produce individual three-component positional time series, from which we isolated an 18-month-long post-seismic time series with seasonal effects, secular motion and offsets due to aftershocks removed (§2.3). We analyze post-seismic displacements up to September 22, 2012.

Post-seismic displacements (Figure 2.4) affect most of northern Honshu and follow a similar pattern as those estimated earlier (*Ozawa et al.*, 2011, 2012). Total estimated horizontal post-seismic displacements are up to 25% of the co-seismic offsets at the region of maximum co-seismic displacement and up to 90% in adjacent regions (Figure 2.4). Surface velocities have not yet returned to pre-earthquake rates (Figure 4.2). The observed change in the pattern of horizontal component of surface deformation between co-seismic and post-seismic periods indicates that co- and post-seismic slip occurs on different regions of the megathrust (Figure 2.4). Similarly, the vertical component of post-seismic deformation shows uplift in the forearc and subsidence in the backarc (Figure 2.4). Such a pattern of vertical deformation implies that post-seismic after-slip on the megathrust is occurring at depths greater than the co-seismic fault slip. An exception to this trend occurs in the region north of Kamaishi, where onland subsidence is occurring near the coast suggesting that after-slip at this latitude is primarily occurring offshore. While we cannot exclude the possibility that the observed complexity of vertical post-seismic displacements reflects at least some contribution from faults other than the megathrust, we interpret these observed surface displacements purely in terms of fault slip on the megathrust.

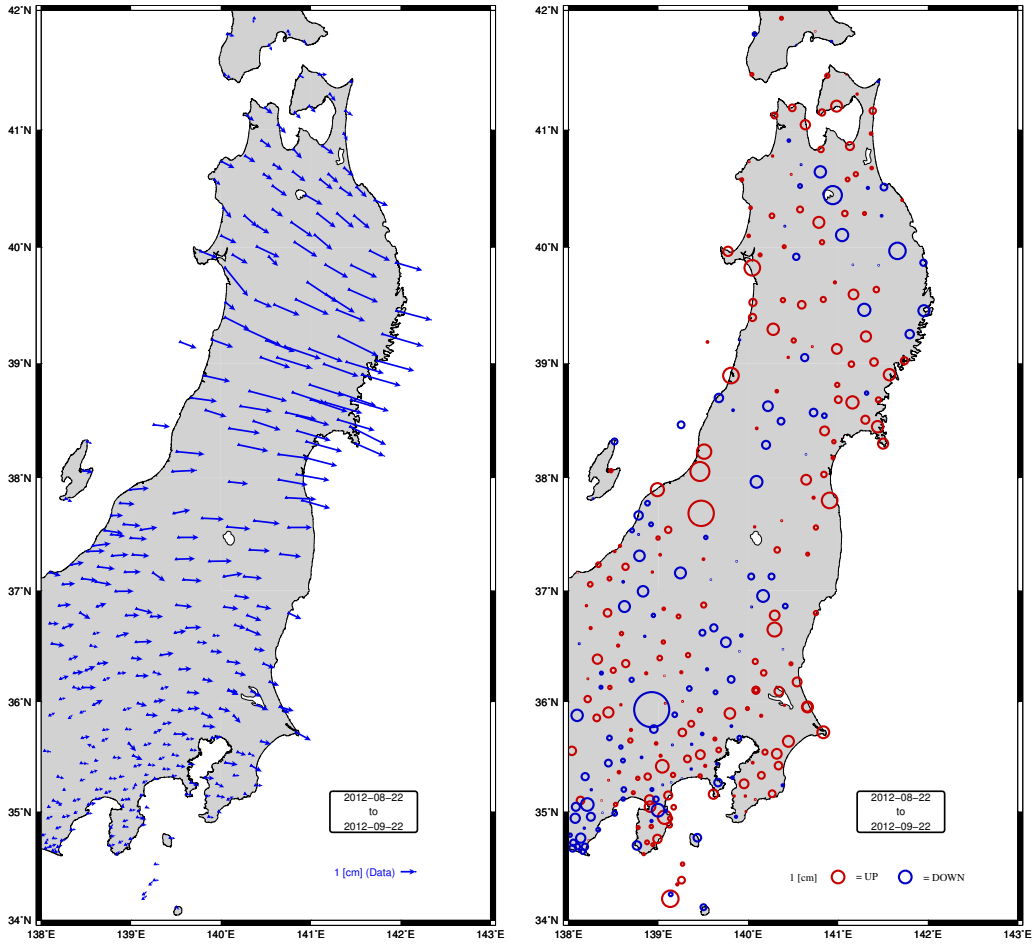

Figure 4.2. Estimates of post-seismic displacement between August 22, 2012 and September 22, 2012. We observe that, during the last month of the analyzed time series, onland deformation still presents a pattern resembling post-seismic deformation, suggesting that it is still ongoing. Since we have removed pre-Tohoku-Oki earthquake secular rates, if post-seismic deformation is not further occurring we expect that this figure will be dominated by scatter unless secular rates have changed after the Tohoku-Oki earthquake

4.5 Results and discussion

We use the geodetic data shown in Figure 2.4 to invert for post-seismic slip models associated to the Tohoku-Oki (Mw 9.0) earthquake. We search for a family of after-slip models due to the non-uniqueness of the inverse problem solution. In Figure 4.3 we show 7 models of after-slip, each one for a different value of the damping parameter, from a highly rough (a) to the most damped (g). Box (h) shows the trade-off curve between data residual ($\|\mathbf{W}_\chi^{1/2}(\mathbf{Gm}-\mathbf{d})\|_2$) and slip roughness

($\|\mathbf{S}^{-1/2}\mathbf{Tm}\|_2$) for a set of selected damping parameters. The apparent range of the trade-off curve may be misleading since it shows a significant change of model roughness, but the change in data misfit is quite marginal. Thus, the traditional method of selecting the damping parameter located at the point of larger curvature of the tradeoff "L-curve" is of little use. Also, the implementation of the positivity constraint on the dip component of slip comes at a high computational cost (several minutes to hours in a 12 core CPU depending on the value of λ). Thus, calculating λ using the classical "leave one out" cross validation technique becomes untractable. The use of the faster Generalized Cross Validation technique (*Aster et al.*, 2012) is not possible due to the use of the positivity constraint. The models shown in Figure 4.3 are good candidates to be solution of the inverse problem and their main features of after-slip are similar among all the shown models, varying mostly in their degree of smoothing. We select (d) as a representative model of the solution space of the inverse problem using a criteria of compatibility with independent geophysical observations (e.g.: location of repeater aftershocks, source regions of large aftershocks and location of HF radiators during mainshock) and also asking for a certain degree of smoothing in the solution. In Figure 4.4 we show model (d) in detail. Figure 4.6 shows the comparison between predicted and observed GPS displacements for the selected model.

An outstanding characteristic differentiating our after-slip models from previously published ones (*Ozawa et al.*, 2011, 2012; *Munekane*, 2012) is the spatial variability and compactness of the inferred post-seismic slip. Robust estimates of 18 months of post-seismic after-slip are found down-dip and south of the region that experienced the largest co-seismic fault slip during the 2011 main shock. With the available data and within the imposed averaging scale of > 100 km (Figure A.1a), we are not able to constrain the extent of any shallow after-slip north of the 2011 event. We estimate that post-seismic slip during the 18 months following the $M_w 9.0$ mainshock has an equivalent moment magnitude of $M_w 8.7$. About 77% of the moment released post-seismically occurs down-

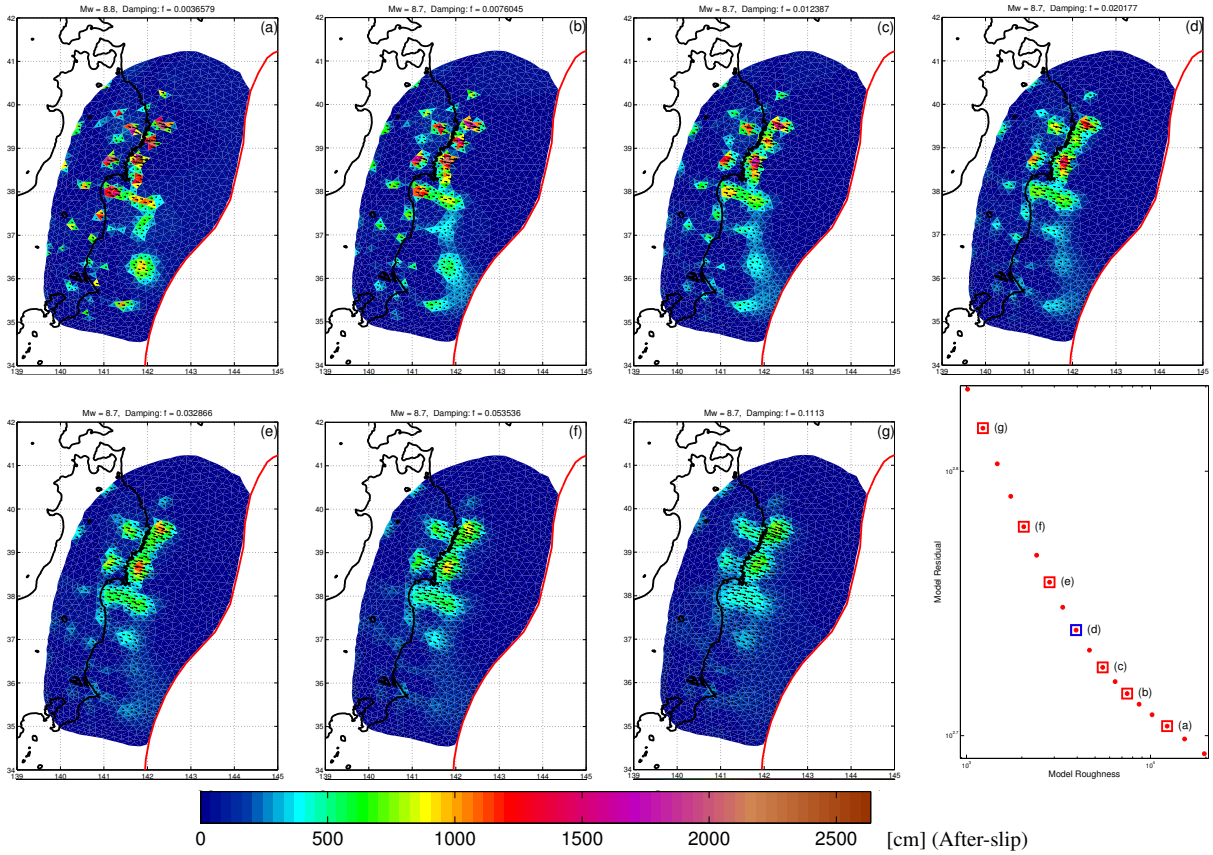

Figure 4.3. Family of after-slip models inferred from onland post-seismic displacements between March 11, 2011 and September 20, 2012. We show 7 models of after-slip in (a) through (g) sorted in order of increasing roughness. In (h) we shows the curve comparing the model misfit and roughness. Red squares indicate the selected model of after-slip and the blue square indicates the model discussed in this study. Note how all the selected models share similarities in the sense that all of them predict high after-slip down-dip of the source region of the Tohoku-Oki mainshock and the offshore Ibaraki $M_w 7.9$ aftershock and after-slip located far off-shore, south of the region of the Tohoku-Oki mainshock.

dip of the 2011 mainshock rupture (Figure 4.5) , where we also infer the largest estimates of after-slip ($\sim$13m).

The inferred region of after-slip complements areas inferred to have ruptured during the Tohoku-Oki mainshock and during the largest aftershocks (orange contours, and ellipse in Figure 4.4) (*Simons et al.*, 2011; *Ozawa et al.*, 2011, 2012; *Lay et al.*, 2011; *Pollitz et al.*, 2011; *Yue and Lay*, 2011; *Kato and Igarashi*, 2012; *Evans and Meade*, 2012). Previous studies also suggest that after great ($M_w \sim 8-9$) earthquakes, post-seismic slip may occur at the surrounding areas of the mainshock

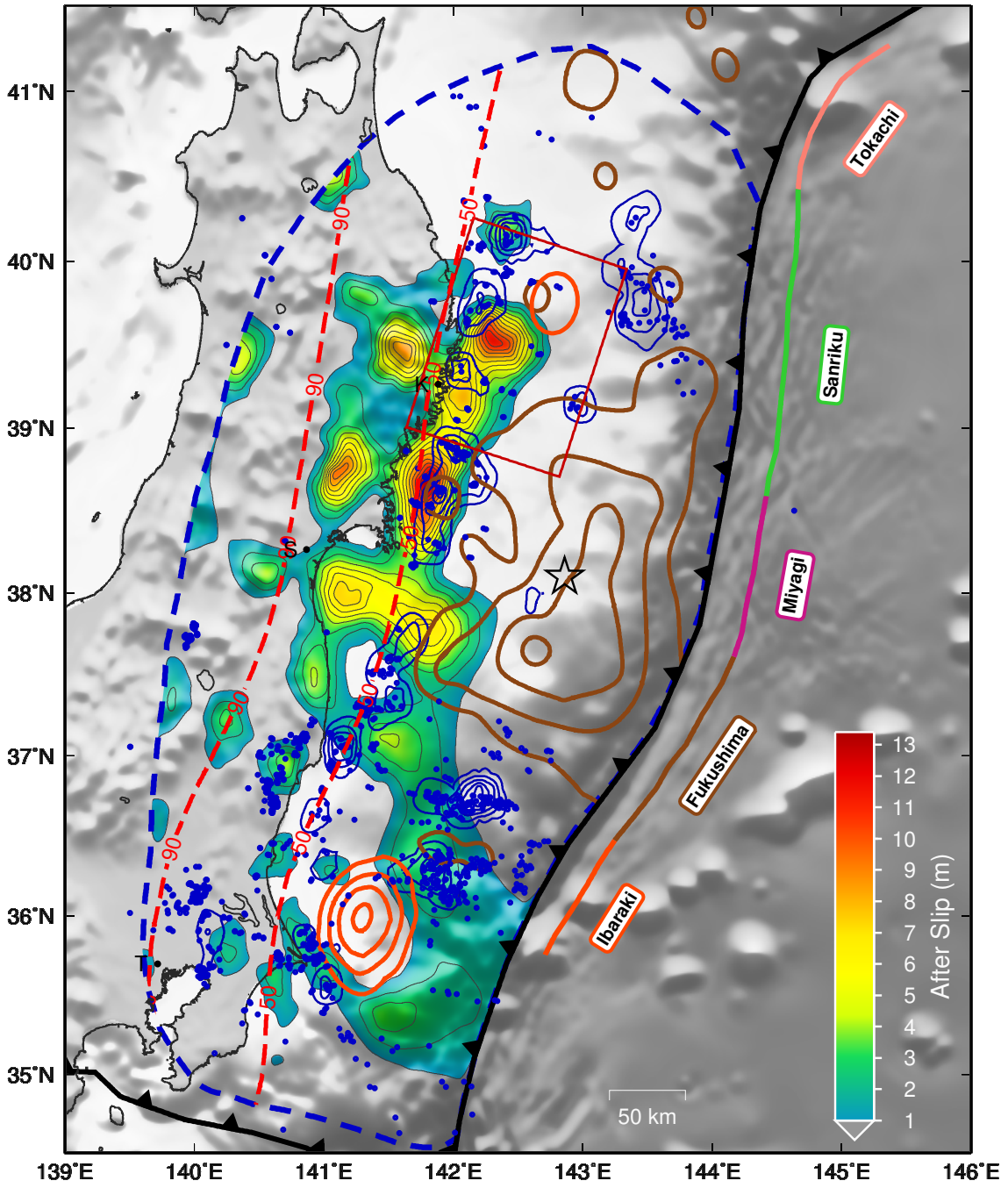

Figure 4.4. Map of Tohoku region of Japan showing the representative after-slip from this study (model (d) in Figure 4.3). 15 m slip contours of the Tohoku-Oki mainshock (*Minson et al.*, 2013) are shown in brown lines and JMA epicenter indicated with black star. Orange 1 meter slip contours and ellipse denote the rupture zones of the M_w7.9 Ibaraki-ken Oki and M_w7.4 Iwate-ken Oki aftershocks, respectively. Rectangular red box indicates the Sanriku-Oki low seismicity region SLSR (*Ye et al.*, 2012). The dashed red lines represent the 50 and 90 km depth contours of the interface between the Pacific-Okhotsk plates. Blue contours and dots indicate the aftershock density and location of repeater aftershocks (*Kato and Igarashi*, 2012).

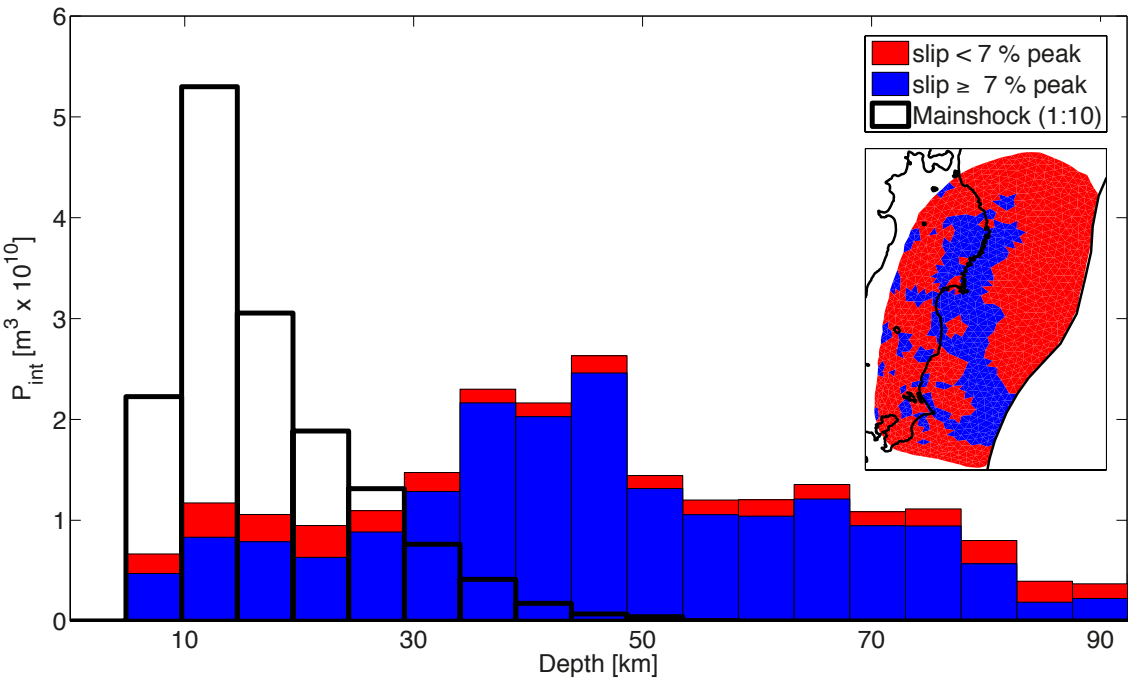

Figure 4.5. Potency as a function of depth for the representative after-slip model (Figure 4.4). Red and blue colors indicate regions of the megathrust inferred to have after-slip below and above 1 meter (7% of maximum inferred value of after-slip). The inset shows a map with the 2 regions of after-slip indicated by the proposed threshold. In terms of potency, $\sim$ 17% of the total potency is associated to the regions of the fault with less than 1 meter of after-slip (red). Nevertheless, the fraction of the total fault surface area contributing to it is $\sim$ 70%. Black transparent bars represent the co-seismic potency associated to the Tohoku-Oki mainshock. The co-seismic potency is scaled by a factor of $\frac{1}{10}$.

rupture zone (e.g., *Pritchard et al.*, 2002; *Yagi et al.*, 2004; *Ozawa et al.*, 2004; *Baba et al.*, 2006; *Hsu et al.*, 2006; *Perfettini et al.*, 2010; *Vigny et al.*, 2011; *Lin et al.*, 2013).

In order to obtain estimates of the spatio-temporal evolution of after-slip, we divide the GPS positional time series into 6 time subintervals with variable timespan, and solve for after-slip using the sensitivity regularized least square inversion (4.1) independently on each time window. Thus, without any consideration on the temporal correlation of the GPS time series and hence on the inferred after slip. Since the signal decay of the post-seismic GPS positional time series can be represented by a logarithmic function, we choose an equal spacing of the time intervals in a logarithmic space in order to ensure that the signal to noise ratio of the estimated post-seismic displacements remains

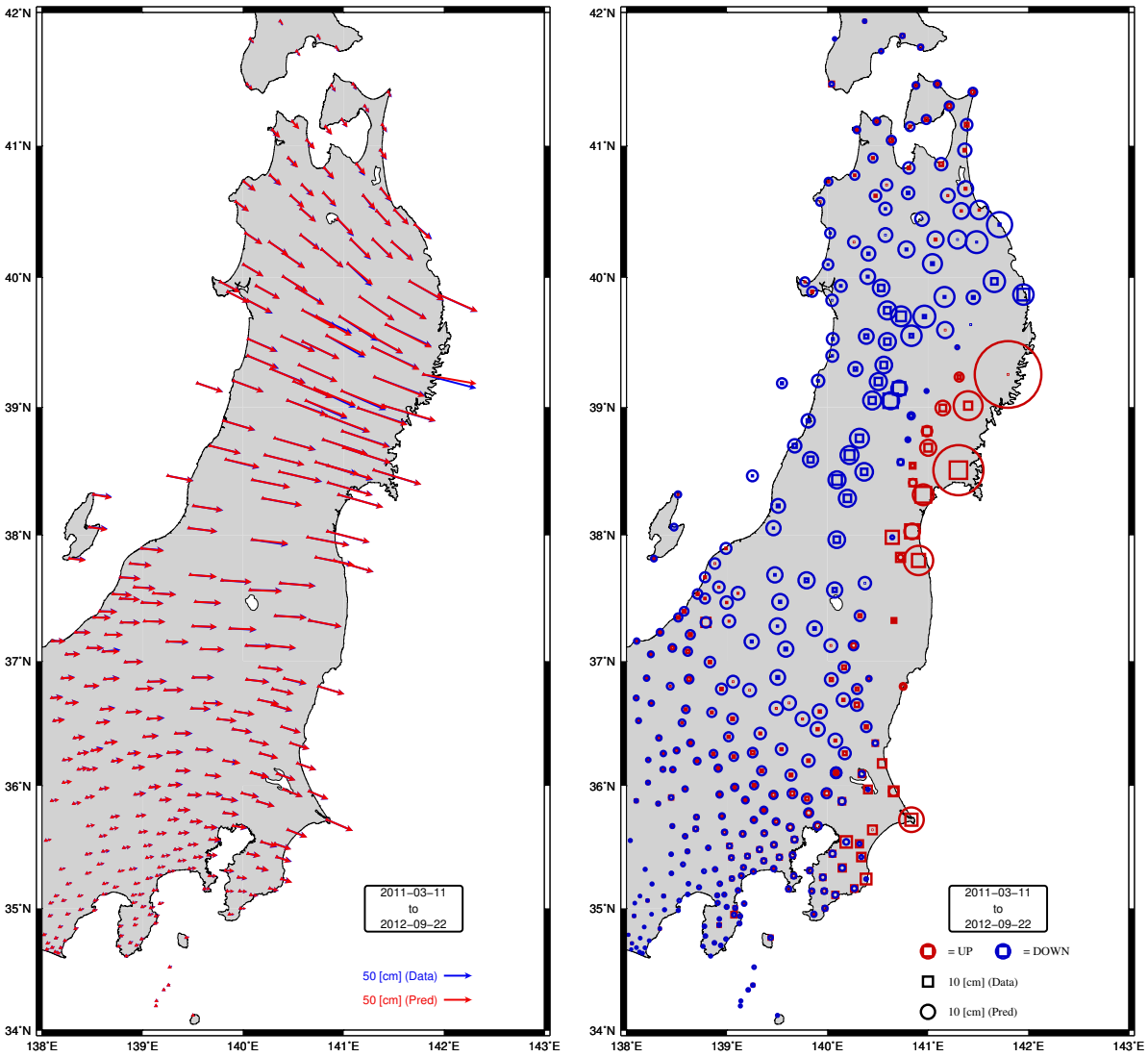

(a) Horizontal **(b) Vertical**

Figure 4.6. Observed and predicted post-seismic GPS displacements between 2011-03-11 and 2012-09-22.

similar in all time windows. The signal to noise ratio of the calculated GPS displacements on each time window is smaller than the one of the displacements calculated over the whole time interval (from mainshock time to September 22, 2012). Thus, the cumulative after-slip obtained by adding the after-slip estimated at all 6 time intervals is slightly different from the one estimated using the total accumulated post-seismic displacements. This difference is more notorious at the less sensitive regions of the megathrust where the partial after-slip estimations are smoothed in a greater degree due to lower signal to noise ratio. However, the differences are mostly in the degree of smoothness of the estimated models, in which the cumulative after-slip tend to be smoother. Figures 4.8 - 4.13 compare observed and predicted GPS displacements corresponding to each time window.

The spatio-temporal evolution of after-slip (Figure 4.7) down-dip of the Tohoku-Oki rupture area show features that decay in time, with a slight spatial migration. A different behavior is observed offshore Ibaraki, where early after-slip occurs down-dip, to the northern and southern extents of the $M_w 7.9$ aftershock and starts to migrate towards the trench surrounding the rupture zone of the aftershock. As up-dip migration continues, it develops a larger transient after-slip event that appears to reach the trench. This transient after-slip up-dip of the source of the $M_w 7.9$ aftershock is equivalent to an $M_w 8.2$ earthquake and is presumably triggered by the stress increase generated by the abrupt termination of the Tohoku-Oki mainshock north and down-dip of this region, as suggested by previous studies in other seismogenic regions (*Perfettini and Avouac*, 2004; *Perfettini et al.*, 2010; *Hsu et al.*, 2006). Given the large spatial correlation induced by smoothing inherent in the estimation process, the transient event may in fact be more spatially compact than what is shown but with correspondingly larger amplitude (§A). Thus, we cannot say with any certainty the extent to which after-slip reaches the trench.

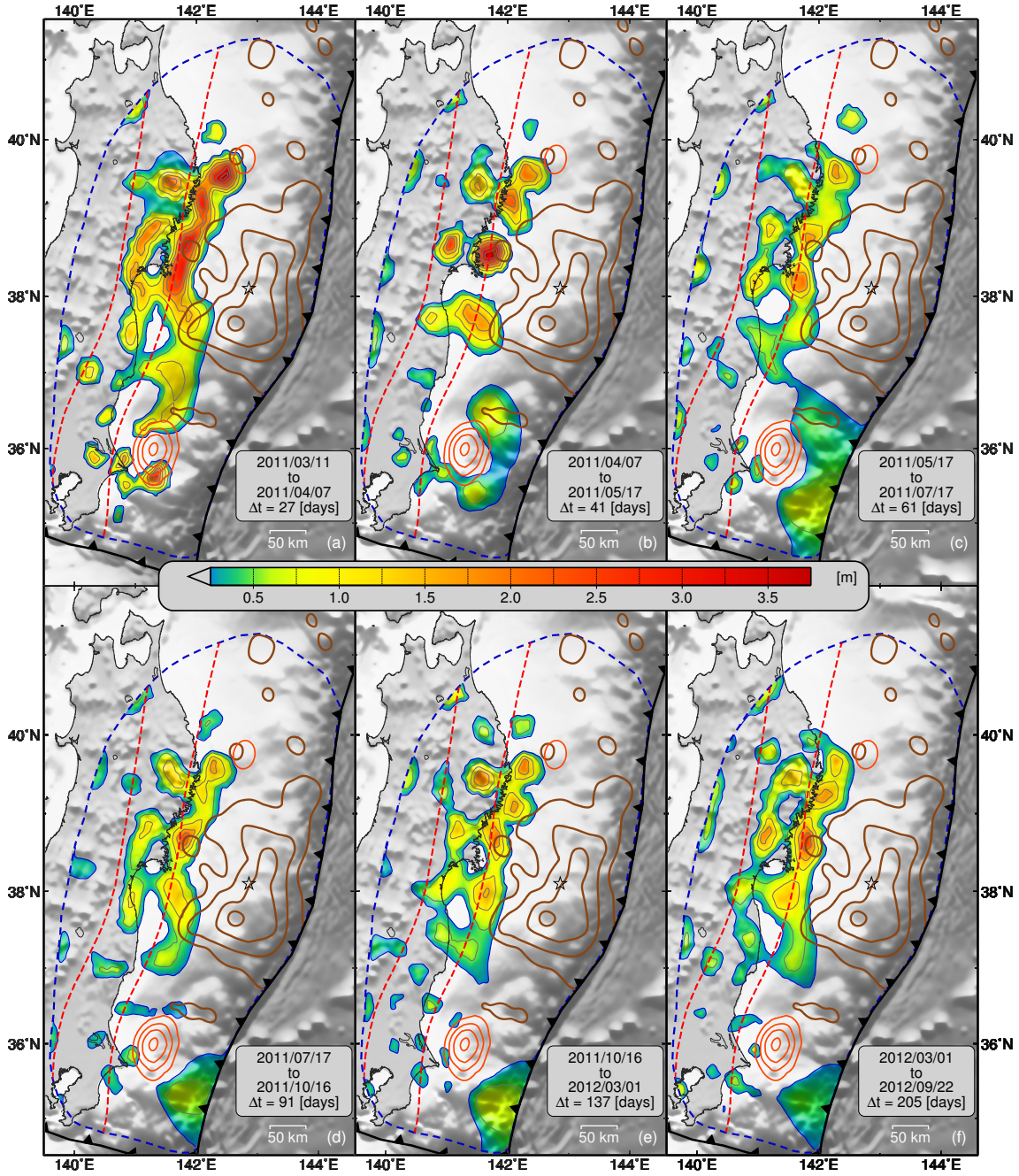

Figure 4.7. Spatio-temporal evolution of after-slip during the 18 months following the Tohoku-Oki mainshock estimated for non-overlapping contiguous time windows with sizes that preserve the signal to noise ratio of the GPS inferred post-seismic displacements. Note the transient event offshore Ibaraki that seems to reach the trench at the time window shown in panel (c). All shown solutions have an equivalent moment magnitude of $M_w 8.2$ and were obtained using the same damping constant. Other features as in Figure 4.4

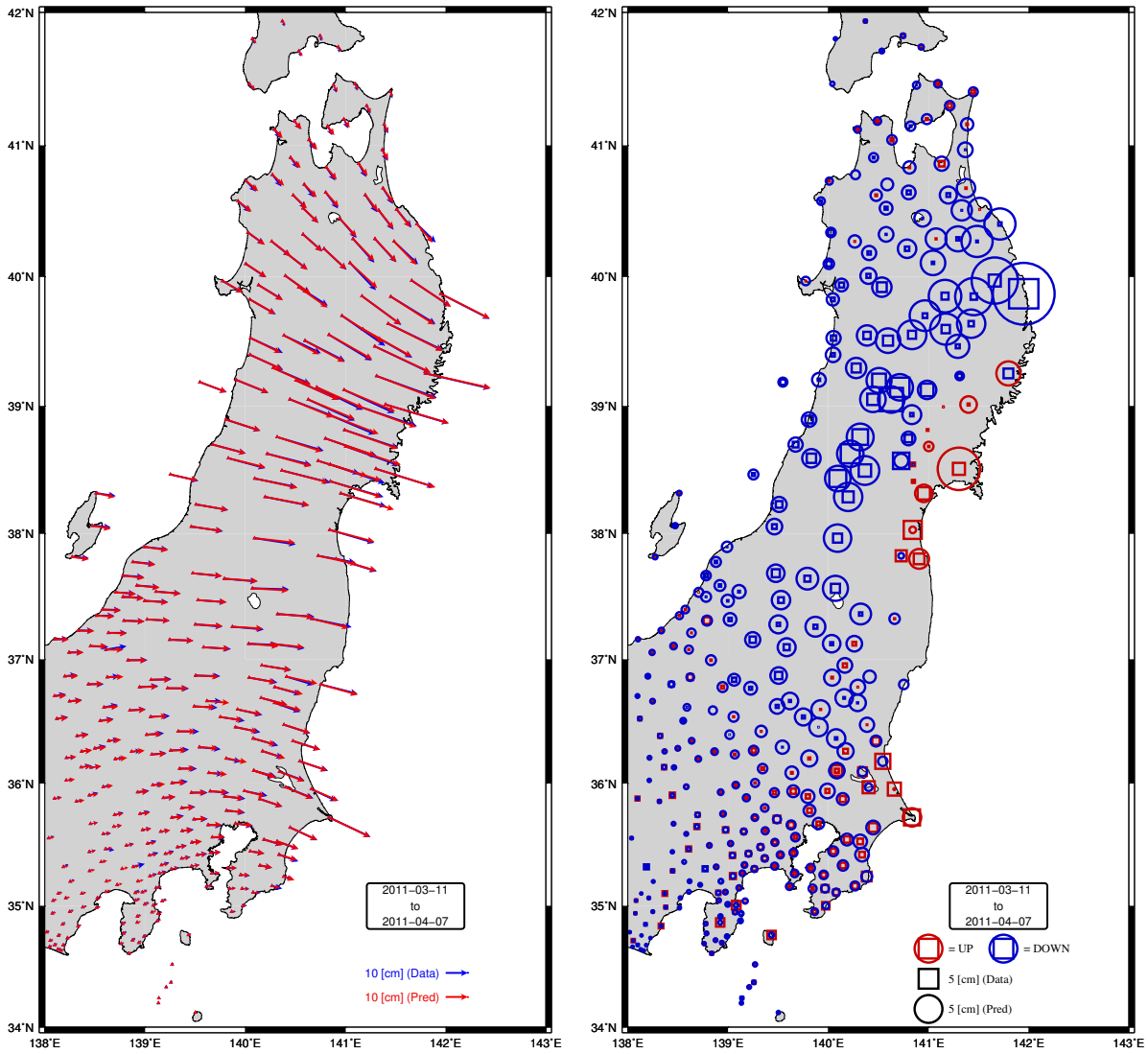

(a) Horizontal **(b) Vertical**

Figure 4.8. Observed and predicted post-seismic GPS displacements between 2011-03-11 and 2011-04-07.

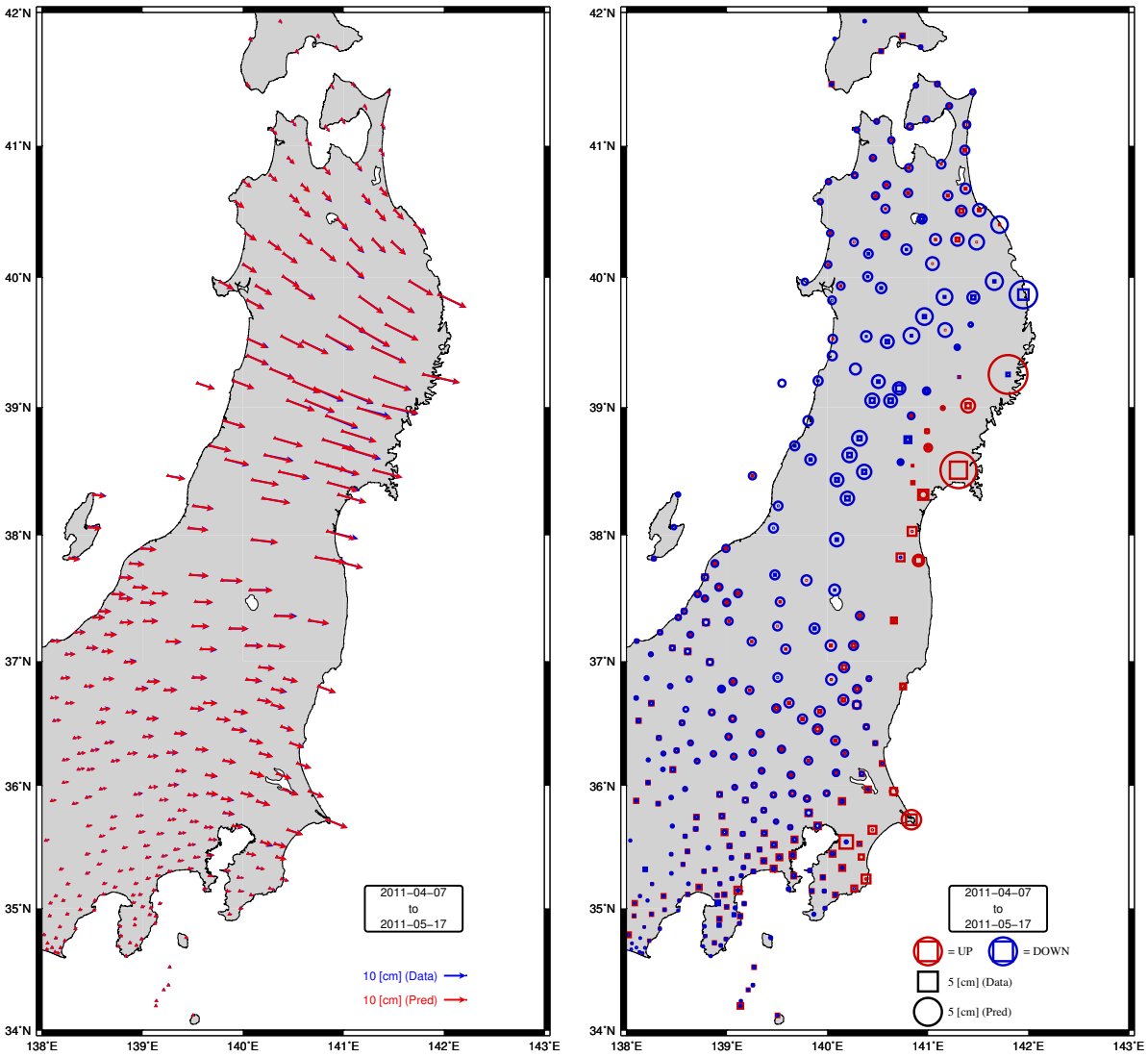

(a) Horizontal **(b) Vertical**

Figure 4.9. Observed and predicted post-seismic GPS displacements between 2011-04-07 and 2011-05-17.

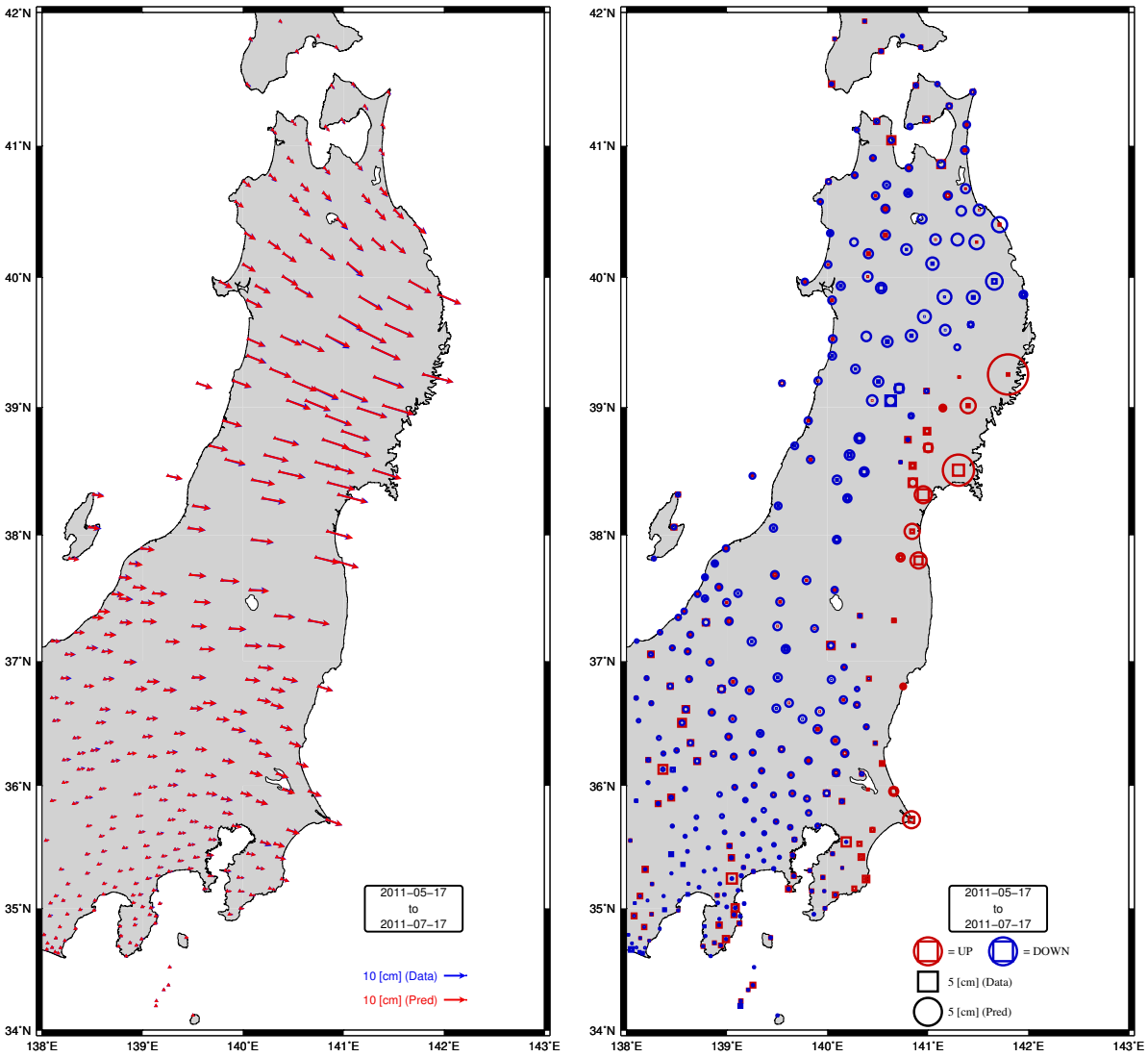

(a) Horizontal **(b) Vertical**

Figure 4.10. Observed and predicted post-seismic GPS displacements between 2011-05-17 and 2011-07-17.

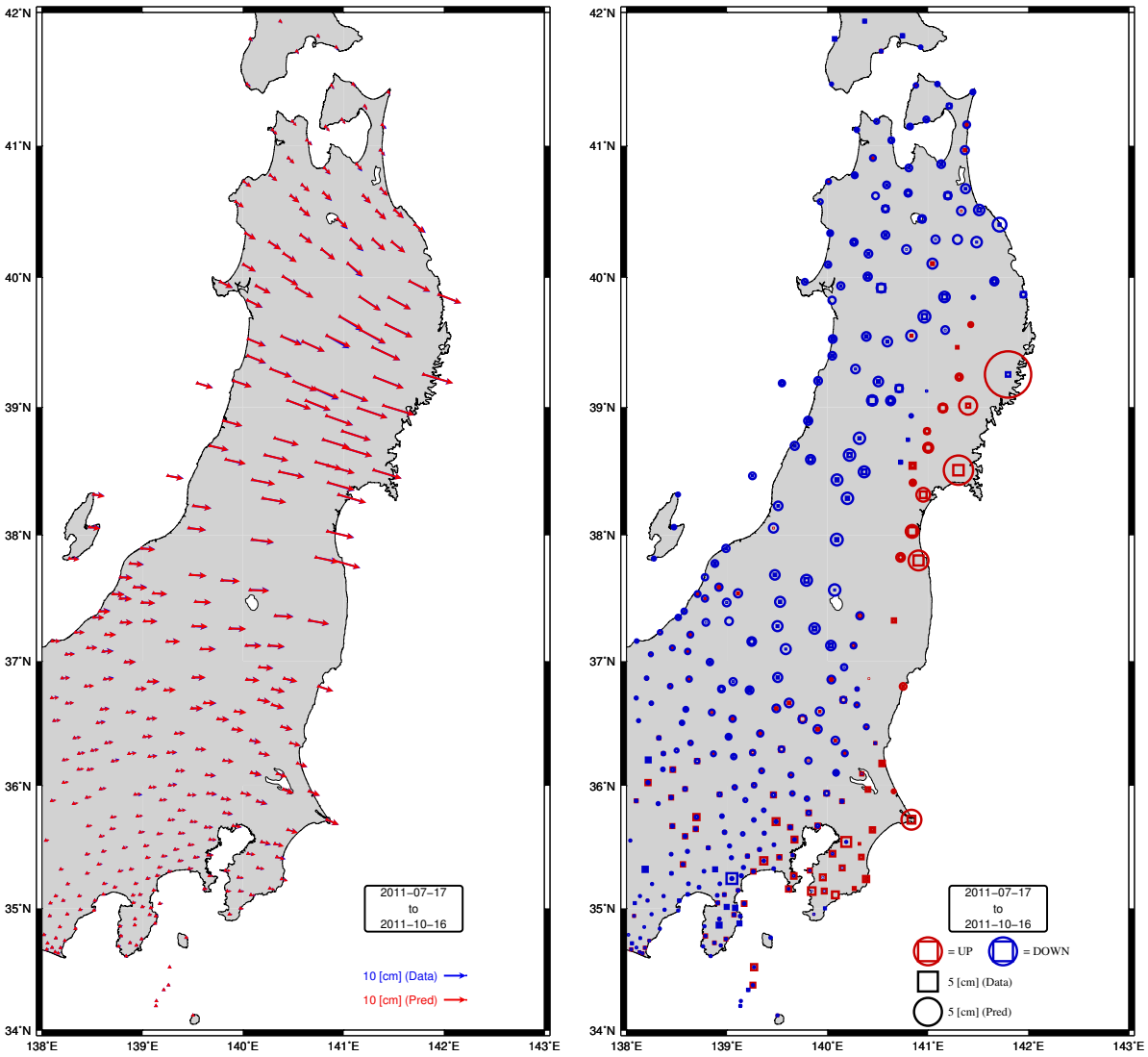

(a) Horizontal **(b) Vertical**

Figure 4.11. Observed and predicted post-seismic GPS displacements between 2011-07-17 and 2011-10-16.

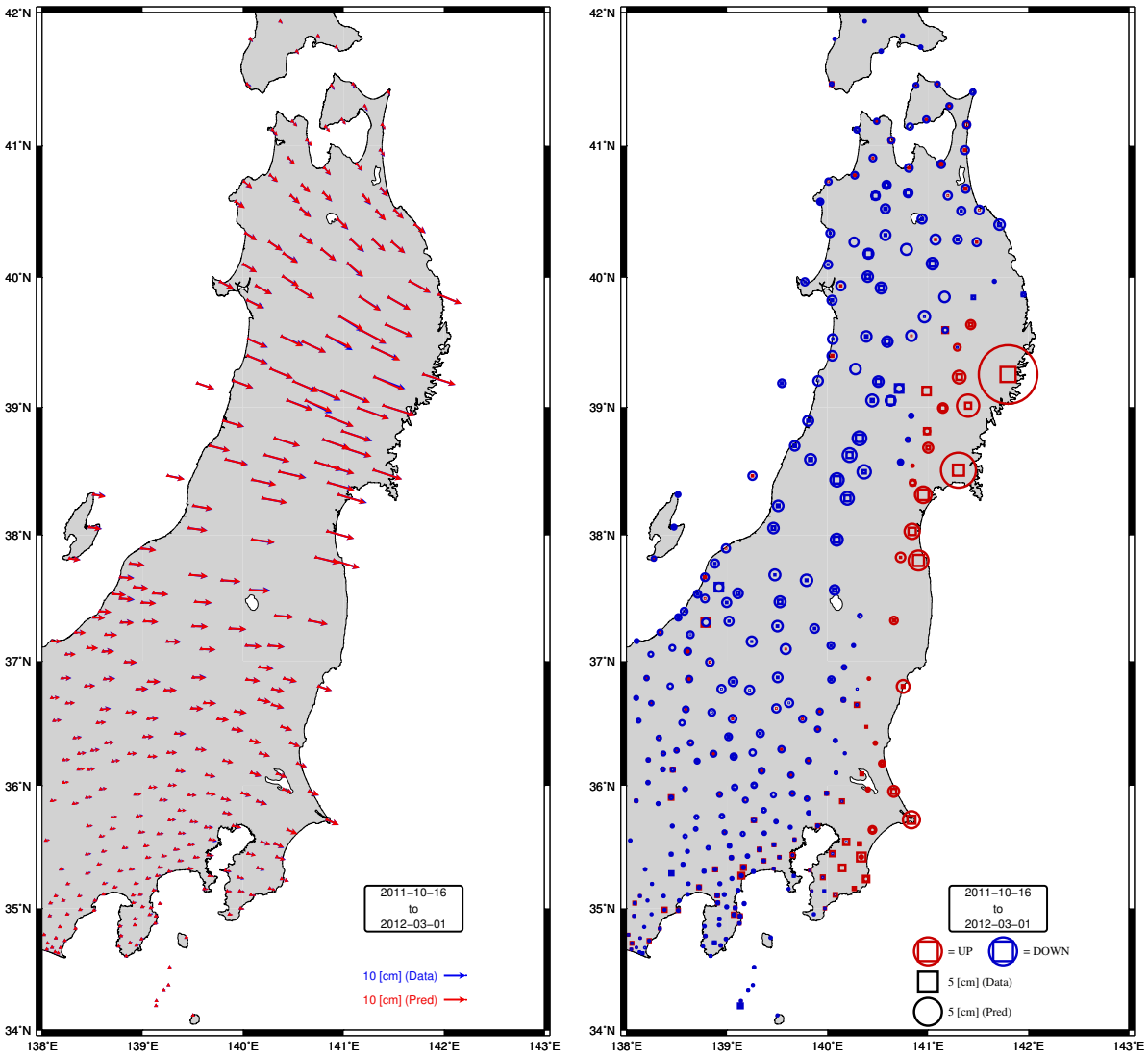

(a) Horizontal **(b) Vertical**

Figure 4.12. Observed and predicted post-seismic GPS displacements between 2011-10-16 and 2012-03-01.

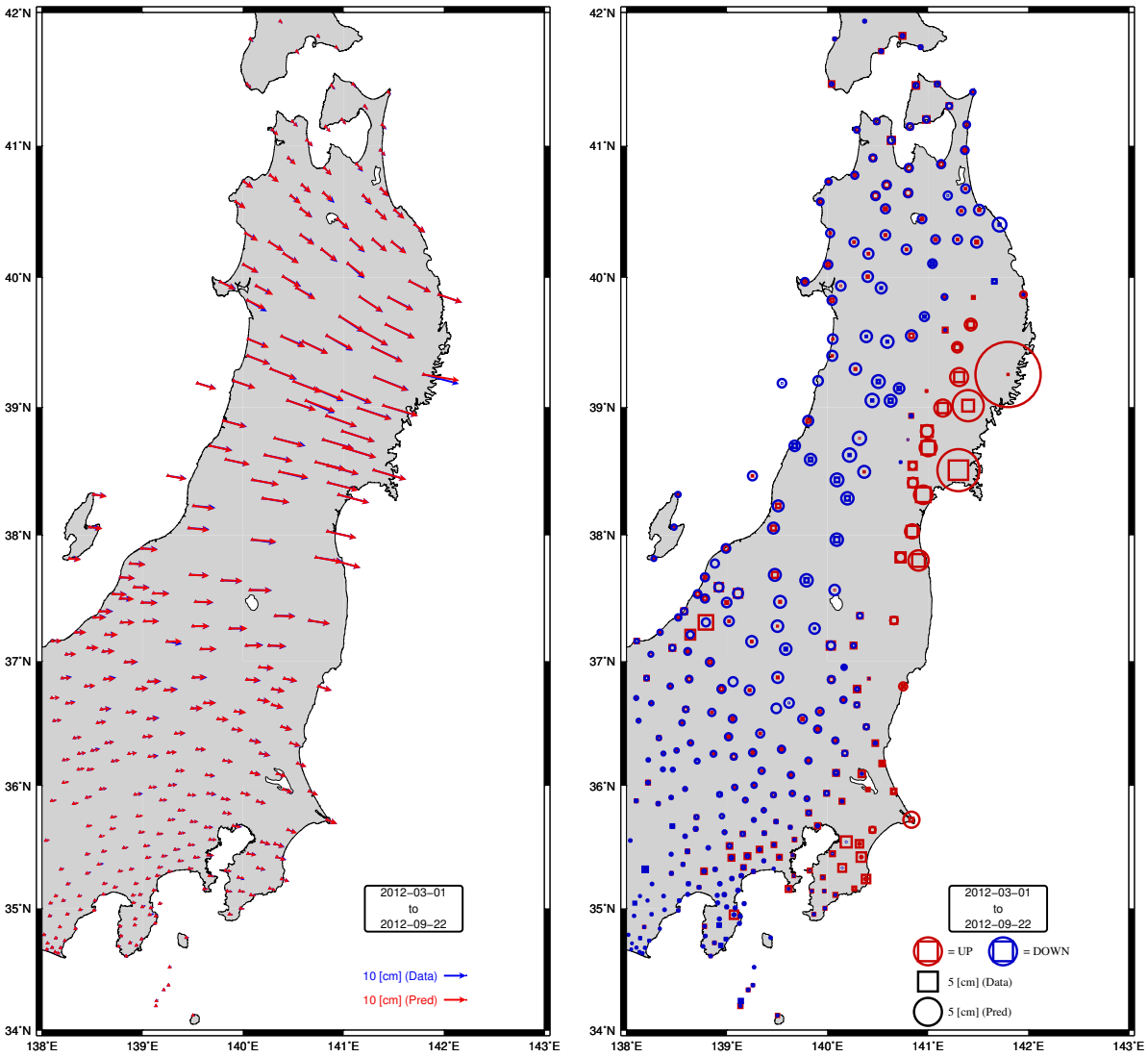

(a) Horizontal **(b) Vertical**

Figure 4.13. Observed and predicted post-seismic GPS displacements between 2012-03-01 and 2012-09-22.

In the absence of more precise geodetic constraints on the deformation in this area, we can consider the presence of repeating earthquakes as a potential proxy for fault creep as these events are considered to be recurrent ruptures on seismic patches of a fault to accommodate quasi-static slip in neighboring aseismically creeping areas (*Nadeau and Johnson*, 1998; *Igarashi et al.*, 2003; *Perfettini and Avouac*, 2004). A large number of repeater events occur in the shallow portion of the megathrust offshore Fukushima and Ibaraki prefectures (Figure 4.4; *Kato and Igarashi*, 2012), and are consistent with ongoing fault creep, suggesting that after-slip may have indeed reached trench depth.

Between 85% and 95% of the inferred post-seismic potency does not occur on portions of the fault inferred to have slipped during the Tohoku-Oki mainshock (Figure 4.4), where the range of values reflects different approaches to estimating overlap between co- and post-seismic fault slip. It is common to interpret the behavior of fault slip along a subduction megathrust in the context of an asperity model controlled by "rate and state" friction, where the megathrust is viewed as a set of stick-slip velocity weakening asperities surrounded by creep occurring on velocity strengthening media (e.g., *Lay and Kanamori*, 1981; *Perfettini and Avouac*, 2004). According to such a model, regions of the megathrust that are known to have experienced earthquakes are unlikely to undergo post-seismic slip due to the increased stress caused by the rupture process of a neighboring earthquake (*Rice and Gu*, 1983; *Segall*, 2010). The small apparent overlap inferred between co- and post-seismic slip, supports the asperity model characterization of the subduction megathrust.

Earlier analysis inferred overlap of fault slip during and after the Tohoku-Oki earthquake and thus called into question the basic idea behind "rate and state" formulism (*Johnson et al.*, 2012). Thus, it is critical to assess the extent and reliability of any such overlap. We find only negligible overlap and it may simply be an artifact of the smoothing in both the co- and post-seismic models. Furthermore, previously inferred asperities associated with past earthquakes and those inferred by

inter-seismic coupling models may well lie in places where no after-slip is occurring. A limited amount of overlap of co- and inter-seismic slip can also be explained by the presence of asperities located within a ductile region of the megathrust. Such asperities will shield the surrounding region during the inter-seismic period causing a stress and slip shadow, thus allowing the build up of slip budget to be posteriorly released as post-seismic slip (*Hetland and Simons*, 2010). Finally, we recognize the possibility that slip on faults (e.g., splay faults) not included in the existing fault models may result in estimating limited amount of spurious slip.

Observations of seismic energy radiated during the rupture process of an earthquake are used to study the source characteristics. Particularly, regions of the megathrust that present heterogeneous frictional properties radiate seismic waves at high frequencies when excited by the rupture process of a large earthquake. Back-projection analysis using array processing techniques on teleseismic waveforms measured at the EU and US seismic arrays were used to obtain the sources of high frequency radiation during the rupture process of the Tohoku-Oki mainshock (Figure 4.14; *Simons et al.*, 2011; *Meng et al.*, 2012). Later in the rupture process, most of the high frequency radiators tend to occur in regions that are inferred to experience co- and post-seismic slip, reinforcing the interpretation that these occur at transition zones between brittle and ductile regions, where the rupture front excites compact brittle asperities embedded in a ductile fault matrix (*Simons et al.*, 2011). Also the high frequency radiators occur in between the regions of larger inferred after-slip with the exception of the region offshore Miyagi, where there is an apparent concurrency of the high frequency radiators, co- and post- seismic slip.

Overall we observe heterogeneous distributions of slip behavior during the different stages of the seismic cycle at the Japan Trench megathrust. The general sparsity of thrust aftershocks and heterogeneous distributions of slip behavior leads to conclude that a strong heterogeneity of material physical properties may be the most likely cause of the general behavior of the Japan Trench

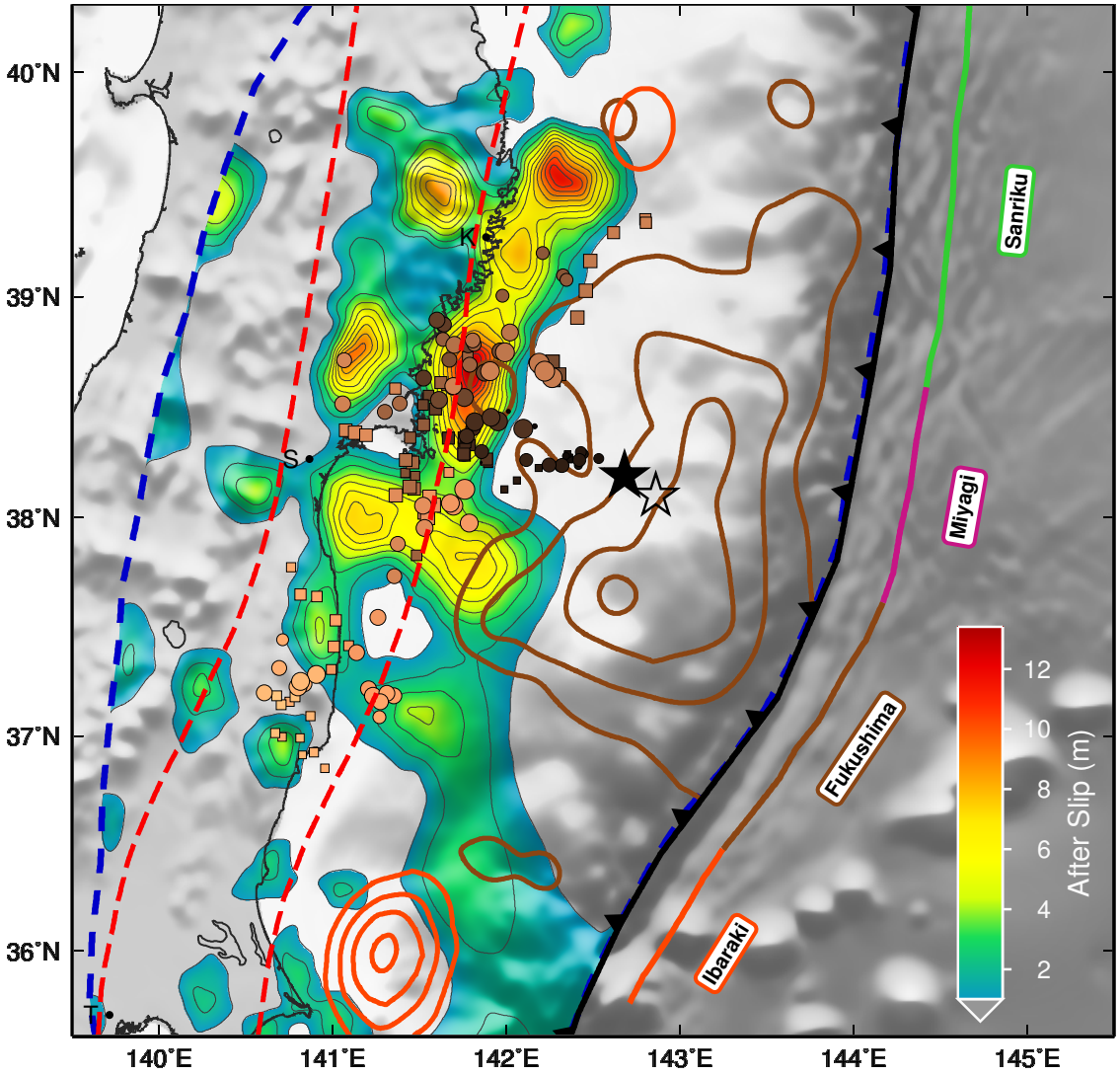

Figure 4.14. Representative after-slip model along with estimates of HF radiators from *Meng et al.* (2012). The filled black star indicates the epicenter of Tohoku-Oki mainshock estimated by *Chu et al.* (2011). Other features as in Figure 4.4

megathrust. Another suggestion for such heterogeneity is given by the spatial distribution of the decay time of the GPS post-seismic time series (Figure 4.15). We estimate the decay time τ through a grid search process in which we isolate and fit the east component of the post-seismic positional time series using several values of τ and the model $d_{\text{post}}(t) = \alpha \log\left(1 + \frac{t - t_{\text{EQ}}}{\tau}\text{H}(t - t_{\text{EQ}})\right)$, where α is a real constant and t_{EQ} corresponds to the time of the 2011 (M_w9.0) Tohoku-Oki earthquake. The expression for $d_{\text{post}}(t)$ comes from modeling after-slip using a rate- and state-dependent

friction law and corresponds to an approximated expression for times that are much smaller than the characteristic relaxation time t_r (see *Perfettini and Avouac*, 2004). We observe a clear latitudinal variation of the decay time, with smaller values consistently located at the segment of the megathrust with shallow after-slip. Surface post-seismic displacements are the integrated response of the physical media due to after-slip occurring at different regions of the megathrust, not all of which have the same relaxation time if material heterogeneity is assumed at the megathrust. Thus, a 1D model with a single relaxation time may not be the best representation. Note that the inferred decay time of the GPS time series is somewhat consistent with a depth dependence of the megathrust rheology as the GPS sites with smaller decay times are grouped at the regions where the source of post-seismic deformation is inferred at shallower depths on the megathrust. As an aside, we can not ignore the possibility that the observed variations in the decay time of the GPS time series may be partially attributed to a localized response of a heterogeneous continental lithosphere. We note as well a spatial regularity in our estimates of after-slip. We believe that such regularity in the variations of after-slip comes from a limited spatial resolution of after-slip inferences due to the correlation length imposed by the regularization and that these represents true variations of the after-slip occurring in the subduction megathrust as these occur in the best resolved regions of the megathrust. Figure 4.7 supports our conclusions as it shows that the inferred patterns of after-slip remains stable for 6 independent (and with different noise) after-slip inversions that sample the time evolution of after-slip. Although unlikely given the after-slip stability shown in Figure 4.7, we recognize the possibility that a slight underdamping of the inverse problem solution may be affecting our after-slip estimates. In future work we will analyze the observed regularity of our estimates of after-slip by using more sophisticated techniques to select the damping parameter, for example, using a more robust technique to select the damping parameter, for example, cross validation or model class selection techniques.

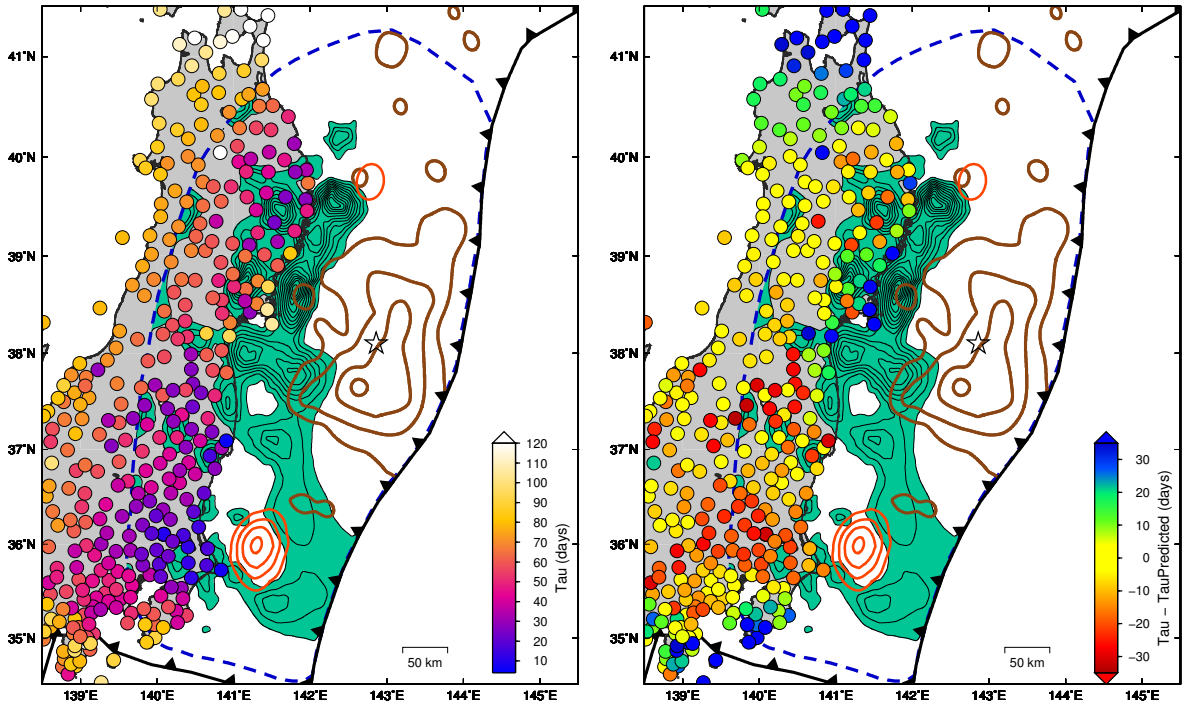

Figure 4.15. Post-seismic decay time of the GPS time series for a subset of GPS sites. (a) Colored circles indicate the decay time that best fits the post-seismic time series (east component) obtained through a grid search process. (b) Colored circles indicate the residual between estimates of the decay time in (a) and a linear trend of the decay time as a function of the distance between the GPS site and the trench. Figure 4.16 shows the decay time as a function of GPS site – trench distance as well as a linear trend representing such relationship.

Our model predicts an average after-slip around 1+ meters at the shallow portion of the Ibaraki segment of the Japan megathrust. The transient event has an equivalent moment magnitude $M_w 8.2$ and occurred just up-dip of the $M_w 7.9$ March 11, 2011 aftershock. Results from inter-seismic coupling models (e.g., *Suwa et al.*, 2006; *Loveless and Meade*, 2010, 2011) consistently suggest low coupling on the shallow portion of the megathrust offshore Ibaraki, where we infer transient after-slip. Moreover, there is no historical record of a large earthquake striking this region apart from the Fukushima sequence in 1938 with a cumulative seismic moment equivalent to $M_w \sim 8.1$ (*Abe*, 1977), and the $M_w \sim 7.9$ March 11, 2011 aftershock. Also relatively low seismicity has been observed in the shallow region of the megathrust offshore Ibaraki (*Ye et al.*, 2012, and references therein). Our results suggest that the shallow-most portion of the megathrust offshore Ibaraki is cur-

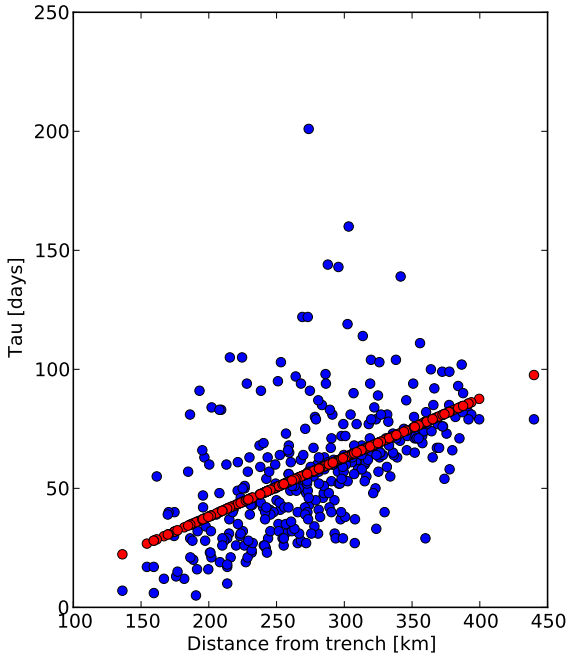

Figure 4.16. Post-seismic decay time of onland post-seismic positional time series for a subset of GPS sites in Japan (Figure 4.15) as a function of the distance between the GPS site and the trench (blue circles). Red circles correspond to the prediction of a linear fit representing the observed dependence between the post-seismic decay time an the GPS-trench distance. The fit was performed using L_1-norm for the misfit in order to minimize any bias induced by possible outliers in the calculation of the decay time of the positional time series.

rently slipping aseismically. This aseismic slip offshore Ibaraki, the inferences of low plate coupling (e.g., *Suwa et al.*, 2006; *Loveless and Meade*, 2010, 2011), and the low seismicity in the region, all suggest that aseismic slip may be the predominant behavior of the shallow-most portion of the megathrust offshore Ibaraki. However, given the low spatial resolution of our models in regions of the megathrust distant from onland geodetic observations and that inferences of coupling are low but not null, we would like to explore the possibility that the region may be able to accumulate some slip budget. If the slip during the inferred transient can be taken as a threshold to calculate the maximum allowable slip budget in the area, and that most of the budget will be released aseismically, on average one would expect the occurrence of transient events every 20 - 40 years. On the other hand, we also explore the existence of small asperities capable of generating large earthquakes in the shallow-most part of the megathrust offshore Ibaraki. Depending on the fraction of

the region that may be coupled, the time necessary to build an earthquake of a given size can be calculated based on the convergence rate of the plates. For example, if we assume that 25% of the region offshore Ibaraki located up-dip of the 11 March 2011 ($M_w 7.9$) aftershock is seismogenic, then approximately 90 years are needed to accumulate enough strain energy to produce a $M_w 8.2$ earthquake and about 1380 years for a $M_w 9.0$ one. There is no historical record of such events occurring in the past.

A limitation of any inverse problem is the observations signal to noise ratio, which limits its resolving capacity. If only inland geodetic observations are used, the slip inversion will only be capable of recovering a large enough source that produces a significant structured signal in the observables, especially if the source is located near the trench. The limitation posed by the spatial distribution of the available datasets makes impossible an accurate interpretation of the near trench behavior of the Japan megathrust offshore Ibaraki and in general for any subduction zone megathrust. Given the relevance of offshore events for seismic and tsunami hazard and to mitigate their effects on the general population, the scientific community and funding agencies need to pay special attention to monitoring the behavior of subduction megathrusts throughout the seismic cycle. At the present, offshore underwater geodetic measurements (*Ito et al.*, 2011; *Sato et al.*, 2011; *Iinuma et al.*, 2012) are the only ones capable of constraining with more precision the near trench megathrust behavior. Until such techniques are improved, or new ones developed and applied systematically, the behavior of the shallow portion of subduction megathrusts will remain unclear. Nevertheless, our results provide us some hints on the behavior of the shallow portion of the megathrust offshore Ibaraki Prefecture. Observations from seismicity, interplate coupling models and the inferred after-slip episode, all consistently suggests that this region of the megathrust may be prominent to undergo aseismic deformation as a mechanism to balance the slip budget.

Chapter 5

A Bayesian Approach to Estimating Apparent Plate Coupling - The Central Andes Subduction Zone

5.0 My contribution in this chapter

- Development of a simplified coupling model for subduction zone megathrusts in which only two states of coupling are allowed, full coupling and uncoupling. The model is parameterized as an in-depth band of the fault that is fully coupled surrounded by uncoupled regions. The depths of the boundaries of the coupled region are the free parameters of the model.

- Estimation of a three-dimensional fault structure modeling the contact between Nazca and South American plates.

- Development of a full Bayesian inversion scheme (and the corresponding computational software) to obtain estimates of apparent coupling in subduction zone megathrusts. Under such framework, I obtain estimates of apparent full-coupling probabilities for the Nazca-South American plate interface in the Central Andes segment, which are constrained by geodetic observations of inter-seismic crustal deformation rates. I analyze the obtained estimates of apparent coupling probability comparing it with the characteristics of past earthquakes in the

region, as well as possible scenarios for future earthquakes in the region, in particular in the Arica bend seismic gap.

5.1 Abstract

We aim to characterize the extent of apparent plate coupling on the subduction zone megathrust with the eventual goal of understanding spatial variations of fault zone rheology, inferring relationships between apparent coupling and the rupture zone of large earthquakes, as well as understanding the implications for earthquake and tsunami hazard. Unlike previous studies, we approach the problem from a Bayesian perspective, allowing us to completely characterize the model parameter space by searching *a posteriori* estimates of the range of allowable models instead of seeking a single optimum model. Two important features of the Bayesian approach are the possibility to easily implement any kind of physically plausible *a priori* information and to perform the inversion without regularization, other than that imposed by the way in which we parameterize the forward model. Adopting a simple kinematic back-slip model and a 3D geometry of the inter-plate contact zone, we can estimate the probability of apparent coupling (Pc) along the plate interface that is consistent with *a priori* information (e.g., approximate rake of back-slip) and available geodetic measurements. More generally, the Bayesian approach adopted here is applicable to any region and eventually would allow one to evaluate the spatial relationship between various inferred distributions of fault behavior (e.g., seismic rupture, post-seismic creep, and apparent inter-seismic coupling) in a quantifiable manner. We apply this methodology to evaluate the state of apparent inter-seismic coupling in the Chilean-Peruvian subduction margin (12^oS - 25^oS). As observational constraints, we use previously published horizontal velocities from campaign GPS (*Kendrick et al.*, 2001, 2006) as well as 3 component velocities from a recently established continuous GPS network in the region (Figure 2.23). We obtain patch-like features for Pc with higher values located above 60

km depth. We analyze the relationships between regions of high or low Pc and regions associated with the rupture process of the 1995 (Mw 8.1) Antofagasta, 2001 (Mw 8.4) Arequipa, 2007 (Mw 8.0) Pisco and the 2007 (Mw7.7) Tocopilla earthquakes (all occurred after the time period of the local campaign GPS measurements); as well as the region identified as the Arica bend seismic gap, which has not experienced a large earthquake since 1877.

5.2 Introduction

Inverse methodologies used to infer various spatial distribution of fault behavior frequently rely on optimization techniques, have non-unique solutions and are often ill-posed, requiring use of *a priori* regularization on the model parameters (*Hansen*, 1998). The solution of the inverse problem is very sensitive to the chosen form and degree of regularization (*Menke*, 2012; *Jónsson et al.*, 2002). Also, in optimization approaches, the form of *a priori* information (ex: positivity constraints) is limited.

A particular case corresponds to the problem of inferring the spatial distribution of apparent fault coupling in subduction zone megathrusts constrained by geodetic observations of inter-seismic crustal deformation. Previously published literature (e.g., *Ito et al.*, 1999; *Mazzotti et al.*, 2000; *Bevis et al.*, 2001; *Klotz et al.*, 2001; *Brooks et al.*, 2003; *Khazaradze and Klotz*, 2003; *Nishimura et al.*, 2004; *Suwa et al.*, 2006; *Chlieh et al.*, 2008, 2011; *Perfettini et al.*, 2010; *Loveless and Meade*, 2010, 2011) use some flavor of optimization approach to solve the inverse problem with different approaches used to describe *a priori* information and/or form of regularization. For example, by minimizing the second spatial differential of the fault slip behavior or using *a priori* information via formulae deduced from Bayes theorem (e.g., Akaike Information Criterion, *Akaike*, 1974), the latter requiring a parametric formulation for the model parameter uncertainties. It is a common practice to assume that the observational and model parameter uncertainties are normally distributed (e.g., least square family methods). Nevertheless, these approximations may induce a bias in the inverse

problem solution and may not be an accurate representation of the *a posteriori* information on the model parameters when these are poorly constrained.

The main advantage of the optimization techniques is that they are computationally inexpensive, therefore providing faster solutions, at least compared to a non-parametric Bayesian formulation of the inverse problem. However, with the increasing capacity of computational facilities (e.g., Beowulf clusters) we can make use of alternative techniques that enable us to avoid the caveats of the optimization approach, such as the bias of the solution introduced by the chosen form of regularization (§3).

In this work, we propose a Bayesian approach in which we search *a posteriori* estimates of the range of allowable models of apparent coupling, sampling the *a posteriori* (non-parametric) probability density function (PDF) of the model parameters constrained by onland geodetic observations of inter-seismic deformation rates. The Bayesian approach, first introduced to geosciences by *Jeffreys* (1931, 1939), although not used until relatively recently due to availability of computational resources, allows us to easily implement any physically plausible *a priori* information (even the homogeneous state of information), the use of any PDF to represent the observational uncertainties and to perform the inversion without regularization other than that imposed by the spatial discretization of the physical model. Moreover, formulating the solution of the inverse problem as the PDF of the model parameters ensures its uniqueness and presents us with a direct representation of uncertainties of the solution(*Tarantola*, 2005; *Minson et al.*, 2013).

We implement a Bayesian framework to invert for apparent plate coupling and apply it to the Central Andes subduction margin (12^oS–25^oS) providing a representation of the ensemble of solutions, a spatial distribution of apparent coupling probability. We contrast our results with previously published co- and post-seismic slip distributions associated with past earthquakes in the region giving insights on the relationship between the segmentation of the Central Andes subduction megath-

rust and the potential for earthquake occurrence.

5.3 Observational constraints: Inter-seismic velocity field

We use GPS inferred crustal velocities to describe the strain accumulation induced by the plate coupling at the subduction interface. Our dataset consist of previously published horizontal crustal velocities from campaign GPS (*Kendrick et al.*, 2001, 2006) as well as 3 component velocities from a recently established continuous GPS network in the region in a collaborative effort of scientists from Chile, France, Peru and United States in the context of the Central Andes Tectonic Observatory (CAnTO).

Campaign GPS velocities were obtained from joint processing the data gathered by the South America Nazca Plate Project (SNAPP *Norabuena et al.*, 1999) and the Central Andes Project (CAP, *Kendrick et al.*, 1999; *Bevis et al.*, 1999; *Kendrick et al.*, 2006, and references therein). The dataset correspond to repeated surveys spanning from January 1993 to March 2001 (supported by neighboring IGS continuous stations) with observation time spans varying from 2 to 7 years. The time span heterogeneity is well reflected in the uncertainties of the velocity field. We isolate 3 component inter-seismic crustal velocities from analysis of the positional time series obtained for the beforementioned continuous GPS network in the region (Figure 2.23). Although observations seems to be consistent, both datasets may be expressed in slightly different coordinate systems, both in a South America fixed reference frame but with unknown location of its origin. Therefore we introduce a reference frame correction to each dataset that is estimated during the inversion process. The correction consist of a translation and rotation of the reference frame for each dataset.

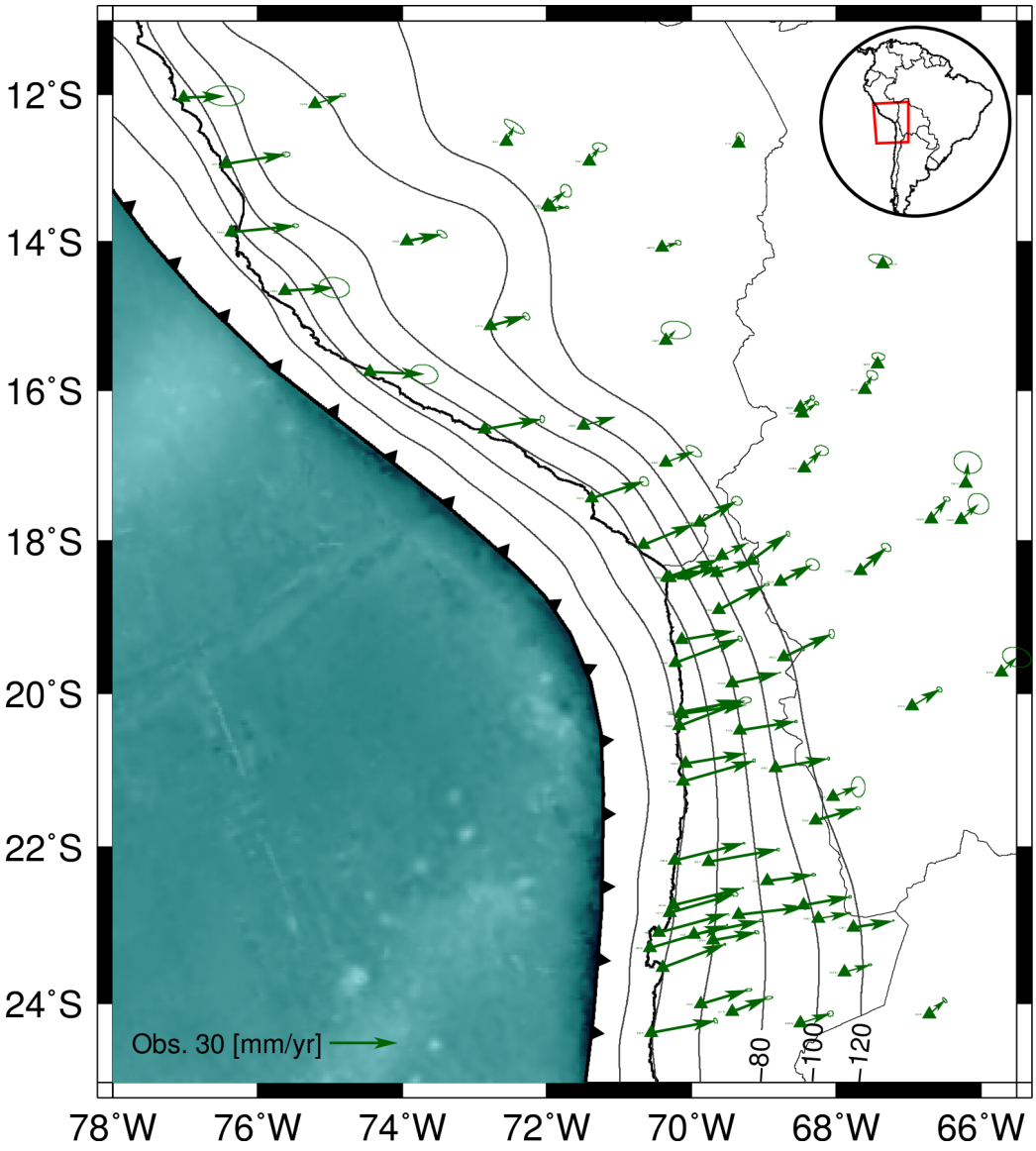

Figure 5.1. Horizontal components of GPS crustal velocities used in this study. The figure includes GPS secular rates from campaign GPS (*Kendrick et al.*, 2001, 2006) as well from a recently established continuous GPS network. Note that each dataset is expressed in a (slightly different) South America Fixed reference frame. Horizontal and vertical rates estimates from the cGPS network can be seen in Figure 2.23 (page 27).

5.4 Subduction model

We build a three-dimensional subduction elastic system by the use of the back-slip model (*Savage*, 1983) to represent the inter-seismic strain accumulation at the plate interface. We define a 2 plate subduction model where the convergence between Nazca and South American plates is represented

by the Euler vector defining the motion of a rigid plate in the sphere (§C; *Cox and Hart*, 1986). We also define a spatially variable distribution of apparent coupling along the plate interface with the aim of incorporating the effects of spatial variations of the mechanical behavior of the plate interface in the elastic model.

As the dominant physical process responsible for the measured inter-seismic crustal deformation, we only model tectonic loading transferred at the coupled regions of the subduction interface. Nevertheless, about 8.5% of the Nz-Sa convergence is achieved in the backarc by underthrusting of the Brazilian Shield beneath the Subandean Zone (*Bevis et al.*, 2001; *Kendrick et al.*, 2003, 2006; *Brooks et al.*, 2003; *Chlieh et al.*, 2011). *Chlieh et al.* (2011) showed that a sliver motion of the Andean belt influences the actual estimation of coupling at the Nz-Sa plate interface producing changes in the inferred coupling patterns depending on the assumed block motion rate of the Andean sliver. We account for that motion within the reference frame correction applied to each dataset. Other processes such as slip partitioning or crustal shortening of the Andean belt are neglected and assumed to be within the misfit errors.

We use the values of relative plate motion as estimated in REVEL (*Sella et al.*, 2002) to model the convergence between the Nazca and South-American plates. REVEL only uses space geodesy data to constrain plate motion, allowing us to use in our model a true instantaneous (averaged over a few years) solution for present day convergence rates. Other studies (e.g., *DeMets et al.*, 1990, 1994, 2010) incorporate magnetic lineations of the sea floor in their constraints (consequently averaging the velocities over millions of years), obtaining higher rates than REVEL for the relative plate motion. Such results are consistent with the hypothesis that the Nz - Sa convergence rate has been decreasing during the last 20My (e.g., *Pardo-Casas and Molnar*, 1987; *Somoza*, 1998; *Norabuena et al.*, 1999; *Sella et al.*, 2002; *Kendrick et al.*, 2003, 2006) and the convergence direction has remain stationary during that period (*Pardo-Casas and Molnar*, 1987; *Somoza*, 1998).

We represent the Nazca–South American plate interface between the 12^oS and 26^oS, by a 3D triangulated surface built using the softwares Gocad (Paradigm ©) and Geomod (in development at Caltech). A three-dimensional representation of the megathrust avoids inversion artifacts on the spatial distribution of plate apparent coupling, as pointed out by *Moreno et al.* (2009) in a study of co-seismic (static) slip inversions where sensitivity analysis are perform comparing 3D and planar fault structures to model the megathrust. To constraint the geometry of the megathrust, we use earthquake catalogs of relocated seismicity (*Engdahl et al.*, 1998; *Engdahl and Villaseñor*, 2002), regional catalogs (e.g., *Comte et al.*, 2004); seismic reflection profiles (e.g., *Oncken et al.*, 1999; *Hampel et al.*, 2004; *Krabbenhöft et al.*, 2004), sea floor bathymetry and topography from ETOPO 02, and a model for subducted Nazca plate top geometry derived from a database of independent geophysical information (*Tassara et al.*, 2006). The obtained plate interface is consistent with the one obtained by *Hayes and Wald* (2009); *Hayes et al.* (2009) that uses relocated seismicity and focal mechanisms of large earthquakes. It is also fairly similar to that obtained by *Cahill and Isacks* (1992) although our model has sharper features, primarily due to improved constraints, because we now have access to better datasets to constrain such surface and the ability to do local 3D spatial interpolation allowing the use of a spatially varying smoothing factors for the surface. The triangulated mesh is composed of regular triangles (close to equilateral), each one with an area $\sim 2-3[km^2]$. A Transverse Mercator map projection, centered at 18^oS , 72^oW, is used to minimize the distortion produced by the map projection.

Previous studies show that most of the GPS velocities can be explained by locking of the upper $50[km]$ of the plate interface (*Klotz et al.*, 2001; *Bevis et al.*, 2001; *Khazaradze and Klotz*, 2003; *Kendrick et al.*, 2003, 2006; *Brooks et al.*, 2003) and thus motivated us to consider only an analogous simple model to represent the tectonic loading. We describe apparent coupling along the plate interface by 2 interpolated curves in depth, the top (Z_{top}) and bottom (Z_{bottom}) boundary of the

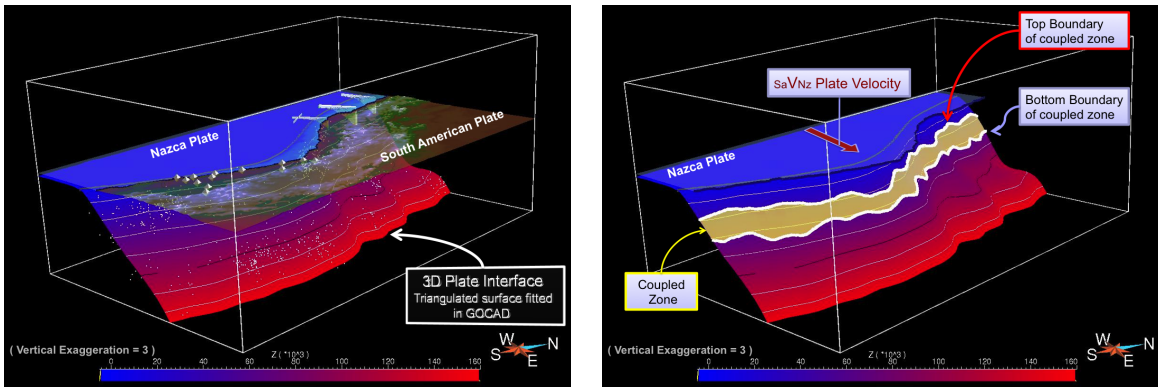

(a) (b)

Figure 5.2. Three-dimensional surface representing the geometry of the top of the Nazca plate colored by depth. (a) An example of seismicity (white dots) and location of seismic profiles used to fit the 3D surface, along with the topography of the South American plate. (b) Illustration of our coupling model: a coupled region (yellow) defined by its top and bottom boundaries (thick white curves).

coupled zone (Figure 5.2b). The plate interface is coupled in the region enclosed by these curves and uncoupled outside. We ignore the possible existence of any transition zones. For practical purposes we also impose that a point $\mathbf{p}$ of the plate interface can be coupled only if it lies within a prescribed region in depth defined by a minimum and maximum coupling depth ($Z_{min}(p)$ and $Z_{max}(p)$, respectively). The latter condition does not constrain the depth values of the previously defined coupled zone boundaries.

We define a trench coordinate system[†] (t, d, z) in order to have a spatial discretization of the forward model that is trench arc-length-wise, i.e., in which we measure the discretization size along the trench curve. For a point $\mathbf{p}$, the transformation from a Cartesian (x,y,u) to a trench (t,d,z) coordinate system is defined as follows: z is its depth (with respect to mean sea level), d is the map distance of the point $\mathbf{p}$ to the trench and t is the arc-length (measured with respect to an arbitrary, fixed, trench point) that minimizes the distance d. If more than one trench point satisfies the latter condition, the one with minimum arc-length is used, in this way a one to one mapping is defined

[†]We do not analyze the metric in the trench coordinate system since it is used solely to compute a mask defining the coupled portion of the plate interface. Any other physical quantity is computed using the original Cartesian coordinate system.

from Cartesian (x,y,z) to trench (t,d,z) coordinate systems. In trench coordinates, the coupling state (C_S) for a point p with coordinates (t_p, d_p, z_p) can be represented by the function,

$$C_S(t_p, z_p) = \Pi_{Z_{min}(t_p)}^{Z_{max}(t_p)}(z_p) \cdot \Pi_{Z_0(t_p)}^{Z_1(t_p)}(z_p) \tag{5.1}$$

where $\Pi_{Z_a}^{Z_b}(z) = H(z - Z_a) - H(z - Z_b)$, is a boxcar function between depth's Z_a and Z_b.

Along strike variations in the boundaries of the coupled zone are described by interpolation of equally spaced knots in trench arc-length (t). Given 2 independent and identically distributed random variables, any non-constant function of this variables will follow a different probability distribution. For example, a linear interpolation between these 2 random variables will produce interpolated values whose PDF is proportional to the convolution of the PDFs of the random variables defining the interpolation knots. Thus, in order to preserve the statistical properties of the interpolation knots for any of the interpolated values we choose a nearest neighbor interpolation scheme. The interpolation formula can be written as,

$$Z_i(t) = \sum_{k=1}^{N} z_k \cdot \Phi_k(t) \tag{5.2}$$

$$\Phi_k(t) = \begin{cases} 1 - H\left(t - \frac{1}{2}[t_1 + t_2]\right) & \text{if} \quad k = 1 \\ H\left(t - \frac{1}{2}[t_{k-1} + t_k]\right) - H\left(t - \frac{1}{2}[t_k + t_{k+1}]\right) & \text{if} \quad 1 < k < N \\ H\left(t - \frac{1}{2}[t_{N-1} + t_N]\right) & \text{if} \quad k = N \end{cases} \tag{5.2a}$$

where i is the name of the boundary curve, N is the number of knots of the curve, $\Phi_k(t)$ is the Nearest Neighbor interpolation formula, t_k, z_k are the arc-length and depth of the curve knots (for Z_{top} or Z_{bottom}) and $H(\cdot)$ is a Heaviside function.

We use a back-slip model (*Savage*, 1983) and a finite rectangular dislocation in an elastic half-space (*Okada*, 1985) in order to model coupled regions and the resulting crustal deformation. Regions of the plate interface where $C_S = 1$ are assumed to be locked (coupled) and where $C_S = 0$,

aseismic steady slip is occurring. In addition, each dataset used to constrain coupling at the plate interface consists of GPS velocities expressed relative to some fixed point in South America. However, the methodology used to define each reference frame may lead to inconsistent GPS velocities. Thus, we need to express such observations in a common reference frame that is consistent with the plate convergence as obtained from REVEL (*Sella et al.*, 2002). Such a correction is estimated during the inversion process by adding a velocity field to each dataset corresponding to the motion of a rigid plate on the sphere (*Cox and Hart*, 1986). The complete set of free parameters of the model are the interpolation knots depth of the boundary curves describing the coupled zone and the three components of the Euler poles modeling each GPS velocity correction.

For a given realization of the model parameters, the coupling state (C_S) defines a mask in depth that indicates which fault patches defining the plate interface are contributing to model the tectonic loading, therefore, to the prediction of the GPS velocities. On each triangular patch we calculate two Green's functions, corresponding to the along strike and down-dip components of the back-slip rate associated to that patch. Unitary dislocations (*Okada*, 1985) on a square with the triangle's area, dip and strike, and centered on the triangles centroid are used to calculate the prediction of the GPS velocity field. Note that we use a dislocation over a finite square fault surface to represent a triangular one. Since the distance between the fault patch and the observation point where the plate velocities are predicted is large compared with the characteristic size of the dislocation region, the predicted velocity field is not sensitive to the shape of the finite dislocation. We also need the small triangles to ensure the precision of the parameterization.

The back-slip rate on each fault patch corresponds to the plate convergence velocity calculated from REVEL at the centroid of each triangular fault patch and projected into the fault surface. The projection is done by first rotating each fault patch along its strike direction in δ^o (dip angle) to make them horizontal. Then, the plate velocity is projected into the strike and down-dip directions

to obtain the along strike and along down-dip back-slip rates (S_{BR} and D_{BR}, respectively). Finally, each fault patch is rotated back to its original position. The predicted velocity at an observation point i due to coupling at the fault patch j is then calculated as follows,

$$d_{ij}^{pred} = S_{BR_j} GmSS_{ij} + D_{BR_j} GmDS_{ij} \tag{5.3}$$

where $GmSS_{ij}$ and $GmDS_{ij}$ are the Green's functions calculated for a unit strike slip and down-dip slip dislocation, respectively, and,

$$S_{BR_j} = V_{E_j} sin(\phi_j) + V_{N_j} cos(\phi_j) \tag{5.4a}$$

$$D_{BR_j} = V_{E_j} cos(\phi_j) - V_{N_j} sin(\phi_j) \tag{5.4b}$$

where ϕ_j is the strike angle and V_{E_j}, V_{N_j} the East and North component of the plate convergence velocity at the centroid of the fault patch j. Now replacing (5.4) into (5.3) and rearranging we obtain,

$$d_{ij}^{pred} = V_{Ej} GmVE_{ij} + V_{Nj} GmVN_{ij} \tag{5.5}$$

where,

$$GmVE_{ij} = sin(\phi_j) GmSS_{ij} + cos(\phi_j) GmDS_{ij} \tag{5.6a}$$

$$GmVN_{ij} = cos(\phi_j) GmSS_{ij} - sin(\phi_j) GmDS_{ij} \tag{5.6b}$$

then $GmVE_{ij}$ and $GmVN_{ij}$ correspond to the Green function matrices as a function of the plate velocity calculated at the fault patch j.

If we consider now the state of coupling at each fault patch (C_{Sj}), the velocity field predicted

by a realization of our model parameters can be written as:

$$d_i^{pred} = \sum_{j=1}^{N_{FP}} \left[V_{E_j} GmVE_{ij} + V_{N_j} GmVN_{ij} \right] \cdot C_{Sj} \tag{5.7}$$

where N_{FP} is the number of fault patches.

5.5 Bayesian inversion

The Bayesian approach uses Bayes theorem to infer the *a posteriori* state of information on the model parameters $\mathbf{m}$ based on previously obtained information on $\mathbf{m}$ and information on the physical relationships between $\mathbf{m}$ and newly acquired observations $\mathbf{d}$ (§3; *Tarantola*, 2005). The relationship between *a posteriori* and *a priori* information can be written as,

$$P(\mathbf{m}|\mathbf{d}) = k \cdot P(\mathbf{m}) \cdot P(\mathbf{d}|\mathbf{m}) \tag{5.8}$$

where $k > 0 \in I\!R$ is a normalization constant, $P(\mathbf{m}|\mathbf{d})$ the *a posteriori* probability on the model parameters given newly acquired observables, $P(\mathbf{m})$ the *a priori* probability on the model parameters and $P(\mathbf{d}|\mathbf{m})$ the Likelihood of the model prediction given a realization of the model parameters $\mathbf{m}$.

To motivate the use of a Bayesian approach for the inverse methodology, we show 2 scenarios for coupling at the plate interface in Figure 5.3. Both cases can be considered as viable solutions of the inverse problem as their predictions are consistent with the observed GPS data. Thus, suggesting large uncertainties in the location of the coupled zone. Here we note the importance of estimating the whole range of possible values for the model parameters, i.e., to properly sample their uncertainties. The Bayesian approach allows us to compute such uncertainties in a form of a probability density function (PDF) without assuming any functional form for it and without *a priori* regularization other

than that imposed by the model parameterization (in our case, the spacing of the interpolation knots and a coupling “in-depth" correlation given by the definition of the Coupling State C_S). It also poses the solution of the inverse problem as the PDF of the model parameters (through millions of sampled models) as opposed to more classical approaches in which an optimum solution is obtained. Such a formulation ensures the uniqueness of the inverse problem solution (*Tarantola*, 2005). Now arises the problem of how to statistically represent a given ensemble of several million models. We could compute the mean or median model among a percentage of the best suited sampled models but we can not say for sure that such models are viable and, in the worst case, it may not be a solution of the inverse problem or may not make physical sense in the context of the parameterization. To avoid these complications we do not use statistical estimators to compute an equivalent model. Instead, we propose an aggregated interpretation of the ensemble of the best suited models by computing the spatial distribution of the probability of apparent coupling on the megathrust (P_c) from all the sampled models[†].

For a given point $\mathbf{p}$ at the plate interface our parameterization defines a state of coupling that is binary (recall that $\mathbf{p}$ is either coupled or uncoupled and no partial coupling is allowed in our model). Thus, $P_c(\mathbf{p})$ is easily computed by calculating the fraction of sampled models that predict $\mathbf{p}$ to be coupled (5.9). As a direct consequence, the probability of the point $\mathbf{p}$ to be uncoupled ($P_u(\mathbf{p})$) satisfies $P_u(\mathbf{p}) = 1 - P_c(\mathbf{p})$.

$$P_c(\mathbf{p}) = \frac{\text{number of sampled models in which } \mathbf{p} \text{ is coupled}}{\text{number of sampled models}} \tag{5.9}$$

5.5.1 Selection of the *a priori*

With a Bayesian approach one can easily implement *a priori* constraints such as limiting the range of any given parameter or describe the *a priori* information in terms of relationships (or rules) between

[†] See appendix D for an alternate interpretation of P_c.

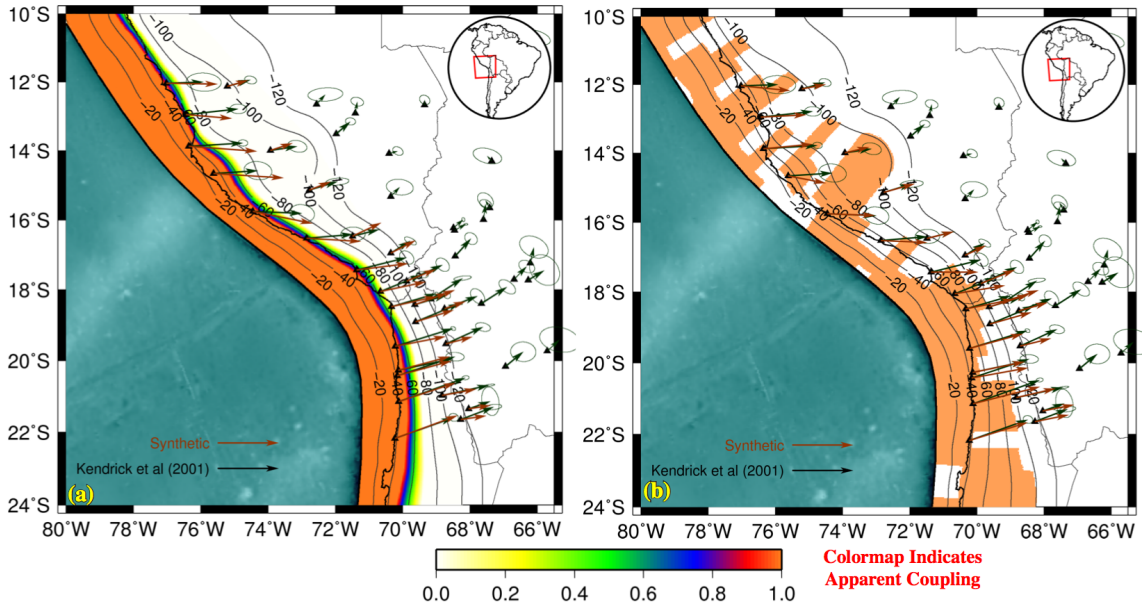

Figure 5.3. Similar GPS velocity predictions for 2 contrasting model scenarios. (a) the plate interface is coupled from the trench up to 50 km depth with a linear transition zone from coupled at 50 km depth to uncoupled below 70 km depth. (b) A handcrafted example using our parameterization. GPS velocities from *Kendrick et al.* (2001).

parameters. However, we must exercise extreme caution when choosing such constraints, because they may add unwanted information to the model parameters that may be inconsistent with some of the posed hypotheses. An important step in any inverse problem, especially for the unregularized Bayesian approach, is to check how the chosen parameterization and *a priori* set of restrictions are adding information to our model parameters. Since the proposed physical model has a bimodal state of coupling (a point $\mathbf{p}$ of the plate interface is either coupled or not), it is straightforward to represent the state of absence of information by choosing an uninformative *a priori* set of restrictions on the model parameters that produce a probability of apparent coupling $P_c = 0.5$ on any point of the plate interface in which coupling is allowed by our model. However, choosing the right set of restrictions without adding unwanted *a priori* information is a challenging problem.

We illustrate how a particular set of a priori restrictions adds unwanted information to the model parameters. In the chosen model parameterization the entire coupled zone is only allowed to lie

between seafloor (trench) and a maximum depth (Z_{min} and Z_{max}, respectively). Thus, a natural choice of restrictions to describe the *a priori* is given by,

$$Z_{top}, Z_{bottom} \approx U\left[Z_{min}, Z_{max}\right] \tag{5.10a}$$

$$Z_{top} \leq Z_{bottom} \tag{5.10b}$$

where Z_{top} , Z_{bottom} are drawn independently, and the restriction (5.10b) comes from imposing that Z_{top} and Z_{bottom} , the top and bottom boundaries of the coupled zone, must never cross. The sampling space of Z_{top} and Z_{bottom} under such restrictions is shown in Figure 5.4a1.

Using the set of restrictions (5.10a) and (5.10b) on the parameters we can estimate the probability of coupling for a point $\mathbf{p}$ with depth $z_p \in [Z_{min}, Z_{max}]$ as,

$$P_c(\mathbf{p}) \quad = \quad P\left(C_S(z_p) = 1 | Z_{top} \leq Z_{bottom}\right) \tag{5.11}$$

where $C_S(z_p)$ is the coupling state of point $\mathbf{p}$ from equation (5.1). Then,

$$\begin{aligned} P_c(\mathbf{p}) \quad &= \quad P\left(Z_{top} \leq z_p \leq Z_{bottom} | Z_{top} \leq Z_{bottom}\right) \\ &= \quad \frac{P\left(Z_{top} \leq z_p \leq Z_{bottom} \cap Z_{top} \leq Z_{bottom}\right)}{P\left(Z_{top} \leq Z_{bottom}\right)} \end{aligned} \tag{5.12}$$

and since Z_{top} and Z_{bottom} are independent (uniformly distributed) random variables, by simple inspection of Figure 5.4a1, we obtain that the probability of coupling P_c as a function of depth of the point in the plate interface is the parabola,

$$P_c(\mathbf{p}) = \begin{cases} \dfrac{(Z_{max} - z_p)(z_p - Z_{min})}{\frac{1}{2}(Z_{max} - Z_{min})^2} & \text{if} \quad Z_{min} \leq z_p \leq Z_{max} \\ 0 & \sim \end{cases} \tag{5.13}$$

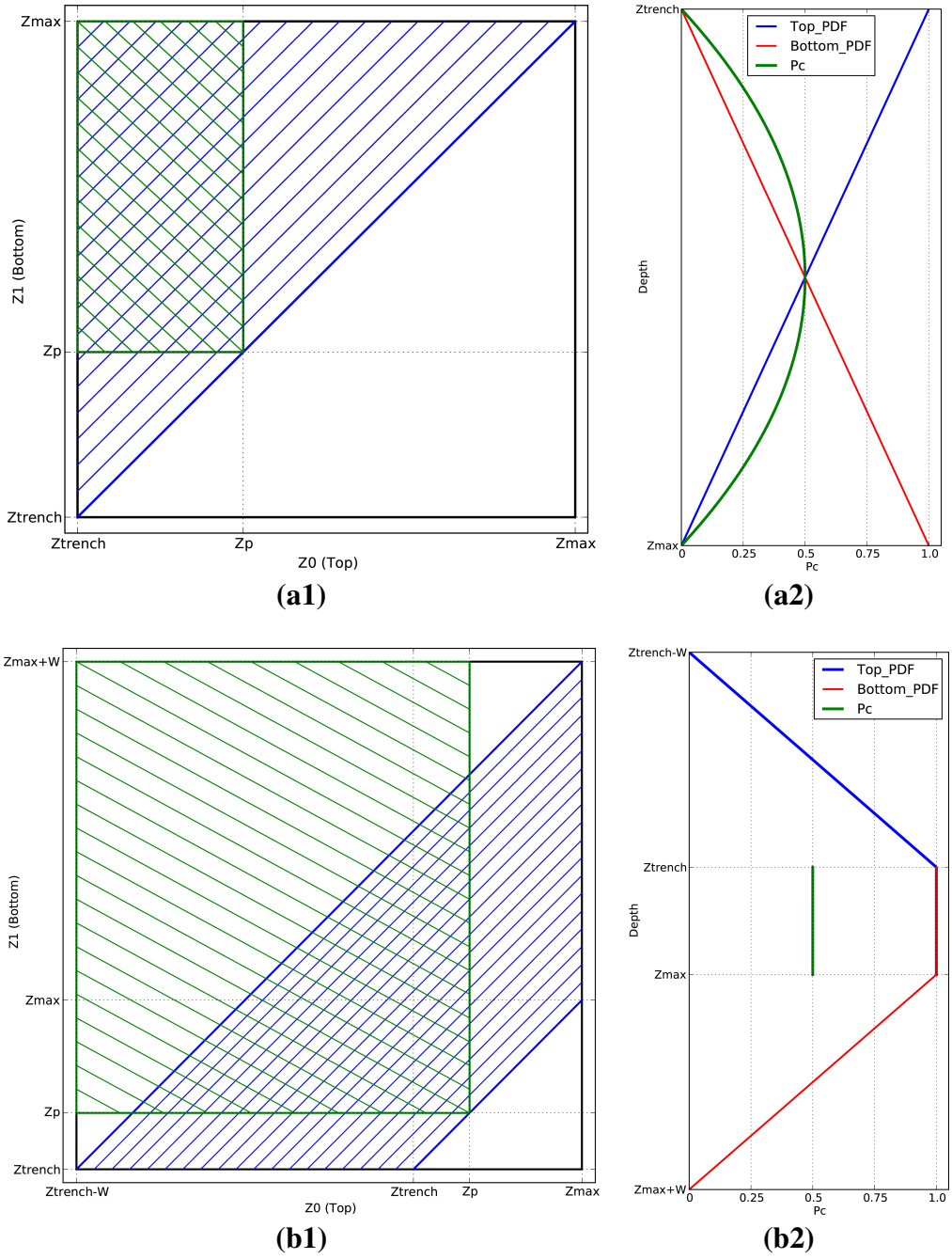

Figure 5.4. Sampling space for Z_{top} and Z_{bottom} in addition to: (a1) the first set of restrictions which gives Pc non-constant in $[Z_{min}, Z_{max}]$ and the triangular-shaped PDFs shown in (a2). (b1) the set of restrictions that gives $P_c = 0.5$ constant and uninformative PDFs (shown in b2) over such region. Note that, since Z_{top} and Z_{bottom} are drawn independently from an uniform probability distribution, their joint PDF can be identified directly by simple inspection of Figures (a1) or (b1) depending on the adopted *a priori* set of restrictions. Note that in both cases P_c is proportional to the area defined by the intersection of the 2 hatched regions.

and the marginal PDFs for Z_{top} and Z_{bottom} are triangular in shape,

$$f_{Z_{top}}(z_p) = \frac{2(Z_{max} - z_p)}{(Z_{max} - Z_{min})^2} \qquad Z_{min} \leq z_p \leq Z_{max} \tag{5.14a}$$

$$f_{Z_{bottom}}(z_p) = \frac{2(z_p - Z_{min})}{(Z_{max} - Z_{min})^2} \qquad Z_{min} \leq z_p \leq Z_{max} \tag{5.14b}$$

Recall that our physical model has a bimodal state of coupling (either coupled or not). Thus, in the absence of observations to constraint the model parameters, one would expect an a priori coupling probability of 50% constant over the plate interface, which is clearly not the case. The chosen set of restrictions is adding information to the model parameters, which is reflected in the triangular shape of the marginal PDFs (5.14a) and (5.14b) (see Figure 5.4a2).

Our goal now is to find a suitable set of a priori restrictions that allows us to estimate a posteriori values of P_c that are constrained only by the GPS observations and not by the in-depth coupling regularization imposed by our definition of the coupling state C_S (5.1). Thus, to obtain an a priori $P_c = 0.5$ constant over the region of the plate interface that is allowed to be coupled.

To accomplish our goal, we need marginal PDFs for Z_{top} and Z_{bottom} that are uninformative (constant) and equally valued in the depth interval $[Z_{min}, Z_{max}]$. We accomplish such a condition by extending the sampling space and adding an extra restriction on its extent. Now follows a proof that the restrictions (5.15a), (5.15b) and (5.15c) suites our needs.

Let $W > 0$ be the maximum distance between Z_{top} and Z_{bottom} and the set of *a priori* restrictions,

$$Z_{top} \sim U\left[Z_{min} - W, Z_{max}\right] \tag{5.15a}$$

$$Z_{bottom} \sim U\left[Z_{min}, Z_{max} + W\right] \tag{5.15b}$$

$$0 \leq Z_{bottom} - Z_{top} \leq W \tag{5.15c}$$

with this *a priori*, recalling the independence and uniformity of the random variables Z_{top} and Z_{bottom} , we can calculate $P_c(\mathbf{p})$ based on Figure 5.4b1. Then,

$$\begin{aligned} P_c(\mathbf{p}) &= P\left(Z_{top} \leq z_p \leq Z_{bottom} | 0 \leq Z_{bottom} - Z_{top} \leq W\right) \\ &= \frac{P\left(Z_{top} \leq z_p \leq Z_{bottom} \cap 0 \leq Z_{bottom} - Z_{top} \leq W\right)}{P\left(0 \leq Z_{bottom} - Z_{top} \leq W\right)} \\ &= \frac{\frac{1}{2}W^2}{\frac{1}{2}(Z_{max} + W - Z_{min})^2 - \frac{1}{2}(Z_{max} - Z_{min})^2} \end{aligned} \tag{5.16}$$

by rearranging terms,

$$P_c(\mathbf{p}) = \begin{cases} \dfrac{W}{2(Z_{max} - Z_{min}) + W} & \text{if} \quad Z_{min} \leq z_p \leq Z_{max} \\ \\ 0 & \sim \end{cases} \tag{5.17}$$

then by choosing $W = 2(Z_{max} - Z_{min})$ we obtain from (5.17) that $P_c(\mathbf{p}) = 0.5 \; \forall \mathbf{p}$ *s.t.* its depth $z_p \in [Z_{min}, Z_{max}]$. Note that, by construction, $P_c(\mathbf{p}) = 0$ for z_p outside the interval $[Z_{min}, Z_{max}]$. With this restrictions, the marginal PDF's for Z_{top} and Z_{bottom} become,

$$f_{Z_{top}}(z_p) = \begin{cases} \dfrac{z_p - (Z_{min} - W)}{W^2} & \text{if} \quad Z_{min} - W \leq z_p < Z_{min} \\ \\ \dfrac{1}{W} & \text{if} \quad Z_{min} \leq z_p \leq Z_{max} \end{cases} \tag{5.18a}$$

$$f_{Z_{bottom}}(z_p) = \begin{cases} \dfrac{1}{W} & \text{if} \quad Z_{min} \leq z_p \leq Z_{max} \\ \\ \dfrac{(Z_{max} + W) - z}{W^2} & \text{if} \quad Z_{max} < z_p \leq Z_{max} + W \end{cases} \tag{5.18b}$$

and these are uninformative and with equal value in the interval $[Z_{min}, Z_{max}]$ (see Figure 5.4b2). Thus, we use the *a priori* restrictions (5.15a), (5.15b) and (5.15c) for our inversion of apparent

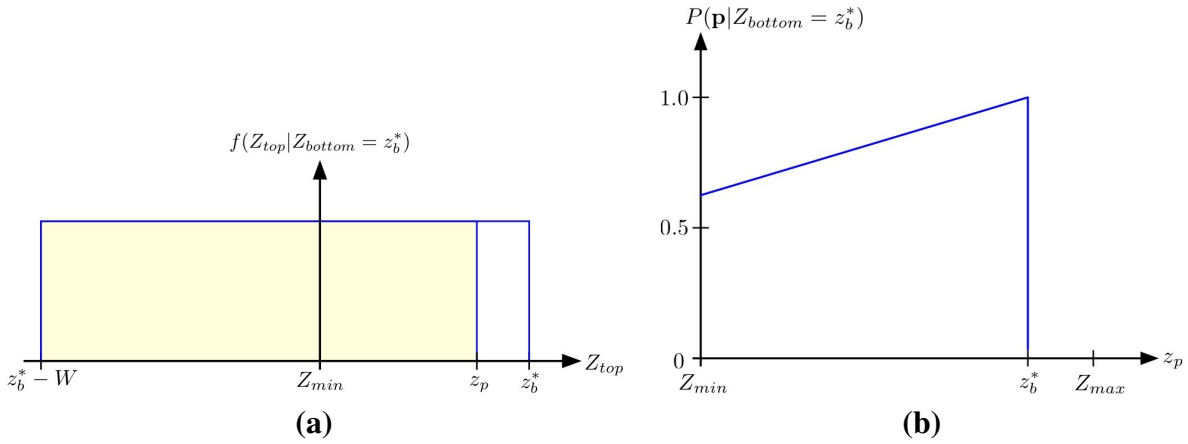

Figure 5.5. Consequences of the chosen parameterization. The figure illustrates an extreme (and unlikely) case in which the down-dip limit of the coupled zone Z_{bottom} is very well constrained and there is no constraint on the up-dip limit Z_{top}. (a) Conditional PDF of Z_{top} for a given value of $Z_{bottom} = z_b^*$. The yellow shaded area corresponds to the region of the sampling space where $Z_{top} \leq z_p$, i.e., that allow the point $\mathbf{p}$ with depth z_p to be coupled. (b) Coupling probability of a point $\mathbf{p}$ of the plate interface given that $Z_{bottom} = z_b^*$ from equation (5.19). Note that in this extreme case, the coupling probability at the shallow-most portion of the modeled region will never be below 0.5. This is a consequence of the depth-dependent correlation imposed by the chosen model parameterization.

coupling.

A caveat of the chosen parameterization may arise when the observational constraint on the top boundary of the coupled zone Z_{top} is not strong enough (or at least considerably weaker than the lower boundary one). We evaluate an extreme (and very unlikely) case where the down-dip end of the coupled zone Z_{bottom} is very well constrained (as seen later in tests with synthetic observations and in our results for coupling in the Central Andes), so it can be treated as a known deterministic variable fixed at $Z_{bottom} = z_b^*$ and that there is no constraint at all to the up-dip boundary of the coupled zone Z_{top} . The conditional a priori PDF for Z_{top} given $Z_{bottom} = z_b^*$ is a uniform distribution (Figure 5.5a) and it can be calculated directly from the a priori joint PDF of Z_{top} and Z_{bottom} (Figure 5.4b1) as $Z_{top} \sim U[z_b^* - W, z_b^*]$. Then the coupling probability of a point $\mathbf{p}$ with depth z_p located above z_b^* and below trench depth Z_{min} can be calculated as,

$$
\begin{aligned}
P_c(\mathbf{p}|Z_{bottom} = z_b^*) &= P(z_p \geq Z_{top}|Z_{bottom} = z_b^*) \\
&= \frac{W - (z_b^* - z_p)}{W} && \text{but } W = 2(Z_{max} - Z_{min}) \\
&= 1.0 - 0.5\frac{z_b^* - z_p}{Z_{max} - Z_{min}} && Z_{min} \leq z_p \leq z_b^* \qquad (5.19)
\end{aligned}
$$

Now we are interested to see the dependency of the coupling probability at the trench given by the value of the down-dip limit of the coupled zone $Z_{bottom} = z_b^*$. Figure 5.5b shows a schematic representation for equation (5.19). In this extreme case when there is no constraint on Z_{top} and Z_{bottom} has a deterministic value we find that P_c at trench depth (Z_{min}) will always be larger than 0.5 as a direct consequence of the in-depth correlation of coupling imposed by the model parameterization (5.1). A more realistic situation where there is some degree of constraint on Z_{top} and a stronger one on Z_{bottom} will have a much complex behavior. Nevertheless, our simple analysis suggests that weaker constraints on the top boundary of the coupled zone, as occur in subduction zones where models are only constrained by onland data, will translate into near trench estimates of apparent coupling probability that are slightly larger than their true value, the difference depending on the relative strength of the constraints provided by the observations.

As for the Cartesian coordinates of the Euler pole defining the reference frame correction, we restrict these parameters to a “wide enough" interval centered at the origin.

So far we have mentioned *a priori* information as restrictions applied to the model parameters. We also use non-parametric *a priori* that corresponds to the geometry of the plate interface, plate motion given by REVEL (Sella, 2002) and the fact that we are disregarding any other contribution to the crustal deformation other than the tectonic loading at the coupled region of the plate interface and a sliver movement of the Andean region.

5.5.2 Sampling the *a posteriori*

We implement a Markov Chain Monte Carlo (MCMC) (*Hastings*, 1970) algorithm to sample the a posteriori probability density functions of the model parameters: depth of the interpolation knots of each coupled zone boundaries and the Cartesian components of the Euler pole corresponding to each reference frame correction. A known problem to Monte Carlo methods is the *curse of dimensionality* , which refers to the exponentially increasing difficulty to sample the model parameter space when there is a high number of parameter to sample. In our case, we choose a knot spacing of 75 km for the boundaries of the coupled interface, which translates into 80 parameters (considering the 3 components of the Euler poles for the 2 GPS velocities datasets). We use the CITerra Beowulf cluster in order to run simultaneously hundreds of independent MCMC chains to substantially improve the sampling efficiency of the high dimensional model parameter space and do it in a reasonable time. Each MCMC chain is previously tuned in order to have an acceptance rate of about $\sim 20 - 30\%$.

The goodness of a model parameter realization ($\mathbf{m}$) is given by the Likelihood function $L(\mathbf{m}) = P(d^{pred}|\mathbf{m})$,

$$L(\mathbf{m}) = \exp\left(-\sum_{i=1}^{N_{obs}} \frac{|d_i^{obs} - d_i^{rot}(\mathbf{m}) - d_i^{pred}(\mathbf{m})|}{\sigma_i}\right) \tag{5.20}$$

$$\sigma_i = \sqrt{\sigma_{obs\,i}^2 + \sigma_{m\,i}^2} \tag{5.20a}$$

where N_{obs} is the number of observations, d_i^{obs}, $d_i^{rot}(\mathbf{m})$ and $d_i^{mod}(\mathbf{m})$ are the i-th observation, reference frame correction and predicted velocity respectively, and σ_i is the uncertainty associated to the i-th observation. The L_1 norm is used in order to have a likelihood function that is less sensitive to observational outliers (*Menke*, 2012). Note that σ_i is composed by the observational uncertainty

σ_{obs} as well as an additional term σ_m with the purpose to recognize that the physical model used in this study is a simple approximation of the physics controlling the velocity field measured through the GPS observations. Note as well that we are artificially inflating the observational uncertainties to take account of model shortcomings and that σ_i is not the result of the convolution of the random variables representing observational error and model prediction uncertainties. By introducing such representation of the model prediction uncertainties we are reducing the amount of information available to estimate the model parameter PDFs, but avoiding artifacts that may occur when trying to overfit the observations with an approximated forward model without additional regularization on the model parameters. Now arises the problem of estimating σ_m, such a task still remains an unsolved problem with the current available techniques (*Tarantola*, 2005; *Minson et al.*, 2013). Since we do not have any kind of *a priori* knowledge on the model prediction uncertainties we impose $\sigma_m = 1mm/yr$ as a minimum threshold for the observational errors.

Before we present any inversion results constrained by the GPS data, we first sample the a priori PDF of our model parameters (Figure 5.6) and perform a series of tests using synthetic data in order to study the resolution of our model parameters (Figures 5.7 and 5.8). In Figure 5.6a, $P_c = 0.5$ is calculated from all the sampled models using formula (5.9) and correspond to a gray tone in the color palette. Note that $P_c = 0.5$ represents a state of absence of information (recall this is the *a priori* P_c, i.e., without considering observational constrains), then when analyzing the inversion results (*a posteriori* P_c), the meaning of any area of the map showing gray tones is that the model is poorly resolved in such areas. Possible causes for such a behavior are that the observations either do not provide enough constraints on such region, are inconsistent among themselves or inconsistent with the physical model. On the latter case, $P_c \approx 0.5$ could mean that there is partial coupling, but reaching that conclusion will require additional knowledge as our modeling can not distinguish between the different causes that lead to obtain $P_c \approx 0.5$ in some areas.

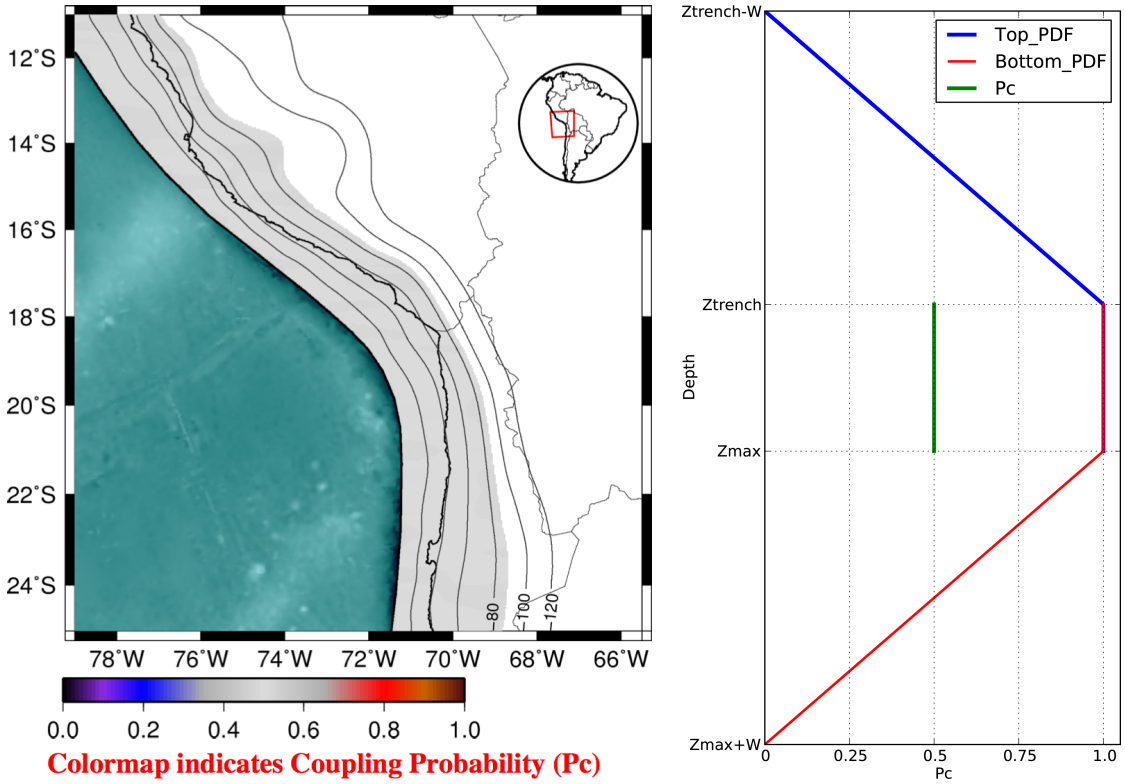

(a) (b)

Figure 5.6. (a) Map of apparent coupling probability (Pc) obtained by sampling the a priori PDF of the model parameters. Here Z_{min} = trench depth and Z_{max} = trench depth + 80 km. Note that the a priori $P_c = 50\%$ for the whole plate interface. (b) The a priori PDF of the top (blue) and bottom (red) edges of the coupled zone (Z_0 and Z_1, respectively) along with the a priori P_c (green) for a trench perpendicular section. Both PDFs are plotted with equal probability (area to the left of the curve is 1). $P_c = 0.5 \in [Z_{trench}, Z_{max}]$ and 0 outside. Note that we show the PDFs over the whole sampling space, which is greater than the region of the plate interface where the apparent coupling is being characterized. As shown in §5.5.1, the extended region is needed to obtain an a priori $P_c = 0.5 \in [Z_{trench}, Z_{max}]$. In subsequent plots of the PDFs for Z_{top} and Z_{bottom}, we also show its values zoomed in over this interval. The area of Z_{top} PDF above trench depth (Z_{min}) is equal to the probability of the model to be coupled up to trench depths. Equivalently, the area of Z_{bottom} PDF below Z_{max} depth corresponds to the probability of a plate interface coupled up to the maximum allowed depth.

In order to test the ability of the model and the set of observations to resolve coupling along different regions of the plate interface, we perform a series of inversion tests with synthetic datasets using the location and uncertainties of the GPS observations used later in this work to infer a posteriori estimates of apparent coupling in the Central Andes. We computed synthetic observations for a plate interface coupled from trench up to 50 km depth and uncoupled below (Figure 5.7a) and for

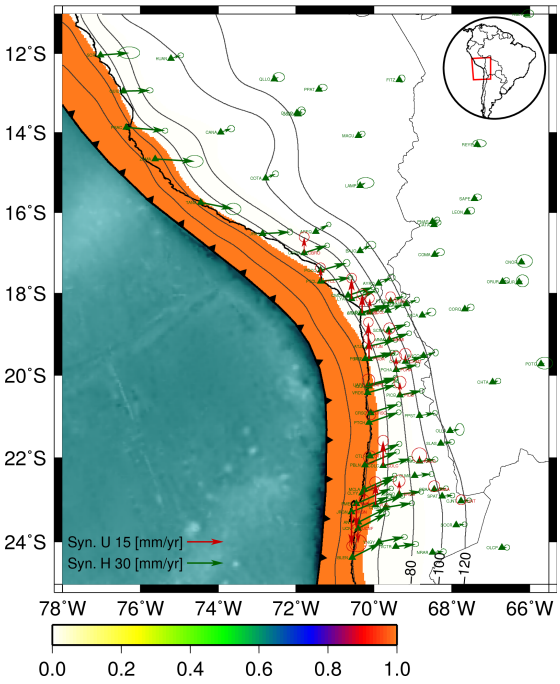

(a) Synthetic Apparent Coupling

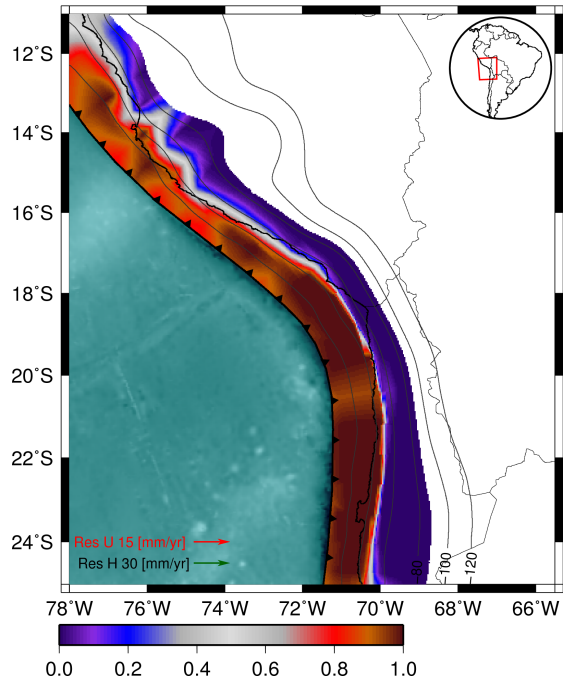

(b) Apparent Coupling Probability from data in (a)

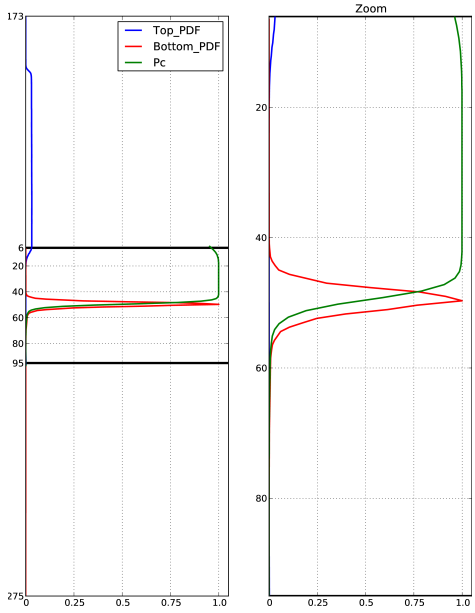

(c) PDFs (Lon=72W,Lat=18S)

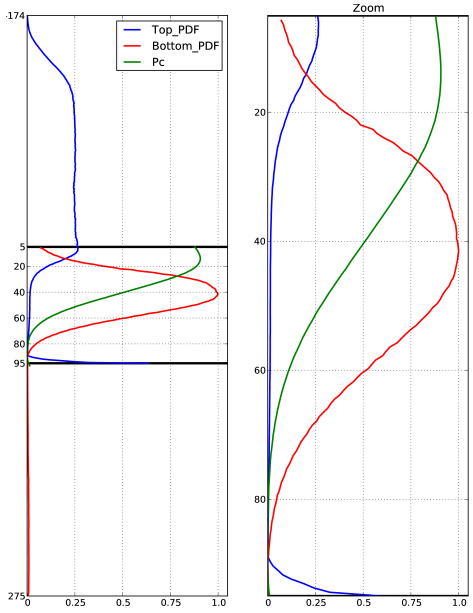

(d) PDFs (Lon=75W, Lat=16S)

Figure 5.7. Results for inversion with synthetic observations generated using a plate interface coupled from trench up to 50 km depth (a). Estimates of apparent coupling probability (P_c) are shown in (b) as well as the coupled zone boundaries PDFs for 2 trench perpendicular cross sections (c, d). Note how coupled and uncoupled regions are interpreted to have very high and low Pc, respectively. Also, the lower boundary of the coupled zone is better resolved than the upper one since its PDF is narrower (c, d).

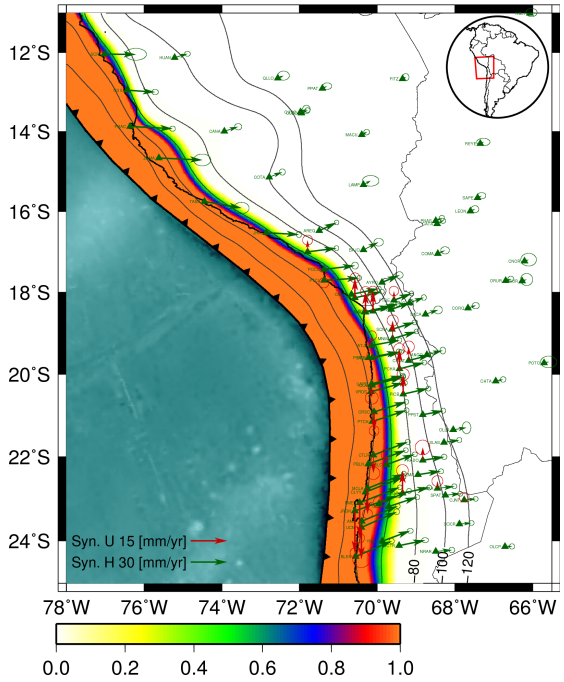

(a) Synthetic Apparent Coupling

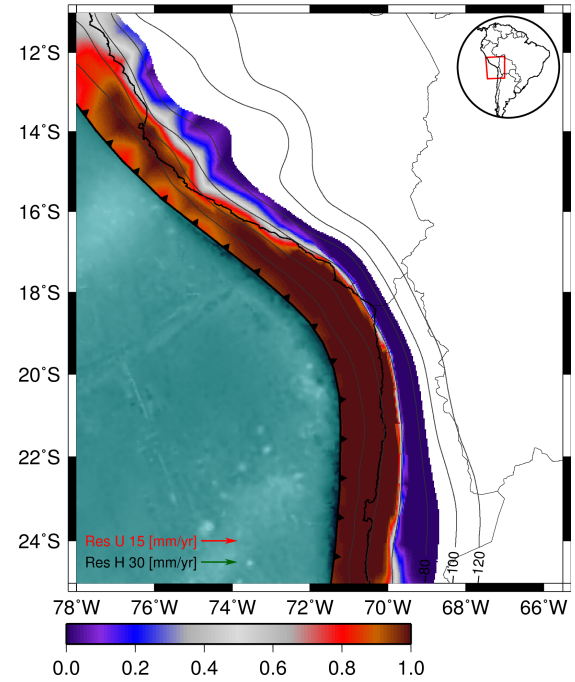

(b) Apparent Coupling Probability from data in (a)

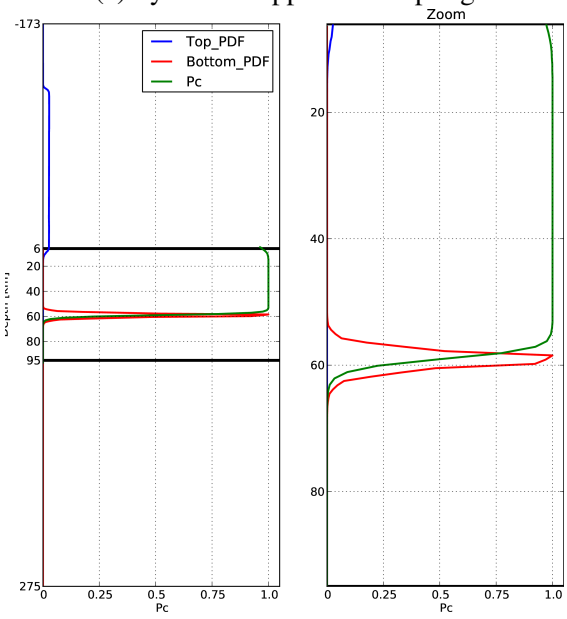

(c) PDFs (Lon=72W,Lat=18S)

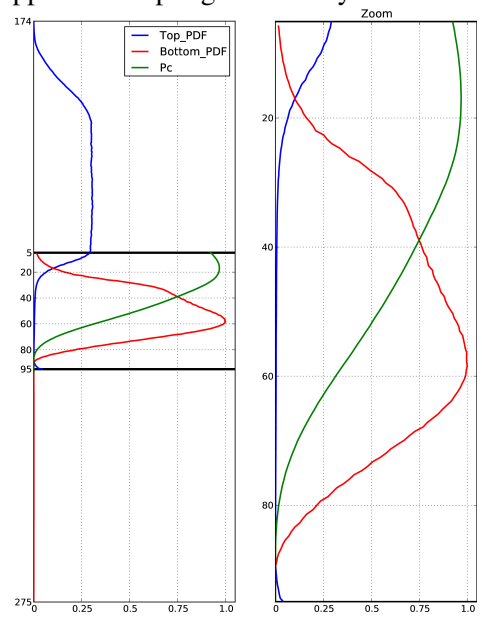

(d) PDFs (Lon=75W, Lat=16S)

Figure 5.8. Results for inversion with synthetic observations generated using a plate interface coupled from trench up to 50 km with a linear transition to 70 km depth (a). Estimates of apparent coupling probability (P_c) are shown in (b) as well as the coupled zone boundaries PDFs for 2 trench perpendicular cross sections (c, d). Note how coupled and uncoupled regions are interpreted to have very high and low Pc, respectively. Also the lower boundary of the coupled zone is much better resolved than the upper one since its PDF is narrower (c, d). Note that P_c remains high until the middle of the transition zone considered when calculating the synthetic observations, as the model parameterization does not allow partial coupling.

a similar case with a linear transition zone from coupled at 50 km to uncoupled at 70 km depth and below (Figure 5.8a). We add a Gaussian random noise to both datasets based on the observational uncertainties. As proposed by *Bevis and Martel* (2001), both cases of synthetic observations show that the obliquity of the crustal velocity predictions is greater than the one of the plate convergence direction for the coastal sites and it rotates towards a trench perpendicular direction as their location moves away from the trench.

The inversion results for the first synthetic data (Figure 5.7a) shows that the coupled and uncoupled regions can be identified by a high ($P_c > 0.75$) and low ($P_c < 0.25$) coupling probability, respectively. For the synthetic dataset where a transition zone is added a similar result is obtained but the down-dip limit of the coupled region is interpreted to be at the middle of the transition zone as a consequence of the parameterization not allowing partial coupling. In both cases, a direct inspection of the sampled PDFs reveals the known issue that the lower end of the coupled region is much better resolved than its upper boundary due to the lack of off-shore observations to constrain the model. The model is much better resolved at the regions where the spatial distribution of the stations is denser. Note that gray areas are less evident in such regions.

5.6 Results and discussion

We present *a posteriori* estimates of apparent coupling probability (P_c, Figure 5.9) constrained by the GPS velocities shown in Figures 5.1 and 2.23. Recall that wherever P_c is close to 0.5 (grayish color) it means that the model is poorly constrained in that region. When P_c is close to 0 it means that the probability for such point to be uncoupled (P_u) is close to 1 (5.9).

From a point of view of interpretation of the apparent coupling probabilities we recall that the physical model does not allow for partial coupling. Therefore, P_c must not be interpreted as the value of the coupling coefficient, except when $P_c \approx 1$ or $P_c \approx 0$ in which the patches showing such

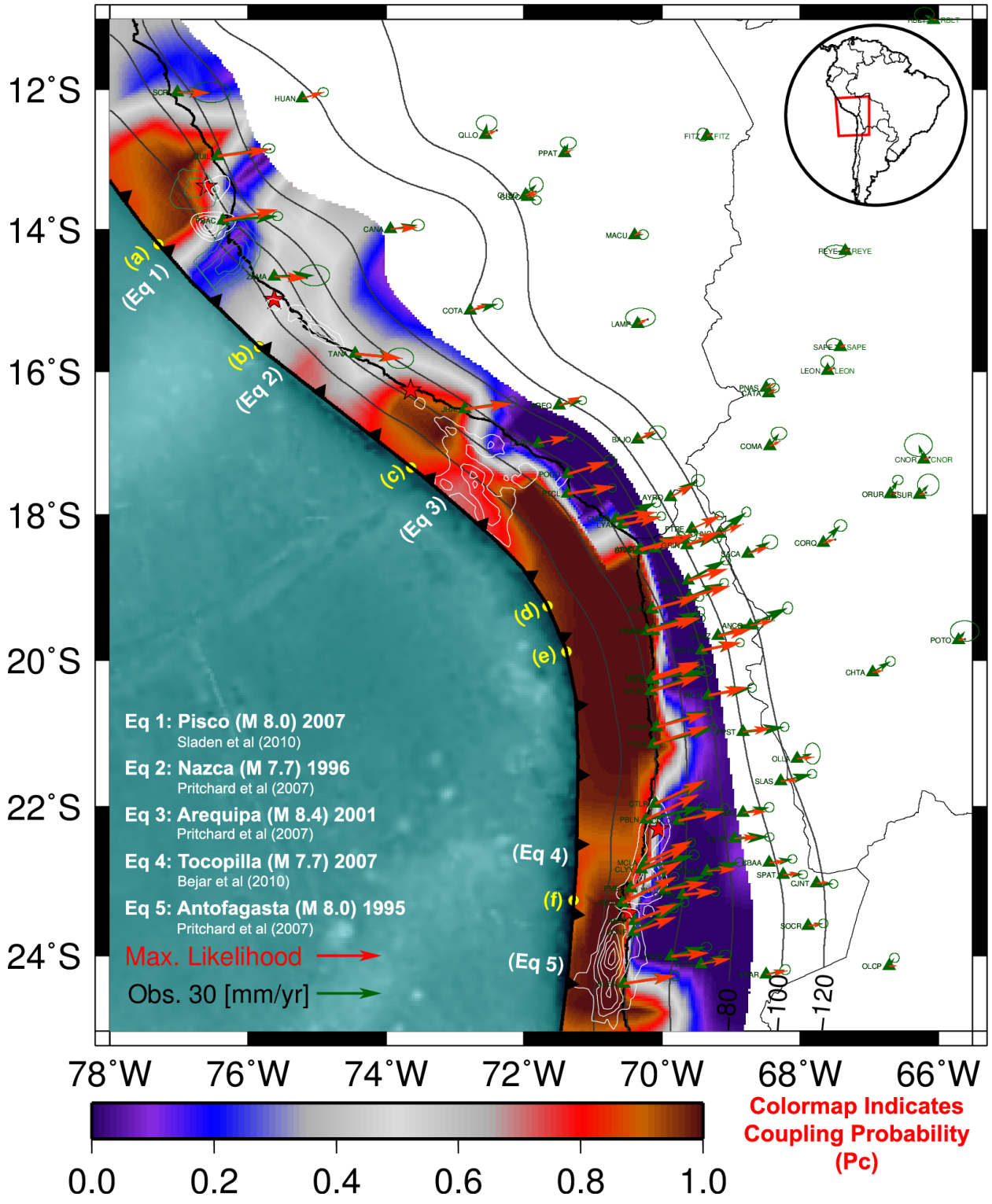

Figure 5.9. Estimates of a posteriori Pc constrained by the GPS velocities (green arrows, reference frame corrected by maximum likelihood Euler poles) along with GPS velocity predictions of the maximum likelihood model (red arrows). Yellow dots and letters at the trench indicate perpendicular sections shown in Figure 5.10, in which Z_{top} and Z_{bottom} PDFs and P_c are plotted for each section. White contours indicate co-seismic slip of large subduction earthquakes in the last century and green contours indicate post-seismic slip for Pisco (M_w8.0) 2007 earthquake from *Perfettini et al.* (2010).

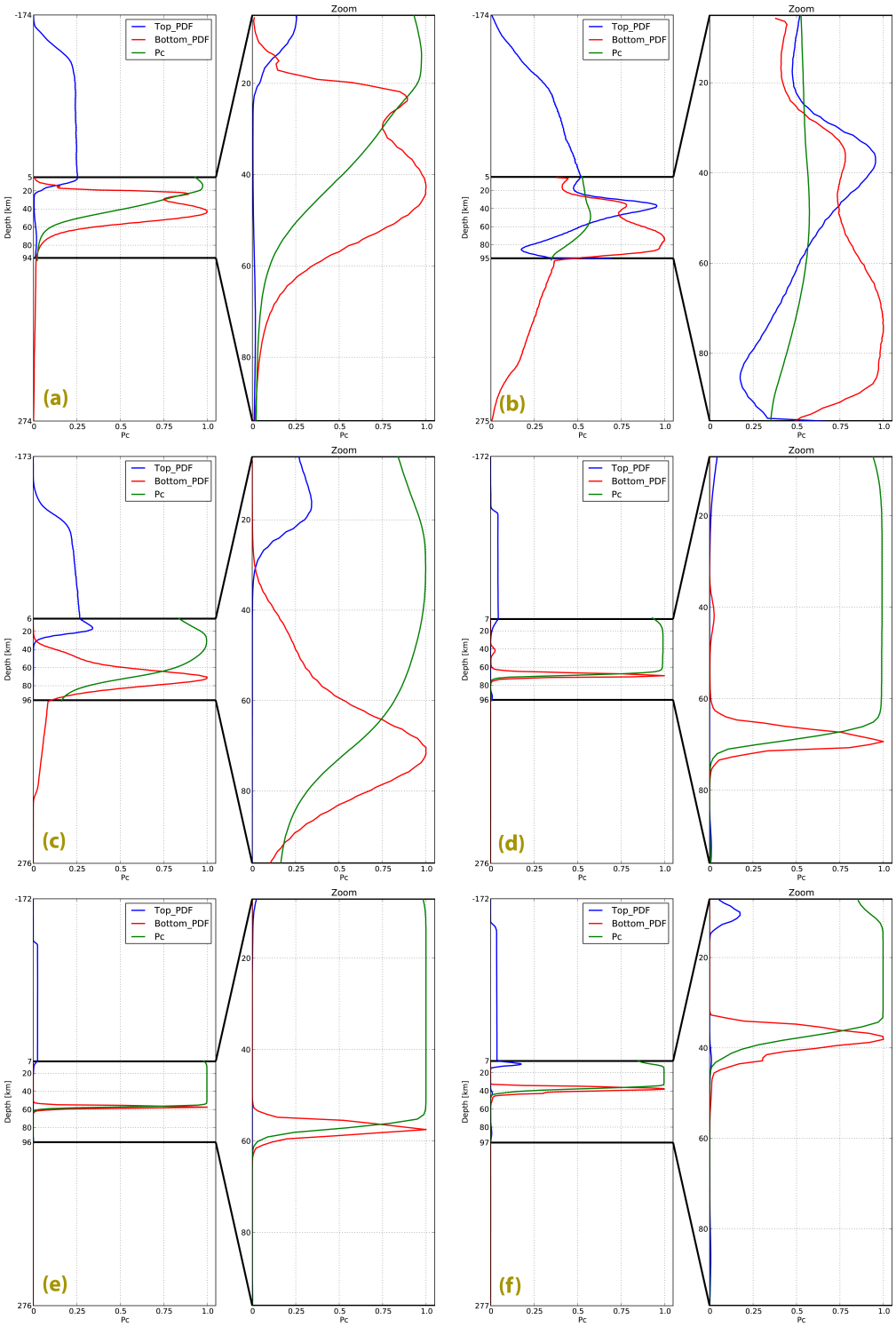

Figure 5.10. A posteriori P_c and Z_{top}, Z_{bottom} marginal PDFs for the trench perpendicular cross sections located at the yellow dots in Figure 5.9. Each panel shows the marginal PDFs over the whole sampling space accompanied by a zoomed plot on the right showing the fraction of the PDFs that lie in the region that is allowed to be coupled. The marginal PDFs are normalized, such that the area under the curves represent probabilities directly.

a behavior may be interpreted as coupled or uncoupled.

Figure 5.10 shows *a posteriori* estimates of the marginal PDFs for the boundaries of the coupled zone. Note how the PDFs for the down-dip limit (Z_{bottom}) are much more concentrated than the PDFs for the updip limit (Z_{top}) denoting the stronger constraint that onland observations impose on the downdip boundary of the coupled zone. With the exception of profile (b), we observe that the boundaries of the coupled zone are very well constrained, being the down-dip limit located at depths coincident with the vertical projection of the coastline and the up-dip limit to be shallower than 20 km depth. Instead, profile (b) shows *a posteriori* marginal PDFs that are very similiar to the *a priori* ones, meaning that the model is not well constrained by the observations or it is inconsistent with the mechanics governing the observations in such region.

We observe in Figure 5.9 a spatially heterogeneous pattern for P_c in which the higher anomalies ($P_c > 0.75$) are mainly located off-shore and shallower than 40 - 60 km depth. If we interpret these regions with high apparent coupling probability as fully coupled ($C_S = 1.0$), our results are in agreement with the findings of *Béjar-Pizarro et al.* (2013) in a inter-plate coupling study based on space geodesy in the North Chile subduction zone, and with the conclusions of *Tichelaar and Ruff* (1993) in a study that characterized the maximum locking depth of the subduction interface by an analysis of the seismicity of the region. As shown in the inversion of synthetic data, these areas with high P_c may include part of the brittle ductile transition zone at the down-dip extent of the coupled zone.

Figure 5.9 shows a comparison between our inferences of apparent coupling (P_c) and estimates of co-seismic rupture extent associated with past earthquakes in the region (*Pritchard et al.*, 2007; *Sladen et al.*, 2010; *Béjar-Pizarro et al.*, 2010). We observe that regions with high coupling probability can not be directly interpreted as the configuration of asperities or co-seismic slip regions. As shown in Figure 5.9, earthquakes may rupture areas characterized by high apparent coupling, or

these may well occur between the inferred coupled and uncoupled regions of the megathrust (e.g., Tocopilla earthquake, *Béjar-Pizarro et al.* (2010)). The Pisco ($M_w 8.0$) 2007 earthquake suggest an anti-correlated relation between P_c and the inferred co-seismic slip in which their rupture areas are enclosed by either regions with very high P_c (interpreted as coupled) and/or very low P_c (interpreted as uncoupled). The Arequipa ($M_w 8.4$) 2001 shows a similar anti-correlation but with regions with distinct values of high apparent coupling probability. In the other hand, the Antofagasta ($M_w 8.0$) 1995 earthquake ruptured entirely in a region predicted to have a high apparent coupling probability.

The 2007 ($M_w 7.7$) Tocopilla earthquake occurs at the down-dip end of the region identified as coupled based on P_c values, which might be identified as a region where a transition between brittle and ductile behavior is occurring from our inversion results using synthetic data (see Figure 5.8). The 2007 earthquake rupture area extends only below 30 km depth, with the exception of its southern extent, where co-seismic slip seems to have propagated up to 25 km depth, beneath Mejillones peninsula (*Béjar-Pizarro et al.*, 2010). Previous work on the region of the Tocopilla earthquake locate the lower end of the seismogenic zone at around 50 km depth, using seismicity– *Tichelaar and Ruff* (1991); *Suárez and Comte* (1993); *Comte and Suárez* (1995); *Delouis et al.* (1996)– and using coupling models inferred from space geodesy–*Bevis et al.* (2001); *Khazaradze and Klotz* (2003); *Chlieh et al.* (2004, 2011); *Béjar-Pizarro et al.* (2013). Our results shows that in the region of the Tocopilla earthquake the apparent coupling probability remains high up to 40 km depth with a very precise location of its down-dip boundary (Figure 5.10). The location of the down-dip limit of coupling can be biased by the existence of a transition zone for coupling, locating it near the middle of the transition zone if such coupling transition is assumed to be linear (Figure 5.8). *Béjar-Pizarro et al.* (2010) interpret the 30 km depth limit as a change in the frictional properties of the plate interface separating the shallower seismogenic zone with potentially larger asperities from a deeper region characterized by a more heterogeneous slip behavior. Also, *Contreras-Reyes*

et al. (2012) identified an abrupt change in the angle of subduction of the Nazca plate at $\sim$ 20 km depth, relating it to an along dip segmentation of the subduction megathrust, which might have arrested the updip propagation of the Tocopilla earthquake. Therefore our coupling inferences may well correspond to a fully coupled plate interface up to $\sim$ 30 km depth followed in depth by a brittle-ductile transition zone up to ~ 50 km depth.

The 2001 ($M_w 8.4$) Arequipa earthquake occurs in a region where the geodetic observations used to derive our inferences of apparent coupling were made before the occurrence of the earthquake. Thus, our estimates of coupling reflect the state of stress during the last part of the seismic cycle on the segment of the megathrust affected by the 2001 event. If we interpret as fully coupled ($C_s = 1.0$) any region inferred with $P_c > 0.75$, it follows that the Arequipa earthquake rupture occurs entirely in within a region that is strongly coupled. Although there have been observations of earthquakes partially rupturing a coupled region (e.g., *Konca et al.*, 2008), stalling of the rupture process in its southern extent can not be explained by the coupling model as interpreted.

Imaging of the rupture process of the Arequipa earthquake based on seismic and geodetic observations (e.g., *Giovanni et al.*, 2002; *Bilek and Ruff*, 2002; *Pritchard et al.*, 2007) locate most of the moment release where our modeling indicates an apparent coupling probability of $P_c \approx 0.8$. Also, the rupture of the Arequipa earthquake is surrounded by regions with $P_c \approx 1.0$ and only a small fraction of the moment released by the earthquake (at the beginning of the rupture process) occurs at areas with $P_c \approx 1.0$. In particular we could explain the southern termination of the earthquake if we associate the lower coupling probability ($P_c \approx 0.8$) in the region which experienced large slip during the Arequipa earthquake with a small decrease in the actual coupling coefficient. Under this assumption, the higher coupling probability located southeast of the Arequipa earthquake source area marks the presence of a stronger asperity that remains unbroken under the shear stress increase produced by the propagating rupture and where two large aftershocks, ($M_w 6.7$ and $M_w 7.7$) occur

lately (*Pritchard et al.*, 2007, and references therein). Nevertheless, we need to justify the inferences of smaller coupling coefficient within the context of a coupling model which does not allow partial coupling.

Based on our analysis of *a priori* information on the up-dip limit of the coupled zone (see Figure 5.5) and inspection of the *a posteriori* marginal PDFs for the up-dip boundary of the coupled zone Z_{top} near the Arequipa earthquake (see c and d boxes in Figure 5.10), we can deduce that the coupling model is well constrained in such regions by the available geodetic data. Now, given that our model does not allow partial coupling, we may attribute variations on our inferences of coupling probability to variations on the consistency of the model with the observables. The inconsistencies of the model that causes the decrease in the estimated coupling probability could be related and not limited to localized deviations from the assumed elastic structure of the media, or heterogeneities in the frictional properties defining the mechanical behavior of the subduction megathrust. If we assume the latter case, we could interpret the variations of P_c between 0.8 and 1.0 as variations in the degree of coupling on the Arequipa earthquake segment of the Nz-Sa subduction megathrust.

Spatial variations in the degree of coupling can be ultimately translated into differences in fault steady state shear frictional strengths. Thus, meaning that the regions of the megathrust where large amplitudes of slip occurred during the Arequipa earthquake has on average less strength than the surrounding fully locked areas. The region of slightly weaker coupling coincides with the subduction of the Nazca Fracture Zone beneath South America. The Arequipa earthquake hypocenter is located down-dip of the northernmost asperity. Analysis of teleseismic body waves reveals that rupture evolves with a small moment release at the beginning of the rupture, followed by a quiescence period to then release more than $2/3$ of the total moment during the last phase of the rupture process (*Giovanni et al.*, 2002). The time evolution of the rupture process is consistent with the spatial distribution of co-seismic slip obtained from joint inversion of seismic and geodetic data (*Pritchard*

et al., 2007) (Figure 5.9, white 4 m contours). Here, we propose that the asperities (stronger regions) surrounding the areas that slipped co-seismically during the Arequipa earthquake, pinned the region of the megathrust in between until the 2001 event started rupturing the northernmost asperity and dynamic stresses induced by the first sequence of the rupture triggered the rupture process at the weaker, less coupled, region where the largest portion of the moment was released.

The region of the Nz-Sa plate interface located between the epicenter of the 2001 ($M_w 8.4$) Arequipa earthquake and the subducting Nazca Ridge is inferred to have a probability of apparent coupling $P_c \approx 0.5$. As discussed before, this value of P_c corresponds to our *a priori* state of information (compare PDFs of Figure 5.10b with the *a priori* PDFs in Figure 5.6). Thus, we can not deduce any interpretation on the actual coupling state. $P_c \approx 0.5$ may be caused by partial coupling in the region, as this region has been previously identified as partially coupled in previous studies (e.g., *Chlieh et al.*, 2011). Nevertheless this area has experienced large earthquakes, 1996 $M_w 7.7$ and 1942 $M_w \sim 8.2$ earthquakes whose ruptured asperities may be associated with the subduction of the Nazca Ridge (e.g., *Dorbath et al.*, 1990; *Chatelain et al.*, 1997; *Giovanni et al.*, 2002). The oblique subduction of the Nazca Ridge may influence the inter-seismic rates used in this study, which could lead to inconsistencies in the model as we represent the Nz-Sa plate interface with a smoothed geometry. Thus, leading to estimates of coupling probability that are close to the *a priori* values.

The 2007 ($M_w 8.0$) Pisco earthquake occurs north of the Nazca Ridge and ruptured 2 asperities located in between regions of high ($Pc > 0.9$) and low ($Pc < 0.2$) probability of coupling (Figure 5.9, *Sladen et al.*, 2010; *Perfettini et al.*, 2010) . Given the along dip orientation of this region of transition from low to high P_c, we assume that such region appears as an artifact due to the averaging scale of coupling imposed by the model parameterization (~ 75 km). Thus, we infer that the asperities ruptured during the Pisco earthquake are associated with the coupled patch inferred

just northwest of the Pisco earthquake. The 2007 event triggered aseismic frictional after-slip in two adjacent regions of the plate interface. The region with largest after-slip remarkably coincides with a patch we infer to be uncoupled on the western flank of the subducted Nazca Ridge. Thus, the west flank of the Nazca Ridge may present aseismic behavior throughout the seismic cycle, possibly caused by changes in the stress regime due to eastward oblique subduction of the range. The smaller post-seismic after-slip patch is located next to the 2 asperities that ruptured during the Pisco earthquake in a region inferred to be coupled by our modeling. Stress shadows associated with the Pisco earthquake asperities may cause that the aseismic region in question to appear as coupled before the Pisco earthquake occurrence (*Hetland and Simons*, 2010).

The largest region inferred as coupled by our modeling coincides with the Arica bend seismic gap, which extends from Mejillones peninsula in Chile, to the city of Ilo in Perú. This large homogeneously strongly coupled segment may be the consequence of the subduction of the Iquique Ridge under South America (*Contreras-Reyes and Carrizo*, 2011). This segment has not experienced a large earthquake since the 1868 ($M_w \approx 8.5 - 8.8$) earthquake in Southern Perú and the 1877 ($M_w \approx 8.7 - 8.8$) (*Dorbath et al.*, 1990; *Comte and Pardo*, 1991). With the aim of providing information for future earthquake hazard studies in the region, we are particularly interested in estimating the extent of the rupture of a future earthquake in the Arica bend seismic gap. We could postulate a possible earthquake that ruptures the whole region identified as coupled, from ~ 22.5S to the southern limit of the co-seismic rupture of the Arequipa earthquake as our coupling model does not give any evidence of segmentation of the subduction megathrust. Nevertheless, we would like to explore the possibility of seismic segmentation within the seismic gap, especially because the 1877 earthquake in northern Chile did not ruptured the whole seismic gap and may have stalled just south of the Arica bend (*Comte and Pardo*, 1991).

Previous studies proposed that topographic and bathymetric features may influence the rupture

extent of large subduction earthquakes (e.g., *Contreras-Reyes and Carrizo*, 2011; *Béjar-Pizarro et al.*, 2013; *Baker et al.*, 2013). While subducting bathymetric features may affect the state of stress at the plate interface and therefore the state of coupling, topographic features may be the consequence of long-lasting heterogeneous spatial distribution of frictional properties at the subduction megathrust. Among examples of such features are the Mejillones peninsula, which coincides with northern and southern limits of the rupture areas of the Antofagasta ($M_w 8.1$) 1995, and Tocopilla ($M_w 7.7$) 2007 earthquakes; the subduction of the Iquique ridge and the Nazca fracture zone which apparently limited the extent of the Arequipa ($M_w 8.4$) 2001 earthquake; and the subduction of the Nazca ridge just south of the source region of the Pisco ($M_w 8.0$) earthquake.

We explore the role potentially played by the Arica bend in seismic segmentation of the seismic gap. For that purpose, we use catalogs of historical large ($M_w > 7.0 - 8.0$) earthquakes with estimates of their trench parallel rupture extent based on local intensities estimated from historical documents (*Dorbath et al.*, 1990; *Comte and Pardo*, 1991, and references therein). We recognize that the extent of the historical events may contain large errors that may come from site effects at the locations where intensities are estimated. The historical events north and south of the Arica bend show a rather unpredictable behavior of the termination of the rupture zone that is closer to the bend, where seismic rupture of some large ($M > 8$) earthquakes seems to occur across the bend and sometimes stall when approaching it, with some smaller ($M > 7$) events occurring just south or north of the bend. Although not incorporating the geometric complexity, a somewhat similar behavior is observed by *Kaneko et al.* (2010) in a study of numerical dynamic simulations of spontaneous seismic and aseismic slip using a simplified subduction-like model that implements an aging rate and state frictional rheology in planar fault where two coupled (velocity weakening) fault segments surround a small aseismic (velocity strengthening) segment between them. Moreover, regional seismic catalogs show a smaller amount of seismicity in the region of the Arica bend

(*David*, 2007). Therefore, suggesting that the region of the megathrust located in the vicinity of the symmetry axis of the Arica bend may have a much smaller degree of coupling . If such region is small enough, stress shadows from fully coupled asperities north and south of the Arica bend, will result in apparent coupling inferences that show the Arica bend to be fully coupled.

Chapter 6

Summary

During the course of my thesis I analyzed geodetic measurements of crustal deformation (GPS positional time series) to infer distributions of fault slip behavior associated with aseismic sources in subduction zone megathrust, with the eventual goal of understanding the mechanical behavior of the subduction interface between large earthquake occurrence, its relationship with fault slip behavior during such earthquakes and implications for earthquake and tsunami hazard. I addressed the underlying estimation problem using both a fully Bayesian and a regularized optimization approach, exploring the benefits and limitations of such methodologies. For the optimization approach, I develop a novel method of regularization that accounts for the spatial variability of fault slip sensitivity to observations, and presented a unified representation and interpretation of the regularization technique under a more general Bayesian framework.

During the development of the theory for sensitivity regularization, I explored different definitions of a "simple" slip model that are often used as *a priori* information and concluded that any measure of simplicity that relies on the knowledge of absolute *a priori* values of slip must be avoided (normally it is assumed that the *a priori* value of slip is zero) as it biases the inferred slip distribution towards the *a priori* absolute values of slip and also introduces artifacts due to inconsistencies between the *a priori* values and the regularization scheme. We propose the use of a sensitivity modulated smoothing regularization based on minimization of the norm of the second

spatial differential of slip in which we choose an *a priori* information on slip that is consistent with such regularization, a constant slip model in which the value of the constant is unknown. In the future, it may be fruitful to expand the sensitivity modulated approach to more general problems related to geophysics, other than static fault slip estimation. For example, in a kinematic finite fault slip inversion, or its application to the problem of estimation of a 3D velocity field from multiple InSAR observations taken from various vantage points.

I applied the sensitivity regularization scheme to obtain estimates of after-slip induced by the Tohoku-Oki ($M_w 9.0$) earthquake in Japan, finding robust estimates of fault after-slip that are remarkably detailed for a slip inversion with a smoothing constraint. The results suggest that the Japan megathrust has highly heterogeneous material properties. Future work should apply the sensitivity-based regularization methodology and/or Bayesian inversion methods to obtain estimates of inter-seismic coupling to enable consistent interpretation of fault slip during the different phases of the seismic cycle.

I applied a fully Bayesian approach to obtain estimates of inter-plate coupling in the Central Andes subduction megathrust. The ensemble of solutions is represented as a distribution of apparent coupling probability in the Nz-Sa plate interface. A comparison between coupling inferences and the co- and post-seismic slip associated with past earthquakes in the region reveals that variations on the degree of coupling may be related to seismic segmentation in the subduction megathrust, as well as that earthquake occurrence may not always occur at the strongest coupled regions of the fault, but may also occur in regions that are inferred to release some slip aseismically. In particular, the region associated with the Arica bend seismic gap, which has not experienced a large earthquake since 1877, is inferred to be fully coupled from trench depth to $\sim 40-50$ km depth, with no apparent along strike variations in apparent coupling probability. Nevertheless, the along strike discretization of coupling parameterization is about 75 km. Thus, coupling inferences may be missing small scale

variations in the degree of coupling which are averaged by the model and those possible missing variations of coupling may influence seismic segmentation in the region. Although, it is not clear that using a parameterization with a finer spatial discretization will reveal such changes as a small region with lower degree of coupling will be masked out by stress shadows from the surrounding regions with higher degree of coupling near the end of the seismic cycle, as is believed to be the case for the Arica bend seismic gap. As shown in Chapter 5, the simple model parameterization used to obtain apparent coupling probability (P_c) estimates, a model that does not allow for partial coupling and that imposes a strong depth-dependent correlation of coupling, tends to overestimate P_c at the shallow-most portions of the megathrust which are less constrained by onland observations of inter-seismic crustal deformation rates. During the realization of this thesis, improved methodologies that allows us to solve larger inverse problems using a full Bayesian framework became available (e.g., *Minson et al.*, 2013), ameliorating the need of an overly simplified model to be able to solve the inverse problem using a full Bayesian framework. Therefore, for future work, I would recommend these improved methodologies to solve the fully Bayesian inversion problem and to parameterize apparent coupling in faults allowing for partial coupling, in a similar manner as slip is parameterized to solve the co-seismic slip estimation problem (e.g., *Simons et al.*, 2011). Here, apparent coupling would be allowed to vary spatially over the fault without imposing *a priori* spatial correlation lengths for the apparent coupling. Thus, avoiding the caveats that arise with the overly simplified physics, and also allowing us to obtain, for example, more direct interpretations of the variations of apparent coupling and possibly to obtain a better relationship between coupling and seismic segmentation without requiring several assumptions that were needed in this work to infer small variations in the degree of coupling based in a model that only allows 2 states of coupling on a fault patch, either fully coupled or uncoupled.

Estimates of distributions of slip behavior representing aseismic processes in the subduction

megathrust can be constrained by the use of geodetic measurements. Currently such measurements are systematically obtained only onland, which limits the spatial resolution of the inferred slip in the shallow-most portions of the subduction megathrust, generally located at great distances from the coast. In Chapter 3 of my thesis I proposed a novel regularization scheme that stabilizes the slip estimates at the shallow-most portions of the megathrust and allows us to obtain more detailed slip distributions at the better resolved areas of the fault (closer to the coast). Nevertheless, such stability is achieved by imposing a large correlation length at the less constrained regions of the megathrust, which decreases the spatial resolution of the slip distribution on such regions. In the study of post-seismic deformation after the Tohoku-Oki ($M_w 9.0$) earthquake, I relied on the location of repeater earthquakes at the shallow-most portion of the megathrust to partially overcome the afterslip low spatial resolution problem and complement our inferences that suggest aseismic behavior on such region. Given the relevance of shallow megathrust offshore events especially for tsunami hazard, a better understanding of the mechanical behavior of the shallow portions of the megathrust is required. Such understanding can only be achieved by direct and systematic measurements of seafloor deformation above the offshore portion of the subduction megathrust. At the present, offshore seafloor geodetic measurements are the only capable of constraining with more precision the behavior of the shallow-most portion of the megathrust. Therefore, the scientific community and funding agencies need to promote the systematic and dense realization of such measurements, especially in regions such as the Japan megathrust in which the offshore portion of the megathrust extends several hundred kilometers from the coast.

Appendix A

The Smoothing Regularization Constraint

We solve the damped least squares problem[†],

$$\min_{\mathbf{m}} \left\{ (\mathbf{Gm} - \mathbf{d}_{obs})^T \mathbf{W}_\chi (\mathbf{Gm} - \mathbf{d}_{obs}) + \varepsilon^2 (\mathbf{m} - \mathbf{m}^*)^T \mathbf{W}_m (\mathbf{m} - \mathbf{m}^*) \right\} \tag{A.1}$$

with family of solutions and associated *a posteriori* covariance matrix,

$$\mathbf{m}_{est}(\varepsilon) = \left(\mathbf{G}^T \mathbf{W}_\chi \mathbf{G} + \varepsilon^2 \mathbf{W}_m \right)^{-1} \left(\mathbf{G}^T \mathbf{W}_\chi \mathbf{d}_{obs} + \varepsilon^2 \mathbf{W}_m \mathbf{m}^* \right) \tag{A.2}$$

$$\widetilde{\mathbf{C}}_m(\varepsilon) = \left(\mathbf{G}^T \mathbf{W}_\chi \mathbf{G} + \varepsilon^2 \mathbf{W}_m \right)^{-1} \tag{A.3}$$

where $\mathbf{W}_\chi$ is the data weights matrix (assumed to be diagonal) defined as the inverse of the misfit covariance matrix, and $\mathbf{W}_m^{1/2} = \mathbf{W}_S \mathbf{T}$ is the weighted Laplacian regularization operator, where $\mathbf{T}$ is a finite difference approximation of the Laplacian operator ∇^2.

The problem can be expressed as the linear system,

$$\begin{bmatrix} \mathbf{W}_\chi^{1/2} \mathbf{G} \\ \varepsilon \mathbf{W}_S \mathbf{T} \end{bmatrix} \mathbf{m} = \begin{bmatrix} \mathbf{W}_\chi^{1/2} \mathbf{d} \\ \mathbf{0} \end{bmatrix} \tag{A.4}$$

[†]For the purposes of this appendix, we are ignoring the possible implementation of positivity constraints. Although their implementation should not change significantly the calculation of the weights, these are considered an approximation when positivity constraints are present due to the inability to directly compute an *a posteriori* covariance matrix of the model parameters.

In the following we show how $\mathbf{T}$ filters our slip models, as well as the effects of sensitivity modulated regularization.

We can rewrite our inverse problem using a Bayesian formulation as follows:

$$P(\mathbf{m}|\mathbf{d}) = \nu \cdot P(\mathbf{m}) \cdot L(\mathbf{d}|\mathbf{m}) \tag{A.5}$$

where $P(\mathbf{m}|\mathbf{d})$ is the a posteriori PDF of $\mathbf{m}$ given the observables $\mathbf{d}$, ν is a normalization constant, $L(\mathbf{d}|\mathbf{m}$ is the likelihood of the observables given the model $\mathbf{m}$ and $P(\mathbf{m})$ is the a priori information on the model parameters inferred by the regularization operator. For simplicity of the analysis, we disregard any effect of the model parameterization on $P(\mathbf{m})$ what is possible if we consider a fault discretization that is fine enough to avoid introducing a priori information on the slip distribution given by large fault patch sizes, and the modeled region of the megathrust is large enough to avoid boundary condition effects. We assume Gaussian uncertainties for the model parameters for consistency with the least squares solution of the problem.

In (A.4), the factor ε allows us to control the roughness of the solution $\mathbf{m}$,i.e., the relative error between the 2 equations . Then, in order to infer the a-priori variances on $\mathbf{m}$ imposed by the regularization, we solve the following least squares problem,

$$\mathbf{W}_S\mathbf{T}\mathbf{m} = \mathbf{r}(\varepsilon) \tag{A.6}$$

, where $\|\mathbf{r}(\varepsilon)\|_2$ is the allowed roughness of the solution (which is a function of ε). The number of triangular fault patches is n, so $dim(\mathbf{T}) = \{n \times n\}$. However, the regularization operator admits a constant solution for $\mathbf{m}$ in its null space, then the rank of $\mathbf{T}$ as defined for our fault slip models is $rank(\mathbf{T}_{n\times n}) = n - 1$, i.e., $dim(Ker(\mathbf{T}_{n\times n})) = 1$[†]. In other words, $\mathbf{T}$ has one zero singular

[†] For an irregular mesh $dim\{Ker(\mathbf{T})\} = 1$ (our case), but for a regular mesh the dimension of $Ker(\mathbf{T})$ will be larger than 1 since it will be exactly representing a discrete Laplacian operator. In any case, this will not affect the inversion process, but it needs to be considered when calculating the induced correlations as done in this appendix.

value. Now we can write the solution of (A.6) as $\mathbf{m}^* = \mathbf{m}_K + \widetilde{\mathbf{m}}$ where $\mathbf{m}_K \in < \{Ker(\mathbf{T})\} >$ and $\widetilde{\mathbf{m}} \in < \{\mathbf{T} \setminus Ker\{\mathbf{T}\}\} >$. For fairly irregular meshes (as in our case) $\mathbf{m}_K = c \cdot \mathbf{1}_{n\times 1} = c \cdot [1, \cdots, 1]^T =< \{Ker(\mathbf{T})\} >$, where $c \in I\!R$. Note that since the null space of $\mathbf{T}$ admits a constant solution, the regularization based on the Laplacian operator does not provide any constraint on the total amount of slip in the fault.

Now we need to find $\widetilde{\mathbf{m}}$. For the moment lets assume that $\mathbf{W}_S = \mathbf{I}_{n\times n}$ (the identity matrix) to check what is the effect on the solution of the regularization itself. Lets calculate $\mathbf{T} = \mathbf{U}\boldsymbol{\Sigma}\mathbf{V}^T$ the singular value decomposition of $\mathbf{T}$ to then compute the truncated decomposition in which $Ker(\mathbf{T})$ is removed: $\widetilde{\mathbf{T}} = \widetilde{\mathbf{U}}\widetilde{\boldsymbol{\Sigma}}\tilde{\mathbf{V}}^T$, then eq (A.6) becomes

$$\tilde{\mathbf{T}}\tilde{\mathbf{m}} = \mathbf{r}(\varepsilon) \tag{A.7}$$

with mean solution of the form :

$$\begin{aligned} \tilde{\mathbf{m}} &= (\tilde{\mathbf{T}}^T\tilde{\mathbf{T}})^{-1}\tilde{\mathbf{T}}^T\mathbf{r}(\varepsilon) \\ &= \tilde{\mathbf{V}}\tilde{\boldsymbol{\Sigma}}^{-1}\tilde{\mathbf{U}}^T\mathbf{r}(\varepsilon) \end{aligned} \tag{A.8}$$

and covariance matrix given by

$$\begin{aligned} \tilde{\mathbf{C}}_m &= (\tilde{\mathbf{T}}^T\tilde{\mathbf{T}})^{-1} \\ &= \tilde{\mathbf{V}}\tilde{\boldsymbol{\Sigma}}^{-2}\tilde{\mathbf{V}}^T \end{aligned} \tag{A.9}$$

Then the proposed regularization can be thought as an a priori Gaussian PDF on $\mathbf{m}$, with covariance matrix $\tilde{\mathbf{C}}_m$, on the deviations of $\mathbf{m}$ from a constant, unknown, slip distribution.

Now when using the sensitivity regularization, the regularization weights are given by $\mathbf{W}_S = \mathbf{S}^{-\frac{1}{2}}$. Each row of the matrix representation of the regularization operator is multiplied with the

square root of the inverse of the sensitivity associated to such patch. The net effect of the weighting is that we augment the "correlation lengths" of the patches corresponding to the equations with higher weights. The weighting process does not affect the null space of $\mathbf{T}$. Now we can rewrite (A.7) as:

$$\mathbf{S}^{-\frac{1}{2}}\tilde{\mathbf{T}}\tilde{\mathbf{m}} = \mathbf{r}(\varepsilon) \tag{A.10}$$

with mean solution of the form :

$$\tilde{\mathbf{m}} \quad = \quad (\tilde{\mathbf{T}}^T\mathbf{S}^{-1}\tilde{\mathbf{T}})^{-1}\tilde{\mathbf{T}}^T\mathbf{S}^{-\frac{1}{2}}\mathbf{r}(\varepsilon) \tag{A.11}$$

and covariance matrix given by

$$\tilde{\mathbf{C}}_m \quad = \quad (\tilde{\mathbf{T}}^T\mathbf{S}^{-1}\tilde{\mathbf{T}})^{-1} \tag{A.12}$$

Here we observe that $\mathbf{S}^{-1}$ is modifying the relative orientations of the singular vectors of $\tilde{\mathbf{T}}$ (or the eigenvectors of $\tilde{\mathbf{T}}^T\tilde{\mathbf{T}}$) thus changing the covariance between the slip patches and also penalizing the allowed roughness $\mathbf{r}(\varepsilon)$ of the fault patches with lower sensitivity.

The effect of the smoothing regularization on the final solution can be obtained by computing the Pearson correlation matrix from the a posteriori covariance matrix of the inferred slip values. For that purpose we use the slip solutions of the synthetic inversion tests described in chapter 3 (Figure 3.6).

The a posteriori covariance matrix for the problem described in (A.4) is:

$$\mathbf{C}_m = \left(\mathbf{G}^T\mathbf{W}_\chi^T\mathbf{W}_\chi\mathbf{G} + \varepsilon^2\mathbf{T}^T\mathbf{W}_S^T\mathbf{W}_S\mathbf{T}\right)^{-1} \tag{A.13}$$

then the associated correlation matrix can be computed as

$$\rho_{ij} = \frac{C_{m_{ij}}}{\sqrt{C_{m_{ii}} C_{m_{jj}}}} \tag{A.14}$$

note that $\boldsymbol{\rho}$ depends on the damping parameter ε. In Figure A.1, we show for selected fault patches their *a posteriori* correlations with the rest of the fault surface (row of the correlation matrix). We use the optimal ε obtained during the inversion of synthetic data using both, the sensitivity modulated Laplacian regularization and the classical (uniformly weighted) Laplacian regularization. Note how the correlation length drastically augments as the patch in question is located at regions with lower sensitivity (increased regularization weights). The damping constant for the strike-slip regularization is set to be 200 times the one for dip-slip regularization, which translates into larger correlation lengths for strike-slip (Figure A.1c,d).

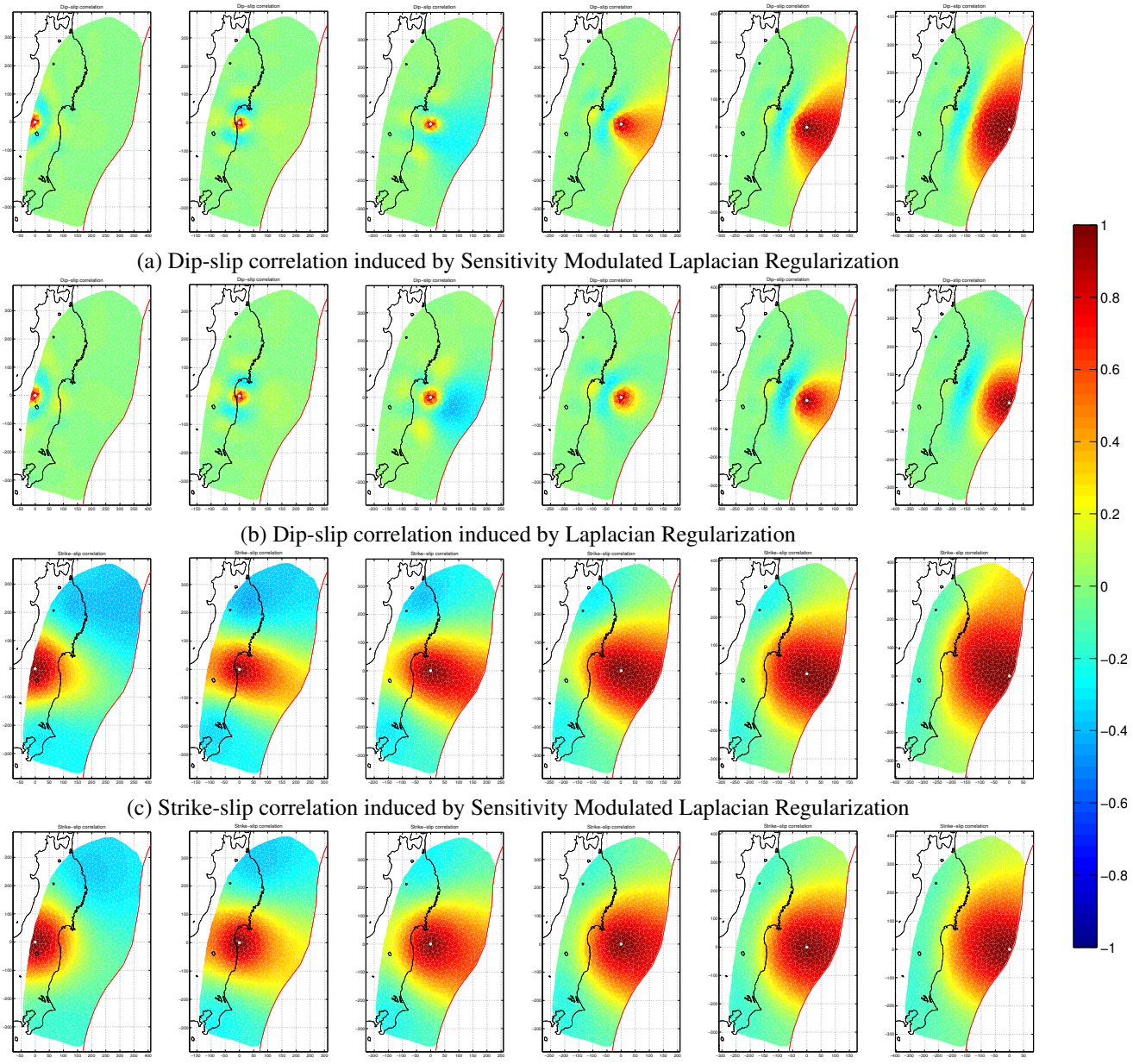

(a) Dip-slip correlation induced by Sensitivity Modulated Laplacian Regularization

(b) Dip-slip correlation induced by Laplacian Regularization

(c) Strike-slip correlation induced by Sensitivity Modulated Laplacian Regularization

(d) Strike-slip correlation induced by Laplacian Regularization

Figure A.1. Strike- and dip- slip a posteriori correlations induced by the Sensitivity Modulated Laplacian regularization (a,c) and uniform Laplacian regularization schemes (b, d). Colorbar indicates Pearson correlation coefficient. See text for explanation of the figure.

Appendix B

After-slip Inversion with a Different Regularization Scheme

In order to test the validity of the after-slip inferred off-shore Ibaraki in our model, we perform slip inversion tests with the observed post-seismic displacements up to September 20, 2012 using both the sensitivity modulated regularization and the minimum norm (order zero Tikhonov) regularization, which minimizes the amount of total inferred fault slip. We find the latter tends to avoid assigning slip at the less constrained regions of the fault surface. *Evans and Meade* (2012) shows similar results for the Tohoku-Oki earthquake slip distribution constrained by on-shore GPS data. Using a sparsity promoting method which minimizes the number of fault patches undergoing slip (through minimization of the slip L_1-norm), they obtain a co-seismic slip distribution that do not predict slip at regions near the trench where evidence suggest several tens of meters of co-seismic dislocation (e.g., *Simons et al.*, 2011; *Ito et al.*, 2011; *Sato et al.*, 2011; *Iinuma et al.*, 2012). We also find a systematic improvement on data fit when using the sensitivity regularization over using L_2-norm slip regularization in our after-slip inversion (Figure B.2). Thus, suggesting that the after-slip inferred by our model near the trench off-shore Ibaraki is actually needed to better explain the observables and not an artifact of the proposed regularization scheme. The comparison is made as explained in the following. Figure B.1 shows a family of solutions using the order zero Tikhonov regularization, in which we select 7 solutions from under damped to over damped, using the L-curve

selection criteria. Given the different regularization schemes used, we do not have a direct method to compare the solutions with the ones obtained for the sensitivity regularized inversion. Thus, in both cases we select 7 representative solutions from under damped to over damped and compare the misfits of these directly.

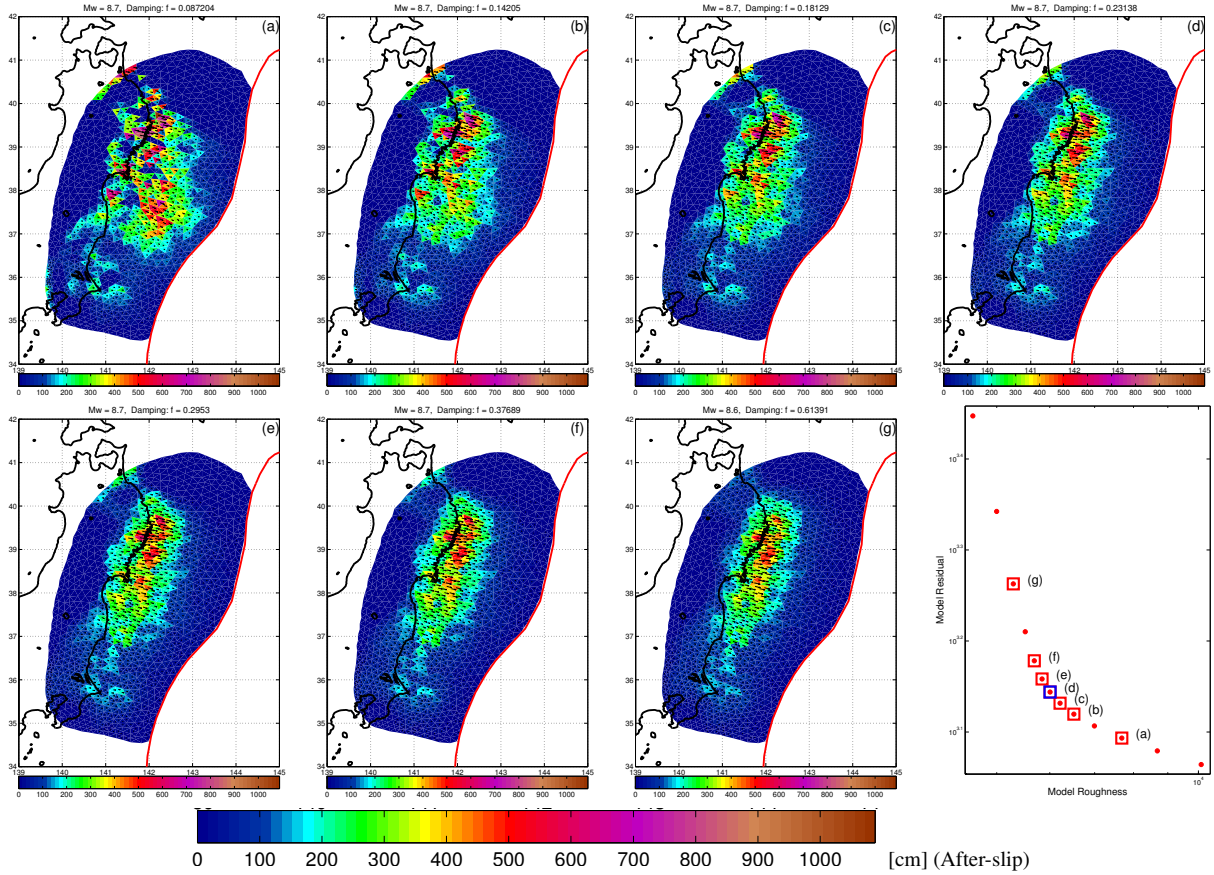

Figure B.1. Family of after-slip models inferred from the inland GPS post-seismic displacements between March 11, 2011 and September 22, 2012 . We show 7 models of after-slip in (a) through (g) sorted by the roughness of the model, being (a) the rougher one and (g) the smoother one. In (h) we shows the curve comparing the model misfit against its roughness in which red squares indicate the shown models of after-slip and the blue square indicates the model selected for further discussion in this study. Note how all the selected models share similarities in the sense that all of them predict high after-slip downdip of the source region of the Tohoku-oki mainshock and its Mw7.9 aftershock and after-slip located far off-shore, south of the region of the Tohoku-oki mainshock.

In order to test the significance of the observed systematic difference in the misfit for the inversions with both regularization schemes we estimate an upper bound on the error of the misfit (shown as error bars in Figure B.2). The estimation is done by using the triangular inequality. If ϵ is the

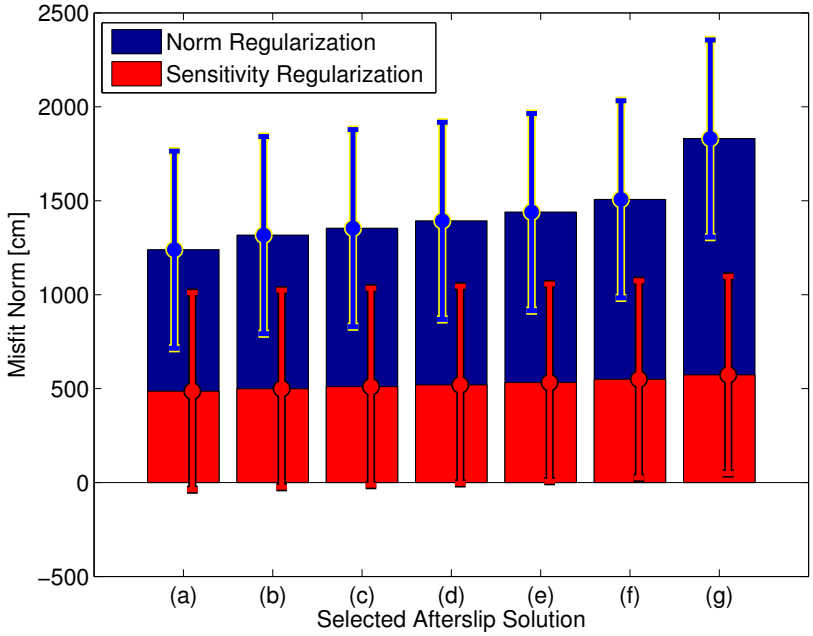

Figure B.2. Comparison of observational misfit between selected solutions obtaind using order zero Tikhonov regularization (blue) and the sensitivity modulated regularization (red) proposed in this study. Note the systematic difference in the misfits and that our methodology is able to consistently better explain the observations.

error in the calculation of the misfit we have

$$\|\mathbf{W}_\chi^{1/2}(\mathbf{Gm}-\mathbf{d}+\boldsymbol{\epsilon})\| \leq \|\mathbf{W}_\chi^{1/2}(\mathbf{Gm}-\mathbf{d})\| + \|\mathbf{W}_\chi^{1/2}\boldsymbol{\epsilon}\| \tag{B.1}$$

Now in order to find $\|\mathbf{W}_\chi^{1/2}\boldsymbol{\epsilon}\|$ we draw N realizations of it ($\boldsymbol{\epsilon}^*$) assuming each of its components follow a Normal PDF with 0 mean and 1 cm standard deviation. For each realization of the vector $\boldsymbol{\epsilon}^*$ we calculate the norm $\|\mathbf{W}_\chi^{1/2}\boldsymbol{\epsilon}^*\|$. Then we approximate the error of the misfit norm as,

$$\|\mathbf{W}_\chi^{1/2}\boldsymbol{\epsilon}\| \approx E^* + 2\sigma^* \tag{B.2}$$

where

$$E^* = \frac{1}{N}\sum_{i=1}^{N}\|\mathbf{W}_\chi^{1/2}\boldsymbol{\epsilon}_i^*\|, \quad \text{and} \quad \sigma^* = \sqrt{\frac{1}{N-1}\sum_{i=1}^{N}\left(\|\mathbf{W}_\chi^{1/2}\boldsymbol{\epsilon}_i^*\| - E^*\right)} \tag{B.3}$$

Then, the half length of the error bars is obtained from the estimation of $\|\mathbf{W}_\chi^{1/2}\boldsymbol{\epsilon}\|$ in Figure B.2.

Appendix C

Equations for Rigid Motion on the Sphere from Cox and Hart

To account for the variability in background plate velocity due to the plate interface extension, we calculate the plate kinematics using the Euler vector describing the relative motion between Nazca and South-American plates . Here we summarize the equations in *Cox and Hart* (1986) used to calculate the instantaneous local velocity $\mathbf{V} = (V_n, V_e, V_u)$ given the Euler vector $\mathbf{E}$ describing the plate motion and the point $\mathbf{P}$ where the velocity is being calculated. The local plate velocity in global coordinates can be defined as:

$$\mathbf{V} = \left(\omega\hat{\mathbf{E}}\right) \wedge (R_{\oplus}\mathbf{P}) \tag{C.1}$$

where ω is the amplitude of the plate's angular velocity (angle must be in radians), $\hat{\mathbf{E}}$ is the normalized Euler vector describing the plate motion, $R_{\oplus}$ is the radius of the earth (6370 km) and $\hat{\mathbf{P}}$ is the point (on a unit sphere) where the local plate velocity is being calculated. In an earth centered

coordinate system we have,

$$\hat{\mathbf{E}} = (E_x, E_y, E_z) \tag{C.2}$$

$$E_x = cos(\lambda_E)cos(\phi_E) \tag{C.2a}$$

$$E_y = cos(\lambda_E)sin(\phi_E) \tag{C.2b}$$

$$E_z = sin(\lambda_E) \tag{C.2c}$$

$$\hat{\mathbf{P}} = (P_x, P_y, P_z) \tag{C.3}$$

$$P_x = cos(\lambda_P)cos(\phi_P) \tag{C.3a}$$

$$P_y = cos(\lambda_P)sin(\phi_P) \tag{C.3b}$$

$$P_z = sin(\lambda_P) \tag{C.3c}$$

where λ_E, ϕ_E and λ_P, ϕ_P are the latitude and longitude of the Euler pole , and of the point on the surface of the spherical Earth. The local plate velocity in the Earth centered coordinate system can be calculated by replacing (C.2) and (C.3) into (C.1), obtaining

$$\mathbf{V} = \omega R_{\oplus} \hat{\boldsymbol{\nu}} \tag{C.4}$$

where,

$$\hat{\boldsymbol{\nu}} = (\nu_x, \nu_y, \nu_z) \tag{C.5}$$

$$\nu_x = E_y P_z - P_y E_z \tag{C.5a}$$

$$\nu_y = E_z P_x - P_z E_x \tag{C.5b}$$

$$\nu_z = E_x P_y - P_x E_y \tag{C.5c}$$

Now we need to transform the local plate velocities expressed in an Earth centered coordinate

system to a local coordinate system (North, East, Down) with origin at the point where the plate velocities are being calculated. The transformation is defined by the matrix $\mathbf{T}$, which defines a linear transformation between from (x,y,z) to (n,e,d) coordinate systems,

$$\mathbf{T} = \begin{bmatrix} T_{nx} & T_{ny} & T_{nz} \\ T_{ex} & T_{ey} & T_{ez} \\ T_{dx} & T_{dy} & T_{dz} \end{bmatrix} = \begin{bmatrix} -sin(\lambda_P)cos(\phi_P) & -sin(\lambda_P)sin(\phi_P) & cos(\lambda_P) \\ -sin(\phi_P) & cos(\phi_P) & 0 \\ -cos(\lambda_P)cos(\phi_P) & -cos(\lambda_P)sin(\phi_P) & -sin(\lambda_P) \end{bmatrix} \tag{C.6}$$

where each row correspont to the unit vectors defining the local reference frame $< \hat{\mathbf{n}}, \hat{\mathbf{e}}, \hat{\mathbf{d}} >$. Thus, the velocity in the local reference frame can be obtained as,

$$\mathbf{V}_{local} = [T] \cdot \mathbf{V}$$

Appendix D

An Interpretation of the Apparent Coupling Probability

The philosophy behind the work in Chapter 5 is to provide a robust Bayesian inverse methodology that allows us to overcome all the caveats inherent to classical optimization approaches in order to fully characterize the apparent coupling on the megathrust by sampling all the possible solutions of the inverse problem. We provide an interpretation of such ensemble of solutions in terms of the spatial distribution of the probability of apparent coupling. The ensemble of solutions (or its interpretation) may now be used in any subsequent geophysical or engineering application requiring a priori knowledge on the apparent plate coupling. Nevertheless, for those applications that need to use our estimates of apparent coupling to feed deterministic models, we propose an apparent coupling model that, while it is not a solution of the posed inverse problem, it explains the mean of the posterior estimates of the corrected crustal velocity field.

Recall that we are solving the linear problem

$$G \cdot m = d = d_{obs} - d_{rot} \tag{D.1}$$

where G is the matrix with the kernels that relate the apparent coupling with the GPS velocities, m ($m_i \in [0, 1]$) is the apparent coupling at each patch of the plate interface and d is the GPS velocities with the reference frame correction.

Instead of solving the linear system, we represent m using the coupling state Cs defined in eq (5.1), turning it into a non-linear inverse problem, but with a much lower number of parameters. Also, Cs imposes a correlation in depth for the apparent coupling and restricts its possible values to $m_i \in \{0, 1\}$. After sampling process, we ask what is the probability for a patch of the plate interface to have an apparent coupling equal to 1 ($P_C = P(m_i = 1)$).

Now let us forget about our nonlinear parameterization for m and focus on the samples obtained for m during the inversion. Let $\tilde{m} = \{\tilde{m}^{\{k\}}\}_{k=1}^{N_s}$ be the set of such samples (N_s is the number of samples).

Now, by observing our inversion results in figure (5.9), we can see that the mean posterior GPS velocity explain well the corrected GPS data. Now using the samples $\tilde{m}$ we would like to find an apparent coupling model that predicts the mean posterior predictions $\bar{d}$. We have,

$$\begin{aligned}
\bar{d_i} &= \frac{1}{N_s}\sum_{k=1}^{N_s} \tilde{d}_i^{\{k\}} \\
&= \frac{1}{N_s}\sum_{k=1}^{N_s} \left(G \cdot \tilde{m}^{\{k\}}\right)_i \\
&= \frac{1}{N_s}\sum_{k=1}^{N_s}\sum_{j=1}^{N_p} G_{ij}\tilde{m}_j^{\{k\}} \\
&= \sum_{j=1}^{N_p} G_{ij}\frac{1}{N_s}\sum_{k=1}^{N_s} \tilde{m}_j^{\{k\}}
\end{aligned} \tag{D.2}$$

recall that

$$P_c(m_j) = P(m_j = 1) = \frac{1}{N_s}\sum_{k=1}^{N_s} \tilde{m}_j^{\{k\}} \tag{D.3}$$

now by making the substitution,

$$\Rightarrow \bar{d}_i = \sum_{j=1}^{N_p} G_{ij} P_c(m_j)$$

$$\Rightarrow \bar{d} = G \cdot P_c(m) \tag{D.4}$$

Therefore, if we choose an apparent coupling distribution that has the same value as the probability of apparent coupling, the GPS velocity prediction is equal to the mean of the corrected a posteriori observations obtained during sampling. Further analysis is required to estimate the uncertainties of this particular spatial distribution of apparent coupling (recall that it is not a solution of the posed inverse problem), but such estimation is out of the scope of this work.

Bibliography

Abe, K. (1977), Tectonic implications of the large Shioya-Oki earthquakes of 1938, *Tectonophysics*, *41*(4), 269–289.

Akaike, H. (1974), A new look at the statistical model identification, *Automatic Control, IEEE Transactions on*, *19*(6), 716–723.

Aoki, Y., and C. H. Scholz (2003), Vertical deformation of the Japanese islands, 1996–1999, *Journal of Geophysical Research*, *108*(B5), 2257.

Argus, D. F., R. G. Gordon, M. B. Heflin, C. Ma, R. J. Eanes, P. Willis, W. R. Peltier, and S. E. Owen (2010), The angular velocities of the plates and the velocity of Earth's centre from space geodesy, *Geophysical Journal International*, *180*(3), 913–960.

Asano, Y., T. Saito, Y. Ito, K. Shiomi, H. Hirose, T. Matsumoto, S. Aoi, S. Hori, and S. Sekiguchi (2011), Spatial distribution and focal mechanisms of aftershocks of the 2011 off the Pacific coast of Tohoku earthquake, *Earth Planets and Space*, *63*(7), 669–673.

Aster, R. C., B. Borchers, and C. H. Thurber (2012), *Parameter estimation and inverse problems*, Elsevier.

Baba, T., K. Hirata, T. Hori, and H. Sakaguchi (2006), Offshore geodetic data conducive to the estimation of the afterslip distribution following the 2003 Tokachi-oki earthquake, *Earth And Planetary Science Letters*, *241*(1), 281–292.

Baker, A., R. W. Allmendinger, L. A. Owen, and J. A. Rech (2013), Permanent deformation caused by subduction earthquakes in northern Chile, *Nature Geoscience*.

Barnhart, W. D., and R. B. Lohman (2010), Automated fault model discretization for inversions for coseismic slip distributions, *Journal of Geophysical Research*, *115*(B10), B10,419.

Béjar-Pizarro, M., D. Carrizo, A. Socquet, R. Armijo, S. Barrientos, F. Bondoux, S. Bonvalot, J. Campos, D. Comte, and J. B. de Chabalier (2010), Asperities and barriers on the seismogenic zone in North Chile: stateâĂŘofâĂŘtheâĂŘart after the 2007 Mw 7.7 Tocopilla earthquake inferred by GPS and InSAR data, *Geophysical Journal International*, *183*(1), 390–406.

Béjar-Pizarro, M., A. Socquet, R. Armijo, D. Carrizo, J. Genrich, and M. Simons (2013), Andean structural control on interseismic coupling in the North Chile subduction zone, *Nature Geoscience*.

Bevis, M., and S. J. Martel (2001), Oblique plate convergence and interseismic strain accumulation, *Geochemistry Geophysics Geosystems*, *2*(8).

Bevis, M., E. C. Kendrick, R. Smalley, T. Herring, J. Godoy, and F. Galban (1999), Crustal motion north and south of the Arica deflection: Comparing recent geodetic results from the central Andes, *Geochemistry Geophysics Geosystems*, *1*(12).

Bevis, M., E. Kendrick, R. Smalley, B. Brooks, R. Allmendinger, and B. Isacks (2001), On the strength of interplate coupling and the rate of back arc convergence in the central Andes: An analysis of the interseismic velocity field, *Geochemistry Geophysics Geosystems*, *2*(11).

Bilek, S. L., and L. J. Ruff (2002), Analysis of the 23 June 2001 Mw= 8.4 Peru underthrusting earthquake and its aftershocks, *Geophysical Research Letters*, *29*(20), 1960.

Blewitt, G. (1997), Basics of the GPS technique: observation equations, *Geodetic applications of GPS*, pp. 10–54.

Blewitt, G. (2007), GPS and Space-Based Geodetic Methods, in *Treatise on Geophysics: Geodesy*, edited by T. A. Herring, pp. 351–390, Elsevier, New York.

Brooks, B. A., M. Bevis, R. Smalley, E. Kendrick, R. Manceda, E. Lauria, R. Maturana, and M. Araujo (2003), Crustal motion in the Southern Andes (26–36 S): Do the Andes behave like a microplate?, *Geochemistry Geophysics Geosystems*, *4*(10).

Cahill, T., and B. L. Isacks (1992), Seismicity and shape of the subducted Nazca plate, *Journal of Geophysical Research*, *97*(B12), 17,503–17–529.

Chatelain, J.-L., B. Guillier, P. Gueguen, and F. Bondoux (1997), The Mw 7.7 Nasca (Peru) Earthquake, November 12, 1996: A Repetition of the 1942 Event?, *Seismological Research Letters*, *68*(6), 917–922.

Chlieh, M., J. B. de Chabalier, J. C. Ruegg, R. Armijo, R. Dmowska, J. Campos, and K. L. Feigl (2004), Crustal deformation and fault slip during the seismic cycle in the North Chile subduction zone, from GPS and InSAR observations, *Geophysical Journal International*, *158*(2), 695–711.

Chlieh, M., J. P. Avouac, K. Sieh, D. H. Natawidjaja, and J. Galetzka (2008), Heterogeneous coupling of the Sumatran megathrust constrained by geodetic and paleogeodetic measurements, *Journal of Geophysical Research*, *113*(B5), B05,305.

Chlieh, M., H. Perfettini, H. Tavera, J.-P. Avouac, D. Remy, J.-M. Nocquet, F. Rolandone, F. Bondoux, G. Gabalda, and S. Bonvalot (2011), Interseismic coupling and seismic potential along the Central Andes subduction zone, *Journal of Geophysical Research*, *116*(B12), B12,405.

Chu, R., S. Wei, D. V. Helmberger, Z. Zhan, L. Zhu, and H. Kanamori (2011), Initiation of the great M w 9.0 Tohoku–Oki earthquake, *Earth And Planetary Science Letters*, *308*(3), 277–283.

Comte, D., and M. Pardo (1991), Reappraisal of great historical earthquakes in the northern Chile and southern Peru seismic gaps, *Natural Hazards*, *4*(1), 23–44.

Comte, D., and G. Suárez (1995), Stress distribution and geometry of the subducting Nazca plate in northern Chile using teleseismically recorded earthquakes, *Geophysical Journal International*, *122*(2), 419–440.

Comte, D., J. Battaglia, C. Thurber, H. Zhang, L. Dorbath, and B. Glass (2004), High-Resolution Subducting Slab Structure Beneath Northern Chile Using the Double-Difference Tomography Method, in *AGU Fall Meeting Abstracts*, p. 0200.

Contreras-Reyes, E., and D. Carrizo (2011), Control of high oceanic features and subduction channel on earthquake ruptures along the Chile–Peru subduction zone, *Physics of the Earth and Planetary Interiors*, *186*(1), 49–58.

Contreras-Reyes, E., J. Jara, I. Grevemeyer, S. Ruiz, and D. Carrizo (2012), Abrupt change in the dip of the subducting plate beneath north Chile, *Nature Geoscience*, *5*(5), 342–345.

Cox, A., and R. B. Hart (1986), *Plate tectonics : how it works*, Palo Alto : Blackwell Scientific Publications.

David, C. (2007), Comportamiento actual del ante-arco y del arco del codo de Arica en la orogénesis de los Andes centrales, Ph.D. thesis, PhD thesis, Universidad de Chile, Santiago.

Delouis, B., A. Cisternas, L. Dorbath, L. Rivera, and E. Kausel (1996), The Andean subduction zone between 22 and 25 degrees S (northern Chile): Precise geometry and state of stress, *Tectonophysics*, *259*(1-3), 81–100.

DeMets, C., R. G. Gordon, D. F. Argus, and S. Stein (1990), Current Plate Motions, *Geophysical Journal International*, *101*(2), 425–478.

DeMets, C., R. G. Gordon, D. F. Argus, and S. Stein (1994), Effect of Recent Revisions to the Geomagnetic Reversal Time-Scale on Estimates of Current Plate Motions, *Geophysical Research Letters*, *21*(20), 2191–2194.

DeMets, C., R. G. Gordon, and D. F. Argus (2010), Geologically current plate motions, *Geophysical Journal International*, *181*(1), 1–80.

Desbrun, M., M. Meyer, P. Schröder, and A. H. Barr (1999), Implicit fairing of irregular meshes using diffusion and curvature flow, pp. 317–324.

Dong, D., P. Fang, Y. Bock, F. Webb, L. Prawirodirdjo, S. Kedar, and P. Jamason (2006), Spatiotemporal filtering using principal component analysis and Karhunen-Loeve expansion approaches for regional GPS network analysis, *Journal of Geophysical Research*, *111*(B3), B03,405.

Dorbath, L., A. Cisternas, and C. Dorbath (1990), Assessment of the size of large and great historical earthquakes in Peru, *Bulletin of the Seismological Society of America*, *80*(3), 551–576.

Dragert, H., K. Wang, and T. S. James (2001), A silent slip event on the deeper Cascadia subduction interface, *Science*, *292*(5521), 1525–1528.

Efron, B., and G. Gong (1983), A leisurely look at the bootstrap, the jackknife, and cross-validation, *The American Statistician*, *37*(1), 36–48.

El-Fiky, G. S., and T. Kato (1999), Interplate coupling in the Tohoku district, Japan, deduced from geodetic data inversion, *Journal of Geophysical Research*, *104*(B9), 20,361–20–377.

Engdahl, E. R., and A. Villaseñor (2002), Global seismicity: 1900–1999, pp. 665–690, International Handbook of Earthquake and Engineering Seismology.

Engdahl, E. R., R. van der Hilst, and R. Buland (1998), Global teleseismic earthquake relocation with improved travel times and procedures for depth determination, *Bulletin of the Seismological Society of America*, *88*(3), 722–743.

Evans, E. L., and B. J. Meade (2012), Geodetic imaging of coseismic slip and postseismic afterslip: Sparsity promoting methods applied to the great Tohoku earthquake, *Geophysical Research Letters*, *39*(11).

Fukuda, J., and K. M. Johnson (2008), A Fully Bayesian Inversion for Spatial Distribution of Fault Slip with Objective Smoothing, *Bulletin of the Seismological Society of America*, *98*(3), 1128–1146.

Giovanni, M. K., S. L. Beck, and L. Wagner (2002), The June 23, 2001 Peru earthquake and the southern Peru subduction zone, *Geophysical Research Letters*, *29*(21).

Hampel, A., N. Kukowski, J. Bialas, C. Huebscher, and R. Heinbockel (2004), Ridge subduction at an erosive margin: The collision zone of the Nazca Ridge in southern Peru, *Journal of Geophysical Research: Solid Earth (1978–2012)*, *109*(B2).

Hansen, P. C. (1998), *Rank-Deficient and Discrete Ill-Posed Problems: Numerical Aspects of Linear Inversion*, SIAM, Philadelphia.

Harris, R. A., and P. Segall (1987), Detection of a locked zone at depth on the parkfield, california, segment of the san andreas fault, *Journal of Geophysical Research: Solid Earth*, *92*(B8), 7945–7962, doi: 10.1029/JB092iB08p07945.

Hashimoto, C., A. Noda, T. Sagiya, and M. Matsu'ura (2009), Interplate seismogenic zones along the Kuril–Japan trench inferred from GPS data inversion, *Nature Geoscience*, *2*(2), 141–144.

Hastings, W. K. (1970), Monte-Carlo Sampling Methods Using Markov Chains and Their Applications, *Biometrika*, *57*(1), 97–&.

Hayes, G. P., and D. J. Wald (2009), Developing framework to constrain the geometry of the seismic rupture plane on subduction interfaces a priori–a probabilistic approach, *Geophysical Journal International*, *176*(3), 951–964.

Hayes, G. P., D. J. Wald, and K. Keranen (2009), Advancing techniques to constrain the geometry of the seismic rupture plane on subduction interfaces a priori: Higher?order functional fits, *Geochemistry Geophysics Geosystems*, *10*(9).

Heki, K. (2006), Secular, transient and seasonal crustal movements in Japan from a dense GPS array: Implication for plate dynamics in convergent boundaries, *The Seismogenic Zone of Subduction Thrust Faults*.

Heki, K., S. Miyazaki, and H. Tsuji (1997), Silent fault slip following an interplate thrust earthquake at the Japan Trench, *Nature Geoscience*, *386*, 595–598.

Hetland, E. A., and M. Simons (2010), Post-seismic and interseismic fault creep II: transient creep and interseismic stress shadows on megathrusts, *Geophysical Journal International*, *181*(1), 99–112.

Hirose, H., and K. Obara (2005), Repeating short-and long-term slow slip events with deep tremor activity around the Bungo channel region, southwest Japan, *Earth Planets and Space*, *57*(10), 961–972.

Hsu, Y.-J., M. Simons, J.-P. Avouac, J. Galetzka, K. Sieh, M. Chlieh, D. Natawidjaja, L. Prawirodirdjo, and Y. Bock (2006), Frictional afterslip following the 2005 Nias-Simeulue earthquake, Sumatra, *Science*, *312*(5782), 1921–1926.

Igarashi, T., T. Matsuzawa, N. Umino, and A. Hasegawa (2001), Spatial distribution of focal mechanisms for interplate and intraplate earthquakes associated with the subducting Pacific plate beneath the northeastern Japan arc: A triple?planed deep seismic zone, *Journal of Geophysical Research: Solid Earth (1978–2012)*, *106*(B2), 2177–2191.

Igarashi, T., T. Matsuzawa, and A. Hasegawa (2003), Repeating earthquakes and interplate aseismic slip in the northeastern Japan subduction zone, *Journal of Geophysical Research*, *108*(B5), 2249.

Iinuma, T., R. Hino, M. Kido, D. Inazu, Y. Osada, Y. Ito, M. Ohzono, H. Tsushima, S. Suzuki, H. Fujimoto, and S. Miura (2012), Coseismic slip distribution of the 2011 off the Pacific Coast of Tohoku Earthquake (M9.0) refined by means of seafloor geodetic data, *Journal of Geophysical Research*, *117*(B7), B07,409.

Ito, T., S. Yoshioka, and S. Miyazaki (1999), Interplate coupling in southwest Japan deduced from inversion analysis of GPS data, *Physics of the Earth and Planetary Interiors*, *115*(1), 17–34.

Ito, T., S. Yoshioka, and S. Miyazaki (2000), Interplate coupling in northeast Japan deduced from inversion analysis of GPS data, *Earth And Planetary Science Letters*, *176*(1), 117–130.

Ito, Y., T. Tsuji, Y. Osada, M. Kido, D. Inazu, Y. Hayashi, H. Tsushima, R. Hino, and H. Fujimoto (2011), Frontal wedge deformation near the source region of the 2011 Tohoku-Oki earthquake, *Geophysical Research Letters*, *38*(15), L00G05.

Jeffreys, S. H. (1931), *Scientific Inference*, Cambridge University Press.

Jeffreys, S. H. (1939), *Theory of Probability*, Cambridge University Press.

Johnson, K. M., J. Fukuda, and P. Segall (2012), Challenging the rate?state asperity model: Afterslip following the 2011 M9 Tohoku?oki, Japan, earthquake, *Geophysical Research Letters*, *39*(20).

Jónsson, S., H. Zebker, P. Segall, and F. Amelung (2002), Fault slip distribution of the 1999 Mw 7.1 Hector Mine, California, earthquake, estimated from satellite radar and GPS measurements, *Bulletin of the Seismological Society of America*, *92*(4), 1377–1389.

Kaneko, Y., J.-P. Avouac, and N. Lapusta (2010), Towards inferring earthquake patterns from geodetic observations of interseismic coupling, *Nature Geoscience*, *3*(5), 363–369.

Kato, A., and T. Igarashi (2012), Regional extent of the large coseismic slip zone of the 2011 Mw 9.0 Tohoku-Oki earthquake delineated by on-fault aftershocks, *Geophysical Research Letters*, *39*(15), L15,301.

Kendrick, E., M. Bevis, R. Smalley, and B. Brooks (2001), An integrated crustal velocity field for the central Andes, *Geochemistry Geophysics Geosystems*, *2*(11).

Kendrick, E., M. Bevis, R. Smalley, Jr, B. Brooks, R. B. Vargas, E. LaurÄśÌĄa, and L. P. S. Fortes (2003), The Nazca–South America Euler vector and its rate of change, *Journal of South American Earth Sciences*, *16*(2), 125–131.

Kendrick, E., B. A. Brooks, M. Bevis, R. Smalley, E. Lauria, M. Araujo, and H. Parra (2006), Active orogeny of the south-central Andes studied with GPS geodesy, *Asoc. Geol. Argent. Rev*, *61*, 555–566.

Kendrick, E. C., M. Bevis, R. F. Smalley, O. Cifuentes, and F. Galban (1999), Current rates of convergence across the central Andes: Estimates from continuous GPS observations, *Geophysical Research Letters*, *26*(5), 541–544.

Khazaradze, G., and J. Klotz (2003), ShortâĂŘand longâĂŘterm effects of GPS measured crustal deformation rates along the south central Andes, *Journal of Geophysical Research: Solid Earth (1978–2012)*, *108*(B6).

Klotz, J., G. Khazaradze, D. Angermann, C. Reigber, R. Perdomo, and O. Cifuentes (2001), Earthquake cycle dominates contemporary crustal deformation in Central and Southern Andes, *Earth And Planetary Science Letters*, *193*(3), 437–446.

Konca, A. O., J.-P. Avouac, A. Sladen, A. J. Meltzner, K. Sieh, P. Fang, Z. Li, J. Galetzka, J. Genrich, M. Chlieh, D. H. Natawidjaja, Y. Bock, E. J. Fielding, C. Ji, and D. V. Helmberger (2008), Partial rupture of a locked patch of the Sumatra megathrust during the 2007 earthquake sequence, *Nature*, *456*(7222), 631–635.

Krabbenhöft, A., J. Bialas, H. Kopp, N. Kukowski, and C. Hübscher (2004), Crustal structure of the Peruvian continental margin from wide?angle seismic studies, *Geophysical Journal International*, *159*(2), 749–764.

Larson, K. M., A. Bilich, and P. Axelrad (2007), Improving the precision of high-rate GPS, *Journal of Geophysical Research: Solid Earth*.

Larson, K. M., M. Poland, and A. Miklius (2010), Volcano monitoring using GPS: Developing data analysis strategies based on the June 2007 Kīlauea Volcano intrusion and eruption, *Journal of Geophysical Research*, *115*(B7), B07,406.

Lay, T., and H. Kanamori (1980), Earthquake doublets in the Solomon Islands, *Physics of the Earth and Planetary Interiors*, *21*(4), 283–304.

Lay, T., and H. Kanamori (1981), An asperity model of large earthquake sequences, in *Maurice Ewing Series*, pp. 579–592, American Geophysical Union, Washington, D. C.

Lay, T., C. J. Ammon, H. Kanamori, L. Xue, and M. J. Kim (2011), Possible large near-trench slip during the 2011 M (w) 9. 0 off the Pacific coast of Tohoku Earthquake, *Earth Planets and Space*, *63*(7), 687–692.

Lin, Y. N., A. Sladen, F. Ortega Culaciati, M. Simons, J.-P. Avouac, E. J. Fielding, B. A. Brooks, M. Bevis, J. Genrich, A. Rietbrock, C. Vigny, R. Smalley, and A. Socquet (2013), Coseismic and Postseismic Slip Associated with the 2010 Maule Earthquake, Chile: Characterizing the Arauco Peninsula Barrier Effect, *Journal Of Geophysical Research-Solid Earth*.

Loveless, J. P., and B. J. Meade (2010), Geodetic imaging of plate motions, slip rates, and partitioning of deformation in Japan, *Journal of Geophysical Research*, *115*(B2), B02,410.

Loveless, J. P., and B. J. Meade (2011), Spatial correlation of interseismic coupling and coseismic rupture extent of the 2011 M W= 9.0 Tohoku-oki earthquake, *Geophysical Research Letters*, *38*(17), L17,306.

Mazzotti, S., X. Le Pichon, P. Henry, and S. I. Miyazaki (2000), Full interseismic locking of the Nankai and JapanâĂŘwest Kurile subduction zones: An analysis of uniform elastic strain accumulation in Japan constrained by permanent GPS, *Journal of Geophysical Research: Solid Earth (1978–2012)*, *105*(B6), 13,159–13,177.

McCaffrey, R., R. W. King, S. J. Payne, and M. Lancaster (2013), Active tectonics of northwestern US inferred from GPSâĂŘderived surface velocities, *Journal Of Geophysical Research-Solid Earth*.

Meade, B. J., and B. H. Hager (2005), Block models of crustal motion in southern California constrained by GPS measurements, *Journal of Geophysical Research: Solid Earth (1978–2012)*, *110*(B3).

Meng, L., J. P. Ampuero, Y. Luo, W. Wu, and S. Ni (2012), Mitigating artifacts in back-projection source imaging with implications for frequency-dependent properties of the Tohoku-Oki earthquake, *Earth Planets and Space*, *64*, 1101–1109.

Menke, W. (2012), *Geophysical Data Analysis: Discrete Inverse Theory - MATLAB Edition*, Elsevier.

Miller, M. M., T. Melbourne, D. J. Johnson, and W. Q. Sumner (2002), Periodic slow earthquakes from the Cascadia subduction zone, *Science*, *295*(5564), 2423–2423.

Minoura, K., F. Imamura, D. Sugawara, Y. Kono, and T. Iwashita (2001), The 869 Jogan tsunami deposit and recurrence interval of large-scale tsunami on the Pacific coast of northeast Japan, *Journal of Natural Disaster Science*, *23*(2), 83–88.

Minson, S. (2010), A Bayesian approach to earthquake source studies, Ph.D. thesis, California Institute of Technology.

Minson, S. E., M. Simons, and J. L. Beck (2013), Bayesian inversion for finite fault earthquake source models I — Theory and algorithm , *Geophysical Journal International*, pp. 1–36.

Miyazaki, S., T. Saito, M. Sasaki, Y. Hatanaka, and Y. Iimura (1997), Expansion of GSI's nationwide GPS array, *Bull. Geogr. Surv. Inst.*, *43*, 23–34.

Moreno, M. S., J. Bolte, J. Klotz, and D. Melnick (2009), Impact of megathrust geometry on inversion of coseismic slip from geodetic data: Application to the 1960 Chile earthquake, *Geophysical Research Letters*, *36*(16).

Mosegaard, K., and A. Tarantola (2002), Probabilistic Approach to Inverse Problems, pp. 237–265, International Handbook of Earthquake and Engineering Seismology.

Munekane, H. (2012), Coseismic and early postseismic slips associated with the 2011 off the Pacific coast of Tohoku Earthquake sequence: EOF analysis of GPS kinematic time series, *Earth Planets and Space*.

Nadeau, R. M., and L. R. Johnson (1998), Seismological studies at Parkfield VI: Moment release rates and estimates of source parameters for small repeating earthquakes, *Bulletin of the Seismological Society of America*, *88*(3), 790–814.

Nakajima, J., A. Hasegawa, and S. Kita (2011), Seismic evidence for reactivation of a buried hydrated fault in the Pacific slab by the 2011 M9. 0 Tohoku earthquake, *Geophysical Research Letters*, *38*(null), L00G06.

Nakayama, W., and M. Takeo (1997), Slip history of the 1994 Sanriku-Haruka-Oki, Japan, earthquake deduced from strong-motion data, *Bulletin of the Seismological Society of America*, *87*(4), 918–931.

Nishimura, T., S. Miura, K. Tachibana, K. Hashimoto, T. Sato, S. Hori, E. Murakami, T. Kono, K. Nida, and M. Mishina (2000), Distribution of seismic coupling on the subducting plate boundary in northeastern Japan inferred from GPS observations, *Tectonophysics*, *323*(3), 217–238.

Nishimura, T., T. Hirasawa, S. Miyazaki, T. Sagiya, T. Tada, S. Miura, and K. Tanaka (2004), Temporal change of interplate coupling in northeastern Japan during 1995–2002 estimated from continuous GPS observations, *Geophysical Journal International*, *157*(2), 901–916.

Nishimura, T., H. Munekane, and H. Yarai (2011), The 2011 off the Pacific coast of Tohoku Earthquake and its aftershocks observed by GEONET, *Earth Planets and Space*, *63*(7), 631–636.

Norabuena, E. O., T. H. Dixon, S. Stein, and C. Harrison (1999), Decelerating Nazca-South America and Nazca-Pacific Plate motions, *Geophysical Research Letters*, *26*(22), 3405–3408.

Okada, Y. (1985), Surface Deformation Due to Shear and Tensile Faults in a Half-Space, *Bulletin of the Seismological Society of America*, *75*(4), 1135–1154.

Oncken, O., E. LuÈschen, J. Mechie, S. Sobolev, A. Schulze, C. Gaedicke, S. Grunewald, J. Bribach, G. Asch, and P. Giese (1999), Seismic reflection image revealing offset of Andean subduction-zone earthquake locations into oceanic mantle, *Nature*, *397*(6717), 341–344.

Owen, S., P. Segall, M. Lisowski, A. Miklius, M. Murray, M. Bevis, and J. Foster (2000), January 30, 1997 eruptive event on Kilauea Volcano, Hawaii, as monitored by continuous GPS, *Geophysical Research Letters*, *27*(17), 2757–2760.

Ozawa, S., S. Miyazaki, Y. Hatanaka, T. Imakiire, M. Kaidzu, and M. Murakami (2003), Characteristic silent earthquakes in the eastern part of the Boso peninsula, Central Japan, *Geophysical Research Letters*, *30*(6).

Ozawa, S., Y. Hatanaka, M. Kaidzu, M. Murakami, T. Imakiire, and Y. Ishigaki (2004), Aseismic slip and low?frequency earthquakes in the Bungo channel, southwestern Japan, *Geophysical Research Letters*, *31*(7).

Ozawa, S., T. Nishimura, H. Suito, T. Kobayashi, M. Tobita, and T. Imakiire (2011), Coseismic and postseismic slip of the 2011 magnitude-9 Tohoku-Oki earthquake, *Nature*, *475*(7356), 373–376.

Ozawa, S., T. Nishimura, H. Munekane, H. Suito, T. Kobayashi, M. Tobita, and T. Imakiire (2012), Preceding, coseismic, and postseismic slips of the 2011 Tohoku earthquake, Japan, *Journal of Geophysical Research: Solid Earth (1978–2012)*, *117*(B7).

Ozawa, T., T. Tabei, and S. I. Miyazaki (1999), Interplate coupling along the Nankai Trough off southwest Japan derived from GPS measurements, *Geophysical Research Letters*, *26*(7), 927–930.

Pardo-Casas, F., and P. Molnar (1987), Relative motion of the Nazca (Farallon) and South American plates since Late Cretaceous time, *Tectonics*, *6*(3), 233–248.

Perfettini, H., and J. P. Avouac (2004), Postseismic relaxation driven by brittle creep: A possible mechanism to reconcile geodetic measurements and the decay rate of aftershocks, application to the Chi-Chi earthquake, Taiwan, *Journal of Geophysical Research: Solid Earth (1978–2012)*, *109*(B2).

Perfettini, H., J.-P. Avouac, H. Tavera, A. Kositsky, J.-M. Nocquet, F. Bondoux, M. Chlieh, A. Sladen, L. Audin, D. L. Farber, and P. Soler (2010), Seismic and aseismic slip on the Central Peru megathrust, *Nature*, *465*(7294), 78–81.

Pollitz, F. F., R. Bürgmann, and P. Banerjee (2011), Geodetic slip model of the 2011 M9. 0 Tohoku earthquake, *Geophysical Research Letters*, *38*(7).

Pritchard, M. E., M. Simons, P. A. Rosen, S. Hensley, and F. H. Webb (2002), Co?seismic slip from the 1995 July 30 Mw= 8.1 Antofagasta, Chile, earthquake as constrained by InSAR and GPS observations, *Geophysical Journal International*, *150*(2), 362–376.

Pritchard, M. E., E. O. Norabuena, C. Ji, R. Boroschek, D. Comte, M. Simons, T. H. Dixon, and P. A. Rosen (2007), Geodetic, teleseismic, and strong motion constraints on slip from recent southern Peru subduction zone earthquakes, *Journal of Geophysical Research*, *112*(B3), B03,307.

Puskas, C. M., R. B. Smith, C. M. Meertens, and W. L. Chang (2007), Crustal deformation of the Yellowstone–Snake River Plain volcanoâĂŘtectonic system: Campaign and continuous GPS observations, 1987–2004, *Journal of Geophysical Research: Solid Earth (1978–2012)*, *112*(B3).

Radiguet, M., F. Cotton, M. Vergnolle, M. Campillo, B. Valette, V. Kostoglodov, and N. Cotte (2011), Spatial and temporal evolution of a long term slow slip event: the 2006 Guerrero Slow Slip Event, *Geophysical Journal International*, *184*(2), 816–828.

Rice, J. R., and J.-c. Gu (1983), Earthquake aftereffects and triggered seismic phenomena, *Pure and Applied Geophysics PAGEOPH*, *121*(2), 187–219.

Sagiya, T. (2004), Interplate coupling in the Kanto district, central Japan, and the Boso Peninsula silent earthquake in May 1996, *Pure and applied Geophysics*, pp. 2327–2342.

Sagiya, T., S. Miyazaki, and T. Tada (2000), Continuous GPS array and present-day crustal deformation of Japan, *Pure and applied Geophysics*, *157*(11-12), 2303–2322.

Sato, M., T. Ishikawa, N. Ujihara, S. Yoshida, M. Fujita, M. Mochizuki, and A. Asada (2011), Displacement Above the Hypocenter of the 2011 Tohoku-Oki Earthquake, *Science*, *332*(6036), 1395–1395.

Savage, J. C. (1983), A Dislocation Model of Strain Accumulation and Release at a Subduction Zone, *Journal of Geophysical Research*, *88*(NB6), 4984–4996.

Scholz, C. H. (2002), *The Mechanics of Earthquakes and Faulting*, Cambridge University Press, Cambridge, UK.

Segall, P. (2010), *Earthquake and Volcano Deformation*, Princeton University Press.

Segall, P., and R. Harris (1987), Earthquake deformation cycle on the San Andreas Fault near Parkfield, California, *Journal of Geophysical Research*, *92*(B10), 10,511.

Sella, G. F., T. H. Dixon, and A. Mao (2002), REVEL: A model for recent plate velocities from space geodesy, *Journal of Geophysical Research*, *107*(B4), 2081.

Shinohara, M., Y. Machida, T. Yamada, K. Nakahigashi, T. Shinbo, K. Mochizuki, Y. Murai, R. Hino, Y. Ito, T. Sato, H. Shiobara, K. Uehira, H. Yakiwara, K. Obana, N. Takahashi, S. Kodaira, K. Hirata, H. Tsushima, and T. Iwasaki (2012), Precise aftershock distribution of the 2011

off the Pacific coast of Tohoku Earthquake revealed by an ocean-bottom seismometer network, *Earth Planets Space*, pp. 1137–1148.

Simons, M., S. E. Minson, A. Sladen, F. Ortega, J. Jiang, S. E. Owen, L. Meng, J.-P. Ampuero, S. Wei, and R. Chu (2011), The 2011 magnitude 9.0 tohoku-oki earthquake: Mosaicking the megathrust from seconds to centuries, *Science*, *332*(6036), 1421–1425.

Sladen, A., H. Tavera, M. Simons, J. P. Avouac, A. O. Konca, H. Perfettini, L. Audin, E. J. Fielding, F. Ortega, and R. Cavagnoud (2010), Source model of the 2007 Mw 8.0 Pisco, Peru earthquake: Implications for seismogenic behavior of subduction megathrusts, *Journal of Geophysical Research*, *115*(B2), B02,405.

Somoza, R. (1998), Updated Nazca (Farallon)—South America relative motions during the last 40 My: implications for mountain building in the central Andean region, *Journal of South American Earth Sciences*, *11*(3), 211–215.

Suárez, G., and D. Comte (1993), Seismic Coupling Along the Chilean Subduction Zone - Comment, *Journal of Geophysical Research*, *98*(B9), 15,825–15,828.

Suwa, Y., S. Miura, A. Hasegawa, T. Sato, and K. Tachibana (2006), Interplate coupling beneath NE Japan inferred from three-dimensional displacement field, *Journal of Geophysical Research*, *111*(B4), B04,402.

Taira, A. (2001), Tectonic evolution of the Japanese island arc system, *Annual Review of Earth and Planetary Sciences*, *29*(1), 109–134.

Takahashi, N., S. Kodaira, T. Tsuru, J.-O. Park, Y. Kaneda, K. Suyehiro, H. Kinoshita, S. Abe, M. Nishino, and R. Hino (2004), Seismic structure and seismogenesis off Sanriku region, northeastern Japan, *Geophysical Journal International*, *159*(1), 129–145.

Tarantola, A. (2005), *Inverse problem theory and methods for model parameter estimation*, Society for Industrial and Applied Mathematics.

Tarantola, A., and B. Valette (1982), Inverse problems= quest for information, *Journal of Geophysics*, *50*(3), 150–170.

Tassara, A., H. J. Götze, S. Schmidt, and R. Hackney (2006), Three?dimensional density model of the Nazca plate and the Andean continental margin, *Journal of Geophysical Research: Solid Earth (1978–2012)*, *111*(B9).

Tichelaar, B. W., and L. J. Ruff (1991), Seismic coupling along the Chilean subduction zone, *Journal of Geophysical Research: Solid Earth (1978–2012)*, *96*(B7), 11,997–12,022.

Tichelaar, B. W., and L. J. Ruff (1993), Depth of seismic coupling along subduction zones, *Journal of Geophysical Research*, *98*(B2), 2017.

Vigny, C., A. Socquet, S. Peyrat, J. C. Ruegg, M. Metois, R. Madariaga, S. Morvan, M. Lancieri, R. Lacassin, J. Campos, D. Carrizo, M. Béjar-Pizarro, S. Barrientos, R. Armijo, C. Aranda, M. C. Valderas-Bermejo, I. Ortega, F. Bondoux, S. Baize, H. Lyon-Caen, A. Pavez, J. P. Vilotte, M. Bevis, B. Brooks, R. Smalley, H. Parra, J. C. Baez, M. Blanco, S. Cimbaro, and E. Kendrick (2011), The 2010 Mw 8.8 Maule Megathrust Earthquake of Central Chile, Monitored by GPS, *Science*, *332*(6036), 1417–1421.

Yagi, Y., T. Mikumo, J. Pacheco, and G. Reyes (2004), Source rupture process of the Tecomán, Colima, Mexico earthquake of 22 January 2003, determined by joint inversion of teleseismic body-wave and near-source data, *Bulletin of the Seismological Society of America*, *56*(5), 1795–1807.

Ye, L., T. Lay, and H. Kanamori (2012), The Sanriku-Oki low-seismicity region on the northern mar-

gin of the great 2011 Tohoku-Oki earthquake rupture, *Journal of Geophysical Research*, *117*(B2), B02,305.

Yue, H., and T. Lay (2011), Inversion of high - rate (1 sps) GPS data for rupture process of the 11 March 2011 Tohoku earthquake (Mw 9.1), *Geophysical Research Letters*, *38*(7).